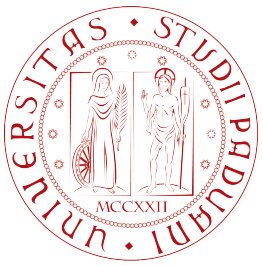

UNIVERSITÀ
DEGLI STUDI
DI PADOVA

Universitá degli Studi di Padova

Dipartimento di Fisica e Astronomia "GALILEO GALILEI"
Corso di Dottorato in Astronomia
Ciclo XXXIV

Study of Pulsars and their Environments through Very High Energy Gamma-ray Observations

Dottoranda:
Alessia Spolon

Coordinatore: Prof. Giovanni Carraro
Supervisore: Prof. Mose' Mariotti
Co-Supervisori: Dott. Rubén López-Coto
Dott. Luca Zampieri

PER ASPERA
AD ASTRA

Study of Pulsars and their Environments through Very High Energy Gamma-ray Observations

Abstract

This thesis illustrates the activities and the results that I have performed during my PhD course at the University of Padova. My work was mainly focused on the study of some classes of Galactic sources: *pulsars*, *millisecond pulsars* and *transitional millisecond pulsars* in the most energetic part of the electromagnetic spectrum, the Very-High-Energy (VHE), >100 GeV, gamma ray regime.

Pulsars are very dense (about 10^{18} kg/m^3), extremely magnetized (10^7–10^{15} G) and rapidly rotating neutron stars, formed after supernova explosions. A standard pulsar has a mass of 1.44 $M_\odot$ and a radius of about 10 km. Most known pulsars are observed in radio but they can also produce detectable optical, X-ray and gamma-ray pulsations, up to the VHE range. Pulsars show complex behaviors and in particular the underlying mechanism by which they emit electromagnetic radiation is still not fully understood. Thanks to their coherent radiation, emitted in the form of collimated beams from the two magnetic poles, they can be exploited as special natural laboratories for fundamental Physics.

Some pulsars rotate at an incredible rate of a few hundred times per second, making them the fastest-spinning stars known in the Universe. They are the so-called Millisecond Pulsars (MSPs). Generally, they have spin-periods of 1–30 ms and lower magnetic fields than standard pulsars (10^7 –10^{10} G). They are "recycled" pulsars that are accreting on already accreted matter and angular momentum from a companion star in a binary system. In particular, there is a class of MSPs, the Transitional MSPs (tMSPs), that are neutron stars rotating at a period of a few milliseconds and undergoing transitions between two states: a bright X-ray pulsar regime powered by the accretion onto the neutron star surface of matter transferred by the companion star and a radio (and possibly gamma-ray) pulsar regime powered by the energy loss due to the fast rotation of the neutron star magnetic field. The transitions between the two regimes take place on short time-scales of less than a few weeks.

My research is mainly focused on searching the VHE emission and gamma-ray pulsation from two of the best pulsars candidates for VHE gamma-ray emission: PSR J0218+4232 (a MSP) and PSR J2229+6114 (a regular pulsar). Up to now, only three pulsars have been detected at VHE: the Crab Pulsar (Aliu et al., 2008), the Vela Pulsar (H. E. S. S. Collaboration et al., 2018a) and, very recently, the Geminga Pulsar (MAGIC Collaboration et al., 2020). In particular I used data taken with the Major Atmospheric Gamma-ray Imaging Cherenkov (MAGIC) telescopes located at the Observatory of the Roque de Los Muchachos in the Canary Island of La Palma. The data were taken with the Sum-Trigger-II system which has an energy threshold of about tens of GeV, in order to increase the detection efficiency at the lowest energies reached by MAGIC. This system is extremely useful to detect soft VHE gamma-ray sources, such as pulsars.

In the search for pulsed emission from both sources, PSR J0218+4232 and PSR J2229+6114, no signal or pulsed emission above 20 GeV was found with the MAGIC telescopes. The sources were also studied using *Fermi*-LAT: PSR J0218+4232 shows high energy pulsed emission above 25 GeV and PSR J2229+6114 above 20 GeV.

During my PhD I dedicated a part of the time also to the study of the prospects for VHE gamma-ray emission from tMSPs, in particular from the two systems PSR J1023+0038 and XSS J12270-4859, during their accretion disk state. I studied their *Fermi*-LAT emission considering different spectral models and then I investigated the feasibility to detect them with the future Cherenkov Telescope Array (CTA) and the prospect for studying them.

Study of Pulsars and their Environments through Very High Energy Gamma-ray Observations

Sommario

Questa Tesi illustra le attività ed i risultati che ho ottenuto durante il mio corso di dottorato presso l'Università degli Studi di Padova. Il mio lavoro si è concentrato principalmente sullo studio di alcune classi di sorgenti Galattiche che emettono nella parte più energetica dello spettro elettromagnetico, le altissime energie VHE (>100 GeV): *pulsars*, *millisecond pulsars* e *transitional millisecond pulsars*.
Le pulsars sono stelle di neutroni estremamente dense (circa 10^{18} kg/m^3) e in rapida rotazione che si formano durante l'esplosione di una stella massiccia ed altamente magnetizzata (10^7-10^{15}G). Una pulsar standard ha una massa di 1.44 $M_\odot$ e un raggio di circa 10 km. Le pulsars più conosciute emettono nella banda radio ma possono anche produrre pulsazioni ottiche, X e gamma, fino al range delle VHE. Mostrano comportamenti complessi e, ad oggi, il meccanismo con cui emettono non è stato ancora del tutto compreso. Grazie alla loro radiazione coerente emessa sotto forma di fasci collimati uscenti dai due poli magnetici, le pulsar possono essere sfruttate come speciali laboratori per studiare la Fisica fondamentale.
Alcune di queste pulsars ruotano ad una velocità incredibile, alcune centinaia di volte al secondo, diventando così le sorgenti che ruotano più velocemente nell'Universo e che per questo vengono definite pulsars al millisecondo, MSPs. In generale hanno periodi di rotazione di 1−30 ms e dei campi magnetici più deboli rispetto alle pulsars normali (10^7-10^{10} G). Sono pulsars "riciclate" che acquistano materia e momento angolare dalla stella compagna. Esiste poi una particolare classe di MSP: le tMSPs. Sono sorgenti che periodicamente passano da una fase in cui si comportano come MSP radio a una fase in cui la pulsazione radio si spegne e si comportano come sistemi binari in accrescimento in cui la stella di neutroni inizia a risucchiare materia dalla compagna, cambiando radicalmente la sua fenomenologia. La transizione tra i due stati avviene in tempi brevi, dell'ordine di quache settimana.
Il mio lavoro è principalmente dedicato allo studio dell'emissione VHE e alla ricerca di pulsazione gamma da parte di due sorgenti candidate ad emettere questo tipo di emissione: PSR J0218+4232 (una MSP) e PSR J2229+6114 (una pulsar regolare). Ad oggi sono state rilevate solo tre pulsars nel range delle altissime energie: Crab Pulsar (Aliu et al., 2008), Vela Pulsar (H. E. S. S. Collaboration et al., 2018a) e, molto recentemente, Geminga Pulsar (MAGIC Collaboration et al., 2020). In particolare, ho lavorato sui dati raccolti con i telescopi MAGIC situati presso l'Osservatorio di Roque de Los Muchachos nell'isola delle Canarie di La Palma. I dati sono stati presi con il *Sum-Trigger-II*, un sistema di trigger che, con una soglia di energia di decine di GeV, è in grado di aumentare l'efficienza dei telescopi MAGIC alle più basse energie. Questo sistema è utile per rilevare sorgenti gamma estremamente deboli, come le pulsar. Purtroppo con i telescopi MAGIC non è stato trovato alcun segnale, o emissione pulsata, superiore a 20 GeV, proveniente dalle due sorgenti. Le due sorgenti sono state inoltre osservate e studiate anche utilizzando i dati raccolti dal satellite *Fermi*-LAT e da quest'analisi risulta che PSR J0218+4232 ha un'emissione pulsata superiore ai 25 GeV, mentre PSR J2229+6114 superiore ai 20 GeV.
Una parte del dottorato l'ho dedicata allo studio delle prospettive di emissione delle tMSPs nel range delle altissime energie, in particolare da parte di PSR J1023+0038 e XSS J12270-4859 durante il loro stato di accrescimento. Ho studiato i dati raccolti dal satellite *Fermi*-LAT considerando diversi modelli spettrali per poi studiare la possibilità di rilevarli con il futuro CTA.

Outline of the Thesis

In Chapter 1 I give a general introduction to cosmic and gamma-ray astronomy. I introduce the basic principles of gamma-ray production, extinction and detection, and I briefly explain the most prominent gamma-ray emitters in the Universe.

In Chapter 2 I explain how cosmic rays, as well as for gamma-ray photons, interact with the Earth's atmosphere, which forms the base technique for their indirect detection from ground. The imaging Cherenkov technique is explained, and also how the Imaging Atmospheric Cherenkov Telescopes (IACTs) work, giving a particular attention to the software and hardware of the MAGIC telescopes. The general and non standard analysis processes of the data taken by this instrument are also detailed. Finally, I summarize the status of the CTA project, and mention its main features.

Chapter 3 explains the basic principles of the physics of pulsars and describes the specific characteristics of the Crab pulsar, together with the current theories that explain its emission focusing at the highest energies. In this chapter I present the MAGIC analysis of the Crab Pulsar that I performed on data taken with the Sum-Trigger-II system. In the last section of this chapter I give a brief description of the other classes of pulsars considered here: MSPs and tMSPs.

Chapter 4 is dedicated to pulsar PSR J2229+6114, also known as the Boomerang pulsar, which is a candidate to emit VHE gamma ray. After a general and multiwavelength introduction to the source, the MAGIC analysis, performed on Sum-Trigger-II data, is presented.

In Chapter 5 I report the work done on the MSP PSR J0218+4232, also presented in the paper by Acciari et al. (2021). After an introduction on the source, the *Fermi*-LAT and MAGIC analyses are presented. In the last section I discuss the possible models that can explain the high and very high energy emission from this source.

Chapter 6 is dedicated to two tMSP systems: PSR J1023+0038 and XSS J12270-4859, and their prospects for detection with the future CTA. The analysis is based on the results obtained for both of them using observations of lower energy performed with the *Fermi*-LAT. In particular, I present also the first independent confirmation of the optical pulsations in PSR J1023+0038 that we detected with the fast photon counter Aqueye+ mounted at the Copernicus telescope in Asiago (Zampieri et al., 2019).

Chapter 7 contains a summary of the aforementioned results on the analyses that I perform with the MAGIC telescopes and on the CTA simulations. An outlook is also given on the possibilities offered by the next generation gamma-ray observatory CTA.

Contents

List of Figures

List of Tables

Part I

Introduction to the non-thermal Universe

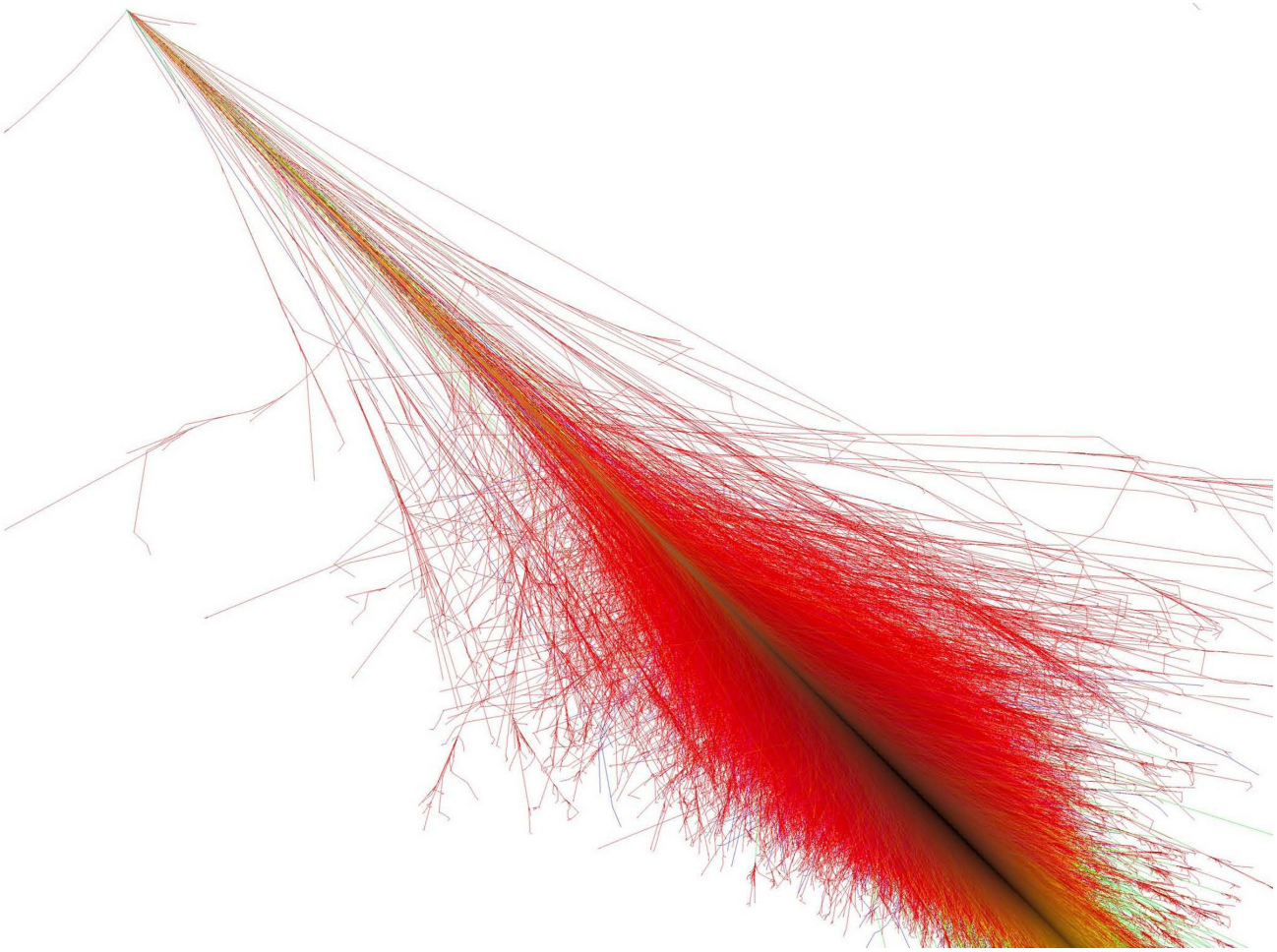

Figure 1 Air shower. Credit: Fabian Schmidt.

1

Cosmic ray and gamma-ray Astronomy

GAMMA-RAY ASTROPHYSICS is a relatively recent branch in Astronomy and the discovery of the Cosmic Rays (CRs) was a milestone for the Physics of the 20th century. The crucial measurements in the discovery of CRs were carried out between 1908 and 1912 by the Italian physicist Domenico Pacini, who in 1911 showed that ionization decreased under water (Pacini, 1912), and by the Austrian Viktor Francis Hess, who demonstrated, thanks to the use of the balloon, that the ionization increased with altitude (Hess, 1912). This radiation was called *Cosmic Rays* by Robert Millikan, in order to refer to all radiation and particles coming from outside the Earth's atmosphere (Millikan & Cameron, 1926).

CRs are composed almost completely of atomic nuclei and a small fraction of electrons and positrons. To date, their origin is still largely unknown and finding the sources of the most energetic CRs, with energies $\gtrsim 10^{15}$ eV, is a very active

research field. One of the characteristics of CRs is that they are composed of both charged and neutral particles. The charged particles are continuously deflected by the magnetic fields that they encounter during their journey to Earth, making it challenging to trace their origin directly to their sources. The best way to get information on the origin of CRs is to study the neutral particles, like neutrinos and gamma rays, that can travel through the Universe without being deflected by the magnetic fields.

In this first chapter I will introduce the processes and sources from which these VHE gamma rays (e.g. > 100 GeV) originate. Furthermore, I will briefly describe the current generations of VHE gamma-ray detectors.

1.1 Cosmic Rays

The term CRs is used to refer to the energetic particles arriving from outside the Earth's atmosphere. They constitute an important fraction of the energy budget of the Universe, hence the importance of the study of their composition, energy range and fluxes. CRs include all naturals elements of the periodic table and many sub-atomic particles: they are composed of 99% of atomic nuclei and 1% of electrons and positrons. Concerning the nuclei, about 89% are hydrogen (protons), 10% are helium (alpha particles) with the remaining 1% made up of heavier elements, which are the final products of the stellar nucleosynthesis.

CRs can be detected by direct experiments (balloons or satellites), and normally these techniques explore CRs up to 10^{14} eV. At higher energies they can be studied by indirect observations in ground-based experiments. These detectors observe the secondary particles produced in Extended Air Showers (EASs), i.e. cascades of particles created by the interaction of primary CRs with the nuclei of the Earth's atmosphere. These EASs, first detected by Pierre Auger in 1938, can extend in areas of tens of thousands of square meters on the ground (Auger et al., 1939). The study of CRs led to important discoveries, such as the existence of the positron (e^+), muons and pions.

1.1.1 Spectrum

CRs, as mentioned in the previous section, are mostly charged particles coming from the space. Their energy spectrum, shown in Figure 1.1, has been measured with very high precision and it extends over almost 13 orders of magnitude in energy (from 10^8 to $\sim 10^{21}$ eV) and 33 orders of magnitude in flux. It can be described by a series of power-law distributions of the type:

$$dN/dE \propto E^{-\Gamma} \tag{1.1}$$

where Γ is the *spectral index*. For energies under $\sim$ 1 GeV, the CR flux consists of charged particles of solar origin. These particles are strongly modulated by the solar wind and, for this reason, the spectrum is difficult to determine and cannot be described by a simple power laws function. In particular, the amount of cosmic radiation reaching Earth is inversely correlated with the number of sunspots through the 11-year solar cycle. Furthermore, the trajectories of the lowest-energy CR primaries are strongly influenced by Earth's magnetic field.

The rest of the spectrum is well defined by power-laws with three different spectral indices, where the different slopes are related to the different origin of the processes that are producing such emission.

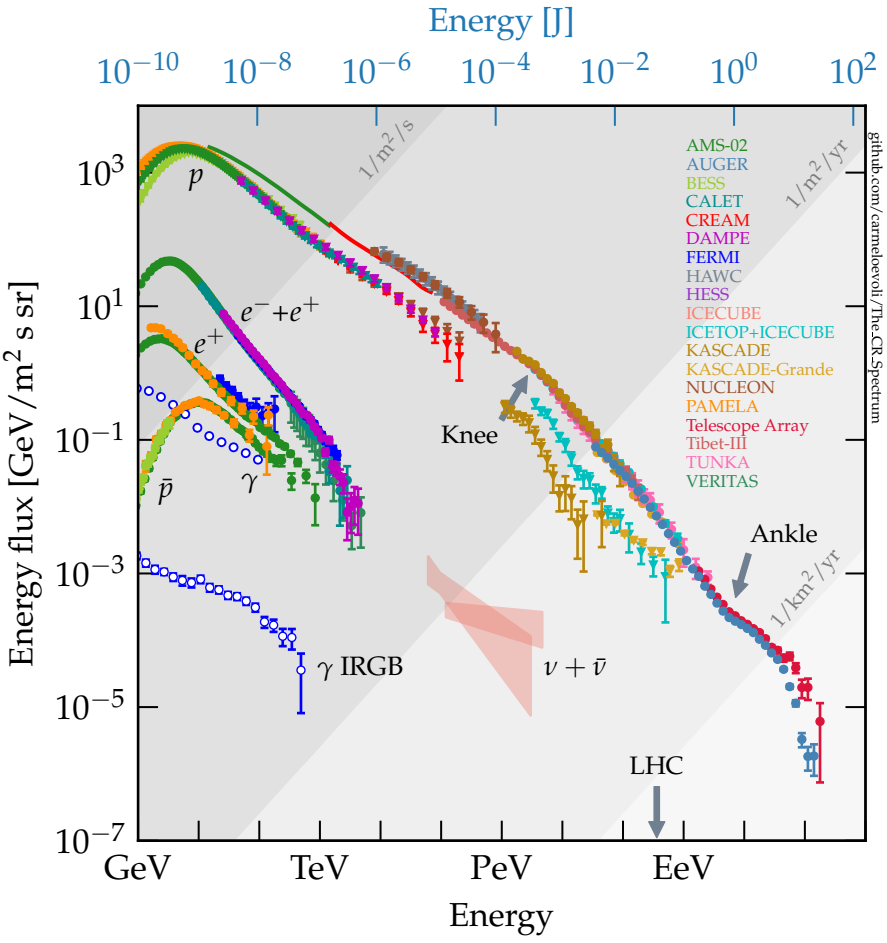

Figure 1.1 CR spectrum obtained with data from different experiments. Prominent features like the knee and the ankle are highlighted. Figure from Evoli (2018).

The first part, from $\sim$ 100 MeV up to $\sim$ 5 PeV, presents a photon index of $\Gamma \sim 2.7$. At that point, the spectrum presents a bend known as the *knee*. This upper limit depends on the charge: particles with higher charge will extend the *knee* to higher energies. After the *knee*, there is again a constant region with $\Gamma \sim 3$ up to about 3 EeV. This part of the spectrum ends with a new hardening that is known as the *ankle*. Finally, beyond the last part of the *ankle* at about 3 EeV, the spectrum hardens again with $\Gamma \sim 2.6$ up to about 30 EeV (Tomozawa, 2013).

The processes that generate such spectrum are still partially unknown. Particles with energies up to the *knee* are thought to be accelerated inside our Galaxy, while particles above the *ankle* likely have extragalactic origin. Between the *knee* and the *ankle*, the origin of cosmic rays is not clear and is currently under debate. Various theories have been proposed to explain the steepening of the spectrum at the *knee*: changes in the acceleration mechanism (for example a different acceleration in Supernova Remnants (SNRs) with one at the shock front and a new re-acceleration in the inner pulsar-driven remnant, Bell (1992)); leakage of CRs out of the Galaxy by diffuse propagation (Ptuskin et al., 1993).

The study of CRs above the *ankle* is particularly difficult due to the extremely low flux (roughly one particle per square kilometer per century at 10^{20} eV) and, at these energies, the measurement of the CR spectrum requires experiments of extraordinary sensitivity. Even the most powerful accelerator on Earth, the Large Hadron Collider (LHC), is able to produce particles only up to $\sim 10^{14}$ eV, more than seven orders of magnitude lower than what would be needed to study the highest energies of CRs. In particular, CRs of energies above 10^{14} eV are difficult to measure by direct experiments (balloons and satellites) because they have very small areas and therefore do not detect enough particles. So, at higher energies, CRs can be detected only indirectly on the ground through the cascade of secondary particles they produce, i.e. through the he detection of so-called *air showers* (see Section 2.1 for a detailed explanation).

The GZK Effect

At the extremely High Energy (HE) edge (E>100 MeV), the CR spectrum is affected by the so-called Greisen-Zatsepin-Kuzmin (GZK) cut-off. This effect is produced by the interaction of the Ultra High Energy Cosmic Rays (UHECRs)

(with energies $\gtrsim 10^{20}$ eV) with the Cosmic Microwave Background (CMB) radiation* through reactions like:

$$\gamma_{CMB} + p \rightarrow \Delta^{+} \rightarrow n + \pi^{+} \tag{1.2}$$

or

$$\gamma_{CMB} + p \rightarrow \Delta^{+} \rightarrow p + \pi^{0} \tag{1.3}$$

The interaction of Ultra High Energy (UHE) protons with the low-energy background photons forms a Δ^{+} resonance. The Δ is a family of barions with masses close to 1232 MeV and they quickly decay through the strong force into a nucleon (proton or neutron) and a pion of appropriate charge. While in the first process, Eq. 1.2, a neutron is created, in the second reaction, Eq. 1.3, the proton is still a result of the equation. In the latter process, where the proton transfers part of its energy to the pion, the resulting GZK cut-off is lower, reaching a few 10^{19} eV.

This interaction with CMB photons leads to absorption of the CRs, that limits to about 50 Mpc the maximum distance that the UHECRs of energies above 10^{18} eV, can travel (Greisen, 1966; Zatsepin & Kuz'min, 1966); in this way these extragalactic CRs should never be observed on Earth. The absorption of these UHECRs confirms the presence of the GZK effect, and also the cosmic-ray propagation through the Universe.

1.1.2 Acceleration Mechanisms

Variable magnetic fields could induce variable electric fields that can accelerate charged CRs. These acceleration processes can be subdivided into two main mechanisms, proposed by Enrico Fermi: *first order* and *second order* Fermi acceleration (Fermi, 1949); they differ in the characteristics of the moving plasma.

- ◇ ***First Order* Fermi acceleration**. The acceleration occurs in a plasma with inhomogeneities between shock waves and magnetic field. Every time that particles, deflected by the magnetic field, cross the shock wave, they get accelerated. The energy gained in each passage is proportional to the relative velocity between the shock and the particle and, the larger the relative velocity, the larger the energy gain. The number of multiple scatterings

*The CMB radiation is the residual electromagnetic energy from the Big Bang. Its spectrum is described by the Planck black body function, with a characteristic temperature of 2.7 K and a density of 415 photons cm^{-3}. The mean photon energy is $E_0 = 6.4 \times 10^{-4}$ eV, in the microwave region of the spectrum.

through the shock wave is directly proportional to the magnetic field strength. This mechanism is very efficient and it is supposed to be responsible for the acceleration of particles up to TeV and PeV.

- ◇ ***Second Order* Fermi acceleration**. This acceleration occurs in magnetized clouds which move randomly and act as "magnetic mirrors", so the particles are reflected off them. Compared to the *First Order*, in this process the directions of the shock wave are randomly distributed. So, if the front of the magnetic field is moving towards the particle, after the reflection the energy increases. The energy gained by the particles in each reflection on average is proportional to the square of the speed of the moving cloud.

When a particle escapes from the accelerating region, it will not be able to gain more energy. Its maximum energy, E_{max}, is related to the *Larmor radius* or *gyroradius*: the radius of the circular motion under the presence of an uniform magnetic field. In particular, the gyroradius cannot exceed the size of the acceleration region, otherwise the particle would not be confined in this acceleration region anymore. This geometrical constraint is known as the *Hillas criterion*. This E_{max} can be expressed as follows:

$$E_{max} = q \, \frac{R}{\text{kpc}} \frac{B}{\mu G} \, 10^{18} \text{eV} \tag{1.4}$$

where q is the charge of the particle, R is the radius and B the magnetic field of the acceleration region.
This equation is represented with the so-called *Hillas plot*, shown in Figure 1.2, illustrating the relation between the magnetic field strength and the radius of the acceleration region. The diagonal lines define the allowed region for the acceleration of CRs at different energies. Objects below each line cannot accelerate those particles up to the indicated energies. From the *Hillas plot* we can conclude that Galactic sources are not able to produce CRs above 10^{15} eV; and so, for the highest energy CRs, one should search for extragalactic sources.

1.2 Gamma-ray Astrophysics

Gamma rays, photons with the highest energies, are produced in the acceleration of CRs or in their interaction with the environment. Their spectrum extends beyond $\sim$ 1 MeV, which is the minimum energy to produce gamma rays in the electron/positron annihilation ($2 \times m_e = 2 \times 0.511$ MeV, where m_e is the mass of the electron). Gamma rays can reach extremely high energies (> PeVs), thus thermal mechanisms cannot be responsible for their production. In particular, the interaction of CRs and gamma rays with their environment can be of three types: interaction with

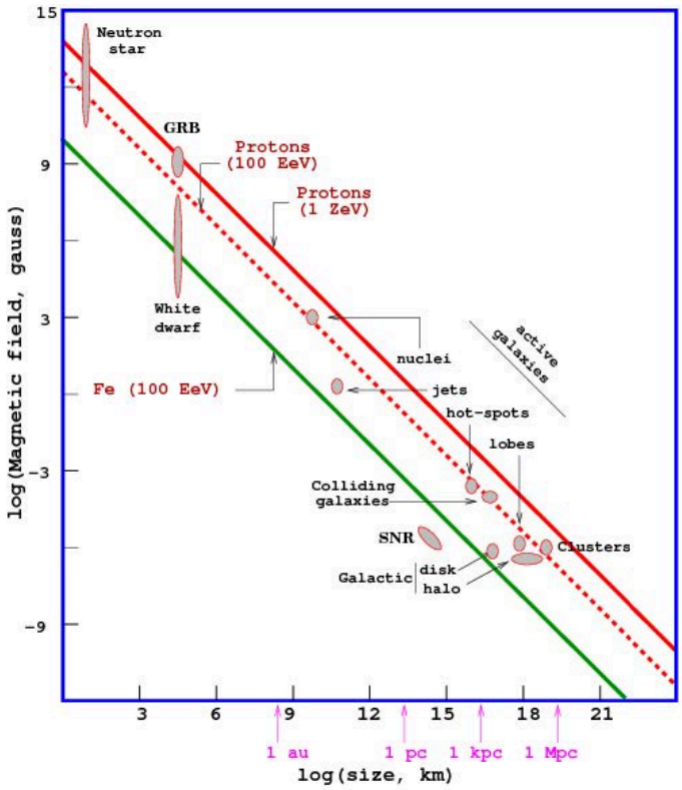

Figure 1.2 The *Hillas plot* describes the possible sources of CRs as a function of their magnetic field strength and size. The lines indicate the allowed acceleration region for different particles at a maximum energy (solid red line for protons with E_{max} = 1 ZeV = 10^{21} eV, dashed red line for protons with E_{max} = 100 EeV = 10^{20} eV, and solid green line for Fe nuclei with E_{max} = 100 EeV). Sources below each line cannot produce CRs with an energy larger than the indicated value. From Hillas (1984).

matter, interaction with magnetic fields and interaction with photon fields. The processes that produce gamma rays are presented in Section 1.2.1; their absorption processes are described in Section 1.2.2.

1.2.1 Gamma-ray Production

In this section I will give a brief description of the various mechanisms involved in astrophysical gamma-ray production. A more detailed description can be found in Longair (2011) and Aharonian et al. (2004).

1.2.1.1 Bremsstrahlung

Bremsstrahlung emission, also called *free-free* emission, is the electromagnetic radiation produced by the interaction of charged particles (e.g. electrons) with the electric field created by ions and atomic nuclei of an ionized gas. When electrons interact with the electric field, they are decelerated, change their trajectory and lose energy in the form of gamma rays (Figure 1.3). This mechanism becomes dominant against ionization when a *critical energy* is reached, defined as the energy at which the energy loss by the two mechanisms is equal. The *bremsstrahlung* energy loss depends on the distance travelled by the electron in the medium, and is expressed as:

$$-\frac{dE}{dx} = \frac{1}{\chi_0} E \tag{1.5}$$

where χ_0 is the *radiation length*, and represents the average distance over which the particle loses $1/e$ of its energy due to *bremsstrahlung*. The radiation length depends on the material: the higher the density of the material, the lower the distance to which the particle can penetrate, and the smaller the radiation length. Since the energy loss is directly proportional to the energy of the charged particle, the *bremsstrahlung* mechanism produces a gamma-ray spectrum that follows the same distribution as that of the charged particles. This is an important mechanism to produce VHE gamma rays through *bremsstrahlung* of UHE charged particles.

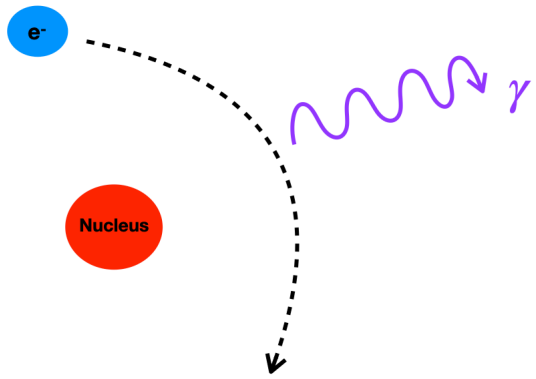

Figure 1.3 Illustration of the Bremsstrahlung mechanism.

1.2.1.2 Electron/positron Annihilation

This process occurs when an electron collides with its antiparticle and vice versa (see Fig. 1.4):

$$e^- + e^+ \rightarrow \gamma + \gamma \tag{1.6}$$

The total energy of the two photons in the center-of-momentum frame of reference is equal to the combined rest–mass energy of the electron–positron pair, $2m_e c^2 \sim 1.022$ MeV. If an electron and a positron are essentially at rest, upon annihilation two gamma rays of equal energy (0.511 MeV) are produced. The simplest possible source of positrons is the direct decay of positive pions; another possibility would be the creation of electron-positrons pairs through photon-photon annihilation or also in the decay of long-lived radioactive isotopes produced for example in the Supernovae (SNe) nucleosynthesis.

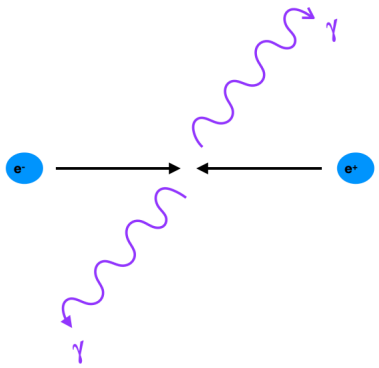

Figure 1.4 Illustration of the electron-positron annihilation.

1.2.1.3 Neutral Pion Decay

The neutral pion π^0 has a rest mass of 135 MeV and a very short lifetime (8.4×10^{-17} s); thus, it quickly decays into two gamma rays (see Figure 1.5), with 99% probability:

$$\pi^0 \rightarrow \gamma + \gamma \tag{1.7}$$

It also has a probability of 1% to decay producing an $e^- e^+$ pair:

$$\pi^0 \rightarrow e^- + e^+ + \gamma \tag{1.8}$$

Each photon in Eq. 1.7 carries half of the particle energy (i.e. 67.5 MeV), and in the case of relativistic pions, these photons are beamed in the same direction of the primary particle.

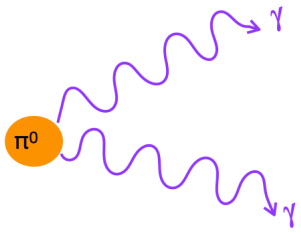

Figure 1.5 Illustration of the neutral Pion Decay.

1.2.1.4 Synchrotron Radiation

When a charged particle embedded in a magnetic field moves in a curved path, it emits electromagnetic radiation and is continuously accelerated by the Lorentz force that makes it rotate around the magnetic field lines (see Figure 1.6). This acceleration causes emission of electromagnetic radiation. If the velocity of the particle is non-relativistic this radiation is called *cyclotron radiation*. Instead, when the motion of the particle becomes relativistic, the emission is named *synchrotron radiation*.

The radiation frequency is given by the relation $\omega = \frac{qB}{mc}$, where q is the electric charge of the particle and m its mass. Synchrotron radiation is emitted along the tangent of the circular motion and is concentrated in a narrow cone of width $1/\gamma$, where $\gamma = \frac{1}{\sqrt{1-\frac{v^2}{c^2}}}$ is the Lorentz factor. The relation between the kinetic energy of the particle and that of the emitted photons can be expressed through:

$$\frac{dE}{dt} = -\sigma_T c U_B \gamma^2 \tag{1.9}$$

where σ_T is the Thomson cross-section and U_B is the magnetic energy. In particular, assuming a uniform magnetic field and that the bulk of the electrons are mono-energetic, the synchrotron gamma-ray spectrum would peak at:

$$E_\gamma \sim 1.5 \times 10^{-5} \left(\frac{B_\perp}{[G]}\right) \left(\frac{E_e}{[TeV]}\right)^2 \tag{1.10}$$

where E_e is the energy of the electrons and $B_\perp$ the perpendicular component of the magnetic field. Normally, the synchrotron emission does not reach VHE, but these emitted photons are very interesting because they are the targets for Inverse Compton (IC) up-scattering (see Section 1.2.1.5).

If the particles follow the curved magnetic field lines, instead of spiraling around them, the emission process is called *curvature radiation*.

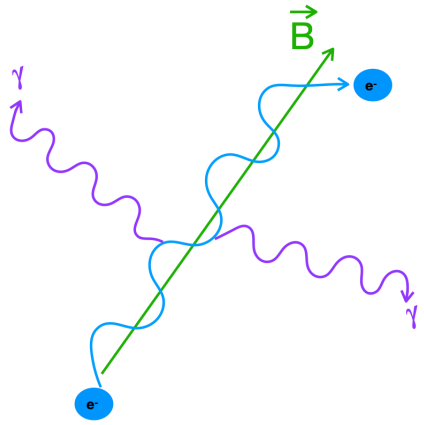

Figure 1.6 Illustration of the synchrotron radiation mechanism.

1.2.1.5 Inverse Compton

The Inverse Compton process is an interaction between relativistic electrons and low-energy photons: the electron transfers part of its energy to the photon, that is re-emitted at higher energy (see Figure 1.7). The process is called *inverse* because the electrons lose energy rather than the photons, the opposite of the standard Compton effect. This is the most effective mechanism for the production of VHE gamma rays. Depending on the initial energy of the electrons (E_e) and the photons (E_γ), we can distinguish two regimes (Longair, 2002):

- The *Thomson regime*, also called non-relativistic regime, occurs when $E_\gamma E_e \ll m_e^2 c^4$. The process has a constant

cross-section, the Thomson cross-section: $\sigma_T = \frac{8}{3}\pi r_e^2$, where r_e is the classical electron radius. Assuming a power-law distribution for the electrons with an index Γ_e, the up-scattered gamma-ray spectrum follows a power-law function with index $\Gamma = (\Gamma_e + 1/2)$. The electron energy losses are proportional to E_e^2.

◇ The *Klein-Nishina regime*, or relativistic regime, happens when the energy of electrons becomes very high and they become relativistic, with $E_\gamma E_e \simeq m_e^2 c^4$. The cross-section in this regime is:

$$\sigma_{KN} = 2\pi r_e^2 \left\{ \frac{1+\varepsilon}{\varepsilon} \left[\frac{2+2\varepsilon}{1+2\varepsilon} - \frac{\ln(1+2\varepsilon)}{\varepsilon} \right] + \frac{\ln(1+2\varepsilon)}{2\varepsilon} - \frac{1+3\varepsilon}{(1+3\varepsilon)^2} \right\} \tag{1.11}$$

where $\varepsilon = E_\gamma / m_e c^2$. If $E_\gamma E_e \gg m_e^2 c^4$, the Klein-Nishina approximation applies: $\sigma_{KN,approx} = \frac{\pi r_e^2}{\varepsilon}[\ln(2\varepsilon) + \frac{1}{2}]$. If the electron spectrum is again described by a power-law with index Γ_e, the resulting gamma-ray spectrum is considerably steeper with a photon index $\Gamma = \Gamma_e + 1$. The energy loss, independent of the electron energy, is proportional to the density of photons (De Angelis & Pimenta, 2018).

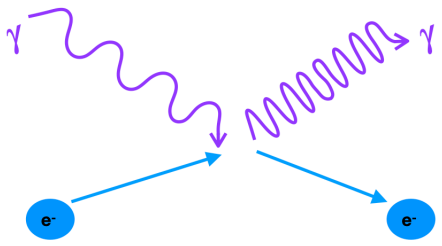

Figure 1.7 Illustration of the Inverse Compton scattering mechanism.

1.2.1.6 Synchrotron Self-Compton

The Synchrotron Self Compton (SSC) emission mechanism is a combination of the previous two mechanisms, where the synchrotron emission by ultra-relativistic electrons is so efficient that a very intense radiation field is created. These photons become the targets for the IC scattering by the same charged particles that produced them in the first place, thus photons are able to reach higher energies than in a simple synchrotron emission process.

1.2.2 Gamma-ray Absorption

1.2.2.1 Pair Production

Pair production, the inverse process of the pair annihilation mechanism described in Section 1.2.1.2, plays a crucial role in gamma-ray astrophysics. The interaction between a HE photon with a lower energy are results in the production of an electron and a positron:

$$\gamma + \gamma \rightarrow e^- + e^+ \tag{1.12}$$

The cross-section of the pair production has a peak at:

$$E_{\gamma_1} E_{\gamma_2} (1 - cos\theta) \sim 2(m_e c^2)^2 \tag{1.13}$$

where E_{γ_1} and E_{γ_2} are the energy of the photons that are colliding with an angle θ, and $m_e = 0.511$ MeV is the electron mass. This process is responsible for the attenuation of extragalactic VHE photons by the Extragalactic Background Light (EBL).

1.2.3 Gamma-ray Sources

At present, the VHE sky, shown in Figure 1.8, counts almost 250 sources. The gamma-ray sources can be divided into two main groups: Galactic and extra-galactic. In this section I briefly describe the gamma-ray characteristics of these sources.

1.2.3.1 Galactic Sources

- **SNRs**

  SN explosions occur at the end of the life of massive stars ($M \gtrsim 8 M_\odot$) and in this event the outer layers of the star are ejected; they expand into the interstellar medium travelling through space for thousands of years forming a shell structure, or a SNR, visible at different wavelengths. Non-thermal gamma-ray emission is produced by the population of relativistic particles (leptons and hadrons) that are accelerated in the SN shocks through the *first order Fermi acceleration* mechanism. In particular, the VHE emission can be explained by IC scattering on energetic leptons (leptonic scenario) and/or by neutral pion decay (hadronic scenario). Several SNRs have

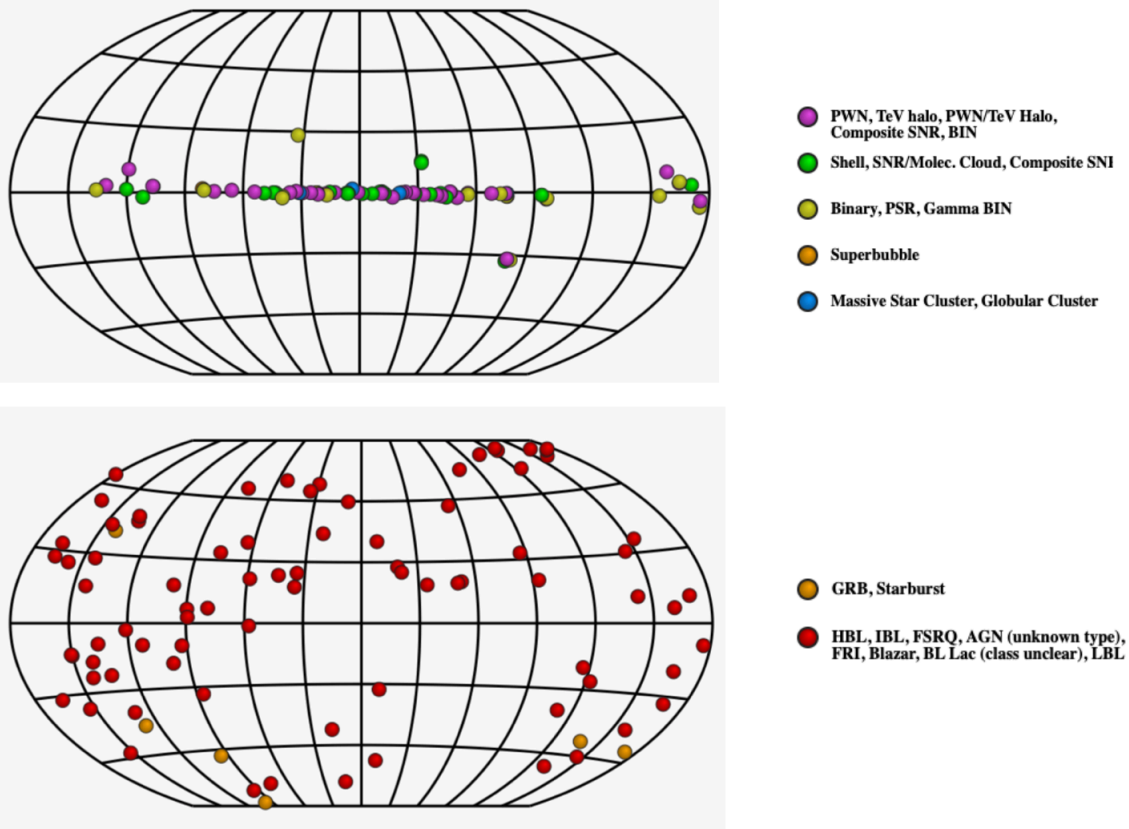

Figure 1.8 Map of the 229 VHE sources detected up to February 2021 (excluding unidentified sources). Galactic sources are in the upper panel, extragalactic ones are in the lower panel (http://tevcat2.uchicago.edu).

been detected in VHE gamma rays: RX J1713.7−3846 (Muraishi et al., 2000), Vela Junior (RX J0852.0-4622) (Katagiri et al., 2005), Cas A (Aharonian et al., 2001), Tycho (Atoyan & Dermer, 2012) (see Figure 1.9b) and SN 1006 (Naumann-Godó et al., 2008).

- **Pulsars**

  Pulsars are isolated Neutron Stars (NSs) with a strong magnetic field and powered by rotation: the pulsar's rotational energy is converted into the relativistic motion of electrons and positrons, which produce narrow beams of photons up to a few TeV. This beam is visible only when it crosses our light of sight because the magnetic field lines and the rotation axis of the NS are not usually aligned. The most famous VHE pulsar, and the first detected, is the Crab pulsar, discovered with the MAGIC telescope in 2008 (Aliu et al., 2008); its pulsed emission above 100 GeV was first detected with the VERITAS telescopes (McCann, 2011). Only recently it was

detected up to TeV energies (Ansoldi et al., 2016) (see Figure 1.9-b). Only two other pulsars have been detected in the VHE gamma-ray band: the Vela pulsar (H. E. S. S. Collaboration et al., 2018b), and very recently the Geminga pulsar (MAGIC Collaboration et al., 2020), at energies up to 75 GeV. H.E.S.S.-II detected pulsed emission also from PSR B1706−44 in the sub-100 GeV energy range (Spir-Jacob et al., 2019a). Gamma-ray pulsars, the subject of this Thesis, will be extensively discussed in Chapter 3.

- **Pulsar Wind Nebulae (PWNe)**

  PWNe are very bright TeV sources. They are highly magnetized nebulae powered by young and energetic pulsars. The energetic emission coming from the inner part of many SNRs is believed to be produced by a wind of relativistic charged particles originating from the pulsar magnetosphere and moving inside a magnetic field. The leptons inside the nebulae, which come from the pulsar magnetosphere and are accelerated up to relativistic velocities, interact with magnetic and radiation fields producing non-thermal emission up to hundreds of TeV. Gamma rays are produced through IC scattering of ambient photons by accelerated electrons. There are more than thirty PWNe observed so far at VHE making them the most numerous class of detected VHE Galactic objects. The brightest and most studied PWN is the Crab Nebula (see Figure 1.9b) which is used as a standard reference for TeV observations; this source will be presented in Chapter 3.

- **Gamma-ray binaries**

  These systems are composed of a compact object (like a NS or a Black Hole (BH)) and a donor star, that can be a low-mass star (Low Mass X-ray Binaries (LMXBs)) or a high-mass star (High Mass X-ray Binaries (HMXBs)). Gamma-ray binaries have been detected from radio up to TeV gamma-rays but most of their emission is radiated in the 1-1000 MeV band, hence their name. The emission above 1 MeV dominates their spectral energy distribution, disregarding the black-body-like component from the companion star. In particular, the gamma-ray emission sometimes is modulated at the orbital period. Two different models have been proposed for them: the *microquasars* and the *pulsar wind* models (see Figure 1.9-c). In the *microquasar* scenario the compact object accretes matter from the stellar wind and part of energy released in the accretion disk is expelled in a relativistic jet. The VHE emission can come from an accretion disc (in the jet) or from the termination shock of the jet with the Interstellar Medium (ISM). In the *pulsar wind* scenario instead, the VHE emission can originate in the intra-binary shock between the relativistic wind of the pulsar and the stellar wind (Dubus, 2013). Up to now, only 10 gamma-ray binaries are regularly observed at TeV energies (Dubus, 2013; Chernyakova et al., 2019);

including PSR B1259−63 (Aharonian et al., 2005), HESS J0632+057 (Aharonian et al., 2007), LS 5039 (Aharonian et al., 2006), LS I+61°303 (Acciari et al., 2008). A particular class of LMXBs, which can potentially emit VHE photons, the tMSPs, will be described in Chapter 6.

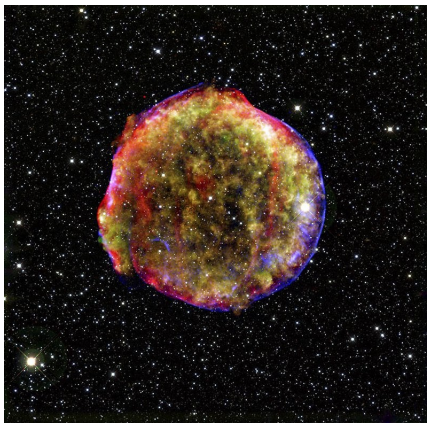

(a) Composite image of the Tycho SNR, located in the Cassiopeia constellation. Credit to NASA

(b) Multiwavelength view of the Crab Nebula and the Crab pulsar (the bright spot at the centre of the image). Credit to NASA and ESA.

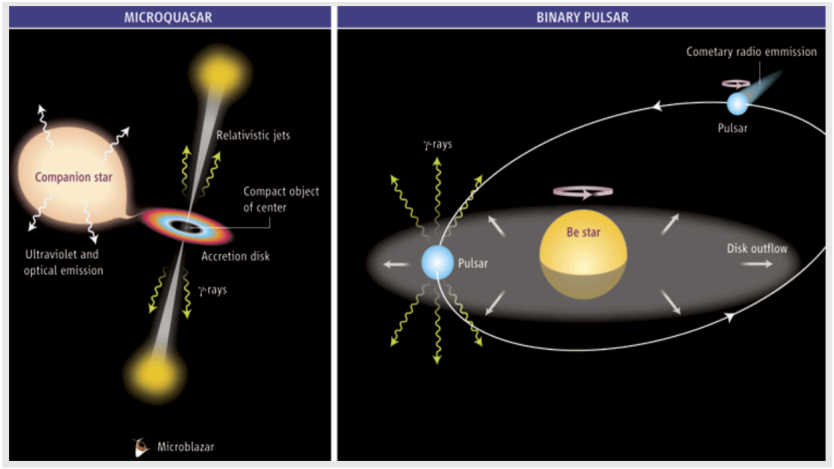

(c) The two models of binary star systems emitting gamma rays. Left: the *microquasar* scenario, right: the *pulsar wind* scenario. Credit to Mirabel (2006).

Figure 1.9 Galactic gamma-ray sources.

1.2.3.2 Extragalactic Sources

- **Active Galactic Nuclei (AGN)**

  These extragalactic emitters are gamma-ray galaxies with a Supermassive Black Holes (SMBHs) at the center

($M_{BH} \gtrsim 10^7$ $M_\odot$) that feeds two relativistic bipolar jets (see Figure 1.10-a). The material from the SMBHs is ejected to speed near the speed of light up to hundreds of kiloparsecs out of the host galaxy. The gamma-ray emission originates both in the accretion disk around the SMBHs and along the ultra-relativistic jets, where charged particles are accelerated.

- **Starburst Galaxies**

  These galaxies are regions with a very high star formation rate, and consequently, with a large SN explosion rate (see Figure 1.10-b). Here, both extragalactic cosmic rays with energy up to 10^{16} eV and VHE gamma-ray photons are produced. To date, only two Starburst galaxies have been detected at VHE: M82 (VERITAS Collaboration et al., 2009), and NGC 253 (Abramowski et al., 2012).

- **Gamma-ray Bursts**

  Gamma-Ray Bursts (GRBs) are the most luminous sources of electromagnetic radiation known in the Universe, which release an incredibly large amount of radiation in a very short time (see Figure 1.10-c). GRBs are produced by relativistic outflows of plasma ejected by newborn NSs or stellar BHs. We can distinguish two classes of GRBs (compact star origin or massive star origin) (Li et al., 2016):

  – short GRBs, typically with duration less than 2 seconds, are believed to be products of compact star mergers, i.e., NS-NS or NS-BH mergers;

  – long GRBs, typically with duration between 2 seconds and several minutes, are supposed to originate from core-collapse of massive stars > 30 $M_\odot$ in general.

  The first GRB observed with the MAGIC telescopes, GRB 190114C event, was detected on January 14^{th} 2019 with a total significance $>50\sigma$ at energies exceeding 100 GeV (MAGIC Collaboration et al., 2019). It was first identified as a long GRB by the *Swift*-BAT instrument and the *Fermi*-GBM instrument at T_0 = 20:57:03 Universal Time. The afterglow following the prompt emission was detected at all wavelengths from radio up to gamma rays. An early estimate of the redshift was reported as being $z = 0.4245 \pm 0.0005$[†]. Triggered by the *Swift*-BAT alert, the MAGIC telescopes – thanks to the automatic repointing of the telescope specifically allowed by the light weight of their structure – observed the GRB 190114C event from T_0 + 57 seconds until T_0 + 15912 seconds. At the moment in which the telescopes started observations, the camera was flooded by signal

[†] https://gcn.gsfc.nasa.gov/gcn3/23695.gcn3

and an off-line analysis reported the detection of gamma rays above 300 GeV.

In the past two years, three GRBs (GRB 180720B, 190114C and 190829A) have been detected at VHE (Fraija et al., 2019; MAGIC Collaboration et al., 2019; de Naurois, 2019).

(a) Artistic illustration of ultra-relativistic jets emitted from a SMBH at the center of an active galaxy. Credit: ESA/Hubble, L. Calçada (ESO).

(b) M82 is an example of a starburst galaxy. Credits: NASA, ESA and the Hubble Heritage Team.

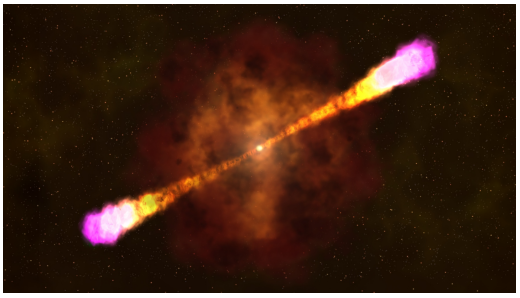

(c) A typical GRB illustration. Credits: NASA.

Figure 1.10 Some extragalactic gamma-ray sources.

1.2.4 Gamma-ray Detection Techniques

The detection of gamma-ray photons is complicated because they are completely absorbed by the Earth's atmosphere, as illustrated in Figure 1.11. In particular, gamma rays with energy $\lesssim 50$ GeV can be efficiently detected by balloons or satellites at high altitude (at about 40 km for balloons and at about 500 km for satellites), while VHE gamma rays can only be indirectly detected by ground-based telescopes. The detection of VHE gamma-ray photons is limited due to their very low flux (a few gamma rays per square meter per year above 1 TeV, for strong sources) and the very short duration of signal flashes ($\sim$ 2ns); this requires very fast and sensitive acquisition systems because space-based instruments are not very efficient due to the limited collection areas of the detector (of the order of 1m^2) (de Naurois & Mazin,

2015). Only the huge collection area of the ground-based telescopes (of the order of 10^5 m^2) make these instruments able to detect photons at the highest energies.

In the following section I will briefly summarize the three different techniques to detect HE and VHE gamma rays: satellites, Water Cherenkov arrays, and IACTs.

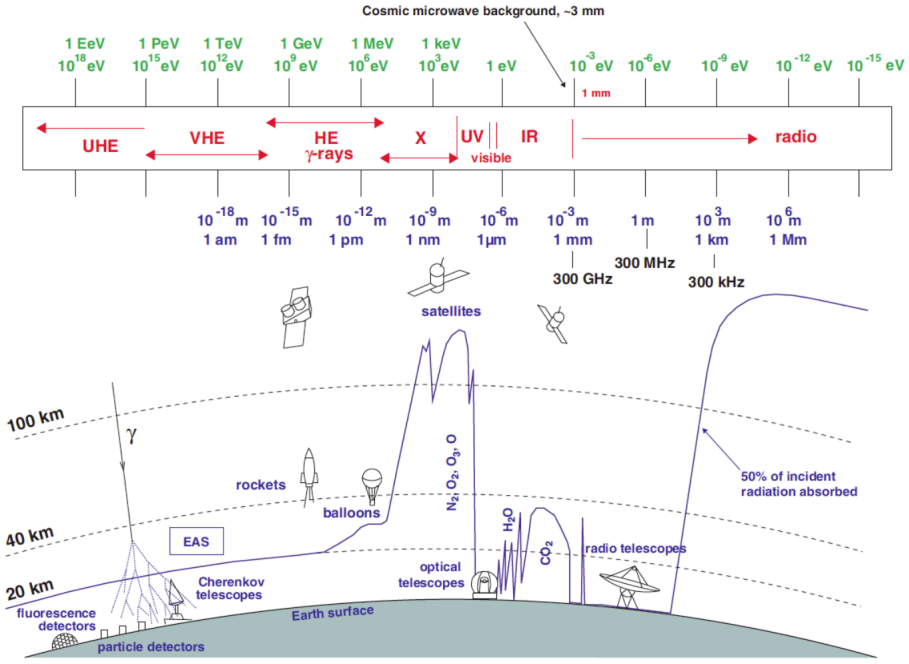

Figure 1.11 Illustration of the electromagnetic spectrum and its corresponding telescopes or observation techniques. The heights at which photons of different energy are completely absorbed by the Earth's atmosphere are also reported. We can see that the HE gamma rays are detected by instruments on high altitude balloons or satellite instead, the VHE and UHE gamma rays are indirectly observed from ground through the absorption process in the atmosphere producing a so-called EAS. Plot adapted form Longair (2011).

1.2.4.1 Satellites

The main characteristics of space satellites are: the effective area, the energy resolution and the angular or spatial resolution (the Point Spread Function (PSF)). As discussed in Section 1.2.4, these telescopes detect primary photons at lower energies than ground-based telescopes because they have a small effective area, which limits their sensitivity. They have a high duty cycle and their energy resolution is very good, with small systematic errors and a low level of background. Currently there are two main gamma-ray satellites in operation: AGILE (Tavani et al., 2009) and *Fermi*-LAT (Atwood

et al., 2009).

The *Fermi* satellite was launched in June 2008 and it consists of two instruments: the Large Area Telescope (LAT), covering an energy range from $\sim$ 50 MeV to $\sim$ 300 GeV, and the Gamma-ray Burst Monitor (GBM), which reaches up to $\sim$ 10-25 MeV. The satellite orbits at a height of about 565 km with a period of $\sim$ 95 minutes, and it completes an entire scan of the sky every two orbits. The scientific aims of the LAT are to understand the nature of the unidentified gamma-ray sources and the origin of the diffuse Galactic emission, the acceleration mechanisms of the particles, and the HE behavior of GRBs and transient sources. The production of $e^- e^+$ pairs at the time of the interaction of VHE photons with matter is the physical principle on which the satellite is based. In particular, the charged particles pass through layers of silicon and tungsten detectors giving rise to an ionization process that produces small, but measurable, pulses of electrical charge. By combining the information from different detector layers, it is possible to reconstruct the path of the particles and therefore, of the primary gamma photons. Then, the particles are carried inside an electromagnetic calorimeter, consisting of a scintillator material (Thallium doped cesium iodide, CsI(Tl), Scintillating Crystal), which allows to measure the total energy of the electrical charges. Finally, the tracker is surrounded by an anti-coincidence detector for the rejection of the cosmic rays.

Figure 1.12 An artistic impression of the *Fermi* satellite with its Large Area Telescope (LAT) shown on the top. Image credit: NASA.

1.2.4.2 Water Cherenkov Detector Arrays

The water Cherenkov technique is able to directly detect the particles of the air shower that reach the ground; and in particular, the median energy of these telescopes, which are arrays of particle counters on the ground, is rather high depending on the altitude of the observatory. When the particles traverse the water, they produce Cherenkov light that can be detected via Photomultiplier tubes and so, through the study of the development of the shower, it is possible to

reconstruct their incoming direction and energy.

One example of a water Cherenkov array is the *High Altitude Water Cherenkov (HAWC)* detector (see Figure 1.13), inaugurated in 2015 and located in the Sierra Negra in Mexico (4100 m). HAWC uses 300 opaque water tanks with a diameter of $\sim$ 7.3 m and 4.5 m in height arranged in a compact layout resulting in a detector area of about 22000 m^2. In late 2018, the HAWC collaboration completed a major upgrade consisting of the addition of a sparse outrigger array of 345 small water Cherenkov detectors surrounding the 300 water tanks of the main array and extending the instrumented area by a factor of 4 (Marandon et al., 2019). With this new sparse outrigger array the reconstruction of those events improved and also the instrument sensitivity improved. The observatory is sensitive to gamma rays ranging from a few hundreds GeV up to about 100 TeV, with an instantaneous field of view of $\sim$ 2 sr and a duty cycle of more than 95%. Those two characteristics compensate the smaller instantaneous sensitivity compared to the imaging atmospheric Cherenkov technique, especially at the highest energies for which fluxes tend to be low. This makes this instrument very well suited to the hunt for sources that can accelerate particles up to the knee of the cosmic ray spectrum ($\sim 10^{15}$ eV) (Marandon et al., 2019).

The *Large High Altitude Air Shower Observatory (LHAASO)* is located in Daocheng, Sichuan, China at 4410 m above sea level. It comprises an array of 5242 electromagnetic detectors and 1188 muon detectors, an array of 18 wide field-of-view Cherenkov telescopes, and 3120 water cherenkov detector units (Kang et al., 2020). A considerable part of the LHAASO detectors have been operating since 2019 and the whole array will be completed in 2021 (Aharonian et al., 2020). LHAASO combines multiple cosmic ray detection technologies for exploring the origin of cosmic rays and it is well-suited for gamma ray energies above 10 TeV. This Observatory is 3.5 time larger and 300 m higher than HAWC and the effective area is an order of magnitude higher than HAWC at energy of 30 GeV. To improve the LHAASO sensitivity at low threshold energy, a larger Photomultiplier Tubes (PMT) with a diameter of 20 inch it is instrumented in the water Cherenkov pool (Kang et al., 2020).

In general, these water detectors have a high duty cycle and a large field-of-view, but a relatively low sensitivity. The energy threshold of such detectors is rather large —a shower initiated by a 1 TeV photon typically has its maximum at about 8 km a.s.l. (De Angelis & Pimenta, 2018). The energy threshold is at best in the 0.5–1 TeV range, so they are built to detect UHE photons as well as the most energetic VHE gammas. At such energies fluxes are small and large surfaces of order of 10^4 m^2 are required. Photons traveling through the water typically undergo Compton scattering or produce an electron–positron pair, also resulting in Cherenkov light emission and this is an advantage of the water

Cherenkov technique, as photons constitute a large fraction of the electromagnetic component of an air shower at ground (De Angelis & Pimenta, 2018).

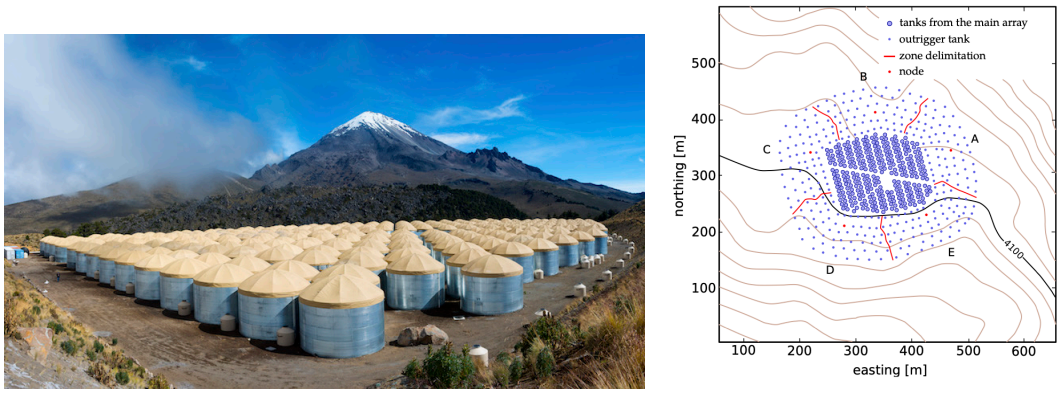

Figure 1.13 **Left**: the HAWC Observatory. Credit: J. Goodman. **Right**: Top view sketch of the HAWC main and outrigger array. The red dots represent the nodes that contain the readout electronics and power supply for each tanks. From Marandon et al. (2019).

1.2.4.3 Imaging Atmospheric Cherenkov Telescopes (IACTs)

Ground-based telescopes use the Imaging atmospheric Cherenkov technique in order to detect gamma rays above some hundreds of GeV. Atmospheric showers, generated by the interaction of a primary gamma ray with nuclei in the atmosphere, are detected through their emitted Cherenkov light. These telescopes use the atmosphere as an indirect detector of gamma rays: this increases both the collection area, up to several square kilometers, and also the energy reach. This technique will be extensively discussed in Chapter 2. IACTs cannot operate during daytime (the PMTs used are extremely sensitive, up to point that they could be damaged if exposed to daylight, Carrasco-Casado et al. (2013)), and only few of them can be operated during moderate Moonlight conditions.

Current major IACTs are H.E.S.S. (Funk et al., 2004), VERITAS (Holder et al., 2008) and MAGIC (Bigongiari, 2005). H.E.S.S. is a system of 5 Cherenkov telescopes located in Namibia sensitive to gamma rays between 100 GeV and 100 TeV. It consists of four telescopes with a dish size of 12m in diameter and one telescope of 28m. VERITAS is an array of four Cherenkov telescopes of 12 meters in diameter sensitive to energies between 85 GeV and 50 TeV. It has been located on Mount Hopkins in Arizona, USA, since 2007. I will discuss extensively the MAGIC telescopes, shown in Figure 1.14, in Section 2.2.

Figure 1.14 The MAGIC telescopes. Image taken from the web page of the MAGIC Collaboration. Credit: Daniel López/IAC.

2

Imaging Atmospheric Cherenkov Telescopes

The first source of VHE gamma rays, the Crab Nebula, was detected by the Whipple telescope in the 1980s (Weekes et al., 1989). This new type of instrument and data analysis became the basis for IACTs and kicked off the current generation of Cherenkov telescopes. In this chapter, I describe in detail the hardware and software of the MAGIC telescopes. In addition, I present an overview of the future generation of Cherenkov telescopes: the CTA. I start with a short overview of the imaging atmospheric Cherenkov technique and describe the two physical phenomena that enable the ground-based astronomy in the VHE band: EASs and Cherenkov radiation.

2.1 Air showers and atmospheric Cherenkov radiation

2.1.1 Cherenkov Light

When a VHE gamma ray enters the Earth's atmosphere, it interacts with one of its molecules producing a cascade of energetic particles, the so-called EASs. For a detailed description see Section 2.1.2. These cascades, formed by neutral and charged particles, travel faster than the speed of light in the atmosphere and, during their path to the ground, they produce the *Cherenkov radiation*, whose wavelength ranges from 300 to 500 nm, with a peak at about 320 nm, in the Ultraviolet (UV) band. The Cherenkov light was predicted by Oliver Heaviside in 1888 and, almost fifty years later, measured by the Russian physicists Cherenkov and Vasilov in 1934 (Cherenkov, 1934). In 1958 they received the Nobel prize for the discovery and interpretation of this effect.

The atmosphere is a dielectric medium and so, when a charged particle passes through it, it changes the polarization of the atmosphere's molecules. In particular, if the velocity of the particle is low ($v < c/n$, where n is the refraction index of the medium), the polarization is symmetric: the electromagnetic field remains null (see Figure 2.1-a). However, if the velocity is higher than the speed of light in the medium ($v > c/n$), the particle travels faster than its electric field and leaves a non-symmetric perturbation (see Figure 2.1-b).

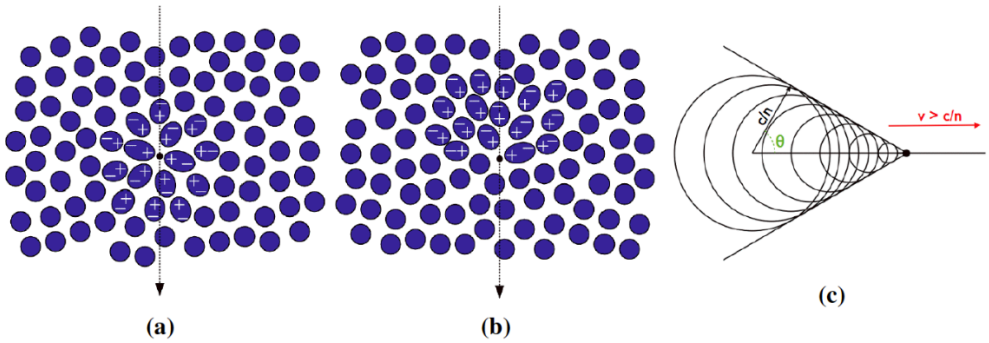

Figure 2.1 Emission of Cherenkov radiation by a charged particle. **a)** polarization of a medium when a charged particle passes through it with a velocity $v < c/n$; **b)** polarization of a medium when a charged particle crosses it with a velocity $v > c/n$; **c)** schematic representation of the Cherenkov radiation emitted by a particle. Credit to de Naurois & Mazin (2015).

The dipoles, to come back to equilibrium, emit these blue Cherenkov flashes in the form of a cone, with an angular

aperture θ, the so-called *Cherenkov angle* (see Figure 2.1-c):

$$cos\theta = \frac{c}{nv} = \frac{1}{n\beta} \tag{2.1}$$

where $\beta = v/c$. In the air, the value of the Cherenkov angle is about 1 degree at 2200 m, and decreases at higher altitudes.

On the Earth's surface, the Cherenkov light of each ultra-relativistic particle track illuminates a donut-shaped ring (the so-called *Cherenkov light pool*) as shown in Figure 2.2.

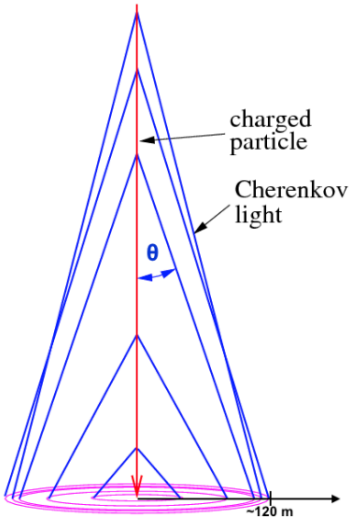

Figure 2.2 The superposition of the Cherenkov light rings produces on the ground the so-called *Cherenkov light pool*: a circle (or an ellipse) of $\sim$ 120m of radius. Image from https://www.mpi-hd.mpg.de.

The circle of the *Cherenkov light pool* has a radius of about 120 m, centered on the shower core at 2200 m above the sea level (a.s.l.), and the light can be collected and studied with Cherenkov telescopes.

The photon density is proportional to the energy of the primary gamma ray and this is important for the reconstruction of the primary particles' energy. The spectral intensity of Cherenkov radiation, and so, the number of Cherenkov photons, is proportional to λ^{-2}, with λ the wavelength of the emitted radiation. As shown in Figure 2.3, most of the Cherenkov light is emitted in the UV range, the absorption effects shift the maximum of the spectrum to larger wavelengths.

The main mechanisms responsible for absorption are:

- **Rayleigh scattering:** it takes space when Cherenkov photons interact with particles smaller than their wave-

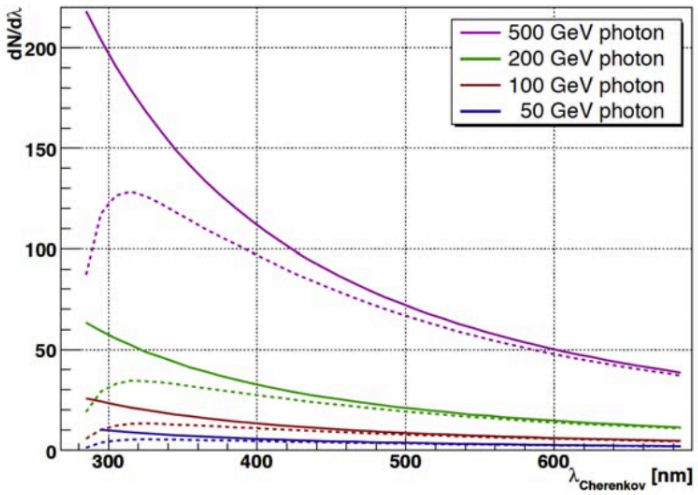

Figure 2.3 Spectra of the Cherenkov radiation for different energies of the primary gamma ray (solid line). The dashed lines take into account absorption mechanisms, like Rayleigh and Mie scattering. Credit to Wagner (2006).

length, i.e. air molecules. The efficiency of this scattering process is proportional to λ^{-4}: the photons with the shorter wavelength are strongly suppressed.

- **Mie scattering:** elastic interaction between Cherenkov photons and aerosol, dust and droplets of water. These particles have a diameter comparable, or greater, than the wavelength of Cherenkov light. This scattering is not very wavelength-dependent. In particular, on the island of La Palma, where the MAGIC telescopes are located, the aerosols are a mix of sea salts from the Atlantic ocean, ice crystals from passing clouds, dust and microscopic sand particles (especially during a *calima*[*] event).

- **Ozone molecules:** responsible for the strong absorption of hard UV photons (< 300 nm).

- **H_2O and CO_2 molecules:** absorption in the Infrared (IR) band.

- **Zenith angle:** the larger the zenith angle, or smaller the elevation angle (i.e. closer to the horizon), the higher the absorption; this affects the cascade because the fraction of atmosphere that it has to pass through is much larger, and consequently the interaction rate is higher. Only the most energetic particles can be detected by Cherenkov telescopes in high zenith angle observations, and the peak of the Cherenkov radiation spectrum shifts to longer

[*]It is a warm or hot wind that carries huge quantities of dust and sand from the nearby Sahara Desert.

wavelengths, i.e. the Cherenkov light becomes redder.

2.1.2 Extensive Air Shower

As discussed in Section 2.1.1, when an ultra-relativistic gamma ray or CR enters the atmosphere, a series of interactions occur, which lead to what is known as an EAS. The primary particle collides with one molecule of the Earth's atmosphere (usually a nitrogen, an oxygen or an argon nucleus) at at an altitude of $\sim$ 5-25 km above sea level (a.s.l.). The altitude depends on energy: the more energetic the particle, the deeper it can travel through the atmosphere and the lower the interaction point is located. The result of these interactions is two or more secondary particles and, since the original particle is very energetic, the secondaries also travel almost at the speed of light. These secondary particles are subjected to further interactions with air nuclei, and a new cascade of thousands of secondary particles is produced. This process continues to take place until the ionization processes become dominant and the energy threshold for pair creation is reached. In the following sections, I describe the showers induced by a gamma ray (the electromagnetic shower) and the ones induced by protons or other nuclei (hadronic showers).

2.1.2.1 Electromagnetic Showers

The Electromagnetics (EMs) showers are initiated by a gamma ray and they are the simplest kind of EMs since they are primarily composed of electrons, positrons and gamma rays. These showers are characterized by three main interaction processes: production of e^-e^+ pair, bremsstrahlung emission(see Section 1.2.1.1) and losses of energy through ionization. When a primary gamma ray of E$\gtrsim$20 MeV interacts with the intense electric field in the vicinity of the nucleus of an air molecule, an e^-e^+ pair is produced (see Figure 2.4-left). These e^-e^+ pairs lose energy via bremsstrahlung, above an energy threshold in air of E_t = 86 MeV, the energy for which the energy losses by bremsstrahlung and ionization are equal.

The energy losses are converted into energetic photons that can undergo additional pair production. The energy loss dE for an electron due to bremsstrahlung is expressed by:

$$\frac{dE}{dx} = -\frac{E}{X_{0,e}} \tag{2.2}$$

where $X_{0,e}$ is the *radiation length* for an e^- or e^+, measured in g cm^{-2}; the atmosphere (dry air) has a radiation length of

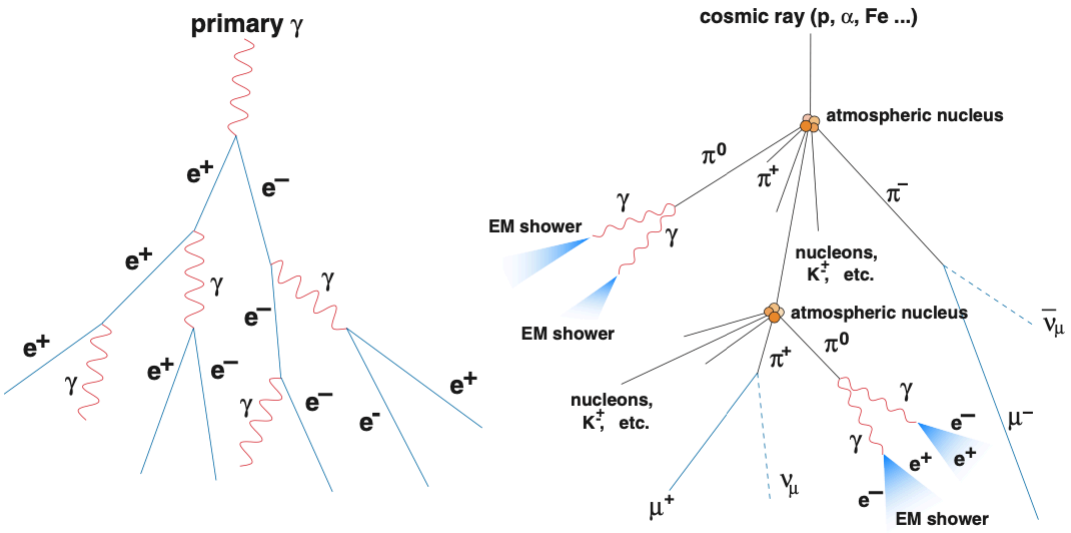

Figure 2.4 Schematic description of extended air showers. Left: EMs shower. Right: Hadronic shower. Credit to Wagner (2006).

36.7 g cm^{-2} de Naurois & Mazin (2015). This parameter indicates the mean amount of matter, projected on a plane, that an electron must cross to lose $1/e$ of its energy by bremsstrahlung. The mean free path of gamma rays for pair production is $7/9\, X_{0,e}$. Another characteristic of EM showers is that they tend to be rather symmetric with respect to the shower axis (see Figure 2.5-left).

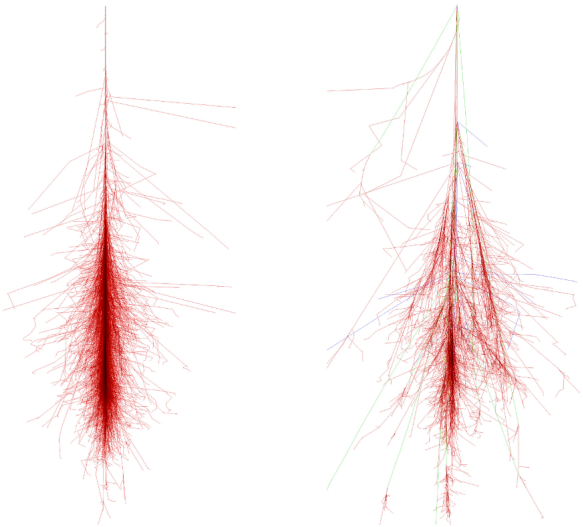

Figure 2.5 Simulated extended air showers. Left: EMs shower with a primary gamma ray of 100 GeV. Right: Hadronic shower with a primary proton of 100 GeV. Images taken from `https://www.iap.kit.edu/corsika/`.

At each step of the shower the number of particles is doubled, while their energy is half of the energy of the previous particle producing the interaction. As mentioned previously, the shower stops when the energy of the $e^- e^+$ pairs reach the E_t and therefore the number of particles reaches its maximum. The height above the sea level where the number of particles reaches its maximum (h_{max}) depends weakly on the energy of the primary gamma ray: $h_{max} \propto 1/ln(E_0)$. For a primary photon with an energy between 50 GeV and 10 TeV, h_{max} is around 6 to 10 km.

2.1.2.2 Hadronic Showers

Hadronic showers are generated when a charged particle (usually a proton) interacts with an atmospheric nucleus through the strong force (see Figure 2.4-right). The main products of these showers are pions ($\sim$ 90%), kaons ($\sim$ 10%), and a small amount of light baryons (protons, neutrons and corresponding antiparticles). The shower continues to undergo hadronic interactions until the energy per nucleon is smaller than the pion production threshold ($E \simeq 1$ GeV). In the hadronic shower we can distinguish three different components:

* **Hadronic component**: consists of heavy particles: nuclei and mesons (pions) which transfer significant transverse momentum in each collision. Pions decay into photons and muons through the following relations:

$$\pi^0 \rightarrow \gamma + \gamma \;\; ; \;\; \pi^+ \rightarrow \mu^+ + \nu_\mu \;\; \text{and} \;\; \pi^- \rightarrow \mu^- + \bar{\nu_\mu} \tag{2.3}$$

* **EM component:** consists of the EM sub-cascades of the shower (electrons, positrons and gamma rays from the decay of π^0); this is the dominant component in the final stages of the shower development.

* **Muonic component:** consists of muons and neutrinos from pion and kaon decay. Neutrinos, due to the lack of charge, do not produce Cherenkov light and so, cannot be indirectly detected by Cherenkov telescopes. By contrast, muons can be detected, as they travel long distance and can reach the ground; they undergo the following decay process:

$$\mu^+ \rightarrow e^+ + \nu_e + \bar{\nu_\mu} \;\; \text{and} \;\; \mu^- \rightarrow e^- + \bar{\nu}_e + \nu_\mu \tag{2.4}$$

Hadronic showers penetrate deeper into the atmosphere compared to EM showers of the same primary energy. Additionally, these showers are more extended than EM ones due to the high transversal momentum that kaons and pions receive compared to those of electrons and positrons (see Figure 2.5-right).

The other difference between EM and hadronic cascades is the duration of their Cherenkov flashes: showers initiated by gamma rays develop in less than 3 ns , while those generated by hadrons last more than 10 ns.

2.1.3 The Imaging Cherenkov Technique

As described in Section 1.2.4.3, in order to measure the gamma-ray emission of astrophysical sources from the ground, the imaging Cherenkov technique was developed. The first IACT was the 10m Whipple telescope (Weekes et al., 1989); it was built in 1968 and detected for the first time teraelectronvolt gamma-ray emission of the Crab Nebula with a 9σ statistical significance. This indirect detection technique combines the spatial and temporal information of the Cherenkov light and differentiates between hadron and gamma-initiated showers. To do this, Cherenkov telescopes with large collection areas and able to differentiate high-resolution time differences are needed. The Cherenkov light is collected and sent to the fast pixelized cameras; then, an important role is played by the trigger system which rapidly selects and records the events. This trigger guarantees that light flashes produced by fluctuations in the Night Sky Background (NSB), formed by light from the stars, airglow, polar and zodiacal light and artificial lights, are discarded because they do not display the spatial and temporal correlations of Cherenkov flashes associated with EAS. The rapid response time is also important to minimize the detection of undesirable gamma-photons, which are product of the background sources. In particular, the predominant background sources are the hadronic showers, where the EM sub-cascades act like an irreducible background for the gamma-ray observations (see Figure 2.6). The other components can be distinguished through the images produced in the camera: muons leave a ring-like structure clearly different than the ellipse produced in EM cascades (see Figure 2.7).

One problem of these large area collectors is that they affect the high-precision time measurements: the difference in the time of arrival to the camera plan of light reflected by different segments of the mirror becomes important. So, the use of parabolic reflectors is important since they are isochronous and this reduces the difficulties in collecting rapid signals. Using several Cherenkov telescopes as a single gamma-ray instrument provides a number of advantages. The imaging telescopes are located at a distance of about 100 m from each other and this increases the sensitivity of the whole instrument, reaching a shower detection area of about 10^5 m^2 (Weekes, 2003). The larger the collection area, the larger the number of air showers detected. Figure 2.8 shows how IACTs work.

Another peculiarity of IACTs is that the diameter of the reflector is large in order to detect air showers generated by low

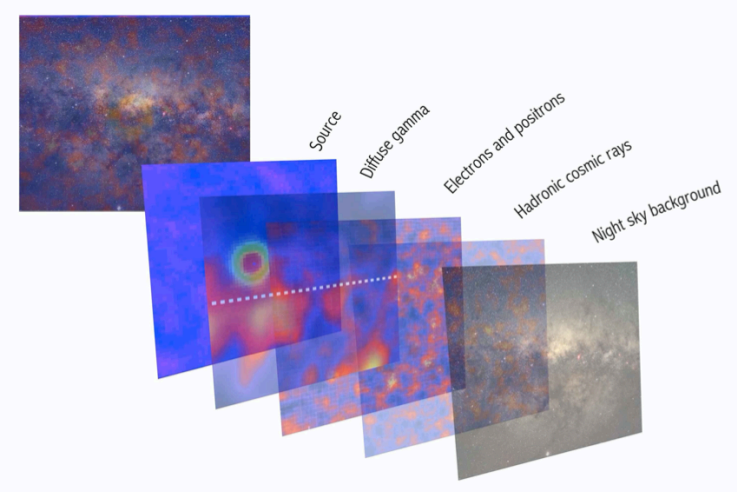

Figure 2.6 Sketch of the different layers of background that must be suppressed to obtain an image a VHE source. Figure from Brun (2012).

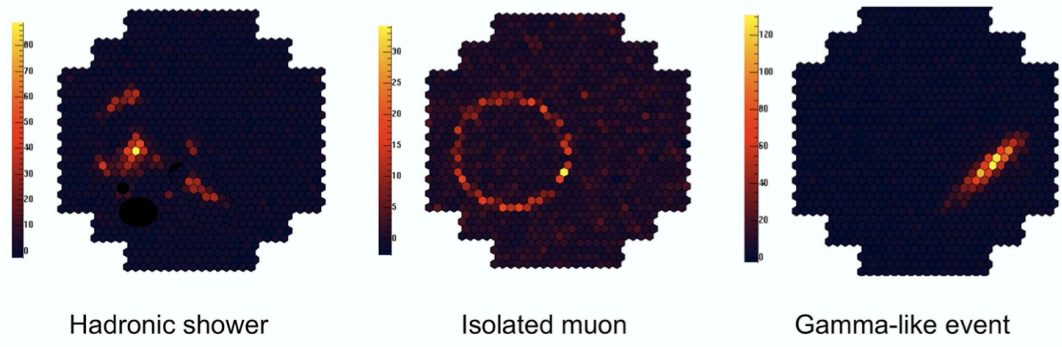

Figure 2.7 Simulated images of atmospheric events induced by cosmic particles, as observed in the focal plane of a Cherenkov telescope (Brun, 2012). From left to right: hadronic shower, isolated muon, gamma-like event.

energy gamma-ray photons. Furthermore, the analysis of multiple images of the same shower (the so-called *stereoscopic observations*) makes it possible to improve the reconstruction of the primary gamma ray energy and initial direction (Aleksić et al., 2012a). The stereoscopic mode improves also the gamma-hadron separation efficiency accepting only events that simultaneously trigger all IACTs under the light pool.

2.2 MAGIC Telescopes

The MAGIC telescopes, see Figure 2.9, is a system of two 17 m diameter telescopes known as MAGIC-I and MAGIC-II. This stereoscopic system is located at the Observatorio del Roque de los Muchachos (ORM) in the Canary island

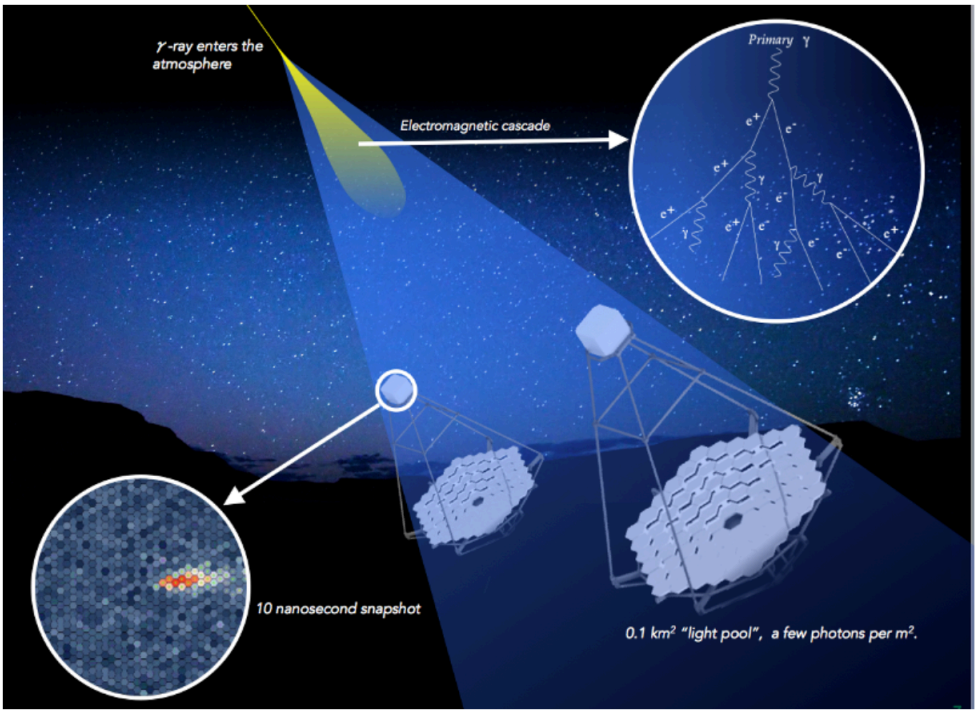

Figure 2.8 Sketch of the imaging Cherenkov technique. The Cherenkov light from the electromagnetic cascade, initiated by a high-energy particle, is reflected by the mirrors and collected in the camera. The signal is then converted into an electronic one by the photomultipliers. Image from http://cta-observatory.org.

of La Palma, Spain (28° 45' N, 17° 53' W) at 2225 m a.s.l.

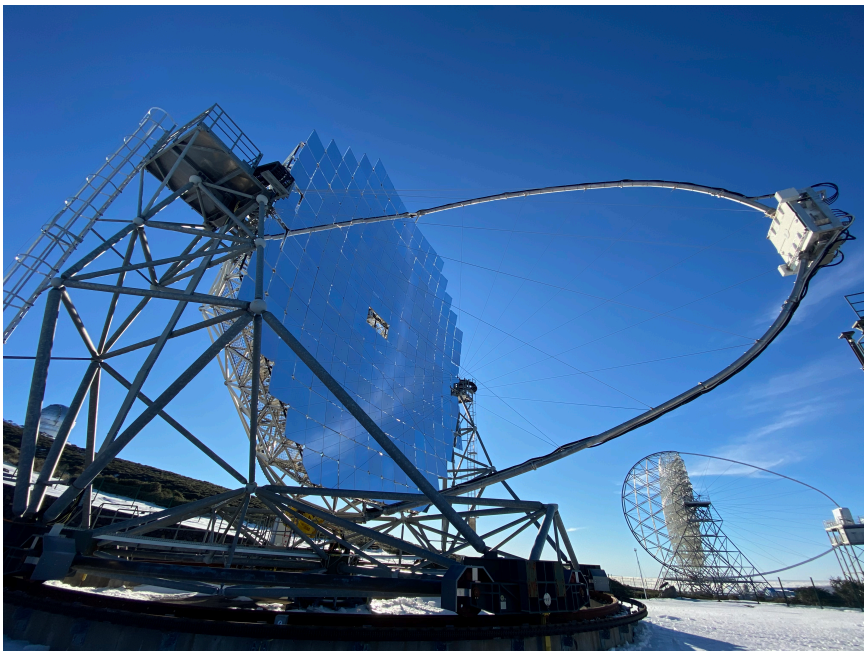

Figure 2.9 Pictures of MAGIC-II, in the background Large Size Telescope (LST)-1, the protopype of the LST, one of the three classes of telescopes to be featured in the future CTA.

The site of the ORM is above the see of clouds for most of the year (see Figure 2.10); clouds that, for a natural phenomenon, stay a few hundred meters above the sea level. Furthermore, here the sky is relatively unaffected by the light coming from the towns on the island. For this reason the ORM was chosen to host one of the largest arrays of telescopes in the world: because of its excellent astronomical conditions, in particular for its high transparency, the great number of clear nights per year, and only minimal variations of temperature during the night. Furthermore, thanks to its high altitude and proximity to the air shower maxima, it is a favorable site for Cherenkov detectors. The site currently hosts about twenty telescopes and instruments of various kinds.

The telescopes are separated by a distance of 85 m. MAGIC-I was inaugurated in 2004 and operated in single-telescope configuration until 2009, when MAGIC-II started the commissioning phase. Since then, the two telescopes have been operating in stereoscopic mode. During the mono configuration, MAGIC-I was able to reach an integral flux sensitivity of about 1.6% of the Crab Nebula flux in 50 hours of observations (Aliu et al., 2009a). In the stereo mode, the performance improved: an energy threshold as low as 50 GeV at low zenith angle was reached and the sensitivity improved to (0.76 ± 0.03)% of the Crab Nebula flux for energies above 290 GeV in 50 hours of observations (Aleksić et al., 2012a). Between 2011 and 2012 the system underwent a significant update that involved the digital trigger, the readout systems and the MAGIC I camera (Aleksić et al., 2016a). These developments allowed to reach an integral

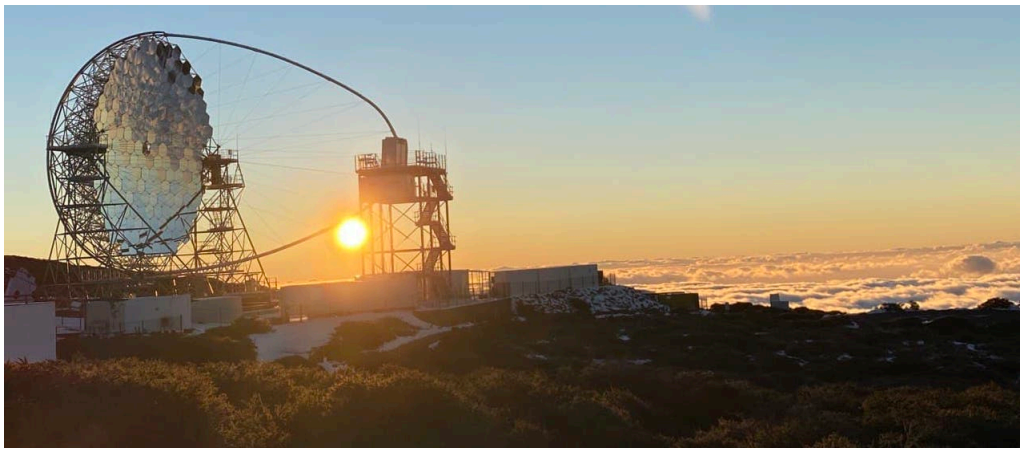

Figure 2.10 Picture of the *sea of clouds*. This is a natural phenomenon and represents the temperature inversion layer that can be clearly seen from the ORM . On the left we can see the first Large Size Telescope (LST-1), part of the future CTA.

sensitivity of $(0.66 \pm 0.03)\%$ of the Crab Nebula flux in 50 hours above 220 GeV (Aleksić et al., 2016b).

In the following sections I will discuss the main hardware and structural components of the MAGIC system, how they work and how the observations are carried out.

2.2.1 Hardware

The main components of the MAGIC telescopes are: the alt-azimuth frame and drive system, the mirrors and reflector, the camera, receivers, the trigger system, the readout system, the Sum-Trigger-II, and other subsystems (weather monitoring, GRB monitoring, etc).

SuperArehucas is the Central Control (CC) software of the telescope and is responsible for all these subsystems. It receives and sends reports, controls all the hardware subsystems, and provides access to most of the functionalities of the telescopes.

2.2.1.1 Structure and Drive System

One of the science goals of the MAGIC telescopes is the rapid follow-up of fast transient events, such as GRBs, Gravitational Waves (GWs) and neutrino alerts. In order to satisfy this, the structure of the telescope should be very light, to allow a rapid re-pointing (less than 20 s, in a special fast-movement mode) and for this reason is made of light carbon fiber tubes hold together by aluminium knots. Thanks to these light materials, the total weight of the octagonal

telescope structure that supports the 17m reflector dish is less then 20 tons; this includes the camera and the reflector support. The camera box is held by an aluminium circular tube secured to the main structure by 20 steel cables. The full structure of the telescope is about 70 tons and is distributed as follow: the camera is about 0.9 tons, the camera bow and counterweights are about 3.4 tons, the carbon fibre dish is about 8 tons, the mirror system is about 9 tons, the towers to access some parts of the telescopes are about 20.2 tons, and the six carriages about 25 tons. The above described structure is placed on a circular rail of 20m in diameter.

Both telescopes have Alt-Azimuth mount and they can be moved in an Azimuth (Az) range from $-90°$ to $+318°$ and in the elevation range, the Zenith distance (Zd) angle, from $-70°$ to $+105°$. The azimuthal movements are provided by two motors with a power of 11kW, and the altitude ones by a motor of same power that is located below the dish structure. In Figure 2.11 the pictures of azimuthal and elevation drive system. Both of the axes are also equipped with end-switches which are useful in order to know in which direction the telescope is moving; this is important in case the telescopes have to be moved manually. During daytime, when the telescopes are not taking data, or when the weather conditions are bad (e.g. strong wind), the telescopes are secured with bolts, which are manually removed by the shifters before switching on the motor power and taking data.

Figure 2.11 **Left**: one of the six mechanical bogies that allow the azimuth rotation of the telescopes. **Right**: the elevation drive, located at the center of the structure and behind the reflective surface.

Pointing Mode and Tracking accuracy Although robust, the mechanical structure is subject of imperfections and deformations which are in general less than 3.5 mm in any direction. These deviations can be corrected

using a *pointing model* which parameterizes deviations from an "ideal" telescope thanks to the Active Mirror Control (AMC) (see Paragraph 2.2.1.2). This pointing model is created using a `TPoint` package that analyses the images taken during the observations by the *T-Point camera* (see Figure 2.12-green box). This camera is a Charge-Coupled Device (CCD) camera located in the middle of the dish and it points all the time to the same direction of the telescopes. It analyses the bright stars in the Field of View (FoV), stars which belong to a catalogue of about 150 stars, comparing them with the FoV in order to find possible mispointings which are related to a shift between the camera center and the real coordinates of the source; all these mispointings are reported in a list of so-called *TPoints*. So, *TPoints* are very important to update the so-called drive *bending models* which are updated every observational period (period between two consecutive full moon breaks) and this enable MAGIC to reach a pointing accuracy of 0.01°.

Moreover, the position of the telescope is constantly monitored during observations with a sensitive CCD camera, the *Starguider camera* (see Figure 2.12-cyan box), mounted also on the center of the mirror dish and aligned with the pointing axis of the telescope. Six markers, created by six Light-Emitting Diodes (LEDs), provide a reference frame for the PMT camera, while the stars are recognized thanks to a dedicated software which compares the images of the *Starguider camera* with star catalogs. These information is used to correct offline any misalignment of the telescope. Furthermore, the comparison of the number of identified stars in the FoV with the expected one from the star catalog can give information about the weather conditions (e.g. the atmospheric transmission) during the observation.

These imperfections and misalignment of the telescopes are analyzed by the software: the starguider *bending models* are applied by the data analysis software (usually at the `star` level), while the *drive models* are applied directly in the software that controls the drive system (called `Cosy`).

A full and detailed description of the MAGIC drive system can be found in Bretz et al. (2009).

2.2.1.2 Mirrors and Reflector

The MAGIC telescopes consist of parabolic reflectors with a diameter of 17m, which corresponds to a total reflecting surface of approximately 236 m^2. The focal length (distance at which the camera is placed with respect to the center of the dish) is equal to the diameter of the telescope, and was chosen to minimize the time spread of the Cherenkov light flashes on the camera plane; indeed, the large size of the reflectors result in a large arrival timing difference of the reflected light from different parts of the dish. Thanks to the parabolic shape of the detectors, however, the incoming

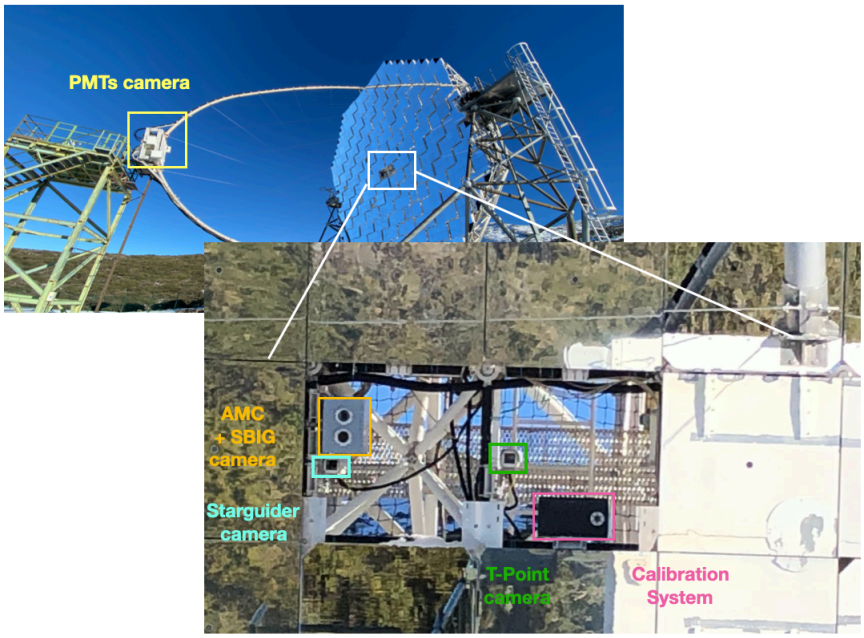

Figure 2.12 The two central mirrors of the MAGIC telescopes are hold by several cameras and sensors, marked with color boxes: the AMC and Santa Barbara Instrument Group (SBIG) camera (yellow), the Starguider camera (cyan), the T-point camera (green) and, the Calibration box system (pink).

light is isochronous, reducing the noise coming from this broadened signal to about 1-2 ns and leading to less background or noise.

The mirrors mounted in the two telescopes are different (Doro et al., 2008). MAGIC-I has mirrors composed of a sandwich of two thin aluminium layers interspaced by a honeycomb structure that ensures rigidity, high temperature conductivity and low weight. There are 740 50 cm $\times$ 50 cm square mirrors designed by Istituto Nazionale di Fisica Nucelare (INFN)-PD, 224 designed by Max Planck Institute (MPI) (Munich) and, from 2011, some Istituto Nazionale di AstroFisica (INAF) aluminum-honeycomb "sandwich" and cold-slumped 1 $\times$ 1 m mirrors. In MAGIC-II the mirror unit tile size increased to 1m^2 and so, the number of mirrors is reduced: there are 143 INFN-PD aluminum-honeycomb sandwich mirrors and 104 INAF cold-slumped mirrors.

Sometimes mirrors must be replaced, due to external damage (e.g. atmospheric conditions). The most common problems are: humidity absorbed in the mirrors and turned into water/ice, inelastic modification due to temperature cycles and, bad micro roughness of the surface due to the diamond-milling technique causing high scattered light.

Active Mirror Control (ACM) and *SBIG Camera* The quality and the status of each mirror can be evaluated through the definition of the PSF. To achieve a good alignment, a good PSF is essential and this is guaranteed by the ACM (Biland et al., 2008). This system is formed by two actuators (stepping motors) which are behind each mirror that move the mirrors around a third fixed point with a precision better than 20 μm. The adjustment of the mirrors is executed through Look-Up Tables (LUTs) binned in Az and Zd. These tables keep a record of the defects and deformations of each mirror and enable the computation of the best configuration in order to provide the best PSF. At the beginning of the each night of observation the ACM is used to center and adjust the mirrors in order to evaluate the quality of the PSF with the so-called *SBIG camera* (see Figure 2.12-yellow box). This CCD camera is placed at the center of the dish and is designed for measuring the optical PSF of the telescope by looking at the reflection of a star in the camera. It can measure the PSF both for individual mirrors or, as is usually done, for the complete reflector. There are three filters used for different purposes; for the PSF measurement, the blue filter is used. Instead, for the Very Large Zenith Angle (VLZA), where LIght Detection And Ranging (LIDAR) cannot work, all the filters are used. Furthermore, in order to keep the mirrors focused, for each source observed, during the repositioning of the telescopes, the values of the actuator's positions are read from the LUTs.

2.2.1.3 Camera

The camera, very similar in both telescopes, consists of PMTs arranged in a circular shape (see Figure 2.13). Here, photons arrive after being reflected by mirrors and then are converted in photoelectrons (phe) by PMTs and an electric signal is created and processed by the readout and trigger systems. Each camera contains 1039 PMTs made by Hamamatsu (model R10408), 25.4 mm in diameter, with a hemispherical photocathode, 6 dynodes and with a hexagonal shape Winston cone mounted on top (Aleksić et al., 2016a). This cone focuses the light on the PMT window and prevents large angle NSB light from entering the PMTs. Each PMT has a FoV of 0.1°, and the whole camera has a total FoV of 3.5°. The Quantum Efficiency (QE) of PMTs is about 34% for light with a wavelength of 350nm (blue band) and their response time is of about 1ns. The PMTs are grouped in 169 clusters of 7 pixels (those at the camera edge are not fully populated) and thanks to this modular design it is easier to control and maintain the camera.

The electric signal is created by PMTs when photons interact with the photocathode and then, this signal is converted into an analog optical signal (by Vertical Cavity Surface Emitting Lasers - VCSELs). The light produced has a wave-

length of 850 nm (near infrared) and a Cherenkov pulse width (Full Width Half Maximum (FWHM)) of about 2.5 ns (Borla Tridon et al., 2009). Through about 160 m long fiber cables, the signal of each pixel is transmitted from the camera to the electronic room in the Counting House (CH). These cables are grouped in 19 bundles of 72 fibers each. The PMTs can be tested during daytime with an electrical signal injected at their base, this signal has a FWHM of 2.6 ns.

Each camera is then formed by other components:

- two cooling aluminum plates that keep stable the pixel temperature;
- several sensors to monitor the humidity and the temperature in the camera;
- a drying unit to lower the humidity level;
- two low voltage power supplies, one for each half of the camera;
- the camera lids (controlled by the lid drive box on the camera side) used to protect PMTs during day and bad weather conditions;
- starguider LEDs, used by the *starguider* camera to find the camera center.

The status of the camera can be monitor my the shifters during data taking through the programs `CaCo1` and `CaCo2` (CaCo stands for "Camera Control").

2.2.1.4 Calibration System

The MAGIC telescopes need a calibration system to ensure the good response of the instrument: PMT signals must be calibrated because they undergo gain fluctuations and changes in the readout chain due to changing of external influences (e.g. temperature). This is executed using the so-called *calibration boxes*, located in the middle of the reflector (see Figure 2.12-pink box). The calibration box contains a Nd:YAG laser of 355 nm wavelength, whose pulses have a FWHM of 0.4 ns in order to be as close as possible to a Cherenkov flash. The intensity of the laser can be varied from 1 to 1000 phe in every pixel by changing the position of two rotating filter wheels with different attenuation factors. The camera plane is uniformly illuminated thanks to a sphere in front of the laser that diffuses the light evenly. Dedicated calibration runs are taken before each observation. A detailed description of the calibration system can be found in Gaug (2006).

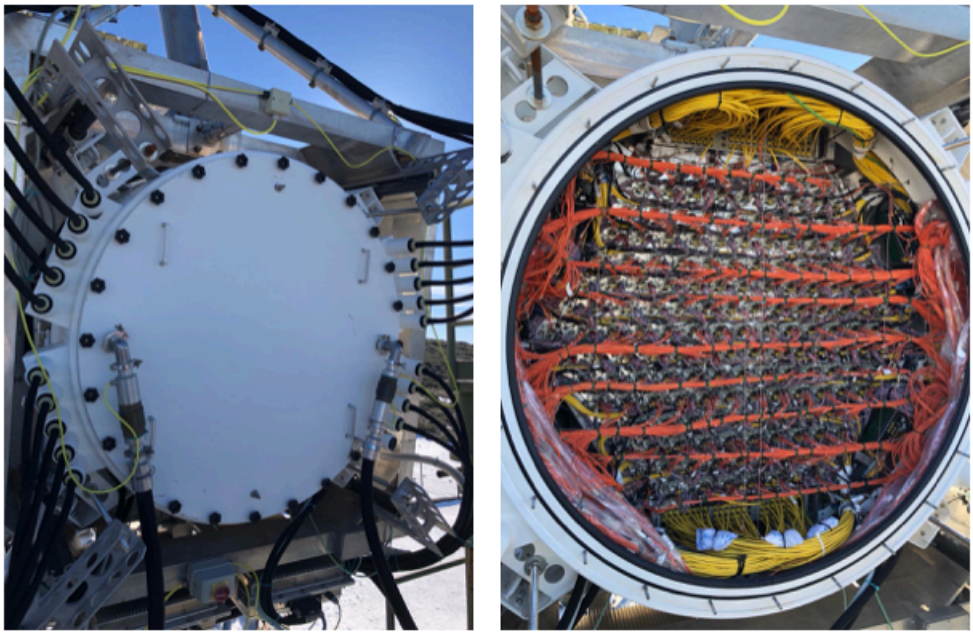

Figure 2.13 Back side of the MAGIC-II camera (left) with the internal view of its 169 PMTs clusters (right). Pictures taken during a technical check during my shift in La Palma (January 2021).

2.2.1.5 Readout Systems

Before going into the details of the readout system, I give an overview of the signal chain in the MAGIC telescopes.

Brief description of the MAGIC signal chain

Once the optical fibers have reached the CH, they are plugged into the *receivers*, where photo-diodes are responsible for converting the optical signal back into an electric signal. At this point the signal is divided into two branch: the digital trigger and the analog readout:

- a digitization branch, where a Domino Ring Sampler version 4 (DRS4) chip based readout stores the signal waiting for the trigger decision.

- a trigger branch, with two sub-branches: a digital one (L0 trigger) which is sent to the L1 trigger and a copy of the starting analog signal that can be sent to the Sum-Trigger-II (SumT). After the first trigger decision (L1 or SumT, one per telescope), the signal is digitalized and sent through the L3 trigger (stereoscopic). If the L3 trigger is positive, the signals stored in the DRS4 buffers (one per telescope) are sent to the Data AcQuisition

(DAQ) after being digitized by a standard Analog-to-Digital Converter (ADC).

Furthermore, since receivers require a constant temperature to work, dedicated air cooling units are placed on top of each cabinet. A scheme of the electronic chain is given in Figure 2.14.

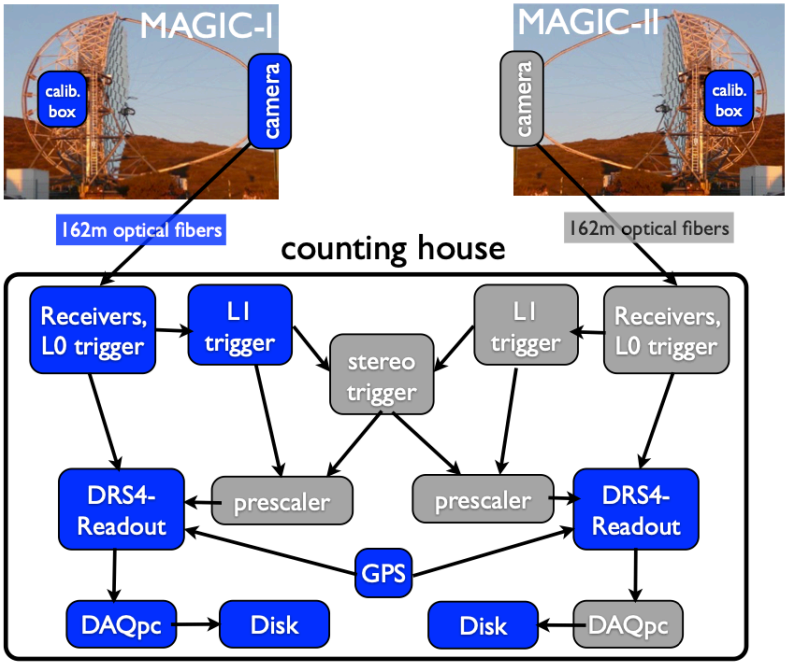

Figure 2.14 Overview of the MAGIC electronic chain, from Mazin et al. (2014).

The sampling of the events is provided by a system of two electronic boards: a motherboard or PULSer And Recorder (PULSAR) board (developed at University of Chicago) and a DRS4 mezzanine designed at INFN/Pisa laboratory. The DRS4 is an ultra-fast analog memory composed of a ring buffer made of 1024 switching capacitors that are read in the event of a trigger using a conventional 14-bit analog to digital converter Discriminator Threshold at low speed (32 MHz). The mezzanine noise is dominated by the noise from the DRS4 chip and in total, the digitization electronics contributes to about 50% of the total noise. The DRS4 chip requires a calibration with three corrections: the mean cell offset, the readout time lapse, and the arrival time of the signal. The first two are applied by the DAQ software, while the last is applied offline. Moreover, the performance of DRS4 chips is temperature-dependent and, as a consequence, the readout electronics need to be switched on about 2 hours before the data taking for the stabilisation of the temperature. The calibration of the mean cell offset is performed through the *pedestal calibration run*, taken at the beginning of the night (and then subtracted from readout values) and it allows the measurement of the average baseline of each capacitor.

The time spreads due to the DRS4 chip (1-4 ns) are corrected instead using *calibration runs* taken every night during data taking. A detailed description of the readout system can be found in Sitarek et al. (2013).

2.2.1.6 Trigger System

The trigger is a complex, multilevel and fundamental system that allows the discrimination of the gamma ray-induced cascades from the hadronic ones and the NSB, and in this way the total number of events that are registered by the readout system is reduced. So, this system is responsible for the selection of the Cherenkov shower signal hidden under several sources of noise. The trigger tells the DAQ when it is possible to store the signal produced by the camera in coincidence with an EAS. The digital signal is produced by the receiver and transmitted to the trigger system, where it is processed by several trigger logics or trigger levels.

The main steps of the trigger, valid for MAGIC cameras working in stereoscopic mode, are the following:

- **Level 0 (LO) trigger.**

  This trigger, located in the receiver boards, emits a squared-shaped signal every time the analog signal from an individual PMT exceeds a certain amplitude threshold, the so-called Discriminator Threshold (DT). If this is not the case, the event will never trigger the data acquisition system and will not be saved to disk. The DT level depends on the level of the moonlight: lower during dark observations and higher during the moonlight. In particular, since during the night the light conditions of the sky might change, the rate of each individual pixel is monitored online and the DT values are automatically and continuously modified to keep a stable rate during variable light conditions.

- **Level 1 (L1) trigger.**

  The L1 trigger works on the signal inputs given by the Lo trigger from each pixel, over 19 overlapping hexagonal cells that cover the entire camera, the so-called *macrocells*, as shown in Figure 2.15. Each macrocell is composed of 37 PMT and with one pixel row in common with the next macrocell and all of them covering the 547 innermost pixels of the camera. The L1 trigger measures the spatial and temporal coincidence between neighbouring pixels: when a number n of neighbouring pixels Next Neighbour (NN) in any macrocell, provides a signal above the DT, the L1 trigger sends a signal. The possible combinations of neighbouring pixels are for n=2, 3, 4 and 5. The macrocells cover a region of about 2.5° diameter. During standard stereo observations, the trigger uses the 3NN configurations. And the L1 trigger is positive only when 3 nearby PMT show a Lo signal. During mono

observations, a 4NN configuration is used, and the L1 signal from each macrocell is processed by a Trigger Processing Unit (TPU).

◇ **Level 3 (L3) trigger.**

The L3 trigger analyses and compares the signal from the two telescopes during stereo observations. The L3 receives the output of the TPU, and if both the telescopes registered an event, the L3 trigger is positive. The signals are artificially stretched to 100 ns (to avoid misalignments of the telescopes) and delayed, one with respect to the other, account for the Az and Zd and the consequent different arrival times of the cascade in each telescope. If L1 signals from both telescopes are closer than 180 ns, then the event is accepted and the readout starts.

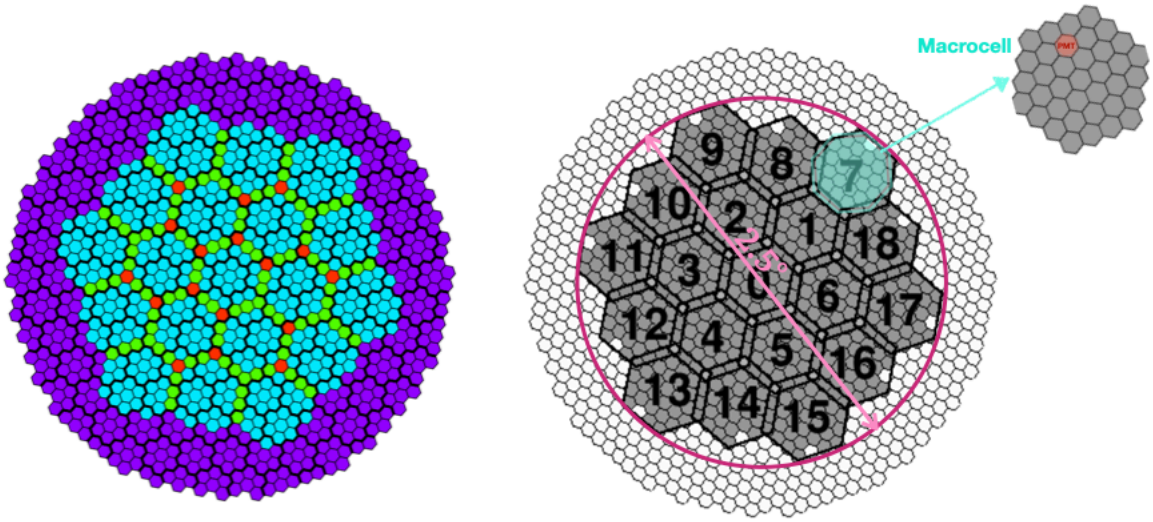

Figure 2.15 **Left**: scheme of the MAGIC camera. Cyan, green and red pixels belong to the trigger region, while the purple ones do not. The 19 L1 macrocells are denoted by the cyan pixels. Green and red pixels belong to two and three macrocells at the same time respectively. Thick black lines represent the 169 PMT clusters. Image taken from Aleksić et al. (2016a). **Right**: hexagonal L1 macrocells in the current MAGIC camera version, each of which contains 37 PMT (one blind). The numbers on the macrocells are the internal MAGIC identification. The trigger FoV is 2.5° diameter. Modified plot from López-Coto et al. (2016).

2.2.1.7 The Sum-Trigger-II System

The Sum-Trigger-II is a new type of trigger developed for the MAGIC telescopes. It has been installed in both telescopes in 2015 and since 2016 is used for special scientific projects in the low-energy domain. The goal of this system is to

lower the trigger threshold down to 25 GeV and observe interesting objects such as Galactic sources (e.g. pulsars), distant Active Galactic Nuclei (AGN) and transient events (e.g. GRB). This low-energy performance is essential for the detection and the study of these objects.

Design The MAGIC camera has been divided into three layers of patches, partly overlapping, (see Figure 2.16), for a total of 55 macrocells (each consisting of 19 PMT) and 529 pixels. This patch size is optimized to obtain the best trigger efficiency for gamma-ray events in the range of few tens of GeV and, in this way, all pixels in a macrocell contribute to the trigger decision, making non negligible also small photon signals that generally are below the sensitivity of the standard trigger. The hexagonal shape of the macrocells ensures both a symmetrical and homogeneous overlap, and a central symmetry of the trigger area. The ideal number of PMT pixels in a camera patch is the result of Monte Carlo simulations with the aim of obtaining an optimal performance in the energy range of 25-30 GeV; with a smaller number of PMT there is the probability to lose an important part of the faint Charenkov light, while a larger number of PMT increases the accidental triggers due to the Light of the Night Sky (LoNS). Furthermore, thanks to these overlapping macrocells, the time required to detect a source is reduced.
As discussed in Section 2.1.2, the development of EASs depends on the energy and nature of the primary particle. If the primary gamma ray is of low-energy, the images of EASs produced will be characterized by:

- low photon density;
- distribution of the photons concentrated in a small region of the camera (by contrast, an EAS generated by a higher energy gamma ray is usually with a elliptical shape, with the most of the charge concentrated in the maximum of the shower development);
- image distorted due to the geomagnetic field.

These characteristics reduce the performance of standard digital triggers, and for this reason, the analog trigger system *Sum-Trigger-II* was developed. The Cherenkov light of low-energy EASs is emitted at about 10-12 km a.s.l. and the showers have an inpact parameter up to 120m, and thus, the images of these EASs are formed around 1 degree from the direction of the primary particle. For this reason, the camera patches are organized in the inner part of the Cherenkov-imaging camera.

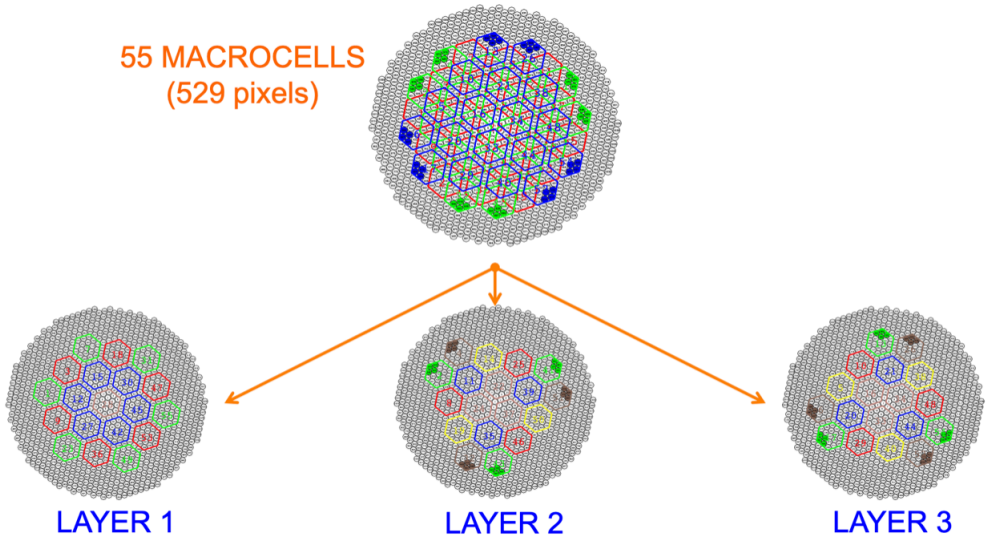

Figure 2.16 Illustration of the the three layers of the trigger region of Sum-Trigger-II. Layer 2 and 3 present the same arrangement, but a different orientation. The full coloured pixels are outside the standard trigger region and cannot be connected. Credit to Dazzi (2012).

System and Subsystems Overview The Sum-Trigger-II is a modular system. Figure 2.17 shows the diagram for the processes limited to a single camera trigger patch. The signals (green pulses), originated in the camera, come from the receiver boards and a mezzanine transmits the analog signal to the *Clip Boards* (orange blocks); then they are synchronized and equalized in amplitude. There are three functional groups:

- **Orange blocks:** represent the adjustment of the delay and gain of the PMT signal of a camera patch. PMT are affected by random and spurious noise pulses called *after-pulses*, which usually appear after the main pulse of a PMT. These *after-pulses* are undesired pulses that can be minimized by cutting (clipping) the PMT signals above a certain amplitude, in this way the clipping purpose is a powerful solution for rejecting these fake triggers. The optimal clipping level was determined with Monte Carlo (MC) simulations and revealed a level corresponding to 8 phe for both telescopes, a value that limits the losses of gammas.

- **Yellow blocks:** this is the summing and signal discrimination block and represent the core function of the Sum-Trigger-II: the isochronous signals are collected and detected. The FWHM is around 3 ns at this stage, sufficiently narrow to lower the rate of fake triggers produced by the LoNS, but wide enough to maximise the detection of Cherenkov photons from EASs.

- **Cyan blocks:** this final blocks represent the digital one. The *"OR"* block joins all the triggers from the single

camera patch in a unique telescope trigger. The *"Computer Control"* block instead inspects and controls everything. Finally, the individual Sum-Trigger-II signals of the two telescopes are then used to perform the L3 trigger as described in Section 2.2.1.6.

The Sum-Trigger-II is composed of two twin analog trigger systems, implemented into the two electronics chains of the MAGIC telescopes; they are arranged in two Rittal closed racks, placed in the electronic room of the CH. As shown in Figure 2.18, each rack consists of 18 *Clip-boards* with their power unit, 19 *Sum-boards*, one *Astro-board*, one *SPI-backplane* (ensures the power distribution and the availability of data transmission), one *Sum-backplane* (that connects the *Clip-boards* to the *Sum-boards*) and a power unit.

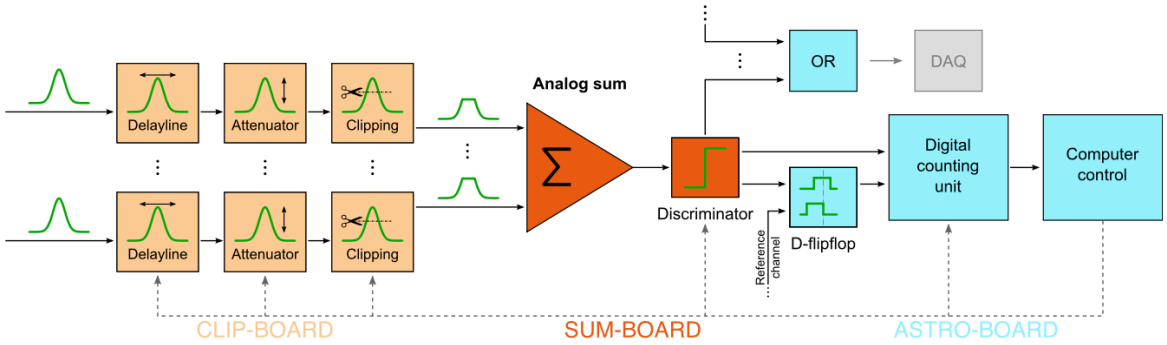

Figure 2.17 The block diagram of Sum-Trigger-II, credit to Dazzi (2012) and Haefner et al. (2012).

Characteristics As mentioned in Section 2.1.2, the EM showers last for 2-3 ns; and the signal generated by PMT must memorize a similar timing profile up to the summing stage. At the input of the Sum-Trigger-II, the PMT signal has a pseudo-Gaussian profile with a small falling tail; the pulse rise is abut 1.6 ns and the FWHM is about 2.3 ns.

The DTs (in terms of phe) must be continuously adjusted due to the small variation of the atmospheric transmission and the LoNS in the FoV of the telescope. Furthermore, the background over the camera is not uniform and so the DTs can change from one camera patch to another and for this reason, during stereo observations, the DTs of the 55 camera patches are continuously controlled.

For Galactic sources observed at low zenith angle (below 30 degrees) and with an atmospheric transmission higher than 0.85 the typical stereo trigger rate is about 500-600 Hz (where 160 Hz are accidental triggers due to the LoNS and which eliminated in the off-line data analysis).

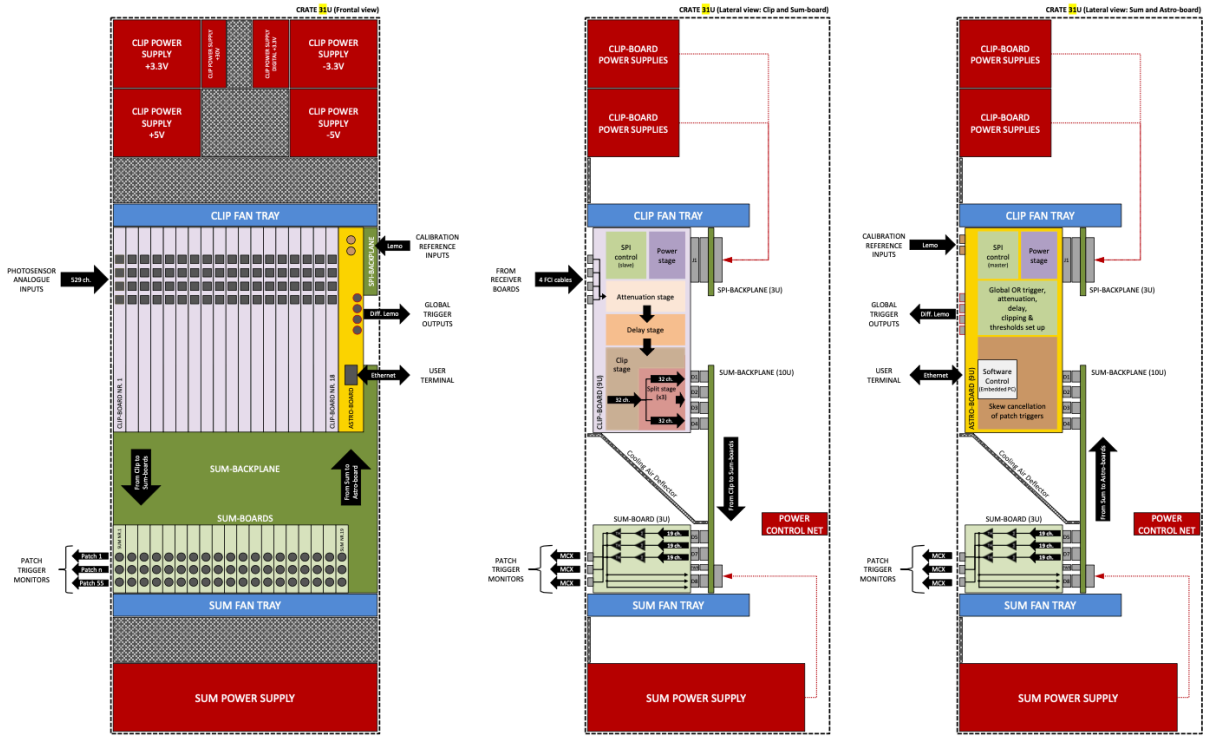

(a) Front view (b) Side view - Clip-board (c) Side view - Astro-board

Figure 2.18 Sketches representing the front (a) and side (b, c) views of one Sum-Trigger-II rack. Credit to Dazzi (2012)

Performance The performance of the Sum-Trigger-II has been determined by simulating the system with 64 million gamma-ray events from a source with a power law spectral index of -2.6, in combination with a simulated LoNS. Figure 2.19 shows that, below 80 GeV, the performance of the Sum-Trigger-II (red line) is better compared to the digital trigger (black line). The Sum-Trigger-II energy threshold is 21 GeV, lower than the one of the standard trigger: 41 GeV. The Sum-Trigger-II collection area, at 20 GeV, is about $9000m^2$, one order of magnitude larger than the digital trigger collection area.

Section 2.2.8.3 describes the dedicated algorithm for calibration and image cleaning of Sum-Trigger-II data.

2.2.1.8 Atmospheric Monitoring Instrumentation

The monitoring of the weather must be performed in order to determine the feasibility of the data taking and to guarantee the safety of the staff and the infrastructure. There are several instruments that monitor in real time the weather conditions at the MAGIC site. The weather station on the roof of the CH, see Figure 2.20-left, measures the atmo-

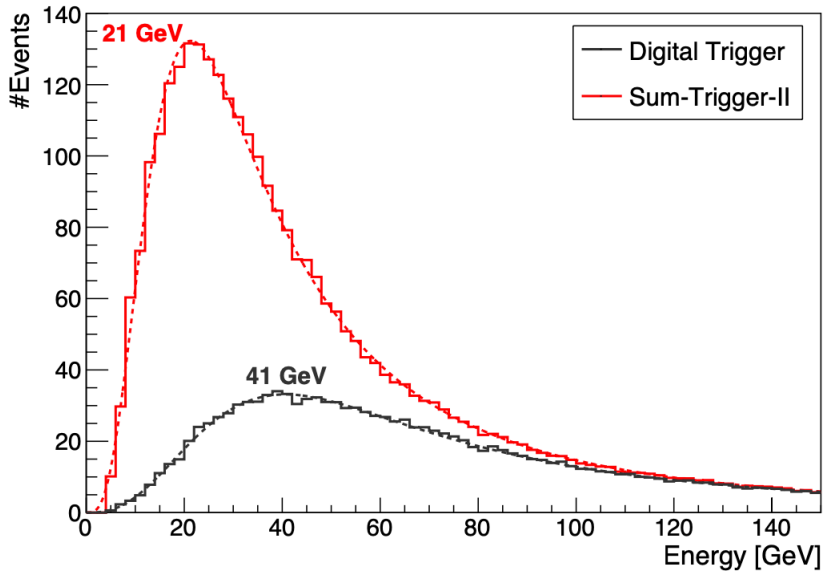

Figure 2.19 Sum-Trigger-II Performance: number of stereo events close to the threshold (peak of the distribution) for the MAGIC digital trigger (black) and the Sum-Trigger-II (red) configurations. Credit to Dazzi (2012)

spheric state variables every two seconds and all the weather information is monitored through an online system called *ATCAguard*. This software displays all the available weather data and warns the shifters if some dangerous atmospheric conditions are met. The weather station provides measurements of several quantities: temperature (in °C), relative humidity (in %), wind speed (km/h), direction and speed of the wind gusts, and pressure in hPa.

Furthermore, a dedicated system is used to monitor the aerosol content of the atmosphere and its vertical distribution: a single-wavelength LIDAR system. It is located under a dome on the CH roof (see Figure 2.20-right), and it is is composed of a 532 nm (close to the Cherenkov spectrum peak) Nd-YAG laser, 60 cm diameter mirror with 150 cm of focal length.

The laser shoots at a position shifted by 4 degrees from the observing source in order not to interfere with the MAGIC observations. The LIDAR is able to measure the transparency of the atmosphere and provides a ratio between cloud/aerosol scattering and molecular scattering. The pulsed light from the laser is backscattered by the clouds and aerosols in the sky. The transparency is measured as a function of the arrival time distribution of the backscattered photons. The LIDAR can provide transmission estimation at different altitudes of 3, 6, 9, and 12 km (Fruck et al., 2014), but the most interesting one for the analysis of MAGIC data is the one at 9 km, where most of the Cherenkov showers form.

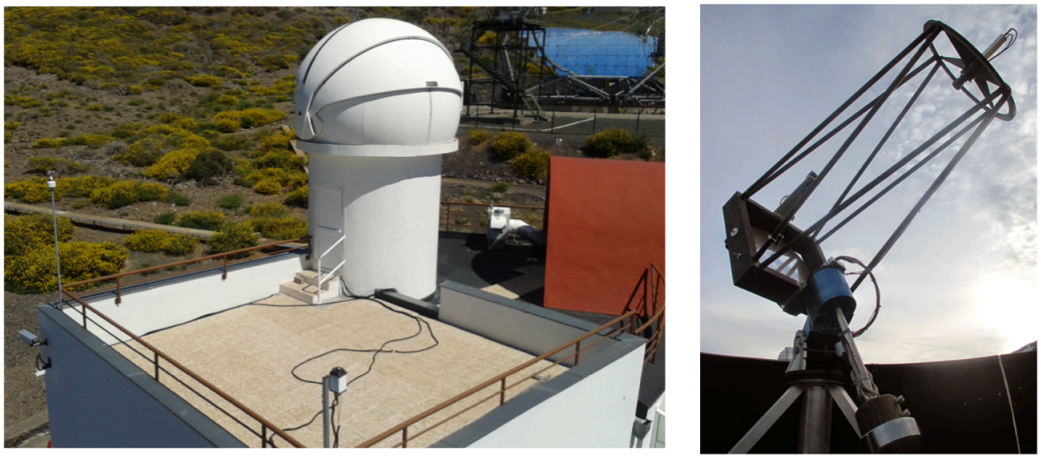

Figure 2.20 **Left**:The atmospheric monitoring instruments placed on the roof of the MAGIC CH. **Right**: The elastic LIDAR system. Images from Will (2017).

The LIDAR system is not essential for the MAGIC operation but it is very useful for estimating the quality of the data. Another important instrument, dedicated to the monitoring of the air quality is the **pyrometer**. This is a remote thermometer that measures the IR radiation emitted by the cloud base and, assuming that the air is an ideal gas, it estimates the height of the clouds. It is installed in the MAGIC-I dish and points in the same direction of the telescope. MAGIC uses a parameter known as *cloudiness* to quantify the weather conditions at the site. This value ranges between 0% (a perfect clear atmosphere) and 100% (the sky is completely covered by clouds) and is well correlated with the transmission obtained with the LIDAR system at the site.

Finally, the other instrument that is used to inspect visually the sky condition (to see if the sky is cloudy) is the **AllSky camera**. This camera, located on the roof of the CH, takes images of the sky above the MAGIC site every two minutes with an exposure time automatically adjusted.

2.2.1.9 Other Subsystems

- **Timing system:** it is composed of a high precision rubidium clock together with a Global Positioning System (GPS) service. The timing system is essential to measure precisely the arrival time of the triggers. The rubidium clock is an oscillator able to provide a precision of 10^{-11} s every second and it is synchronized with the GPS system, which has a precision of the order of 10^{-9} s.

- **Central pixel:** the central pixel of MAGIC-II is a modified PMT able to perform optical observations. The purpose is to study slow variations of the flux of optical sources, like pulsars.

- **GRB alert system:** this system continuously monitors the GRB Coordinate Network (GCN) in order to alert of a possible GRB event. The GCN is a system that distributes real-time information (called *notices*) like the direction of an incoming GRB detected by space-based instruments (e.g. *Swift*, *Fermi*, INTEGRAL ecc.). The *notices* solicit follow-up observations that may be performed by ground and space-based observatories. The GCN system also automatically distributes messages, called *circulars*, that inform of the performed follow-up observations.

  The alert is evaluated in terms of observability (zenith range, distance to the Moon and Sun, uncertainties on the coordinates) and, if the alert meets certain conditions, the CC takes control of the telescopes and moves them automatically to the GRB position, in only 20 s, initiating follow-up observations. The software that takes care of this procedure is the so-called `GSPOT`: *Gamma Sources POinting Trigger*.

- **Cooling System.** The MAGIC telescopes consume about 8.4 kW of power. The cooling system keeps the temperature of the electronics under control. This system consists of three chillers, ten heat exchangers placed above the racks of the readout electronics (and also of the Sum-Trigger-II electronics) and of circuits for the distribution of the water and cool air.

- **Central Control:** is a program, as discussed in Section 2.2.1, called *SuperArehucas (SA)*, that ensures the correct and safe operation of all the subsystems involved in MAGIC. It is a complex LabView software responsible for gathering all the information from the different subsystems. To simplify the work of the MAGIC operators at the site, several automatic procedures are implemented in SA (i.g. list of tasks to start up and to shut down the system). It shows warnings on subsystems, communication problems or unusual trigger rates.

- **On-Site Analysis (OSA).** RAW data, collected with the MAGIC telescopes, are temporarily stored in La Palma, and only later sent to the permanent data storage at Port d'Informaciò Cientifica (PIC) in Barcelona. This transferring process takes time (hours) because the size of raw data is quite large (about 1-2 GB). In order to avoid this, a standard on-site MAGIC analysis is performed, as soon as RAW data are available, with a dedicated software called `OSA`. The OSA reduces the data up to the `melibea` level; then, when the reduced data are available, they are ready to be transferred to the PIC. Furthermore, thanks to OSA, the first steps of the analysis are already

done so that producing high-level results (i.e. θ^2 plots, skymaps, light curves and spectra) will be faster for the analyzers. This is valid only for data taken under dark conditions and without the Sum-Trigger-II; when such conditions are not met, the analysis must start from calibrated or RAW data.

- **MAGIC OnLine Analysis (MOLA).** The analysis of MAGIC data requires a dedicated off-line analysis; but, for the shifters it is very useful to have a first rapid evaluation of the signal that the telescopes are registering from a certain source. For example, if a source is flaring, the observation can be extended in order to get the maximum signal and perform variability studies. This very preliminary real time analysis is particularly interesting for the whole community: if the MAGIC telescopes register some event, an alert to other observatories can be sent and follow-up observations of the source could be performed. MOLA, have MAGIC On-Line Analysis, is a C++ program that evaluates the charge and the arrival time for each pixel of the camera (evaluated from the two DAQ systems independently). MOLA performs the calibration and calculates the image parameters; and so, the stereo analysis and the gamma/hadron separation is done, and finally, it produces the high-level analysis results like the θ^2 plots, the sky maps and the light curves. The analysis is performed in two energy ranges, Low Energy (LE) and HE, defined by the image size greater than 40 phe and 125 phe respectively; these values correspond approximately to 110 GeV and 350 GeV during Crab Nebula observations at low zenith.

2.2.2 Data Taking

2.2.3 Telescope Operations and Shift roles

Since 2004, the MAGIC telescopes have been operating by collecting data in 16 yearly cycles of observations; each period is 28-days long and is based on the lunar cycle. In each *shift* period there is a crew of 4 people (5 in some winter periods) belonging to the MAGIC collaboration that operate the telescopes during the nights, following the source schedule prepared in advance by the MAGIC scheduling group. The shifters have to perform the planned observations, monitor the weather and the telescopes conditions, and be able to solve problems that occur during data taking. In the group there are different roles, depending on the experience of the people:

- two **operators**: not-experienced scientists, usually at MAGIC telescopes for the first time, who have to learn all the safety and data taking procedures.

- two **Deputy Shift Leaders (DSLs)**: these supervise the operators and transfer their knowledge to them.

- one **Shift Leader (SL)**, the person with the most experience in the group, is the one with the main responsibilities: safety, decision taking, teaching the other shifters.

These roles are progressive and usually, after one shift, everyone is upgraded to the next role. Furthermore, the telescopes are maintained by two senior postdocs who are on call during the nights if some particular problems occur. They can be on site during the day and, thanks to their great knowledge of all the subsystems of the MAGIC telescopes, are able to perform almost all the maintenance tasks at the site.

During a year, MAGIC can observe both during dark time (no Moon) and, thanks to advanced techniques of image cleaning, during Moon time (with some limits). The average efficiency of the MAGIC observations (the fraction of dark time actually observed) is usually around 60%, the rest is lost because of technical problems or bad weather conditions.

2.2.3.1 Safety Limits

During MAGIC operations, the telescopes must always be monitored for possible bad weather conditions that could damage them. For this reason, some safety limits must be respected all the time, otherwise the telescopes cannot operate or observations have to be interrupted and the telescopes parked in a secure position. In this safe position the telescopes are secured with a sufficient number of bolts (manually removed by the shifters before switching on the motor power and taking data). The main limits on the weather and technical conditions are:

- Mean wind speed below 50 km/h.
- Wind gusts below 40 km/h.
- Humidity below 90%.
- No rain, snow, or ice.
- Mean DC for the overall camera below 30 μA.
- Individual pixel Direct Current (DC) lower than 47 μA. If this limit is not fulfill, the Individual Pixel Rate Control (IPRC) switches off the High Voltage (HV) for the PMT (usually when there is a star in the FoV).
- Humidity inside the camera below 60%; sometimes, it can increase and observations are stopped until it is dry.

- Temperature of the camera below 40°; a temperature higher than this would probably indicate that there is a problem in the cooling system.
- Zd must be above 1.5°.

These limits guarantee that the telescope hardware will not be damaged during regular data taking. Furthermore, if the fence around the telescopes is open (probably because somebody is inside the telescope area), the drive system is automatically stopped to avoid the movement of the telescope. If all these safety conditions (operations and good weather) are fulfilled, the MAGIC telescopes can start observations.

2.2.3.2 Pointing Modes

Observations with the MAGIC telescopes can be done with two different pointing modes: the *ON/OFF mode* and the *wobble mode*.

- **ON/OFF mode.** The telescopes are pointing directly to the position of the source in the sky and the target is always in the center of the camera. This is called *ON observation*. The background estimation is obtained with a second observation in the so-called *OFF mode:* a patch of the sky without known gamma-ray sources with the same conditions as the *ON region* (same zenith and azimuth distribution, same epoch, and atmospheric conditions) is observed for the same time as the ON observation. One disadvantage of this method is that for each source the required observing time is twice that assigned to the source (to account for the ON observations and the OFF observations).
- **Wooble mode:** In this mode the telescopes are not pointing directly to the target but the source is always in a predefined offset with respect to the center of the camera. This offset, optimized with MC simulations, is usually 0.4 degree (for point-like sources). The background, in this *wobble mode*, is estimated simultaneously and under the same conditions as the signal (Fomin et al., 1994). *Wobble* observations are performed for equal time at opposite offset positions with respect to the center of the camera. These opposite positions are called *wobble positions* and, for standard observations, are at 0 degrees (W1), 90 degrees (W2), 180 degrees (W3) and 270 degrees (W4). A representation in Figure 2.21. Usually, the observation of a source starts with W1, then it switches to W2, W3, and finally W4. After this cycle, the observations restart from W1. Each position is usually

observed for 20 or 15 minutes (the so-called *runs*). One disadvantage of this pointing mode is that the gamma-ray detection efficiency decreases due to the shift of the source: the telescopes are pointing at 0.4 degree from the target, and some fraction of the EM cascades lies outside the trigger region. Furthermore, the systematic errors in the background estimation arise from the fact that ON and OFF regions are not taken from the same part of the camera, so the signal is overestimated or underestimated.

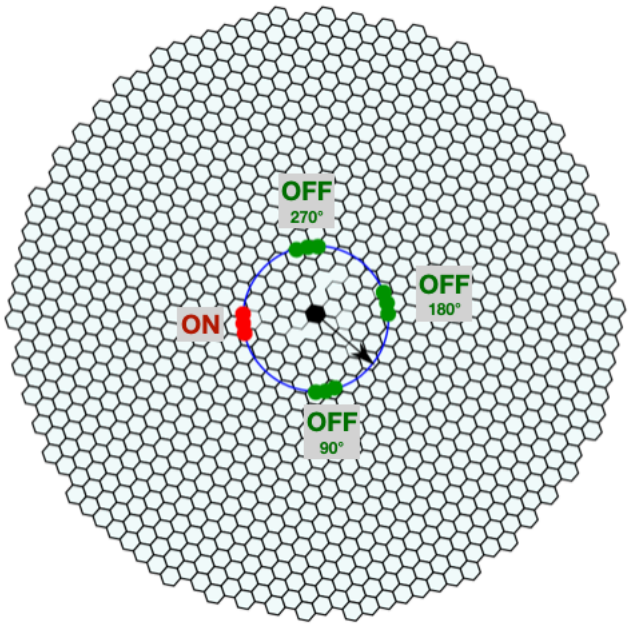

Figure 2.21 Schematic view of the wobble pointing mode. The blue circle has a radius of 0.4 degree, equal to the wobble offset used during observations. The black pixel is at the center of the camera. The source is the red dot; the green dots are the OFF regions (three in this case) used for background estimation.

2.2.3.3 Data Types

During the night, different types of data, for different purposes, are taken by the MAGIC telescopes. I briefly introduce them:

⋆ **Pedestal subtraction run (*pedsub*):** this run has to calibrate the pedestal noise of each Domino Ring Sampler (DRS) capacitor and set to 1000 counts its zero level, to avoid problems at negative values due to fluctuations. It is taken with the camera lids closed at the beginning of the night, before starting observations, and it is applied to all the subsequent runs. This procedure lasts around 6 minutes and is done once per night. The DRS chips are temperature dependent so, the readout system must be switched on at least 1 hour before taking the *pedsub* runs, to let the temperature stabilize.

In cases when the electronics are switched off for more than 30 minutes, this run must be taken again.

⋆ **Pedestal run (*_P_*) :** the baseline of the DRS chips are stable in a time scale of 1-2 hours. In case of small variations of the baseline, these are corrected with dedicated pedestal runs at the beginning of each observation and with interleaved runs. These runs, taken with the camera open (to evaluate the effect of the NSB and readout noise) are performed online by the DAQ.

⋆ **Calibration run (*_C_*):** these runs contain events from the calibration system and are used to update constantly the conversion factor between ADC counts and the number of phe and the arrival times. Calibration runs are taken before observing a source and are used later, during the analysis, to calibrate the data. As the Pedestal runs, they are taken also during the observations.

⋆ **Data run (*_D_*):** these runs contain all the events triggered by the telescopes during observations. One Data run corresponds to 20 or 15 minutes of observation (the time of duration of one wobble) and they are subdivided in subruns of 2 minutes which contain about 1 Gb of data.

2.2.4 Standard Data Analysis

2.2.4.1 Data Analysis Chain

The MAGIC data are analyzed with a dedicated software: MAGIC Analysis and Reconstruction Software (MARS), see Zanin et al. (2013)). This software, always updated and developed, is written in an object-oriented ROOT framework and the main language is C++. The goal of the analysis is to determine whether an event is generated by a gamma ray or a hadron to obtain the energy and direction in case of gamma ray-induced showers. In the following Sections I will summarize how the reconstruction of the events is performed by the MAGIC software. There are three main levels of analysis (illustrated in Figure 2.22):

- **Low Level:** the RAW data from each telescope are calibrated and cleaned. At this stage, the *Hillas Parameters* are calculated. The routines of MARS applied to data are:

  - `merpp`: data converted into readable ROOT format and includes subsystem reports;

  - `sorcerer`: calibration and signal extraction;

  - `star`: image cleaning and Hillas parameters calculation.

- **Intermediate Level:** the data from the two telescopes are merged and then, the stereoscopic information is estimated. For each event, the energy and the arrival direction are determined. The MARS routines applied to date are:

  - `superstar`: merging of both telescopes and calculation of stereo parameters.

  - `coach`: Random Forest training (gamma/hadron separation, arrival direction parameters) and energy separation.

  - `melibea`: application of Random Forest to assign an energy and hadronness to each event.

- **High Level:** this stage is the final one where the sky maps, signal search, spectrum and, light curve are calculated. The routines of MARS applied to data are:

  - `flute`: flux, spectrum and light curve estimation.

  - `odie`: significance computation.

  - `caspar`: 2D skymap production.

The low level stage is performed by the OSA (see Section 2.2.1.9) and it is done by the analyzer only in case of moon data or Sum-Trigger-II data. Instead, the intermediate and high-level analyses are performed in the standard off-line analysis chain.

Next, I will describe the processing of the data taken by the MAGIC telescopes in stereoscopic mode, from RAW to high level products.

2.2.5 Low Level Data Reconstruction

2.2.5.1 Monte Carlo Data

MC simulations are essential to reconstruct the energy of the primary gamma ray and its arrival direction. Only with MC simulations can the analysis of real data be performed. These simulations are produced with a modified version of COsmic Ray SImulations for KAscade (CORSIKA) (Heck et al., 1998), called `mmcs`, which makes it possible to have the direction and position of the Cherenkov photons on the ground. The MC gamma rays are simulated with two methods (see Figure 2.23):

- **ringwobble MCs:** these MC simulate a ring of 0.4 degree of radius from the center of the camera (this is the standard offset used for the wobble mode) and are used for point-like sources;

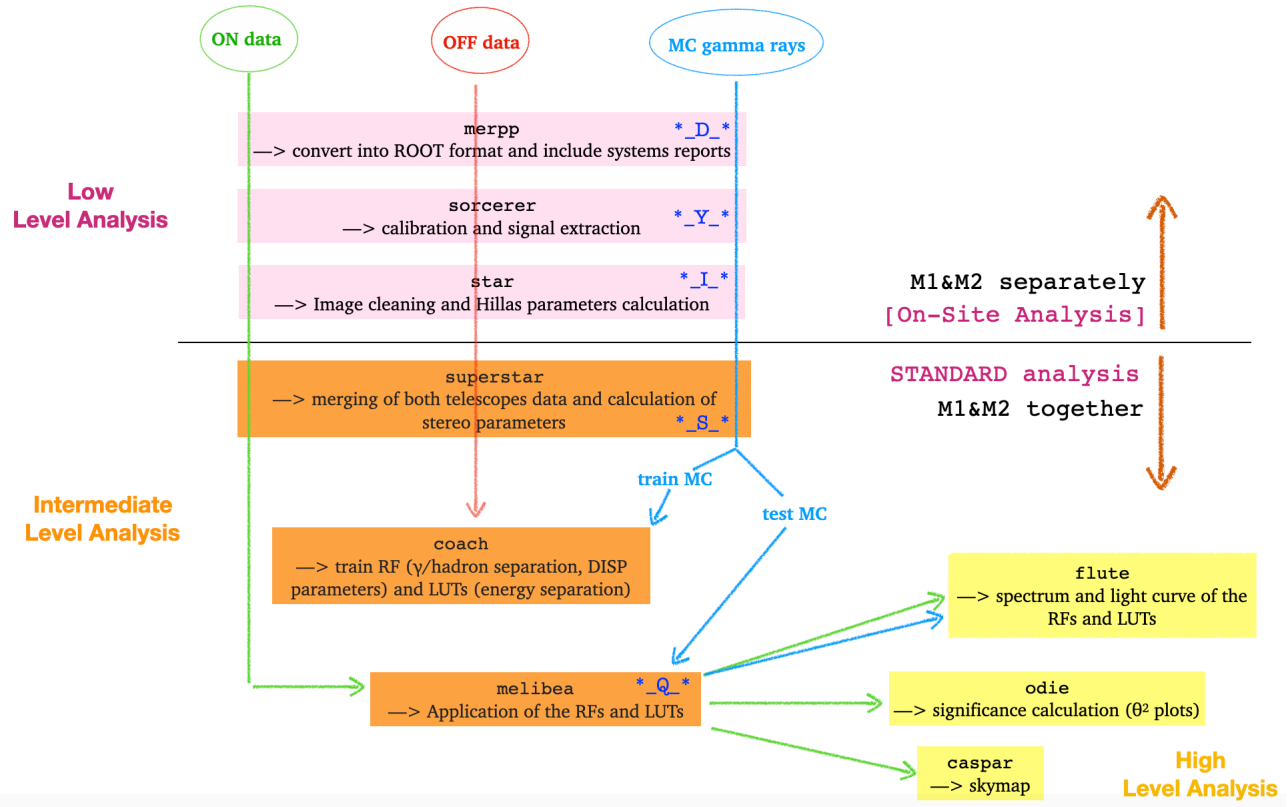

Figure 2.22 Flowchart of MAGIC stereo analysis chain.

- **diffuse MCs:** usually used for extended sources; in this case the diffuse gamma rays are simulated covering a circle of 1.5 degree of radius.

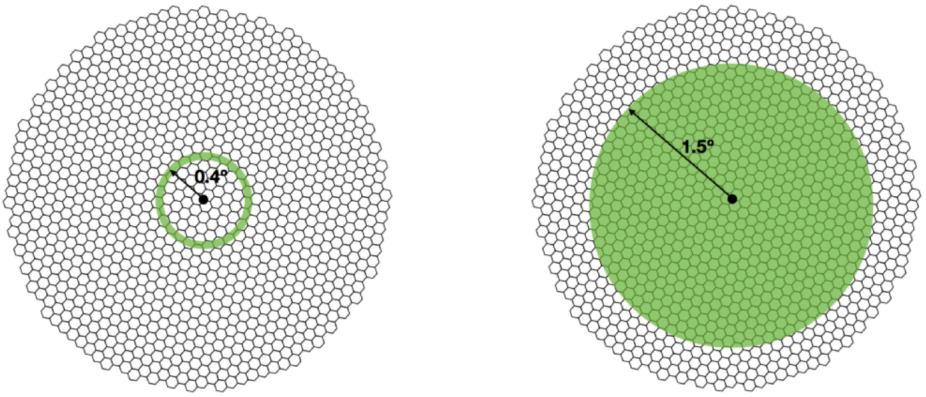

Figure 2.23 The MC modes. **Left**: the ringwobble MC mode, on the **right:** the diffuse MC mode.

The MC are created for different Zd angles:

- low Zd range (5° - 35°);

- medium Zd range (35°- 50°);

- high Zd range (50° - 62°);

- and very-high Zd range (62° - 70°).

The spectrum of the simulated gamma rays follows a power-law with a spectral index of Γ=1.6. When the MC photons are produced, the program `reflector` computes their propagation and absorption in the atmosphere; it considers also the reflectively of the mirrors and the position and the time of the incoming photons in the camera. Then, the program `camera` simulates the response of the PMT and of the whole electronic chain, considering also the noise from the NSB. At the end of the whole simulation chain, the events are saved in `ROOT` files and can be analyzed like real data with the software MARS. Every time that the hardware of the system is updated or telescopes need maintenance, MC simulations must be upgraded; for this reason in the history of MAGIC there are several MC productions. These productions are tagged as ST.XX.YY, where ST means "stereo", XX defines the major hardware changes and YY is the analysis period corresponding to minor hardware changes.

2.2.5.2 Signal Extraction and Calibration

The MAGIC `RAW` files contain the waveforms of the signal for each event and for each pixel. To analyzed these files, one needs to convert them into `ROOT` format. This is done by the program `merpp` (*MERging and Prepoccesing Program*) which attaches the report files[†] to these `ROOT` files.

The first step in the analysis chain is the signal extraction: the calculation of the charge in phe that hits the PMT and of the arrival time of the signals. The waveform, converted into 50 time bins of 0.61 ns each, is composed by the signal and its baseline. The baseline is estimated with the *pedestal runs* (events with random triggers and so without any pulse) binning the signal from each time slice into a single histogram and fitting it with a Gaussian, whose mean is taken as the baseline. When the baseline is known, the signal can be extracted. After the signal extraction, the calibration process can start. The signals are given in integrated readout counts, but what it is needed is their value in phe. The conversion in phe is done through the *F-Factor* (for the details see Mirzoyan 1997), and the basic assumption is that the number of phe follows a Poisson distribution.

This calibration process is done with the MARS program `sorcerer`(*Simple, Outright Raw Calibration; Easy, Reliable Extraction Routines*) in two steps: *C-mode* and *Y-mode*. In the *C-mode*, the pedestal runs and the calibration runs

[†]The reports contain essential information like the telescope pointing, the status of the camera and the mirrors, the wobble, etc.

files are processed to get the baseline, the pedestal bias, the RMS, the mean arrival times and, the conversion factors. The *Y-mode* runs over the output files of the *C-mode* (*_Y_* files) and in this step the events are calibrated and the *pedestal/calibrated runs* are used to update the values calculated in the *C-mode*. The output files are ROOT data which contain information about calibration.

2.2.5.3 Image cleaning and Hillas Parameters Calculation

The image of the shower usually covers only a small part of the total camera surface. The rest of the pixels contain random noise and fluctuations from the NSB, electronic noise or light from stars. To improve the results, these pixels need to be screened out before characterizing the Cherenkov shower image in terms of geometrical parameters. Both steps, image cleaning and parametrization, are done at once by `star` (*STandard Analysis and image Reconstruction*) MARS program. The input files are the previous calibrated ones , the output files are called *star files*.

The default image cleaning method is divided in two steps (see Aleksić et al. (2012a) for more details):

1. **Sum Image Cleaning:** the signals are first clipped in amplitude[‡] (to reduce biases due to after-pulses and strong NSB fluctuations) and combinations of 2, 3, or 4 compact neighboring pixels are identified (referred as 2NN, 3NN and 4NN). The pixels of each combinations are not discarded if their charge is above a certain threshold and the difference between the arrival time of the pixels is defined in a fixed time window. The charge threshold and the time window depend by the number of neighboring pixels (more strict for smaller groups).

2. **Time-constrained Absolute Image Cleaning:** the remaining pixels are defined as *core* or *boundary* pixels. Pixels with a charge greater than a reference value Q_{core} are tagged as *core* pixels (if at least one neighbor pixel survived in the previous step). Furthermore, if the mean time of arrival is outside a 4.5 ns time window, the *core* pixel is discarded. After that, there is the selection of the *boundary* pixels: they must have a core pixel as a neighbor, a charge above a second reference level ($Q_{boundary}$) and a time difference with respect to the core pixel of 1.5 ns.

The `star` program can remove *hot pixels* (pixels with high signal) produced in the camera by bright stars in the FoV. This step is extremely important in the image cleaning of Sum-Trigger-II data (see later Section 2.2.8.3).

An example of the before and after the image cleaning process is shown in Figure 2.24.

Now that the images are cleaned, the *parameterization* process can start. In this step the *image parameters* are calculated. Some of them were introduced for the first time by Hillas (1984) to discriminate between showers initiated by hadron

[‡]The clipping level is set to 750 phe.

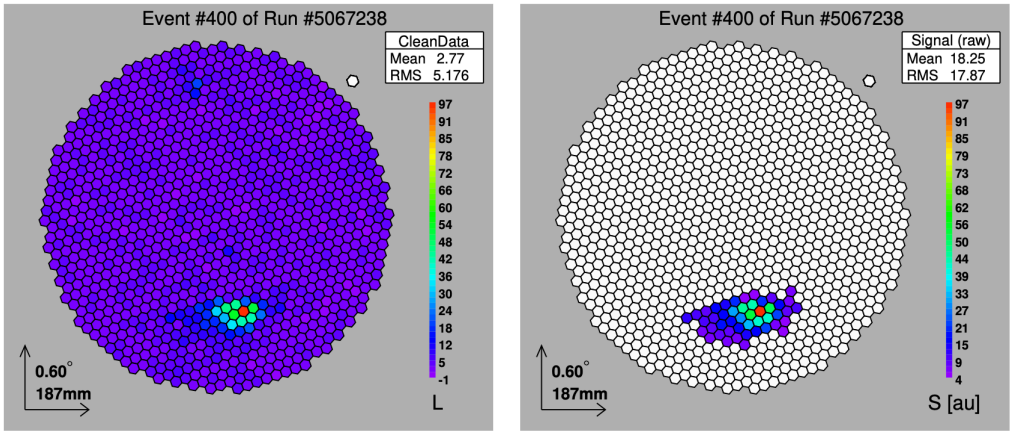

Figure 2.24 Example of the *image cleaning process*. **Left**: the raw signal coming from the camera; **right** the camera signal cleaned with the average background removed.

and gamma rays. To obtain these parameters an ellipse is fit to the surviving pixels and the momenta of the fit (up to second order) are the parameters used in the analysis of MAGIC. The information of the parameterization of each event is saved in ROOT files for both telescopes separately. The Hillas parameters are listed in Table 2.1 and some of them are reported in Figure 2.25.

Parameter	Description
size	Total number of phe in the image. At zero-order approximation, it is proportional to the energy of the primary particle.
length	Half length of the major axis of the ellipse.
width	Half of the minor axis of the ellipse.
alpha	Angle between the major axis of the ellipse and the line connecting the reference point and the center of gravity.
center of gravity (CoG)	Coordinates X and Y in the camera reference frame representing the center of gravity of the shower image.
conc-n	Given the *n* brightest pixels, it represents the fraction of phe contained in those pixels.
asym	Difference between the peak of the charge distribution in the image and the center of gravity.
number of islands	Number of different islands of the image (island: a group of isolated pixels survived after the cleaning).
leakage	Given the last 1/2 camera pixel rings, it is the fraction of signal distributed in them with respect to the image size.
M3long	Third moment (asymmetry) of the image along the major axis of the ellipse.
dist	Distance of the center of gravity from the reference point.
time-gradient	Angular coefficient of the linear function used to fit the arrival time distribution of each pixel after their coordinates have been projected on the major axis of the ellipse
time-rms	Spread of the arrival time distribution of the pixels belonging to the image

Table 2.1 List of the main *Hillas parameters* used by the star routine of the MARS software.

2.2.5.4 Data Quality Selection

The MAGIC telescopes operate without any protection (e.g. a dome) and so they are not protected against bad weather conditions. Observations, as described in Section 2.2.3.1, cannot be performed if some conditions are outside the *safety*

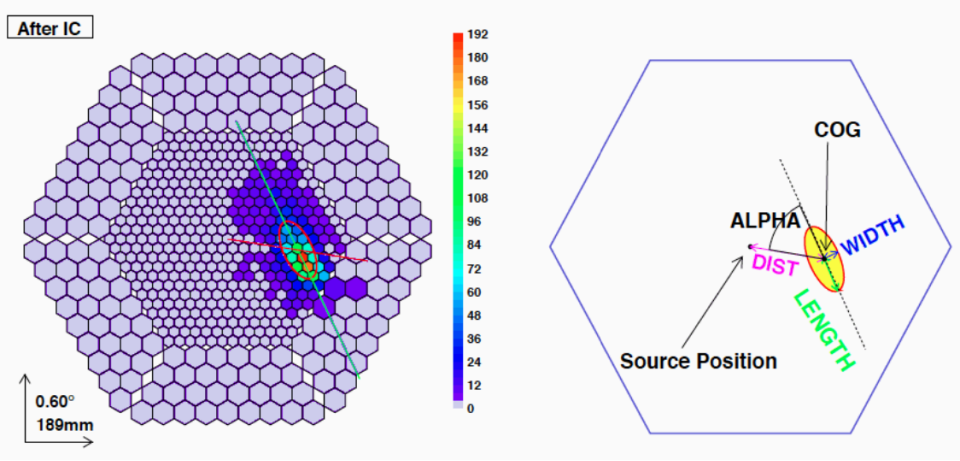

Figure 2.25 **Left**: parameterization of a shower image after image cleaning and, on the **right**, representation of some Hillas Parameters.

limits but it can happen that data are affected by hardware failures or by cars passing at the MAGIC site (so-called "car flashes") and by particular atmospheric conditions. The Cherenkov gain is affected by the presence of clouds or calima, which modify the quantity of aerosols and water vapors, and also by the photon scattering, absorption and the change of the refractive index of the atmosphere. The essential parameter is the total *transmission* of the atmosphere, which can be monitored with the LIDAR system (see Section 2.2.1.8). The transmission is usually calculated at 9km, T_{9km}, because 10km is the average height where the showers develop (LIDAR computes the transmission at 3km, 6km, 9km and, 12km). A low transmission implies a degradation of the shower images and thus, a worse parameters estimation. Data are considered to be taken under good quality atmospheric conditions if $T_{9km} > 0.85$. When the data are characterized by limited transparency, $0.55 < T_{9km} < 0.85$, they can still be used, but taking particular care by applying corrections in the next steps of the analysis (in the energy estimation). However, data with $T_{9km} < 0.55$ cannot be corrected and thus cannot be used.

In particular, data taken with the Sum-Trigger-II system are characterized by sub-100 GeV particles showers which are fainter than higher energy showers, and consequently, they are more affected by the lower atmospheric transmissions. For this reason, Sum-Trigger-II data require excellent atmospheric conditions ($T_{9km} > 0.85$).

2.2.6 Intermediate Data Reconstruction

2.2.6.1 Stereo parameters reconstruction

So far, the data analysis is performed individually for each of the telescopes. Once good data have been selected, the `superstar` MARS program combines the information coming from the two MAGIC telescopes with the goal of reconstructing a 3D image of the Cherenkov shower, calculating the so-called *stereo parameters*. This step takes as input the *star files* (one per telescope and subrun); the results are stored in *superstar* ROOT files, one for each data run. The most important stereo parameters are the following (see Figure 2.26):

- **Shower Axis.** This axis is characterized by a direction and an impact point on the ground. The direction of the incoming shower can be reconstructed from the intersection of the major axes of the two images of the shower in the camera. The impact point is the intersection of the major axes of the two elliptical images starting from the telescope positions (taking into account the distance between the two telescopes). Through the shower axis it is possible to calculate the angle θ between the estimated shower direction and the true source position. Generally, the θ^2 is used, since the modulus of this distance is considered.
- **Impact Parameter:** is the perpendicular distance between the shower axis and the telescope pointing axis.
- **Shower Maximum Height:** is the estimation of the height at which the shower had its maximum. This height is obtained by using the angle at with the Center of Gravity (CoG) is viewed from each telescope and is the intersection point between the shower axis and the lines going from each telescope to the centroid direction in the sky. The height of the shower maximum depends on the energy of the primary particles: higher energy showers penetrate deeper into the atmosphere, hence their maxima are closer to the ground.
- **Cherenkov Radius and Density:** radius and density of the Cherenkov light pool on the ground. The light density is calculated from the ring generated by the electron after it has traveled a one-meter track.

2.2.6.2 Event Characterization

After calculating the image and stereo parameters, the nature and properties of the events can be determined. The events triggered by the MAGIC telescopes are of various types (accidental triggers, muons, hadrons and gamma rays) and a

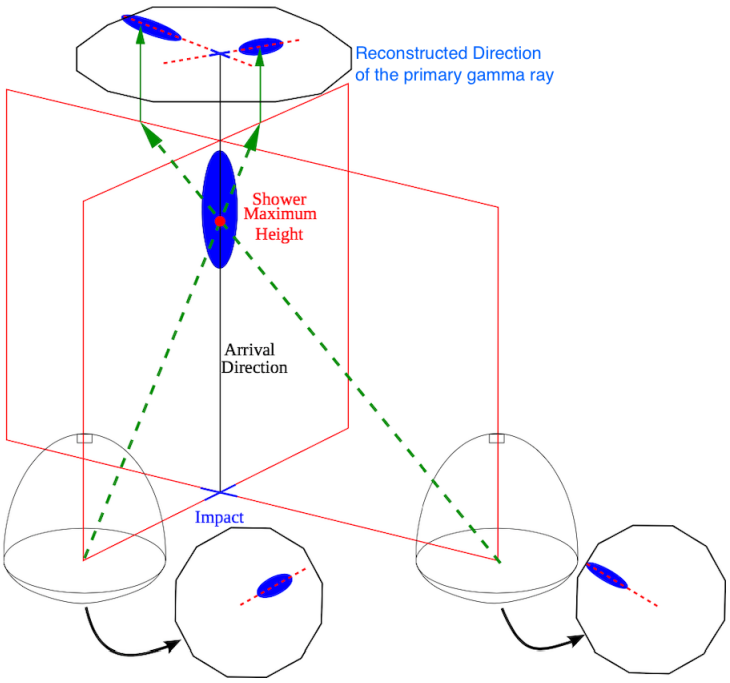

Figure 2.26 Example of the reconstruction of some stereo parameters.

powerful tool is necessary to recognize gamma rays events from this dominant background. The other two properties needed for the high-level analysis are the energy and arrival direction of the events.

The separation between gammas and hadrons (gamma/hadron separation) is carried out using a classification method called Random Forest (RF) (Albert et al., 2008), the energy estimation with LUTs and the arrival direction uses the so-called *DISP* parameter. All these methods are implemented in the MARS program `coach` and are described in the following paragraphs. Then, the estimation of the nature of the particle, its energy and arrival direction is performed by the executable `melibea` which uses the output files `coach`.

Gamma/Hadron Separation As discussed above, the analysis needs a robust tool in order to select the events that are likely gamma rays from a dominant background (showers originated by hadrons). Moreover, even in bright sources, like the Crab Nebula, the number of hadrons is three orders of magnitude greater than the number of gammas. So, to reject almost all hadrons, the classification method called RF is used: image, stereo parameters and timing information are combined simultaneously to reach the highest degree of separation between the hadronic and gamma events. This RF method is used to compute a parameter called *hadronness*, correlated with the probability for the event being hadron-like. This parameter has a value between 0 and 1: events with *hadronness* close to zero are most likely

gamma events. The inputs needed for coach are a MC dataset of simulated gamma-ray events and a set of OFF data with mostly hadronic events. In particular, the MC data set are divided into two subset: one, called *training sample*, is used in the RF method while the other, the *test sample*, is used for the computation of the instrument response function. Both gamma MC and OFF data samples must be chosen in the same zenith range as the ON data and the OFF data should have the same data taking conditions as the ON data (dark or moon, Galactic or extragalactic).

Energy reconstruction The standard method for the estimation of energy for stereo observations depends on LUTs. The sample of gamma MC is binned in some image parameters, and for each bin the mean energy and Root Mean Square (RMS) of the MC events is computed. A real event is then attributed to one of these bins, and consequently it acquires the related energy. This process passes through different approximation stages. The main assumption is that the energy of the primary particle is proportional to the number of Cherenkov photons in the shower and this results in a proportionality between the energy and the size of the images. The table is filled with corrections of E/size instead of the true energy (first order). In the end, small corrections are applied related to atmospheric optical depth, geomagnetic field, image leakage and, zenith angle (important at high zenith angles, where the Cherenkov light is absorbed more). The final energy estimation E_{est} is an average between $E_{est,1}$ and $E_{est,2}$ (weighted with the inverse of their RMS) which are calculated for each telescopes separately.

Arrival Direction Reconstruction With the so-called DISP (Distance between the Image centroid and the Source Position) RF method the arrival direction of the primary gamma ray with respect to the produced electromagnetic shower can be determined (Aleksić et al., 2016b). This complex method uses the shape of the image as seen by an individual telescope to reconstruct the angle between the direction of the shower maximum of each event and the incident direction of the gamma-ray or source position. Once the DISP is known, the reconstructed source position is not uniquely determined: there are two possible solutions along the major axis of the ellipse. In the case of stereoscopic observations, the two images of the same event are taken on the same plane and the four reconstructed source positions (2 per image) are found. The four distances between these positions are computed and the pair with the smallest distance is taken. The final estimated source position is an average of these two positions weighted by the number of pixels in each image. The estimated arrival direction will be the line connecting the CoG to the reconstructed source position. In particular, if none of the distances are smaller than 0.22°, the reconstruction is not accepted as valid by the algorithm. The DISP method is shown in Figure 2.27.

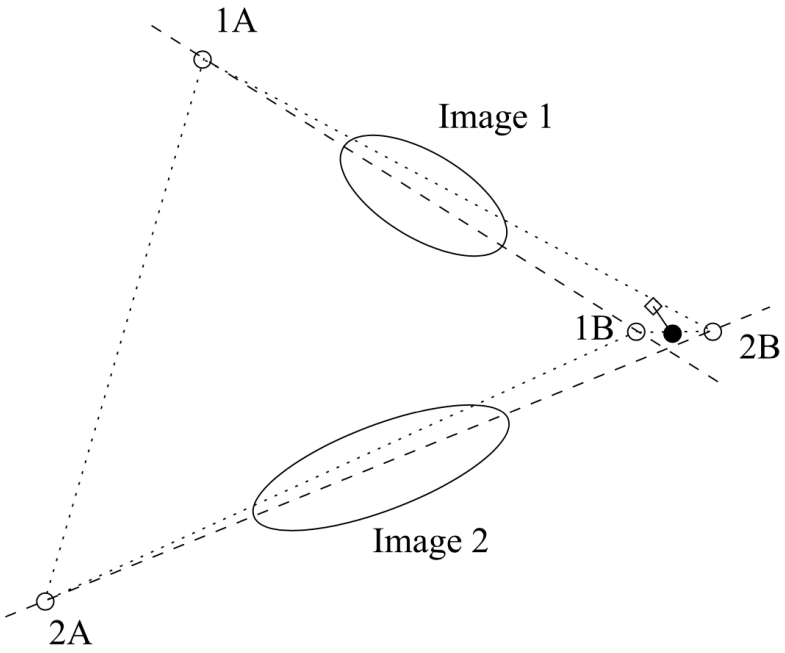

Figure 2.27 Graphical representation of the DISP method for the reconstruction of the arrival direction of the events. Given two images for the same event, there will be four reconstructed source positions (empty circles). The angular distances between them are shown by dotted lines: the closest pair is chosen (in this example 1B-2B) and their weighted average is taken as the final reconstructed position for the source (black dot). The solid line is θ, the angular distance between the true (empty diamond) and reconstructed position of the source. From Aleksić et al. (2016b)

2.2.6.3 Signal Significance

After having evaluated hadronness, reconstructed energy and direction of the events, it is possible to evaluate whether the data sample contains a signal. This step is performed with the MARS program `odie`, that computes the angular distance θ between the reconstructed and the expected position of the source. The result is represented in the histogram called θ^2-plot. Only the events that survive the analysis cuts (size, hadronness and zenith) are included in the *signal histogram*. There are standard cuts for the MAGIC analysis, optimized on an independent data sample (usually Crab Nebula data), which define specific energy ranges for the analysis, as reported in Table 2.2.

Energy range	E_{th} [GeV]	θ^2	*Hadroness*	Size in M1 [phe]	Size in M2 [phe]
Low energy (LE)	100	<0.02	<0.28	>60	>60
High Energy (HE)	1000	<0.007	<0.01	>400	>400
Full Range (FR)	250	<0.009	<0.16	>300	>300

Table 2.2 Standard cuts for the different energy ranges in the MAGIC analysis.

The events that survive all the cuts and fill the *signal histogram* are defined as "events in the signal region" with the number N_{on}. These events are not only gamma rays coming from the source, but also gamma-like hadrons, $e^{\pm}$, and diffuse gammas. To estimate of how many non-gamma events are inside the signal region, a different θ^2 histogram, the so-called *background histogram*, is filled. Now, the θ_{off} is the distance between the reconstructed position and the OFF position; where the OFF position is the position situated at the same angular distance as the source from the center of the camera, but on a different region (see Figure 2.29). This *background histogram* defines the number of OFF events, N_{off}, which are uniformly distributed over the whole histogram since the camera should be homogeneous close to the center, where the source lies. For this reason, the gamma-ray events, produced by the source, peak at small values of θ^2. An example of a typical θ^2 plot is shown in Figure 2.28.

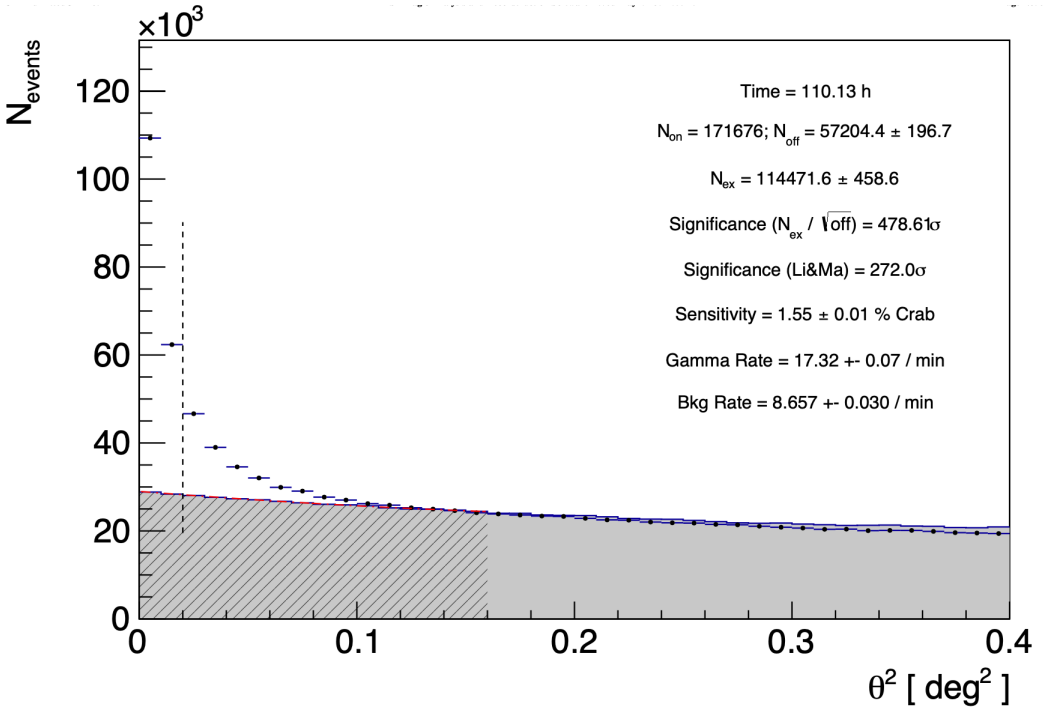

Figure 2.28 Example of θ^2 plot of the Crab Nebula, represented as distribution of the events for the MAGIC observations. The vertical dashed line indicates the defined signal region from which the significance of the detection is calculated.

The number of excesses N_{ex} is calculated as:

$$N_{\mathrm{ex}} = N_{\mathrm{on}} - \alpha N_{\mathrm{off}} \tag{2.5}$$

where the scale factor α is the normalization between N_{on} and N_{off} and is equal, in case of *wobble* observations, to

1/(number of OFF regions), where the number of OFF regions can be 1, 3 or 5 for standard observations.

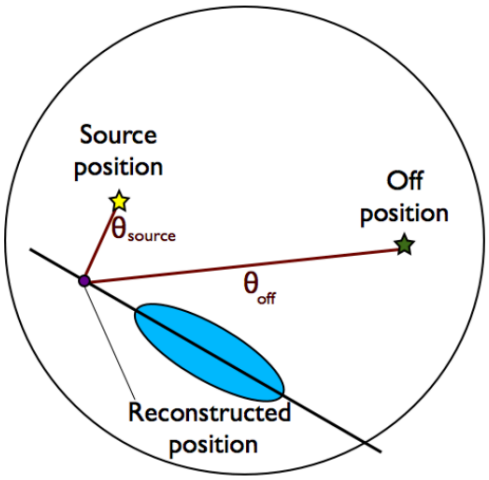

Figure 2.29 Sketch illustrating how the angle θ is calculated with respect to the source and OFF positions. From Lopez-Coto (2015).

Once the N_{ex} is known, it is possible to define the statistical significance of the signal. VHE gamma-ray astronomy relies on the statistical method called *Likelihood Ratio Test* to determine whether a source is detected or not. In this method two hypothesis are compared in terms of their Likelihood. The null hypotheses ($\mathscr{L}_0$) refers to the case of having, in the data sample, only background events (no signal); while, an alternative hypothesis ($\mathscr{L}_1$) refers to the case that is tested and where the signal is expected. The ratio between the likelihoods computed on the two hypotheses relates the chance probability that the excess is due to a spurious fluctuation. In the MAGIC analysis, this method is applied to the evaluation of the significance of the gamma-ray signal through the equation n.17 of Li & Ma (1983):

$$\sigma_{\mathrm{LiMa}} = \sqrt{2\left(N_{\mathrm{on}} \ln\left[\frac{1+\alpha}{\alpha}\frac{N_{\mathrm{on}}}{N_{\mathrm{on}}-N_{\mathrm{off}}}\right] + N_{\mathrm{off}} \ln\left[(1+\alpha)\frac{N_{\mathrm{off}}}{N_{\mathrm{on}}-N_{\mathrm{off}}}\right]\right)} \tag{2.6}$$

The Li&Ma significance depends on the number of OFF positions used for the background extimation. The Gaussian approximation of equation 2.6, can be given as:

$$\sigma_{N_{\mathrm{ex}}/\sqrt{N_{\mathrm{off}}}} = \frac{N_{\mathrm{ex}}}{\sqrt{N_{\mathrm{off}}}} \tag{2.7}$$

A source is considered detected in the VHE gamma-ray range if the significance of the excess of gamma events over

background events exceeds 5σ.

2.2.6.4 Sensitivity

The sensitivity is used to quantify the performance of an instrument. The usual definition of the IACT sensitivity is the minimum flux that can be detected in 50 hours of observation with a significance of 5σ, with the Gaussian approximation: $\sigma_{N_{\mathrm{ex}}/\sqrt{N_{\mathrm{off}}}}$. It is useful to compare the performance of different instruments and usually this is expressed as a fraction of the Crab Nebula flux in a particular energy range, often referred to as Crab Units (C.U.).

Considering an observation of the Crab Nebula where a number of observed excesses N_{ex} and background events in the signal region N_{off} are observed in a time t, the significance in a time t_0=50 hours is given by:

$$\sigma_{N_{\mathrm{ex}}/\sqrt{N_{\mathrm{off}}}}(t_0) = \sqrt{\frac{t_0}{t}} \frac{N_{\mathrm{ex}}}{\sqrt{N_{\mathrm{off}}}} \tag{2.8}$$

from which it is possible to deduce that the relation between significance and observation time: $\sigma \propto t_0$. So, the sensitivity S of an instrument, given as the minimum flux that can be detected in t_0=50 hours and with a significance 5σ in C.U. is:

$$S = \frac{5\sigma}{\sigma_{N_{\mathrm{ex}}/\sqrt{N_{\mathrm{off}}}}(t_0)} \tag{2.9}$$

Usually the sensitivity is calculated in two ways:

- **Integral sensitivity:** the integrated signal above a given energy threshold that allows for the detection of the signal itself;

- **Differential sensitivity:** the integrated signal in small energy bins with a given energy threshold that allows for the detection of the signal itself.

The current MAGIC integral and differential sensitivities are reported in Figure 2.30 from Aleksić et al. (2016b). The MAGIC telescopes have a better sensitivity at low energies, especially with the Sum-Trigger-II system.

2.2.6.5 Instrument Response Function

The Instrument Response Function (IRF) of an IACT is governed by its hardware design, software design, and the criteria for the selection of the events. IRFs are calculated through MC simulations and separately for each analysis; they depend on the cuts applied to the data and on the technical settings and performance of the telescopes at the time

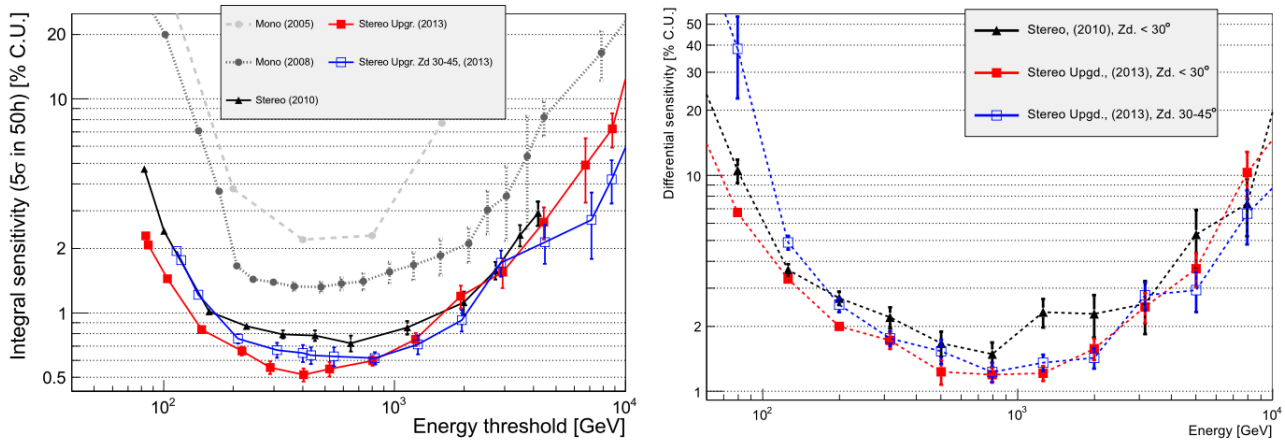

Figure 2.30 MAGIC integral (left panel) and differential (right panel) sensitivity as a function of energy. Grey and dark grey dots: mono era with different readouts. Black triangles: stereo era with old MAGIC-I camera. Red squares: current MAGIC sensitivity for low zenith observations (below 30°). Blue empty square: current MAGIC sensitivity for observations between 30° and 45°. From Aleksić et al. (2016b).

of the observations. In this Section, I describe the main characteristics of the three functions describing the IRFs of the MAGIC telescopes: the effective collection area, the angular resolution, and the energy resolution.

Effective Collection Area The effective area A_{eff} is the geometrical area around the telescopes where a signal coming from the gamma-ray shower is detected. The value of A_{eff} depends on the gamma-ray efficiency of all the cuts applied during the analysis and, in particular, on the spatial coordinates, the gamma-ray energy, zenith and azimuth angle. Since A_{eff} is a result of many parameters, it is calculated in bins of energy, zenith and, azimuth angle.

The effective area in MAGIC is computed by applying the same cuts and analysis procedures to a sample of MC simulated gamma rays. It is calculated dividing the number of detected gamma rays surviving the analysis cuts ($N_{\gamma,\text{final}}$) by the number of simulated gamma rays in a given energy range ($N_{\gamma,\text{total}}$) multiplied by the simulated area ($\mathcal{A}_{\text{sim}}$), or the area of an ideal telescope that would detect all the simulated gamma rays (Aleksić et al., 2016b). So, the effective area is defined as:

$$\mathcal{A}_{\text{eff}} = \mathcal{A}_{\text{sim}} \frac{N_{\gamma,\text{final}}}{N_{\gamma,\text{total}}} \tag{2.10}$$

The MAGIC effective area is shown in Figure 2.31 and the order of magnitude of the effective area is about 10^5 m^2 for gamma rays of 300 GeV.

The effective area strongly depends on the zenith angle. Showers coming from different zenith angles illuminate the

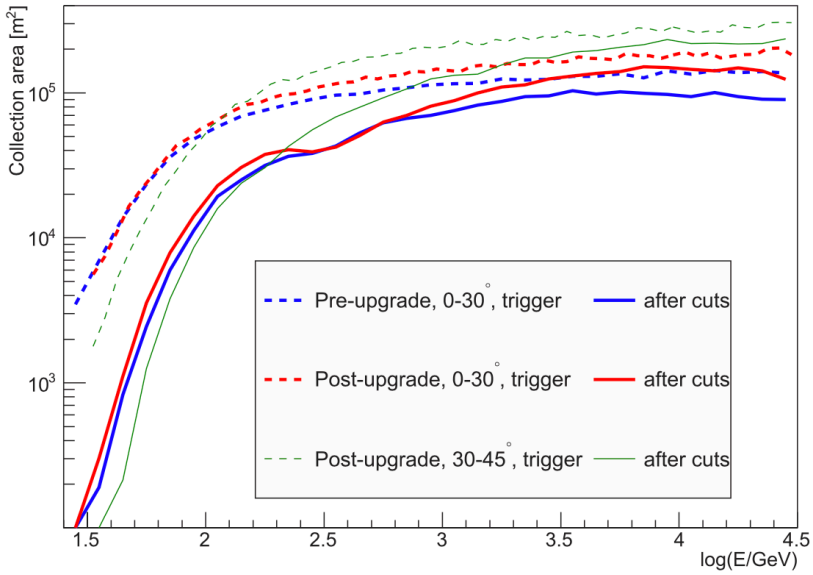

Figure 2.31 Effective collection area of the MAGIC telescopes in two different zenith ranges (red lines: $0° - 30°$; green lines: $30° - 45°$). Blue lines: pre-upgrade period. Both trigger (dashed lines) and after all cuts (solid lines) effective areas are shown. From Aleksić et al. (2016b).

ground in different ways:

- at low zenith angles, the light pool is smaller and the corresponding photon density is higher;

- at high zenith angles, the light pool might increase, but the corresponding photon density decreases. In particular the light coming from the impact point of the primary gamma ray has to travel through a much thicker layer of atmosphere, and for this reason absorption processes (e.g. pollution and clouds) decrease the rate of low energy events. This results in an higher energy threshold and larger effective area at high energies (showers are dimmer due to the larger extinction).

Angular Resolution The angular resolution of the instrument is the ability of reconstructing the incoming direction of gamma rays. In MAGIC, two methods are used (Aleksić et al., 2016b):

- angular resolution Θ_{gauss}: is the standard deviation of the 2-dimensional Gaussian function fitted to the distribution of the reconstructed arrival direction of the gamma-ray excesses;

- angular distance Θ_{68} around the source position which encloses 68% of the excess events.

These values are different and usually $\Theta_{gauss} < \Theta_{68}$. The angular resolution depends on the energy: showers of high-

energy events are better reconstructed, and so the angular resolution improves with the energy. For example, at low energies (about 100 GeV) the angular resolution is about 0.1°, and it improves to 0.04° at TeV energies. Figure 2.32 shows the angular resolution of the MAGIC telescopes.

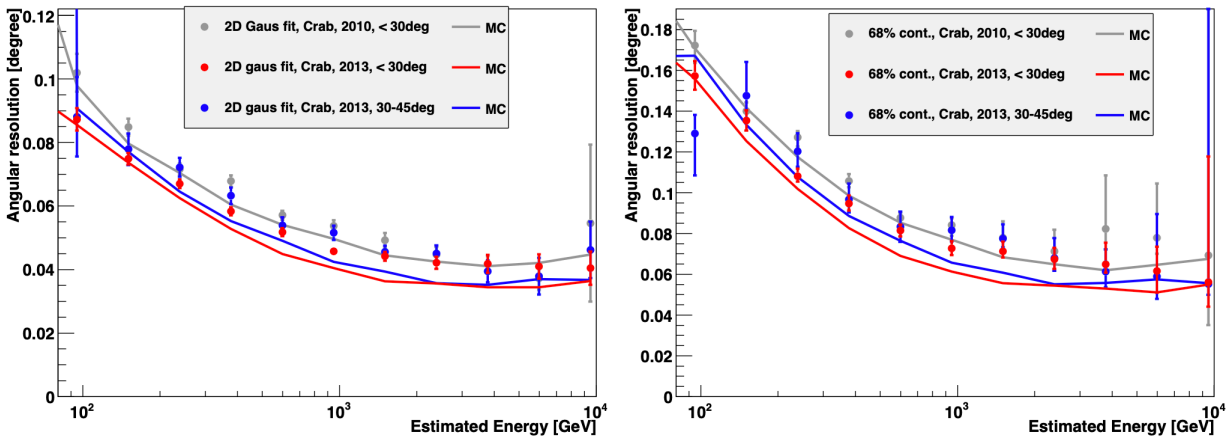

Figure 2.32 Angular resolution of the MAGIC telescopes as a function of the estimated energy obtained with the Crab Nebula data sample (points) and MC simulations (solid lines). On the **left** panel: 2D Gaussian fit; on the **right** panel: 68% containment radius. Red points: low zenith angle; blue points: medium zenith angle. Grey points: Angular resolution at low zenith angle before 2012-2013 upgrade of telescopes. From Aleksić et al. (2016b).

Energy Resolution The energy resolution gives an estimation of the quality of the energy reconstruction for the main event, and its performance is evaluated with gamma−ray MC simulations. The energy resolution is defined as the standard deviation of a Gaussian fit to the peak of the $(E_{est} - E_{true})/E_{true}$ distribution. At higher energies the energy resolution degrades due to an increasing fraction of truncated images, as in the low energy range, it degrades due to worse precision in the image reconstruction (in particular the impact parameters). The difference from zero of the peak of the $(E_{est} - E_{true})/E_{true}$ distribution is called *energy bias*; this value is less than 5% for low zenith observations above a few hundred GeV while, at low energies, it increases up to 20% due to threshold effects. Figure 2.33 shows both the energy bias and resolution as a function of the true energy.

Energy Threshold Aleksić et al. (2016b) defines the Energy threshold of an observation as the peak of the energy distribution of the simulated MC data for a source with a power law spectrum with a spectral index Γ_{MC} = -2.6. Considering that the observed source can have a power-law spectral index Γ_{source}, the correct energy threshold is computed

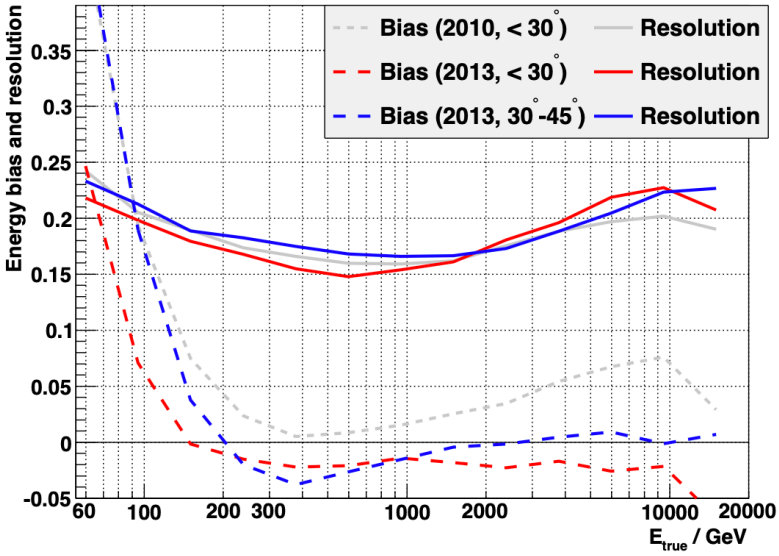

Figure 2.33 Energy bias (dashed lines) and resolution (solid lines) after reconstruction, obtained from MC simulations. Red, blue, grey points: low zenith (<30o), medium zenith (30o-45o) and low zenith angle before 2012-2013 upgrade. From Aleksić et al. (2016b).

with respect to the fixed Γ_{MC} as $\Gamma_{\text{correct}} = \Gamma_{MC} - \Gamma_{\text{source}}$. The MAGIC energy threshold, reported in Figure 2.34, is quite stable for low zenith angle observations, but increases rapidly when the zenith becomes higher, or when analysing moon data (larger absorption of the Cherenkov light in the atmosphere). The Energy threshold of the Sum-Trigger-II system is reported in Section 2.2.1.7, Figure 2.19.

2.2.7 High Level Data Analysis

Now that the data are selected with optimized cuts, it is possible to produce higher level results: sky maps, light curves, integral and differential spectra (in case of signal detection) or upper limits (in case of non detection). All these results depend on MAGIC IRF (see Section 2.2.6.5). In this last step of the analysis the signal is no more measured in instrumental units (counts), but in physical quantities.

2.2.7.1 Skymaps

The skymap is a 2D representation of the incoming direction of gamma-ray events. It contains arrival directions, in sky coordinates, of all the gamma-ray events that survive after the analysis cuts and after the subtraction of the expected background. The skymaps are helpful to detect unexpected sources in the FoV of the observation or to study the mor-

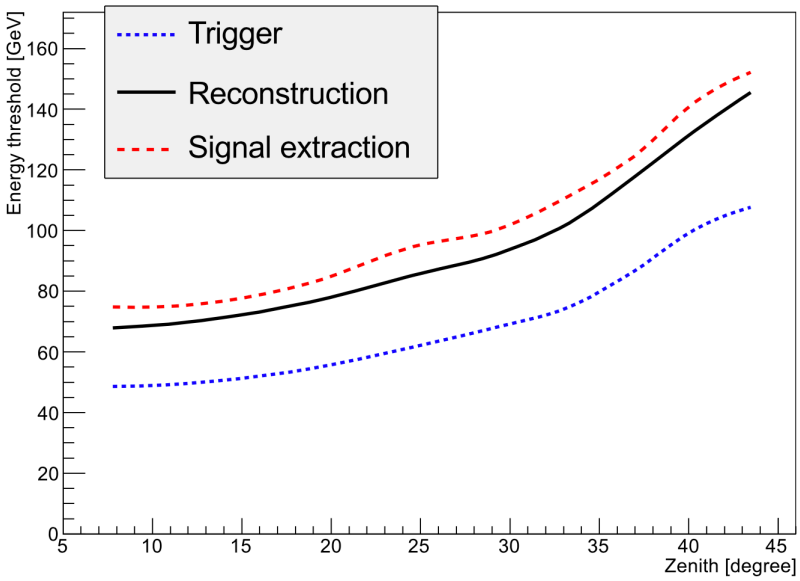

Figure 2.34 Energy threshold of the MAGIC telescopes as the function of zenith angles of the observation. It is represented at different analysis stages: trigger level (blue dotted line), reconstruction level (after image cleaning and with size > 50 phe, black solid line) and signal extraction level (hadronness < 0.5 and θ^2<0.03$^{\circ 2}$ (red dashed line). From Aleksić et al. (2016b).

phology of extended sources. Starting from melibea data, the executable `caspar` is responsible of creating skymaps. The main challenge in producing sky maps is the correct estimation of the background, that is affected by the inhomogeneities in the pixel response, stars in the FoV and observations at different Zd and Az angles. In the case of *wobble* observations, the advantage is that the background can be extracted from the same data sample as the signal, avoiding contamination from the signal region. The significance of a signal in a sky map is expressed as Test Statistics (TS), which is the Li&Ma significance (Li & Ma, 1983) applied on a smoothed and modelled background. The histogram of excess events is obtained by subtracting the signal sky map from the background one; this histogram is smoothed using the PSF of MAGIC added in quadrature with a Gaussian kernel to smear the number of excesses obtained.

2.2.7.2 Spectrum and Light Curve

In order to estimate the flux of a gamma-ray source we need to define some observable quantities:

Effective Observation Time T_{EFF}. Each time that an event triggers the telescopes, there is a dead time for which the data acquisition system is busy 'building' the event and during this time the system cannot accept any new events. For MAGIC, the dead time d per event is due to the DRS4 based readout and its value is 26 μs. The effective

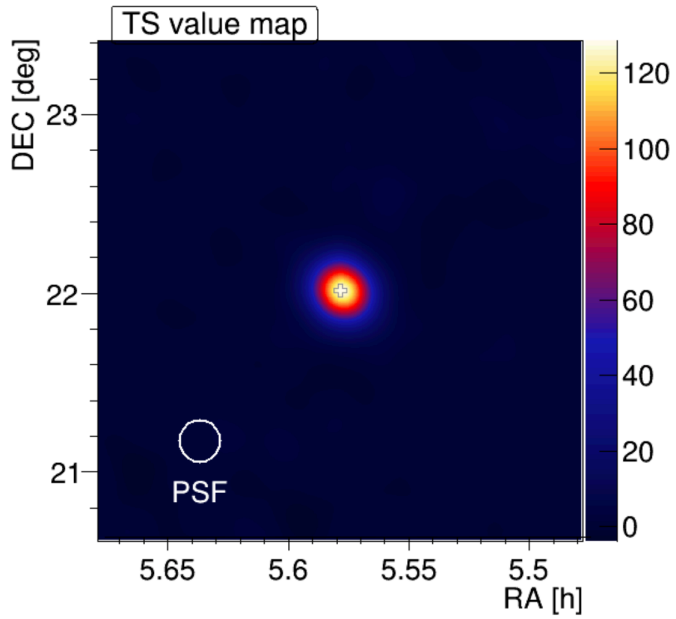

Figure 2.35 Example of a skymap created with `caspar` from Crab Nebula data.

time is given by:

$$t_{\text{eff}} = \frac{t_{\text{elapsed}}}{1 + \lambda d} \tag{2.11}$$

where λ is the rate of the events and t_{elapsed} is the time elapsed during the observation. The effective time is calculated in the program `flute`.

Collection Area A_{eff}. For details, see Section 2.2.6.5.

Number of Gammas. The number of gamma rays in the energy range E is estimated as the number of excess events in that energy range $N_\gamma(E)$, which is defined as $N_{ex} = N_{on} - N_{off}$. The calculation is similar to what the program `odie` does but the difference now is that the cuts on hadronness and θ^2 are optimized for each energy range according to a predefined efficiency: MC data are binned in energy and hadronness. So, for each energy bin, the optimal cut is the one where the number of events exceeds the efficiency. The same for the θ^2. With this method we are not searching for a signal and so the cuts are looser than the `odie`'s cuts.

Once that N_γ, t_{eff} and A_{eff} are calculated in each energy bin, it is possible to define the differential energy spectrum of

a given source as the number of photons per unit of energy, time and area:

$$\frac{d\Phi}{dE} = \frac{dN_\gamma(E)}{dE\, dA_{\text{eff}}(E)\, dt_{\text{eff}}} \tag{2.12}$$

In MAGIC, the spectrum is calculated using the program `flute` which takes the output of `melibea` in order to define N_γ, t_{eff} and A_{eff}.

Migration Matrix. The reconstructed estimated energy E_{est} of the events is not the same as their true energy E_{true}. This effect is called *spillover effect*: when the spectrum is calculated in bins of estimated energy, it is necessary to use the effective area, defined in terms of true energy, to correct it. The true energy of the MC depends on the simulated spectrum which is different from the spectrum of the source of interest. For this reason, it is necessary to re-weigh the spectrum of MC simulated gamma-ray events to match the one of the source and obtain a reliable effective area. With the *migration matrix* it is possible to compare the quantities binned in estimated energy and the ones binned in true energy. An example of a migration matrix is reported in Figure 2.36. The migration Matrix represents the fraction of events in bin of E_{true} moving into bin of E_{est} due to the finite energy resolution, and is obtained via the MC simulations.

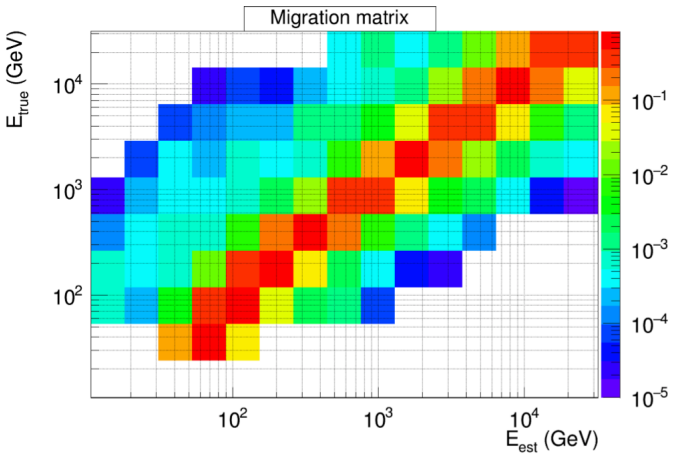

Figure 2.36 Example of a migration matrix produced with MC data.

Light Curve. The program `flute` can generate the light curve of the data sample dividing the data into time bins and, for each of these bins, estimate the integral flux above a certain threshold. The differential energy spectrum (Equa-

tion 2.12) is obtained for each time interval and then integrated over the energy range considered [E_1,E_2]:

$$\Phi = \int_{E_1}^{E_2} \frac{d\Phi}{dE} \; [cm^{-2}\, s^{-1}] \tag{2.13}$$

Upper Limits. If in any of the energy bins there are no significant excess events, `flute` will calculate an Upper Limit (UL). To compute the UL, the number of excess events N_{ex} and background events N_{off} are needed. Furthermore, a Confidence Level (C.L.) and systematic errors should be defined. Now, as described in the method of Rolke et al. (2005), it is possible to calculate the maximum number of expected gamma rays events N_{ul}.

In MAGIC, a 95% C.L. is used and a systematic uncertainty of 30% is assumed. Usually the spectral shape of the source is unknown so, a power-law function with a photon index $\Gamma = 2.6$ (Crab-like spectrum) is assumed. Once N_{ul} is computed with the Rolke method, an UL to the integral flux can be found. An assumption on the spectrum is needed:

$$\Phi(E) = K\, S(E) = K\left(\frac{E}{E_0}\right)^{\Gamma} \tag{2.14}$$

And the integral flux above the energy E_0 would be:

$$\int_{E_0}^{\infty} \Phi(E)dE = K \int_{E_0}^{\infty} S(E)dE = \frac{N_{\mathrm{ul}}}{\int_{E_0}^{\infty} \int_0^{t_{\mathrm{eff}}} A_{\mathrm{eff}}(E)dEdt} \tag{2.15}$$

where t_{eff} is the effective time of the observation. The UL on the integral flux can be obtained from the above equation:

$$\mathrm{K_{ul}} < \frac{N_{\mathrm{ul}}}{t_{\mathrm{eff}} \int_{E_0}^{\infty} S(E) A_{\mathrm{eff}}(E)dE} \;\; [\mathrm{TeV\ cm^{-2}\ s^{-1}}] \tag{2.16}$$

2.2.7.3 Unfolding Spectrum

The correction of the spillover effect done by `flute` can be considered as a first correction of the systematics due to the energy reconstruction. In particular, if other effects are considered, like those resulting from the imperfections in the detectors (limited energy resolution, detection efficiency, etc.) or systematic distortion (threshold effects), an *unfolding* procedure is applied. These affect the calculation of the spectra, where an estimated energy is measured instead of the true energy. Through the *unfolding* procedure it is possible to obtain a spectrum as function of the true energy E_{true}. Some important points about the *unfolding* technique are:

- It is computationally intensive; the numerical application to real data, involving matrix inversions and approximations, can be unsuccessful or require very long computing time.
- There are many different unfolding algorithms with many parameters each;
- Unfolding can be ambiguous. Each choice of algorithm and/or parameters can produce different spectra: none of these is technically wrong, but some are more plausible than others based on the input data.
- Unfolded data have correlated errors, which results in ambiguities: many solutions can be "correct" at the same time.
- Unfolding noisy data with a noisy response matrix from discrete simulations leads to fluctuating solutions because of the matrix inversions. This requires the application of a smoothing called *regularization*: although there are some recipes on how much to regularize, its so-called weight is basically a free parameter.

In the analysis of MAGIC data, the *unfolding* procedure consists of six different methods that differ only by the application of the minimizer (such as MINUIT or Gauss-Newton), a tool to find the minimum value of a multi-parameter function and analyses the shape of the function around the minimum. When comparing the final data points, the six methods should give compatible results. For a detailed explanation of the differences between these methods and their application to the MAGIC analysis, see Albert et al. (2007). In MAGIC, the *unfolding* procedure can be done with two tools: `CumbUnfold` and `fold`. The `CumbUnfold` macro is numerically complex because it involves matrix inversions and approximations; the solution can be ambiguous and sensitive to noise and fluctuations and this requires the regularization of the data, in order to smooth them. The `fold` software instead takes care of correcting the spectrum and is valid especially for bins with low number of events. Its results are a spectrum and a Spectral Energy Distribution (SED) with individual points. These points are obtained from the excess rates measured in bins of estimated energy, and converted into flux points using a collection area which contains a "spillover correction", calculated using `fold`'s best-fit spectrum.

2.2.7.4 Systematic Uncertainties

All instruments are affected by systematic uncertainties and many factors contribute to this. Most of them are not constant during a single night or display night-to-night variations. The nature of systematic errors in IACTs are several:

the atmosphere, the approximations used in the MC simulations, the PMT response and aging, differences between PMTs, mirrors reflectivity and inhomogeneities in the cameras. The following are some of the main systematics (for details see Aleksić et al. (2016b)):

* **Background subtraction.** The distribution of events in the camera is not homogeneous due to differences between PMT, stars in the FoV and NSB variations. To estimate these inhomogeneities in the background, the number of background events in two reflected regions in the sky (without known gamma-ray sources) were estimated. The difference between the number of estimated events is $\lesssim 1\%$ (Aleksić et al., 2016b). The estimation of the measured flux, and thus the evaluation of light curves and spectra (spectral index), are directly affected by the background estimation.

* **Pointing position systematics.** During the observations, the pointing accuracy of MAGIC is modified because the structure of the telescopes is not fixed but can be deformed by the gravitational load and the camera sagging due to its own weight. Most of this effect is corrected by the AMC and the starguider camera, but some residual mispointing can affect the accuracy of the determination of the sources position. To evaluate this effect, the Crab Nebula data, night by night, were analyzed (several samples of data taken in different conditions between October 2013 and January 2014) and the resulting systematic uncertainty on the reconstructed source position was determined to be $\lesssim 0.02^{\circ}$ (Aleksić et al., 2016b).

* **Energy Scale.** The absolute energy scale of IACTs is complicated to determine because it is affected by many systematic effects such as atmospheric transmission (which is not well known), mirror reflectivity, properties of the PMT, etc. In particular, MAGIC-I and MAGIC-II have a slightly different light scale (amount of light generated by an event at a given energy): MAGIC-II has a response larger of about 11%. This effect is considered during the production of the MC. A miscalibration in the energy/light scale of the telescopes affects the spectrum reconstruction at the lowest energies and near the threshold, this leads to a lower collection area and a lower flux estimation. A pile-up effect is expected below the energy threshold because of the fast decrease in the collection area.

* **Night to Night variations.** The flux of a steady source measured over various nights is slightly different due to night to night variations. The reason for these uncertainties are the atmospheric variations. In MAGIC, these are minimized, via the use of the LIDAR system, but some residual systematics remain and they create a

mismatch between the simulated shower development in the MC gamma rays and the actual observations. The relative systematic uncertainty is estimated to be around 11%.

2.2.8 Non Standard Data Analysis

One of the main subjects of this thesis is the analysis of pulsars. The emission of these sources is quite weak in the high and very high energy domain, and so, as discussed in Section 2.2.1.7, they are observed with the Sum-Trigger-II system, in order to try to reach the lowest energies (around 20 GeV). In this Section I will briefly introduce some peculiarities of the pulsar analysis and the dedicated cleaning required in the use of the Sum-Trigger-II data.

2.2.8.1 Pulsar Observations

Concerning the pulsars analysis and their signal detection, there is no geometrical difference between the events emitted by the pulsar and those from the surrounding nebula. Therefore, the definition of the OFF- and ON-regions is based on a time criterium: the OFF events are those emitted when the pulsar beam is not crossing the Earth and the ON events are those emitted while the pulsar beam is pointing in our direction. The ON-region is defined as the interval of pulsar phases where emission is expected and the OFF-region where no emission is expected. Then, the ratio α corresponds to the ratio between the phase widths of the ON and OFF regions.

As discussed earlier, the pulsar analysis is based on the search and the measurement of the periodic signal. The distinction between ON and OFF regions is based on the arrival time of the gamma-ray and on the direction they come from in the sky. The signal of a pulsar is periodic and so it is useful to use the pulsar phase φ to represent the pulsar light curve. Pulse phase is usually measured in terms of 2π radians, so $0 < \varphi < 1$. The phase is the fraction of a complete rotation that the pulsar has undergone at the time of arrival of the gamma ray. To perform the conversion between the Time of Arrival (ToA) and the pulsar phase, a pulsar *ephemeris* (or timing model) is needed. The ephemeris contains all the spin parameters and, in the case of binary pulsars, also the orbital parameters used in the timing model. This file includes the pulsar frequency ν and its first and second derivatives, $\dot{\nu}$ and $\ddot{\nu}$. These quantities are necessary to compute the phase φ of a photon that arrives at time t, measured from the reference system of the MAGIC telescopes (in our case). In the next Session the details of the timing analysis are briefly explained.

2.2.8.2 Timing Analysis

Barycentering of Arrival Times The time-dependent phase $\varphi(t)$ of a pulsar can be approximated by the following Taylor expansion:

$$\varphi(t_{\text{bar}}) = \varphi_0 + \nu\,(t_{\text{bar}} - t_0) + \frac{1}{2}\,\dot{\nu}\,(t_{\text{bar}} - t_0)^2 + \ldots \tag{2.17}$$

where t_{bar} is the arrival time of the gamma ray, $\varphi(t_0)$ and t_0 are arbitrary reference phases and times for each pulsar. Since the observatories or telescopes are located at a certain position on the rotating Earth surface, the local reference system is not inertial and so not appropriate to estimate the phase of a pulsar. For this reason it is necessary to transform the local time coordinate to the Solar System Barycenter (SSB), t_{SSB}. Therefore, we need to transfer the pulse ToAs measured with the observatory clock (*topocentric arrival times*) to the center of mass of the Solar System as the best approximation to an inertial frame available. Furthermore, the pulsar signal suffers different distortions (as travelling through the ISM) which cause delays of its ToAs in its path before being detected with radio telescopes on Earth. The transformation of a topocentric ToA to such *barycentric arrival times* (t_{SSB}) is given by:

$$t_{SSB} = t_{topo} - t_0 + t_{clock} - \frac{\Delta D}{f^2} + \Delta_R + \Delta_E + \Delta_S. \tag{2.18}$$

where:

⋆ t_{topo}: is the topocentric site arrival time of the pulsar signal at the respective observatory.

⋆ t_{clock}: represents the clock corrections that account for differences between the observatory clocks and terrestrial time standards.

⋆ $\frac{\Delta D}{f^2}$ is the frequency-dependent dispersion delay caused by the ISM (f is the frequency of the SSB).

⋆ Δ_R: the *Roemer delay* (is the classical time which takes the light, of the observed pulsar, to travel from the telescope, to the SSB). It is a geometric effect caused by the nature of the Solar System in which the Earth orbits around the Sun: when the Earth is closer to the pulsar than the Sun (on its rotation around the latter), the signal from the pulsar will arrive earlier at the respective observatory on Earth than at the SSB. If the Sun is closer to the pulsar than the Earth, the pulsar signal will arrive earlier at the SSB. Therefore, during the course of a year the arrival times of the pulsar signal encounter a delay which has a sinusoidal form.

⋆ Δ_E: the so-called *Einstein delay*. It describes the combined effect of gravitational redshift and time dilation due to the motion of the Earth and other bodies.

⋆ Δ_S: the *Shapiro delay*. It takes into account the effect of the mass on space and is a relativistic correction that accounts for an extra delay due to the curvature of space-time in the solar system.

For more details see Becker et al. (2018).

Preparation for Barycentering - The Observation file The barycentering of the topocentric ToA is carried out with the pulsar timing software `Tempo2` (Hobbs et al., 2006a). In this step the files containing the topocentric ToAs need to be converted into arrival time files. These files contain the arrival times of the pulsar signal detected at the respective observatory and they are, together with the parameter file (see next paragraph), the input files for the barycentering process.

Preparation for Barycentering - The Ephemeris file The *ephemeris* file is a text file that contains a set of parameters as instructions for the calculations executed with `Tempo2` and a rotation model of the respective pulsar for which the parameter file was originally built. An example of the used parameter file for the Crab pulsar is given in Figure 2.37. A complete description of all parameters which can be included into an *ephemeris* file can be found in the `Tempo2` documentation[§]. Each parameters has a label, a value and may have an uncertainty and a flag indicating whether `Tempo2` should fit for this parameter (=1) or hold constant (=0).

Glitches and Timing Noise Some young pulsars present particular rotational irregularities as cusps, for instance, which are sudden changes in the pulsar's spin rate during a glitch[¶]. The origin of these structures, visible in the residuals, is unknown and are related to the "timing noise". They are usually related to processes that happen in the interior of the neutron stars. It is very important to remove this kind of noise in order to obtain the most accurate pulsar's positional and proper motion parameters and the measure of the dispersion. To obtain the right barycentering of the pulsar data, the ephemeris must be built in the same time in which the observations took place and corrected for these rotational irregularities.

[§] `https://www.jb.man.ac.uk/~pulsar/Resources/tempo2_manual.pdf`

[¶] A glitch is a sudden increase in the rotational frequency of a rotation-powered pulsar, which usually decreases steadily due to braking provided by the emission of radiation and high-energy particles.

```
PSRJ                J0534+2200                      Pulsar Name
RAJ                 05:34:31.972                    J2000 Right Ascension
DECJ                22:00:52.07                     J2000 Declination
F0                  2.962482049529615e+01   0     1.534278507226316e-09 Rotational Frequency
F1                  -3.686154067521771e-10  0     3.383696073360809e-16 First Derivative of Rotational Frequency
F2                  1.369929140833693e-20   0     2.974183223039792e-22 Second Derivative of Rotational Frequency
TRES                30.379930922                    Rms timing residual
PEPOCH              58438                           Epoch of period determination
POSEPOCH            58438                           Epoch of position measurement
START               58423                           (MJD)
FINISH              58453                           (MJD)
TZRMJD              58438.000000102664028           Prediction mode: Time
TZRFRQ              0.0                                          Frequency
TZRSITE             COE                             Site for which template was built
EPHEM               DE200                           Solar System Ephemeris which needs to be used
EPHVER              2
CLK                 TT(TAI)                         Definition of used clock correction files
UNITS               TDB                             Time format which needs to be used by Tempo2
PLANET_SHAPIRO      Y
CORRECT_TROPOSPHERE N
T2CMETHOD           IAU200B                         Method for transforming from terrestrial to celestial frame
TIMEEPH             FB90                            Which time ephemeris to use
```

Figure 2.37 Example of ephemeris file for the Crab Pulsar.

Once the phase of each event is computed (at the level of `melibea` files), it is possible to check if the source shows any kind of periodic signal. In order to do this, the MAGIC data are reported in the phase diagrams, also called *phaseograms*, which are determined with different cut optimization techniques. This dedicated analysis is used in the case of pulsars since it is not possible to see individual pulses in the gamma-ray energy range, as in the optical or radio band. More details on the pulsar analysis are provided in Section 3.3.5.

2.2.8.3 MaTaJu Cleaning-Analysis

The MaTaJu cleaning, developed by Maxim Shayduk (**Ma**), Takayuki Saito (**Ta**) and Julian Sitarek (**Ju**), is a special low energy-focused cleaning algorithm and is a complicated code that involves slower data processing. The purpose of this special cleaning is this: the image cleaning and signal extraction are tightly bound and shall be carried on together, in order to aim for the lower energy showers. The signal extraction is the process for determining the charge and the timing of a pulse in single pixels from the PMT waveforms themselves and is done by `sorcerer` program.

As discussed in Section 2.2.5.3, the fundamental idea is that, depending on the charge and timing in a certain pixel, the signal extraction in neighboring pixels is also adjusted; different next-neighbors geometries are considered, and if a condition on charge/timing coincidence is met, the pixels are preserved, while pixels that do not pass the conditions are discarded. In this way the cleaned image is built using only pixels that survive this procedure. Only `sorcerer` can extract the signal and manipulate the waveforms (that afterwards are discarded), for this reason the MaTaJu cleaning,

that must be initialized from RAW data, requires special inputcards.

During the signal extraction and calibration the information from each pixel is reduced from 50 values (uncalibrated) of charge versus slices to just one value of the calibrated charge of the pixel and the time of the pulse. In the special case of the MaTaJu, the cleaning is performed during the signal extraction and a list of survived pixels is computed and written to the *calibrated* ROOT files. In the next step, the `star` MARS program (see Section 2.2.5.3), needs special input cards because bright stars (and so the circle of pixels around them) must be removed from the FoV. In the standard data analysis (higher energies) such bright stars do not affect the data so much because they are automatically removed by `star`, which disables pixels with high noise, and in the case of larger shower (i.e. larger charge in the image), the problem is not so significant. But this is not the case for the MaTaJu cleaning. If the star is too bright, its light passes the low threshold of the MaTaJu cleaning and can spoil completely the reconstruction of the Hillas parameters. Furthermore, both stereo reconstruction and hadronness calculation are affected. The input card has a dedicated section where it is possible to specify corresponding holes of different dimension around the position of the bright star in the FoV; the radius of the region depends on the magnitude of the star that should be removed (see Table 2.3).

Once the `*_I_*` files have been produced, the data analysis can proceed normally through the stereo reconstruction with the `superstar` program. It is very important that the MC files used both for training the RF and for the effective area computation are all reduced with the MaTaJu cleaning. Another important point is that, in the subsequent steps of the analysis the average macro-cell threshold is set to a value roughly corresponding to 20 equivalent photo-electrons (compared to 50 phe for the standard analysis). This is crucial for the Sum-Trigger-II analysis, especially for soft sources like pulsars, in order to not discard low-energy events.

The analysis of Sum-Trigger-II data is very time-consuming (takes a long time to be run and computationally intensive) and requires a large memory allocation because the RAW data are very large.

Magnitude	Radius
$m > 6$	star not so bright, can be ignored
$5 < m < 6$	30 mm
$4 < m < 5$	60 mm
$3 < m < 4$	90 mm
$m < 3$	particular and complex case

Table 2.3 Magnitude of the Star vs Radius in the Field of View

2.3 CTA: Cherenkov Telescope Array

The next generation IACTs will be the CTA[‖]. It will be an open observatory with two main sites: one on the island of La Palma (see Figure 2.38), to observe the Northern sky, and one in Chile (see Figure 2.39), to observe the Southern one. The full array will consist of more than 100 IACTs of different sizes in order to allow a full-sky coverage in gamma rays from 20 GeV to more than 300 TeV. The sensitivity of CTA will be up to an order of magnitude better than existing instruments such as H.E.S.S., MAGIC, and VERITAS (see Figure 2.40). The construction of CTA is being carried out by a consortium of scientists and institutes from all over the world.

Figure 2.38 Artistic impression of the CTA Northern hemisphere site; image taken from https://www.cta-observatory.org.

2.3.1 Location

The CTA Observatory (CTAO) consists of two different arrays, located one in each hemisphere, along with two administrative locations. The CTAO Headquarter is located in Bologna (Italy) and the Science Data Management Center (SDMC) is located in Berlin-Zeuthen (Germany). The CTA Consortium (CTAC) is a collaboration consisting of more than 1400 scientists and engineers from 32 countries around the world.

As anticipated, the Northern array site will be in La Palma at the Observatory of the Roque de Los Muchachos (Canary Islands), at the same site as the MAGIC telescopes. The Southern array will be constructed in Chile in the Atacama desert, near the European Southern Observatory (ESO) Paranal site. Figure 2.41 shows an illustration of the South and North array layouts.

[‖] https://www.cta-observatory.org

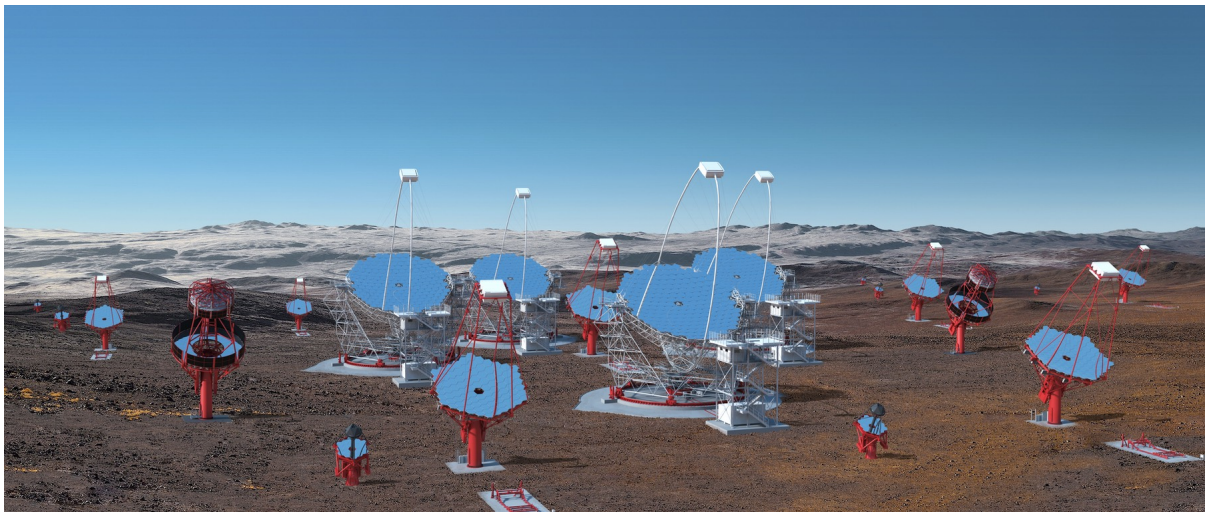

Figure 2.39 Artistic impression of the CTA Southern hemisphere site; image taken from https://www.cta-observatory.org.

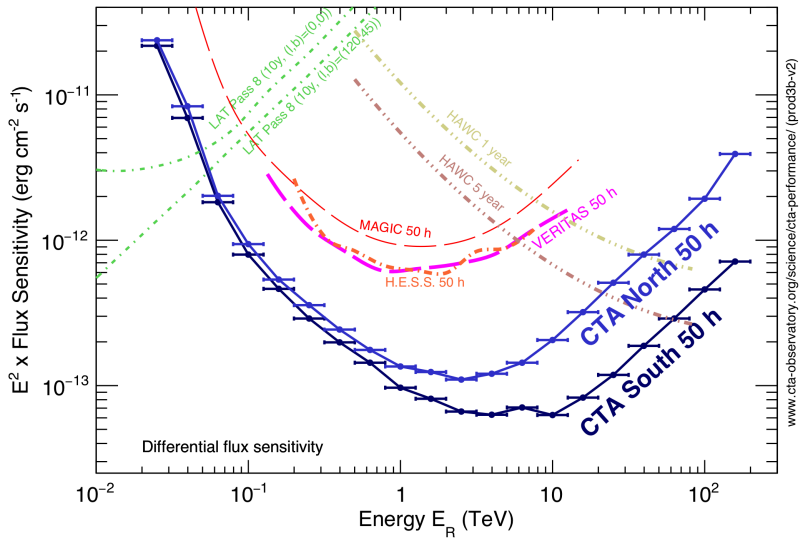

Figure 2.40 The differential sensitivity of CTA (both Northern and Southern arrays) with respect to other current gamma-ray observatories. The sensitivity is defined as the minimum flux needed by CTA to obtain a 5-standard-deviation detection of a point-like source, calculated in non-overlapping logarithmic energy bins (five per decade). Figure taken from https://www.cta-observatory.org/science/cta-performance/.

2.3.2 Telescopes and Technology

The two arrays will consist of a different number of telescopes. In order to cover the 20 GeV - 300 TeV energy range, telescopes with different dish sizes are needed. The larger telescopes are more sensitive at low energies, instead the

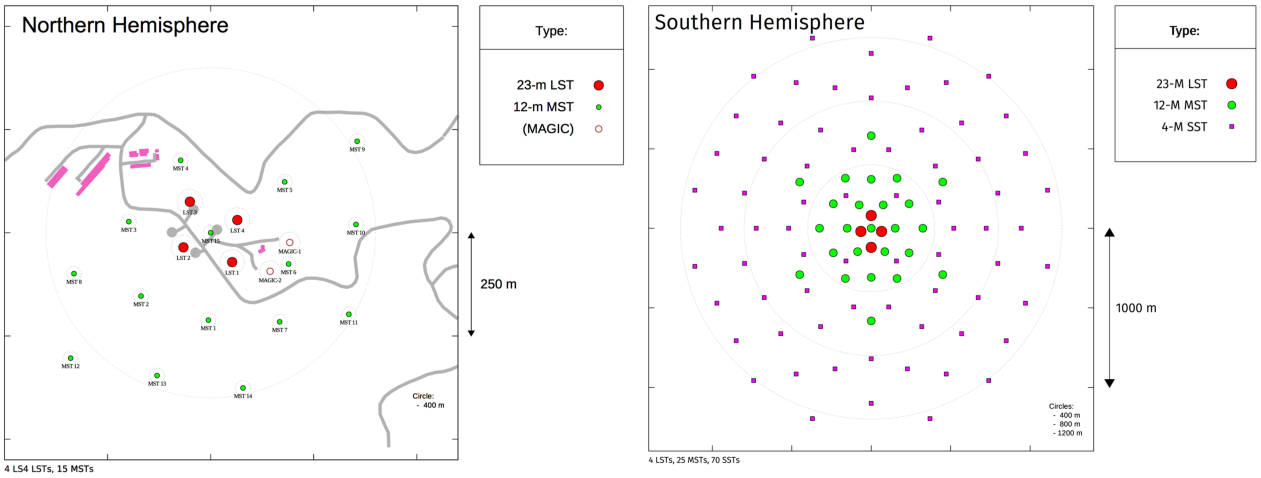

Figure 2.41 Possible layouts for the baseline arrays for CTA North (left) and CTA South (right). Illustration taken from https://www.cta-observatory.org/project/technology/.

smaller ones, that cover a big area of about a square kilometer, provide the sensitivity at high energies. The telescopes that will be constructed are (Acharya et al., 2013):

- ◇ **Large-Size Telescope LST**. The LSTs (4 for each hemisphere) will have a 23 m diameter parabolic reflector held by a carbon-fiber structure and a PMT camera with a 4.3° FoV. The LST prototype design is illustrated in Figure 2.43-left. Their light-structure, despite its 45 m height and a weight of around 100 tonnes, allows the telescope to re-pointing within 20 s. This fast re-point will give the possibility to detect Galactic transients, GRB, high redshift AGN and low-energy dominated sources. Indeed, these telescopes are designed to achieve the lowest energies, down to 20 GeV. The best sensitivity of the LSTs will be in the energy range between 10-20 GeV and 150 GeV (Mazin et al., 2017). The first LST (LST-1), see Figure 2.42 -left, was inaugurated in La Palma (Canary Island) in October 2018 and recorded its first Cherenkov light during the night between 14-15 December 2018 (see Figure 2.42 - right). Between January and February 2020, LST-1 detected for the first time the Crab Pulsar and this milestone domonstrated how LST-1 is already performing at an extraordinary level, detecting a challenging source in record time (11.4 hours of data).

- → **Medium Size Telescope (MST)**. The MSTs (25 at CTA-South and 15 at CTA-North) have a dish of 12 m in diameter and a Davies-Cotton design (Davies & Cotton, 1957). The PMT camera has a FoV of 7.5°. The best sensitivity of MSTs is achieved in the energy range 100 GeV - 10 TeV, therefore they are designed to cover

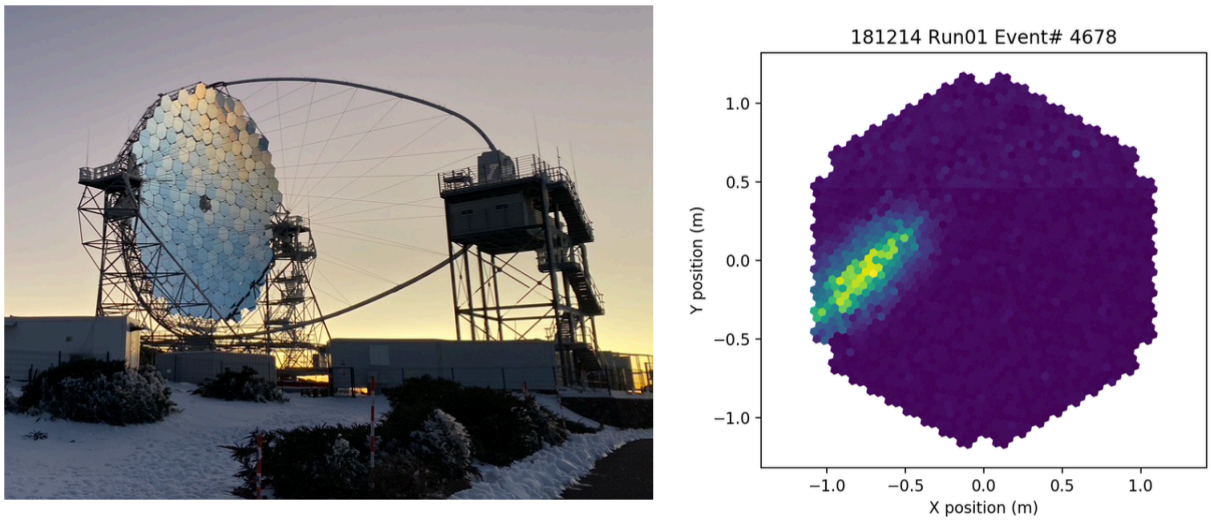

Figure 2.42 **Left:** Picture of LST-1 taken during my shift in January 2021. **Right:** One of the first-light events registered by the LST-1 prototype. From https://www.cta-observatory.org/lst-prototype-records-its-first-light/.

mid-energies. A representation of the MST in Figure 2.43-middle. At present, a MST prototype is installed in Berlin for testing purposes.

→ **Small Size Telescope (SST).** Three prototypes are proposed for the SSTs. All of them have a primary dish of 4 m and a Silicon PhotoMultiplier (SiPM) camera with a FoV close to 10°. Two configuration have a dual-mirror Schwarzschild-Couder optical design (SST-2M ASTRI and SST-2M GCT), and one configuration has a single mirror (SST-1M). About 70 SSTs will be installed at CTA-South, to study mostly Galactic sources, and they will be sensitive in the energy range between 5 and 300 TeV. These telescopes will also cover a very wide area on the ground (about 4 km^2) to detect all the VHE CRs that enter the atmosphere. In June 2019 the CTA Council decided that the SST design should be based on the ASTRI design, illustrated in Figure 2.43-right.

2.3.3 CTA Science

The main scientific goals for CTA are:

- To study the origin and the role of CRs.
- To investigate the extreme particle acceleration inside pulsars,PWNe, jets, SNRs, etc.

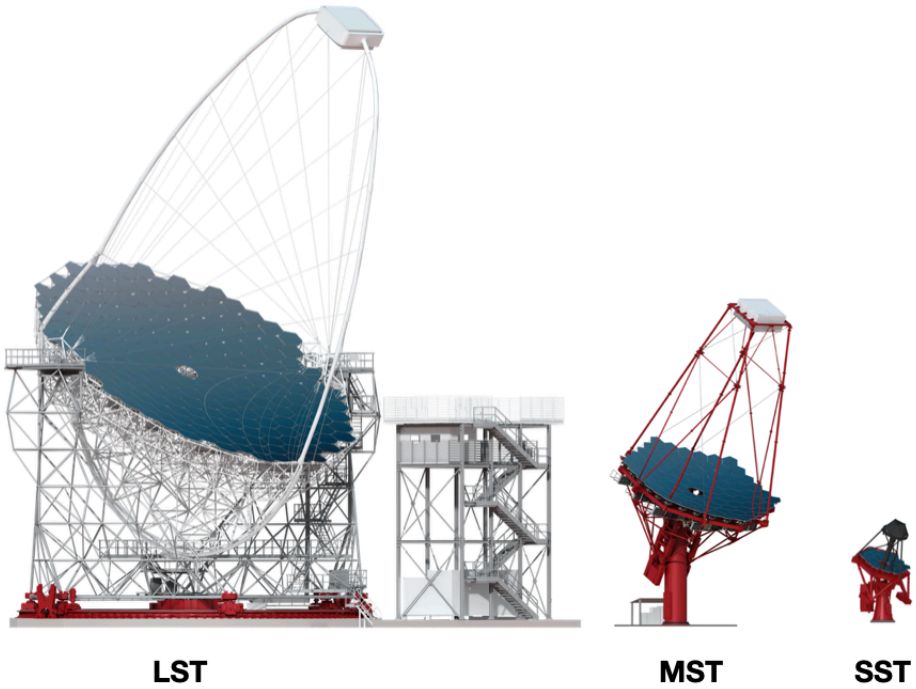

Figure 2.43 From Left: the LST prototype design, the MST and the SST prototype design. Image adapted from https://www.cta-observatory.org/project/technology/.

- To study the nature of dark matter and probe the Physics beyond the Standard Model.

To do this, the CTAC has defined a series of core programs that will have a high scientific impact that can be accomplished only with a considerable amount of observing time. These programs are referred to as Key Science Projects (KSPs) and they are: the Dark Matter Program, Galactic Center Survey, Galactic Plane Survey, Large Magellanic Cloud Survey, Extragalactic Survey, Transients observation, Cosmic- ray PeVatrons, Star-Forming Systems, Active Galactic Nuclei, and Clusters of Galaxies. For specific information on the science planned with CTA, the reader can refer to CTA Consortium (2019).

Part II

Science

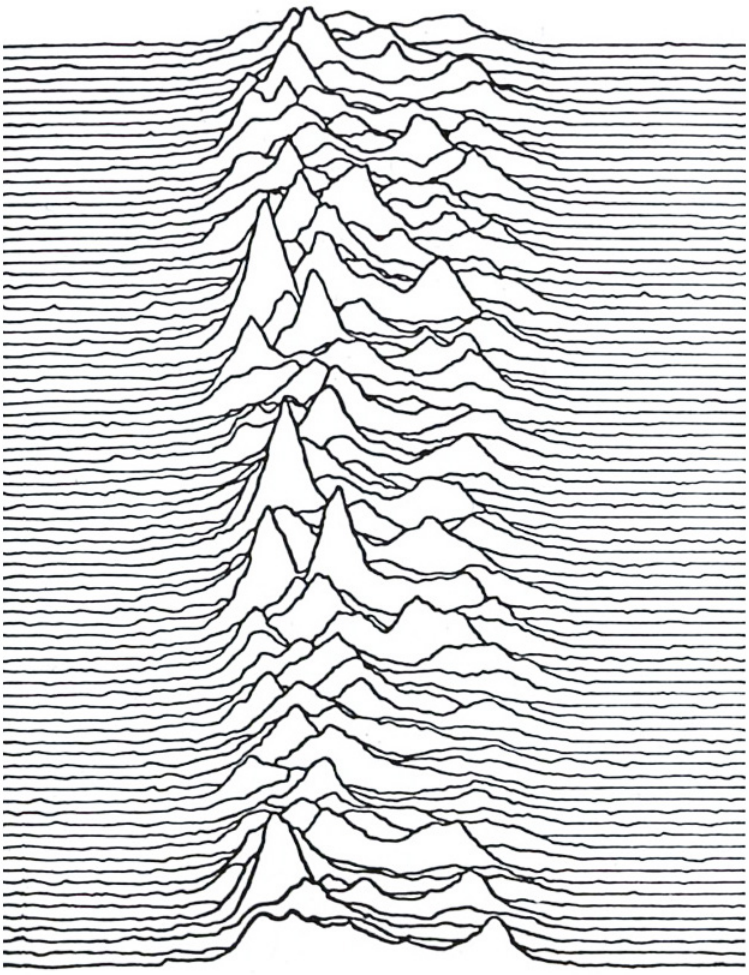

Figure 2.44 Successive pulses from the first pulsar discovered, CP 1919, superimposed vertically. The Graphic designer Peter Saville used this image in his iconic cover for Joy Division's 1979 debut studio album Unknown Pleasures.

3

Introduction to Pulsars

In this chapter I will provide a general theoretical background for a proper study of the population of millisecond pulsars. A general view of the neutron star properties and on the pulsar phenomenology, focusing on the physical processes that characterize their peculiar signals will be given. Then, I will show what is and how forms a millisecond pulsar, presenting the number of different evolutionary scenarios that create the exotic zoo of these objects. A short description of the particular class of the transitional millisecond pulsars will be also given.

I will also give a more detailed description of the VHE gamma-ray emission of pulsars and the modeling of this emission. I've included in the chapter the Crab Pulsar and Nebula MAGIC analysis, giving a short explanation of the physical processes that produce the observed HE and VHE emission, according to the current models.

3.1 Neutron Stars

3.1.1 Star Fate

NSs are rapidly spinning and magnetized compact stars composed mainly of neutrons. They are the leftovers from the gravitational collapse of massive stars ($M > 11 M_\odot$) which eject their envelopes through SN explosions. NSs were postulated for the first time by Baade & Zwicky (1934) who pointed out that a massive object made mainly of neutrons at very high density would be much more gravitationally bound than ordinary stars.

The primary source of energy of a star is given by thermonuclear fusion reactions, which can sustain the stellar structure until the exhaustion of the thermonuclear fuel (i.e. Hydrogen (H), Helium (He) and heavier elements till, at most, the iron group elements like Iron (Fe) and Nichel (Ni)). Once this fuel is finished, the only source of energy left is the gravitational one. The objects that are formed at the end of the life of the stars depend on their initial mass:

- $M < 11 M_\odot$[*]: stars end their life as White Dwarfs (WDs). A WD is a compact ($R \sim R_\oplus$) and hot ($T \sim 10^{4-5}$K) star sustained by the pressure of degenerate electrons and mainly composed by Carbon (C) and Oxygen (O) or of O, Neon (Ne) and Magnesium (Mg).

- $11 M_\odot < M < 25 M_\odot$: stars become NSs: extremely compact objects ($R \sim 10$km) sustained by the pressure of degenerate neutrons. I will extend their description in this Chapter.

- $25 M_\odot < M < 40 M_\odot$: if the mass of what remains is high enough to overcome the neutron degeneration pressure with its gravitational force, a BH is generated, after the SN explosion.

- $40 M_\odot < M < 140 M_\odot$ or $M > 260 M_\odot$: there is no visible SN explosion, but a BH is directly formed without a significant creation of heavy elements.

- $140 M_\odot < M < 260 M_\odot$: nuclear reactions inside the star generate gamma rays which produce pairs of $e^\pm$ and this pair-instability is so violent that the star is completely disrupted without leaving remnant.

3.1.2 Generalities of Neutron Stars

The formation of a NS is preceded by the violent emission of most of the star gravitational energy through an explosion known as "core-collapse SN". During this process, the outermost layers of the star are blown away, and only a

[*] $1 M_\odot = 1.9 \times 10^{33}$g

small inner core is left, formed from the collapse of the previous star nucleus, mainly composed of iron group elements and degenerate electrons. This nucleus undergoes the *free fall collapse* because its mass is expected to exceed the *Chandrasekhar limit*[†] M_{ch} of $1.44 M_\odot$ and what remains is a remnant of neutrons. During this phase, the density in the core is large enough to favor the neutronization of matter through β-decay reactions:

$$p + e^- \rightarrow n + \nu_e \tag{3.1}$$

this electron's capture by protons produces an enormous amount of neutrons, of the order of 10^{57}.

NSs are extremely compact objects. The minimum radius is about 1.5 times the *Schwarzschild Radius* (R_S)[‡]:

$$R_{\min} \simeq 1.5 R_S = \frac{3GM}{c^2} = 6.2 \text{ km} \left(\frac{M}{1.4 M_\odot} \right) \tag{3.2}$$

where M is the mass of the NS, G the gravitational constant and c the speed of light.

The maximum radius can be obtained assuming that the rotating star is stable against centrifugal forces:

$$R_{\max} \simeq \left(\frac{GMP^2}{4\pi^2} \right)^{1/3} = 16.8 \text{ km} \left(\frac{M}{1.4 M_\odot} \right)^{1/3} \left(\frac{P}{\text{ms}} \right)^{2/3} \tag{3.3}$$

where P is the rotational period of the NS.

Considering that the NS is born from the collapse of a WD-like structure with a radius similar to that of the Earth, it follows that its final radius can be up to about 500 times smaller than that of the progenitor. Indeed, most models predict that NSs have a radius of 12–20 km (Lattimer & Prakash, 2001).

We said that NSs are rapidly rotating stars: assuming that during the gravitational collapse there is no loss of mass and/or of angular momentum in the stellar core and that the NS is a sphere of uniform density, applying the conservation of the angular momentum law before and after the collapse, we have:

$$I_i \Omega_i = I_f \Omega_f \Rightarrow \Omega_f = \Omega_i \frac{R_i^2}{R_f^2} \tag{3.4}$$

[†]This is the mass limit below which a system supported by the pressure of degenerate electrons (such as a glsWD) is stable. Above this mass, electron degeneracy pressure is not enough to prevent gravity from collapsing the star further into a NS or BH.

[‡]It is also called *gravitational radius* and is the radius below which the gravitational attraction between the particles of a body must cause it to undergo irreversible gravitational collapse. It is defined as $R_S = \frac{2GM}{c^2}$ where M is the mass of the object, G the universal gravitational constant and c the speed of light.

where $I = \frac{2}{5}MR^2$ and $\Omega = 2\pi/P$ are the momentum and the angular velocity of the NS, respectively. In particular, defining a R_i=500R_f, the final period is P_f=$10^{-6}P_i$; and if we consider a P_i=10^3s, the final period will be P_f=10^{-3}s. At the beginning of their life NSs are extremely hot: the temperature can reach a value of about 10^{11}K. Then, thanks to efficient cooling mechanisms, their temperature, in a time-scale of 10^5 years, can go down to a value of 10^6K (Potekhin et al., 2015).

Another possible mechanism for the formation of a NS is the so-called "Accretion-Induced Collapse": if a massive WD in a binary system is accreting material from a standard star, its mass can exceed the Chandrasekhar limit. Then, a gravitational collapse will follow and can create a NS. More details about this process can be found in Freire & Tauris (2014).

3.1.3 Internal Structure of a Neutron Star

The structure of the NS can contrast the gravitational collapse thanks to the pressure of the degenerated neutrons. This structure is described by an equation of state that provides a link between the density and the pressure of the star at different stellar radii (Lattimer, 2004). The description of this equation is beyond the goals of this thesis, but in most of these equations the majority of the NSs have a mass of the order of 1-2 $M_\odot$ and a radius between 10 and 12 km (Lyne & Graham-Smith, 2012). Such values of masses and radii determine an average density for NSs of the order of about 10^{14} g/cm^3. However, the expected densities in NSs have a rather wide range, and the internal structure of these objects can be described by an "onion"-like structure. The precise composition of a NS is currently not known due to its unknown equation of state. Current theoretical approaches for a NS with a mass of 1.44$M_\odot$ suggest that its interior is composed of several layers and a sketch of this inner structure can be seen in Figure 3.1. It is possible to distinguish different regions:

- the *atmosphere* is the outermost external layer made of plasma where the observed thermal spectrum of NS is formed. The thickness varies from some centimeters (in the hot NSs) to a few millimeters (in the cold NSs). The atmosphere is thought to be composed of H, He or C.
- the *outer crust* is extended from the atmosphere up to few hundred meters below. It is a solid region with heavy nuclei that form a Coulomb lattice in β-equilibrium (i.e. in equilibrium with respect to weak interaction processes) with the extremely degenerate electron gas which becomes ultra-relativistic at densities $\rho > 10^6$ g/cm^3

(Burke & Graham-Smith, 2014). Moving toward the interior of the NS, the density increases and produces the electron capture process on nuclei; in this way the star becomes predominantly made of neutrons. When the density reaches a value of $\rho_{drip} \simeq 4 \times 10^{11}$ g/cm^3, neutrons start to "drip out" of the nuclei. The beginning of the neutron drip defines the border between the *outer* and the *inner crust*.

- ◇ the *inner crust* is thick one kilometer and has a density between ρ_{drip} and 1.4×10^{14} g/cm^3. In this region there is a mixture of very neutron-rich nuclei arranged in a Coulomb lattice, electrons and free neutrons that can form a superfluid. The existence of a superfluid region inside of a NS has been indicated by observations of anomalies in the rotation of NSs known as *Glitches* (see Section 2.2.8.2). Furthermore, Pons et al. (2013) have shown that this layer is highly resistive and this naturally limits the spin period of an isolated pulsar to a maximum value of 10-20 seconds; this suggested that the *inner crust* can be an amorphous layer.

- ◇ the *outer core*. It "starts" at densities about 10^{14} g/cm^3, where the nuclear clusters break up into their constituents (neutrons and protons). The creation of muons is also energetically favored. This layer, several kilometers thick, is made of a quantum fluid with densities between 1.4×10^{14} g/cm^3 and 5.6×10^{14} g/cm^3. For low-mass NSs, the *outer core* is the entire core of the object.

- ◇ the *inner core*: in this region, thick several kilometers, the density overcomes the nuclear one. The composition of the *inner core* is not well known; there are different hypotheses (defined as *exotic* matter): hyperonic matter, pion and kaon condensates, or deconfined quark matter.

3.1.4 Neutron Star Zoo

Since the discovery of the first NS, a large variety of different types of NSs have been discovered. A general and complete review can be found in Harding (2013). NSs have detectable pulsations at different wavelengths, since they are rapidly spinning and their emission patterns are highly anisotropic. They are classified according to the primary power source for their emission and the spin evolution:

- ***Rotation-Powered Pulsars (RPPs)***: are NSs with a high rotation frequency gained during the core-collapse of the progenitor which is spinning down due to its loss of angular momentum, caused by the emission of magnetic dipole radiation and particle emission. The rotation is the only source of power for this kind of NS. The group of RPPs consists of ordinary and millisecond pulsars. The difference between both kinds of pulsars is their evolution history and

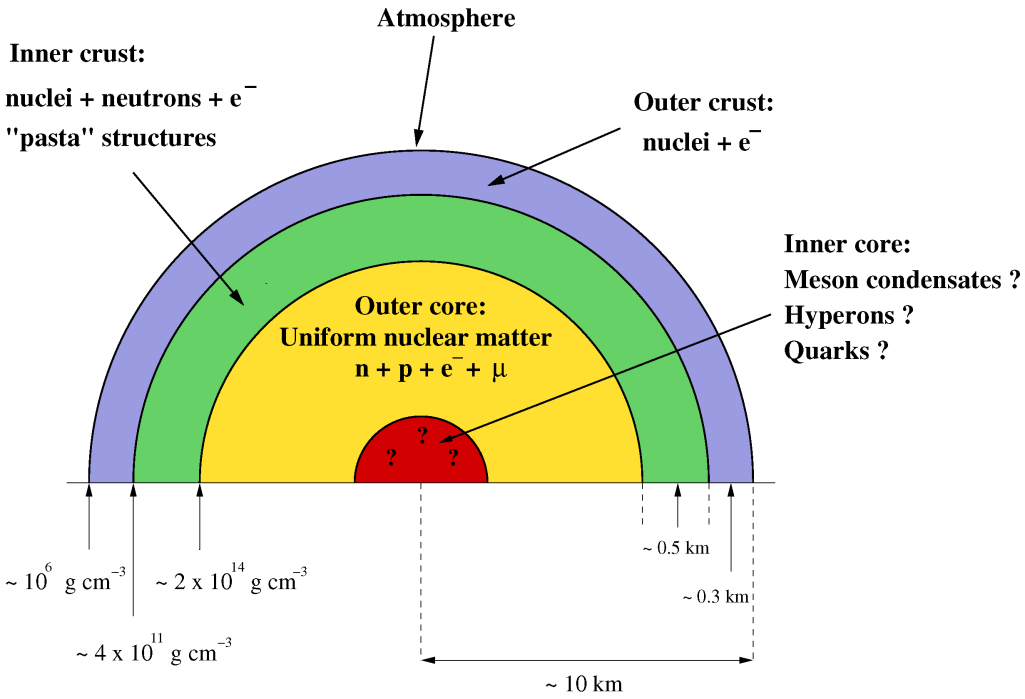

Figure 3.1 Internal structure of an NS. Image from Vidaña (2018).

their resulting characteristics. In next Sections I will describe both of them.

- ***Magnetars***: they are solitary NSs with the highest magnetic fields known: 10^{14-16} G. For this reason the magnetic field is assumed to be the source of energy of this object.

- ***Compact Central Objects (CCOs)***: visible only as soft X-ray sources inside young SNRs and are quiet at all other wavelengths. They have very low magnetic fields in the range $10^{10} - 10^{11}$ G; their observed spectra are purely thermal.

- ***Isolated Neutron Stars (INSs)***: they are thermally cooling with no emission outside the soft X-ray band, except for faint optical/UV counterparts. They have no observable associated SNR or nebula.

- ***Accretion-Powered Neutron Star (APNS)***: are NSs in a binary system which emit pulses at X-ray wavelengths. These pulses are generated through the accretion of matter from their companion, or donor star. When the latter exceeds its *Roche lobe*[§] an accretion disk forms out. The matter falls on the magnetic poles of the NS and creates hot spots on its surface. Based on the composition of the binary system (i.e. the mass of the companion, the properties of the accretion and the NS magnetic field strength), different subclasses of binary pulsars have been found:

⋆ LMXBs: a binary system consisting of a compact source (like a NS or a BH) and a donor star (which could be a

[§]The region around the donor star in which the once gravitationally bound matter starts to be transferred on the compact source through an accretion disk.

low-mass main sequence star, a white dwarf, or a red giant).

⋆ Intermediate Mass X-ray Binaries (IMXBs): it is a system which consists of a compact source and a donor with a mass ranging between $1M_\odot$ and $5M_\odot$.

⋆ HMXB: it is a system which consists of a compact object and a high mass star ($M > 5M_\odot$) of type O, B, or Be. In this system, the compact object accretes material from the wind of the companion star or from a Be star disk.

⋆ tMSPs: they are a particular class of sources that I will explain in Section 3.5. These systems swing between a pure accretion powered state and a rotational powered state, where it behaves like an eclipsing radio MSP.

Figure 3.2 gives a summary of the different classes by plotting rough contours in the period and surface magnetic field space.

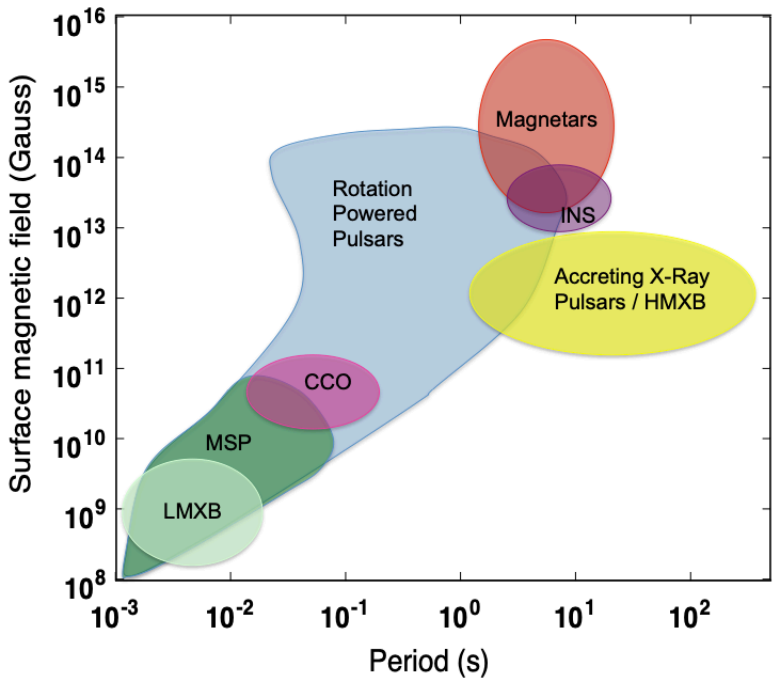

Figure 3.2 Schematic plot of NSs populations with respect to their periods and derived surface magnetic field strengths. Image taken from Harding (2013).

3.2 Pulsars

Pulsars (from *pulsating stars*) are rapidly rotating NSs that emit periodic radiation by spinning their strong magnetic field through space. As already explained, they are formed during the SN explosions of massive stars. One of their

most remarkable characteristic is the regular occurrence of their pulses, with a precision of atomic clocks. Pulsars were discovered serendipitously in 1967 by Jocelyn Bell, a research student in a Cambridge team of astronomers lead by Anthony Hewish, with the detection of the radio pulsar PSR B1919+21 at 81.5 MHz (Lyne & Graham-Smith, 1990). Even though they have been under study for several decades, their emission mechanisms are not yet fully understood. Pulsars can emit radiation over the whole electromagnetic spectrum, from radio up to VHE gamma rays.

In this Section a short outline of the basic properties of pulsars is given.

3.2.1 The Lighthouse model

When the NS spins, charged particles are accelerated along magnetic field lines forming a beam. The accelerating particles emit electromagnetic radiation, most at radio frequencies, as a sequence of observed pulses. Each pulse is produced as the magnetic axis (the radiation beam) crosses the observer's line of sight each rotation. The repetition period of the pulses is therefore the rotation period of the NS. A representation of the *lighthouse effect* in shown in Figure 3.3. This rotating NS model predicts a gradual slowdown and an increase in the pulse period as the outgoing radiation carries away rotational kinetic energy (Pacini, 1968; Gold, 1968).

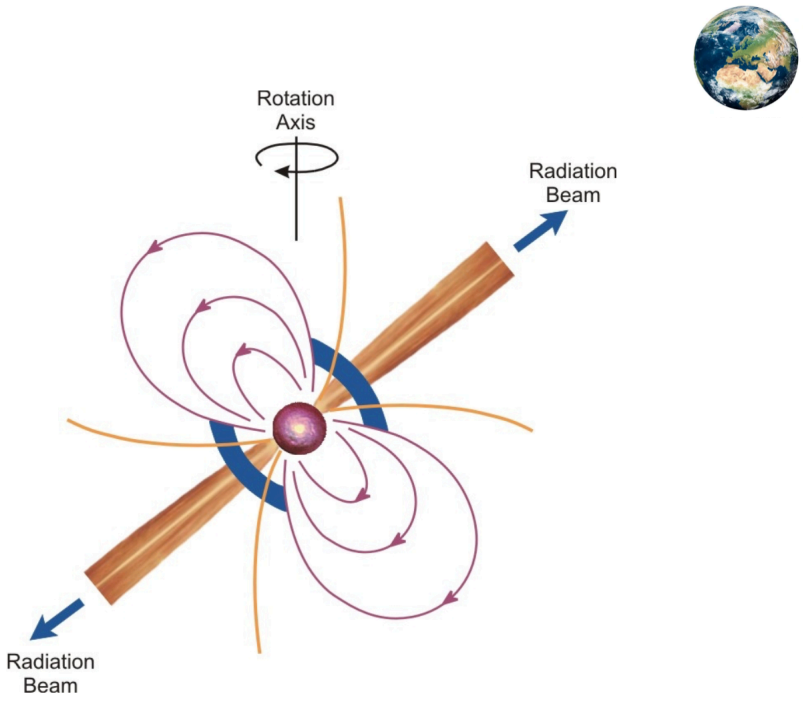

Figure 3.3 Illustration of the "lighthouse" effect.

3.2.2 The P -$\dot{P}$ Diagram

Pulsars are usually described with their rotational periods P and its first derivative $\dot{P}$, the so-called spin-down (in the process of emission, the rotational kinetic energy decreases over time and, as a consequence, the pulsar slows down over time). Therefore, the diagram called P - $\dot{P}$ (Figure 3.4) is used to categorized the pulsar population with the observed rotational period in the abscissa and the respective derivative in the ordinate (the values are expressed on logarithmic scale).

The radio pulsars occupy the largest region of this phase space with their population extending from the very short period and low $\dot{P}$ for the MSPs, up to the high P and $\dot{P}$, with high magnetic field pulsars that reach the magnetar range. The magnetars have the highest $\dot{P}$ and some of the longest periods in the NS zoo (some of them have a period of about 11 seconds). The INSs, with periods similar to those of magnetars, have a $\dot{P}$ and magnetic fields about a factor of ten lower than those of the magnetars. The group of CCOs have very low $\dot{P}$, like that of MSPs, but their spin periods are more like those of young Rotating Radio Transients (RRATs). About the HE pulsars, they have the highest spin-down power but are not the youngest; many of the very old MSPs are efficient X-ray and gamma-ray pulsars. The MSPs' group forms a cluster towards the bottom left corner of the plot: they have, compared to the normal pulsars, smaller periods ($1 \lesssim P \lesssim 30$ms) as lower spin-down rates ($10^{-21} \lesssim \dot{P} \lesssim 10^{-18}$ s s^{-1}). They have surface magnetic field strengths between 10^8 and 10^{10} G. This class of objects will be described in Section 3.4.

Apart from the separation of different populations, simple dipole models of pulsar magnetosphere allow us to obtain an estimate for various pulsar parameters like the surface magnetic field strength, the characteristic age and the spin-down luminosity.

According to the most possible evolutionary scenarios (Lorimer & Kramer, 2004), pulsar are born with small spin periods (around tens of milliseconds) and large spin-down rates ($\lesssim 10^{-15}$), thus they are located in the upper left area of the P-$\dot{P}$ diagram. While they slow down and lose rotational kinetic energy, they move towards the bulk population with a period around 0.5 s. This evolution is accompanied by a decrease of the magnetic field strength and a decrease of the spin-down rate. This process of slow down of their rotation keeps moving the pulsar toward the rightest regions of the diagram where they can cross the so-called "death line" and enter in the "pulsar graveyard". This is a region where the combination of spin periods and spin-down rates is not suitable to provide an efficient emission mechanism and for this reason the NS is not able to emit as a pulsar anymore. The majority of the pulsars population is located close to the death line because the evolutionary time scales from the birth region to this region of the diagram is quite fast;

the typical timescale is about 10^{5-6} years. Indeed, young pulsars have short spin periods and strong magnetic fields that allow an efficient energy emission, and thus a rapid slowdown. When they reach spin periods larger than about 0.5 s the evolution in the diagram is slowed down. After 10^7 years, the emission becomes too weak to be detectable and the pulsar moves towards and beyond the death line. However, if the dead NS is located in a binary system, accretion phenomena can transfer mass and angular momentum from the companion to the NS. This spins-up the NS until periods of the order of milliseconds and the emission mechanism can be reactivated making the NS visible again in the radio band as a MSP. This is the reason why MSPs are observed in the lower left region of the diagram.

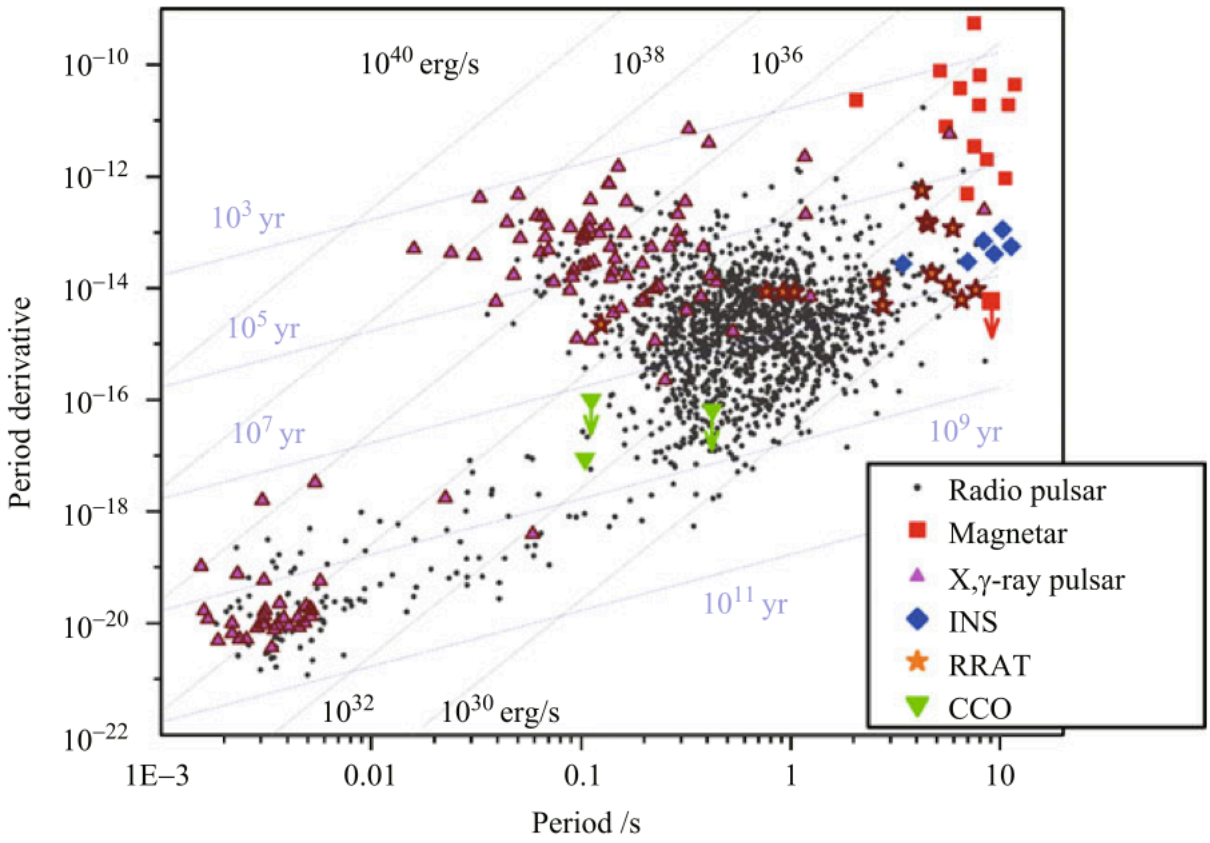

Figure 3.4 Plot of P versus $\dot{P}$ for the currently known rotation-powered pulsars, INS, CCO, RRATs and magnetars. Lines of constant characteristic age ($P/2\dot{P}$) and dipole spin-down luminosity ($\dot{E}_d$) are drawn. Plot from Harding (2013).

3.2.3 Pulsar Magnetosphere

The NS surface and atmosphere are composed of charged particles which are subject to Lorentz forces much stronger than the gravitational ones. In a rotating and magnetized system, such as a NS, this leads to the formation of a strong electric field able to extract plasma from the surface following the magnetic field lines and creating the "pulsar magnetosphere". Shortly after the discovery of the first pulsar, Goldreich & Julian (1969) presented the model for the magnetosphere. This model assumes that the spin and magnetic axes of the pulsar are aligned (i.e. aligned rotator) and shows that in any point of the sphere, the magnetic field induces an electric field $\mathbf{E} = (\Omega \times \mathbf{r}) \times \mathbf{B}$, with Ω the angular velocity. In a perfectly conductive sphere this will be balanced by a distribution of charges that create an electric field able to give, at any point $\mathbf{r}$, a *force-free* state. This can be expressed as:

$$\mathbf{E} + \frac{1}{c}(\mathbf{\Omega} \times \mathbf{r}) \times \mathbf{B} = 0 \tag{3.5}$$

Assuming that there is vacuum outside the sphere, the surface charges induce a quadrupole moment that corresponds to a surface electric field that induces an electric force on charged particles that is stronger than the gravitational pull. As a consequence, these particles are easily extracted from the surface and create a dense plasma. This plasma acts as a perfect conductor under the condition that the NS provides a free supply of charged particles. The charge distribution around the NS is arranged in such a way that the longitudinal electric field $E_{\parallel}$ is preserved and thus the force-free state ($\mathbf{E} \cdot \mathbf{B} = 0$) is maintained also outside the star. This plasma is subjected to the same electromagnetic field as the NS interior and thus the charged particles are forced to rigidly co-rotate with the star. Co-rotation can occur up to a distance where the plasma is rotating at a speed equal to the speed of light. This co-rotation limit defines a radius known as *light cylinder radius* R_{LC} and is given by:

$$R_{LC} = \frac{c}{\Omega} = \frac{cP}{2\pi} \simeq 4.77 \times 10^4 \mathrm{km} \left(\frac{P}{\mathrm{s}}\right) \tag{3.6}$$

The R_{LC} divides the pulsar magnetosphere into two distinct regions, as shown in Figure 3.5: the region inside the Light Cylinder (LC) is where the magnetic field lines are closed and the external region is where the magnetic field lines are open. The particles attached to the open lines escape the LC region. In areas of the pulsar magnetosphere in which the magnetic and electric field compensate each other, no acceleration of the charged particles can take place. However, there are several regions in which an acceleration process is possible; they will be explained in Section 3.2.5.

Where there are the open magnetic field lines, current outflows from the pulsar surface into the interstellar take space.

The sign of these outflows depends on the electric potential of the interstellar medium and a critical field line is defined where the potentials match each other (see Figure 3.6). The current outflows are called *pulsar wind* and energize the surrounding environment and can lead to the formation of a pulsar wind nebula. The pulsar wind also carries energy and angular momentum away from the pulsar, providing a slow down of the NS rotation.

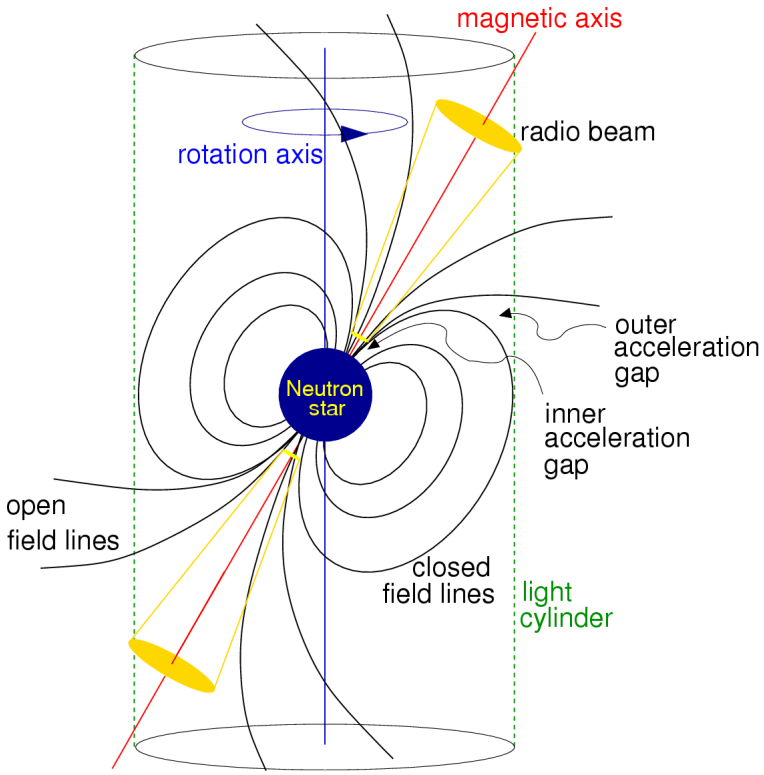

Figure 3.5 Schematic representation of a rotating NS and its surrounding magnetosphere.

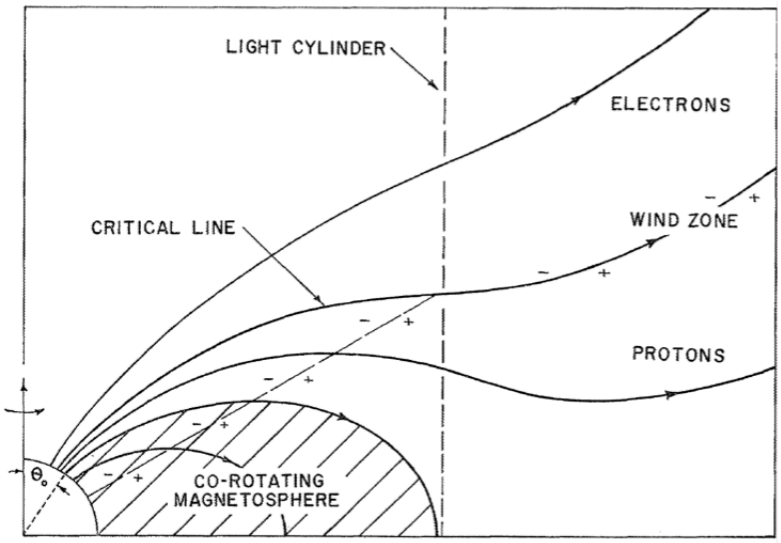

Figure 3.6 Sketch of the model for the pulsar electrodynamics by Goldreich & Julian (1969).

3.2.4 Derivation of the Pulsar Physical Parameters

The emission of a pulsar occurs at the expense of the kinetic rotational energy. This is the reason why pulsar periods increase with time. The spin-down rate is related to the rotational kinetic energy as follows (Lorimer & Kramer, 2004):

$$\dot{\mathrm{E}} = -\frac{dE_{rot}}{dt} = -\frac{d(I\Omega^2/2)}{dt} = -I\Omega\dot{\Omega} = 4\pi^2 I\frac{\dot{P}}{P^3} \tag{3.7}$$

where $\dot{E}$ is the spin-down luminosity and represents the kinetic energy output emitted by the NS. Only a tiny part of this energy loss is converted in electromagnetic emission, while most of it is converted to bulk energy of particles of the *pulsar wind*. Assuming a typical moment of inertia I= 10^{38} km m^2, we find that $\dot{E}$ of known pulsars ranges between 10^{28} and 10^{39} erg/s.

The general pulsar's spin-down relation, in terms of the energy loses, is:

$$\dot{\Omega} = -k\Omega^n \tag{3.8}$$

where k is a positive constant that depends on the moment of inertia and the magnetic dipole moment of the NS and n is the so-called *breaking index*. It can be determined using the second derivative of the angular frequency:

$$n = \frac{\Omega\ddot{\Omega}}{\dot{\Omega}^2} \tag{3.9}$$

For a pure magnetic dipole radiation, the index is $n = 3$. However, other dissipation mechanisms may exist (e.g. the *pulsar wind*) that can carry out part of the rotational kinetic energy; in this case the measured values of n vary from 1.4 to 2.9.

If we rewrite equation 3.8 in terms of the spin period derivative, a first order differential equation is obtained and integrating it, the age of the pulsar is:

$$t_{age} = \int_{P_0}^{P} \frac{1}{KP'^{2-n}} dP' = \frac{P}{(n-1)\dot{P}}\left[1 - \left(\frac{P_0}{P}\right)^{n-1}\right] \tag{3.10}$$

where P_0 is the initial period of the pulsar. Assuming $P_0 \ll P$ and $n = 3$, this formula can be simplified and we obtain the *characteristic age* of a pulsar:

$$\tau_c = \frac{P}{2\dot{P}} \tag{3.11}$$

This value is not a very reliable measurement of the true pulsar age, usually it is overestimated and this indicates that the assumptions made are not exact.

We saw that pulsars are systems highly magnetized. A estimation of their intensity of the magnetic field strength can be obtained assuming that it is originated by a dipole:

$$B_S \simeq 3.2 \times 10^{19} (P\dot{P})^{1/2} \text{ G} \tag{3.12}$$

As for the characteristic age, given all the assumptions, this equation does not provide a precise measure of the true surface magnetic field, but only a rough estimate. The value can cover a broad range, from about 10^8 to 10^{15} G.

3.2.5 Models for the Pulsar Gamma-ray Emission

The theoretical scenarios for gamma-ray emission in pulsars depend on the location of the emission region (Figure 3.7 shows a picture of a pulsar illustrating the location of the three emission model):

- **Polar Cap (PC).** This model predicts emission near the magnetic pole of the NS, at a distance of about 30 km from the pulsar surface (Sturrock, 1971; Fawley et al., 1977; Arons & Scharlemann, 1979). The edges of the PC on the NS surface are defined by the last closed field lines. The charged particles are accelerated by the electric field, aligned with the magnetic field, and will acquire negligible energy transversal to the magnetic field line, so the synchrotron emission will be negligible. Then, due to their motion in a curved magnetic field, the charged particles will emit curvature radiation. The emitted curvature photons will create pairs via magnetic pair creation process: $\gamma + B \rightarrow e^{\pm}$. Due to the absorption of curvature photons by the magnetic field, a super-exponential cut-off is expected in the spectral energy distribution of the photons arising from the PC. Therefore, in this model is the curvature radiation that produces gamma-rays and initiates the cascade of $e^{\pm}$.

- **Slot Gap (SG).** Towards the edges of the PC region, $E_{||}$ decreases, and so particles must be accelerated over larger distances in order to reach energies high enough to radiate photons able to materialize as pairs (Arons & Scharlemann, 1979; Arons, 1983). They form a SG along the last closed field line. The emitted photons, due to their higher emission altitude, do not undergo magnetic absorption. Radiation from the SG produces a wider cone of emission than in the PC scenario (Harding & Muslimov, 2005).

- **Outer Gap (OG).** This model appears to be one of the best candidates in order to reproduce HE emission from pulsars. The OG model is based on the assumption of an oblique rotator, with $\Omega \cdot \mathbf{B} < 0$, surrounded by a magnetosphere filled with a co-rotating plasma (Cheng, 1986; Romani, 1996; Hirotani, 2008). In these vacuum gaps charged particles can be accelerated. The gap is bounded on one side by a surface layer on the boundary of the last closed field line (the *null surface* where $\Omega \cdot \mathbf{B} = 0$) and on the other side by a charge layer on the surface of an open magnetic field line. An $e^{\pm}$ plasma is generated within the gap in the regions where the accelerating electric field is intense enough to support gamma ray creation with energy high enough to produce pairs. The two main mechanisms of pair creation within the gap are by collision of gamma-ray and X-ray photons arising from synchrotron emission of secondary $e^{\pm}$ generation, or by collision of gamma rays with soft optical or IR photons. In the gap the HE photons arise from curvature radiation from accelerated $e^{\pm}$ and from IC scattering

of $e^{\pm}$ on soft photons.

The PC and SG models have difficulties to reproduce the observed spectrum of gamma-ray pulsars. Instead, the OG model, extending from the null surface to the vicinity of the light cylinder, appears to be more suitable to explain HE emission. This model was extended to explain the VHE gamma-ray emission from the Crab pulsar (Hirotani, 2011, 2013; Aliu et al., 2008). The TeV emission is explained in terms of IC scattering of secondary and tertiary $e^{\pm}$ pairs created in the collision of primary gamma rays emitted by curvature radiation and UV- IR photons.

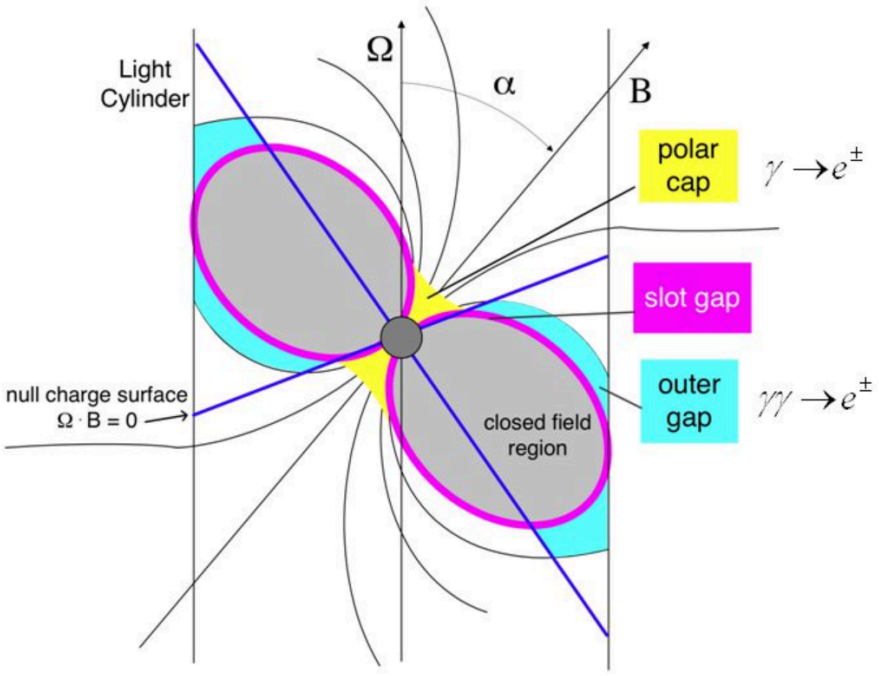

Figure 3.7 Sketch of the three pulsar emission models: PC, SG and OG.

- **Wind Zone.** In this model the acceleration zone is placed beyond the light cylinder in the current sheet of the pulsar wind (Pétri, 2012; Arka & Dubus, 2013). Emission at VHE is due to IC scattering of the X-ray photons with the $e^{\pm}$ existing in the wind. These X-ray photons are produced in the magnetosphere and/or in the pulsar surface. The pulsar wind is dominated by its radiation component near the LC and it becomes a kinetically-dominated wind towards the nebula region, between 20 to $50R_{LC}$. This emission region extends at least up to $70R_{LC}$. More details can be found in Kirk et al. (2009). In Figure 3.8 a sketch of this model.

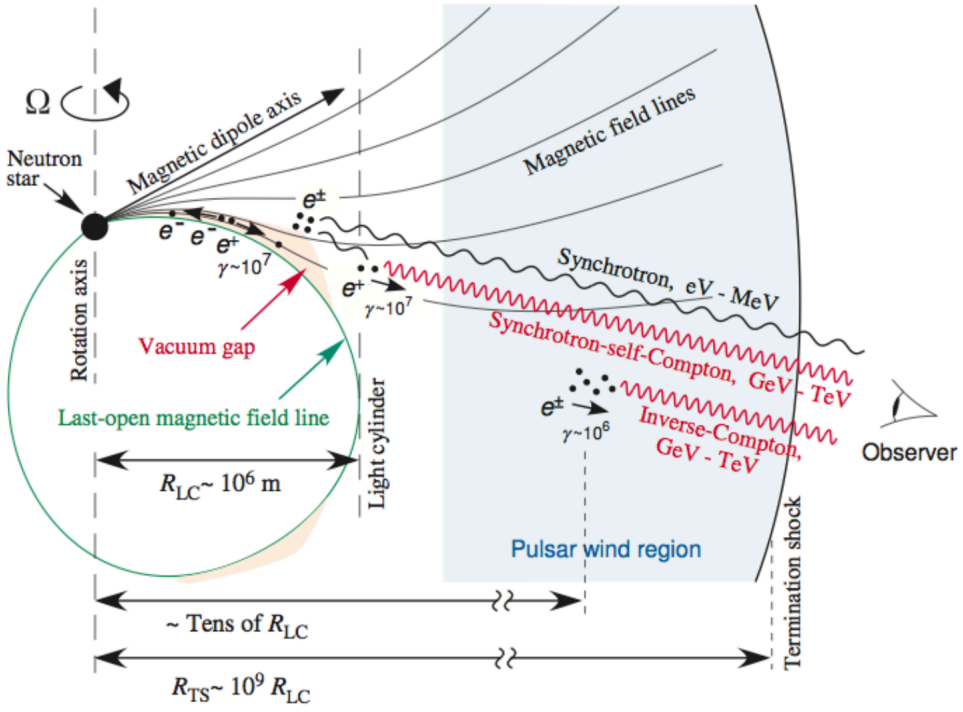

Figure 3.8 Sketch of the pulsar wind zone model as well as the pulsar magnetosphere. $e^{\pm}$ pairs are accelerated in the region called *wind acceleration zone* that is at a distance of several R_{LC} from the pulsar. Image from Aharonian et al. (2012).

Up to now, only three pulsars have been detected at VHE: Geminga is the first middle-aged pulsar detected by IACTs (MAGIC Collaboration et al., 2020) and the third pulsar detected by these type of telescopes after the Crab (Aliu et al., 2008) and Vela (H. E. S. S. Collaboration et al., 2018a).

3.3 The Crab Pulsar and Nebula

3.3.1 Introduction

The Crab Pulsar, PSR B0531+21, and its surrounding Nebula (Figure 3.9) are the remnant of the SN explosion of 1054 AD (SN1054) reported by Japanese and Chinese astronomers (Lundmark, 1921; Duyvendak, 1942). The name of the nebula was given in 1844 by William Parson who, the first time he looked at it, found a similarity with the *crab* crustacean. The age of the Crab Pulsar is about 960 years, so it is among the youngest pulsars ever observed. The Crab Nebula was the first VHE gamma-ray source ever detected by an IACT (above 700 GeV), by Whipple (Weekes et al., 1989), and has been the subject of detailed studies by all subsequent Cherenkov observatories. Since then, it is

the standard candle for energies of hundred of GeV, having the highest flux (above 200 GeV is 2.3×10^{-10} cm^{-2}s^{-1}) amongst the steady VHE gamma-ray sources; the Crab has been used as a calibration source for the different telescopes.

Figure 3.9 Multiwavelength view of the Crab Nebula and the Crab Pulsar which is the bright spot at the centre of the image. [Image Credit: NASA, ESA, G. Dubner et al.; A. Loll et al.; T. Temim et al.; F. Seward et al.; VLA/NRAO/AUI/NSF; Chandra/CXC; Spitzer/JPL-Caltech; XMM-Newton/ESA; Hubble/STScI].

The non-thermal emission of the Crab Nebula is due to HE electrons and positrons which emit via synchrotron process and IC scattering (Aharonian, 2004).

The Crab is the most powerful pulsar in our Galaxy, with a spin-down luminosity of $\dot{E} = 4.6 \times 10^{38}$ erg s^{-1} and it is located at a distance of (2.0 ± 0.2) kpc (Trimble, 1973). It has a rotational period of 33.63 ms and a first period derivative $\dot{P} \sim 4.21 \times 10^{-13}$ s/s, which gives a characteristic age of about 1270 years (close to the true age). It can be observed along the entire electromagnetic spectrum, from radio to TeV gamma rays. Measurements show that we are observing it from an angle of about 60 degrees from its rotation axis.

The Crab Pulsar emits Giant Radio Pulses (GRPs) (Staelin & Reifenstein, 1968). These features are observed in other few pulsars and is a phenomenon extremely short, of the duration of millisecond. The GRPs are a form of sporadic pulsar emission with radio fluences at least on order of magnitude higher than those of regular pulses (Enoto et al., 2021). Their origin is still unknown.

3.3.2 Discovery

The Crab Pulsar, initially discovered as a radio pulsar by the Arecibo telescope (Staelin & Reifenstein, 1968), was the first pulsar discovered in optical (Cocke et al., 1969). The pulsar was then detected in X-rays (Fritz et al., 1969) and the gamma-ray emission was detected in 1972, from 10 up to 100 MeV, by Albats et al. (1972) with gas Cherenkov detector systems. In 1977 *COS-B* [¶] detected the pulsed emission from 2 to 12 keV and from 50 MeV up to 1 GeV (Bennett et al., 1977). Then, in 2004, *XMM-Newton* satellite reported, between 0.6 and 15 keV, a harder spectrum for the interpulse and the intermediate pulse region than the main pulse (Kirsch et al., 2004). The emission up to 100 MeV was confirmed by the *EGRET* and *COMPTEL* telescopes (Kuiper et al., 2001; Nolan et al., 1993); furthermore, *EGRET* observed an extension of the pulsed emission up to 5 GeV. This pulsation was confirmed by *AGILE* and *Fermi*-LAT satellites (Abdo et al., 2010a; Pellizzoni et al., 2009).

In 2008 MAGIC telescopes detected a pulsed emission above 25 GeV from the Crab Pulsar (Aleksić et al., 2011); later, both VERITAS and MAGIC detected pulsed emission above 100 GeV with an extension up to 400 GeV (VERITAS Collaboration et al., 2011; Aleksić et al., 2012b). Five years ago, the MAGIC collaboration reported the most energetic pulsed emission ever detected from the Crab Pulsar reaching up to 1.5 TeV (Ansoldi et al., 2016). More details are given in Section 3.3.4.

The flow of the ultra-relativistic charged particles in the pulsar wind of the nebula is considered as a "cold wind" (without radiation) until it begins to interact with the surrounding medium at the termination surface, at a distance of about 3×10^{17} cm from the pulsar. The wind can be studied through the synchrotron nebula surrounding it, whose size is inversely proportional to the frequency and this is interpreted as due to a cooling of the HE electrons. At the outer edge of the nebula there is a second shock driven by the pressure of the synchrotron nebula into the thermal gas surrounding it.

3.3.3 Multi-wavelength Characteristics of the Crab Pulsar

As we see, one distinctive characteristic of the Crab Pulsar is that it emits pulsed emission over the entire electromagnetic spectrum, ranging from radio to gamma-wavelengths. The different shapes of the Crab Pulsar light curves in different energy bands are shown in Figure 3.10. It is possible to see that the Crab Pulsar emission profile is characterized by two

[¶] It was the first ESA mission to study gamma-ray sources. *COS-B* operated for over six years (1975 - 1982) and it was a forerunner of the current *Integral* mission.

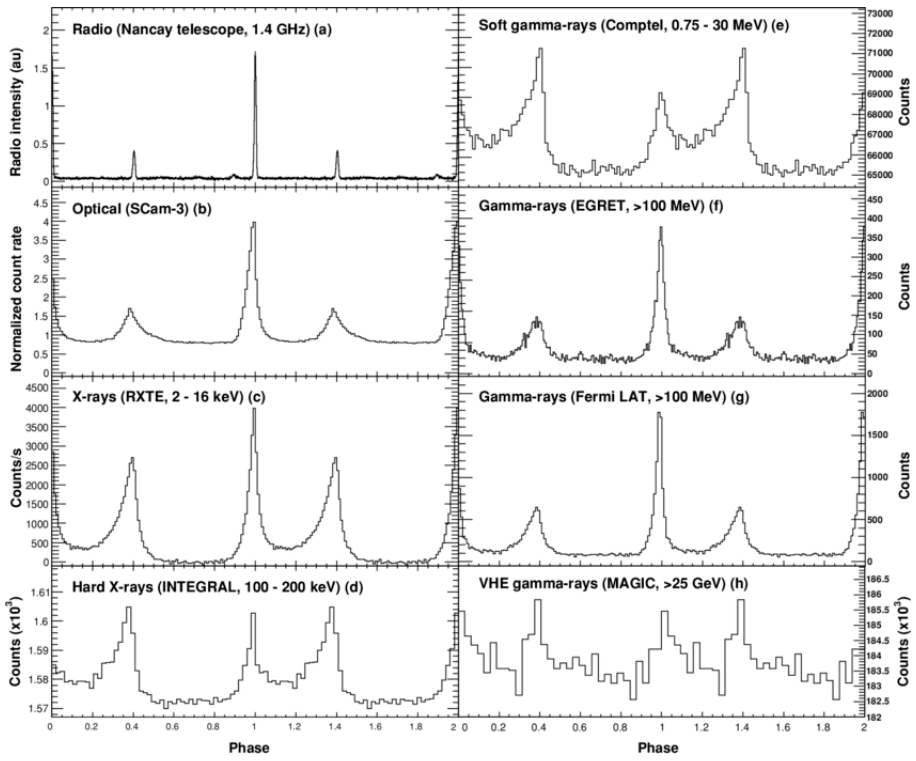

Figure 3.10 Light curves of the Crab pulsar for different energy ranges. Plot from Abdo et al. (2010a).

peaks: the interpulse (P2), coming at around 0.4 in phase, and the main pulse (P1) located at phase 0. P1 is observable at all wavelengths with an extreme stability in the phase position of the peaks across the whole electromagnetic spectrum. A third component is visible in the light curve of the pulsar, the Bridge, which is defined as the region between the main pulse and the second pulse. This bridge definition was chosen due to the fact that the peaks get wider as the energy decreases. The position of the peaks are compatible in the various energy band and the amplitude of each pulse depends on the energy (Kuiper et al., 2001). At the radio energies P2 appears to be fainter than P1 with a pulse width twice as big, imitating the optical pulse. In the gamma-ray regime, instead, P2 becomes dominant above 25-50 GeV, whereas the Bridge is only detected up to 150 GeV (Aleksić et al., 2014).

3.3.4 A view of the Crab Pulsar at gamma-wavelengths

The HE gamma-ray emission is thought to be produced by ultra-relativisitic electrons and positron via curvature radiation; whereas at VHE, IC scattering is believed to be the dominant emission mechanism. The first *Fermi*-LAT observations of the Crab Pulsar spectrum (reported in Figure 3.11) validates the presence of a spectral cutoff at 5.8 GeV (Abdo

et al., 2010a). However, the gamma-ray emission later discovered at VHE between 25 and 400 GeV (VERITAS Collaboration et al., 2011; Aleksić et al., 2012a) is not compatible with the flux predictions based on synchrotron-curvature emission of the previous studies. This new and unexpected spectral component, described by a power-law function with a photon index of 3.5, required a new explanation. Some models considered the same synchro-curvature mechanism responsible for the sub-TeV emission, under extreme conditions (Bednarek, 2012); instead others proposed a new mechanism: the IC scattering on seed photon fields (from infrared to X-rays). In this last model, as we already saw in Section 3.2.5, different VHE gamma-ray production regions have been considered from the acceleration gap in the pulsar magnetosphere to the ultra-relativistic cold wind that extends from the LC to the wind termination shock.

In the last work of Ansoldi et al. (2016) they investigated the maximum energy reached in the Crab Pulsar spectrum, analyzing 300 hours of data obtained with the MAGIC telescopes from February 2007 to April 2014. They reported the most energetic pulsed emission ever detected from the Crab Pulsar reaching up to 1.5 TeV; this new results impose different constraints on where and how the electron population produces gamma rays at these energies. The TeV pulsed emission cannot be produced with synchro-curvature radiation, but can be originated by the IC process that dominates the emission of gamma rays above 50 GeV. In particular, the joint fit of *Fermi*-LAT and MAGIC data from about 10 GeV up to 1.5 TeV suggests that the Compton up-scattering of soft photons off HE electrons can be the mechanism for produce both P1 and P2. Figure 3.12 shows the SED of P1 and P2 at HE and VHE (*Fermi*-LAT and MAGIC).

Two scenarios can be considered: the magnetospheric synchrotron-self-Compton model (Aleksić et al., 2011) and the IC in the pulsar wind region model (Aharonian et al., 2012). In the first one there are acceleration gaps in the outer magnetosphere where primary positrons propagate outwards and escape, and are then illuminated by a strong magnetospheric IR photon field which is then up-scattered by positrons to TeV-scale energies. These primary TeV photons are then absorbed by the same IR field and materialize as secondary $e^{\pm}$ pairs with GeV to several TeV energies. These secondary pairs are created at a greater distance where there is a lower photon-field density near and outside the LC, and can up-scatter the IR-UV photons into 10 GeV–5 TeV photons (via SSC process). About the pulsar wind scenario, it considers the IR scattering off the synchrotron, pulsed IR, and X-ray photons by the particles of the cold relativistic wind. The pulsar wind is magnetically dominated near 20-50 LC radii and in this narrow cylindrical zone, electrons and positrons are rapidly accelerated (Ansoldi et al., 2016).

In summary, none of the models presented identify 400 GeV as fundamental cut-off in the Crab Pulsar spectrum. The

maximum photon energy emitted by pulsars is still an open question and at the same time, it is an important ingredient for a better understanding of the emission mechanism at work.

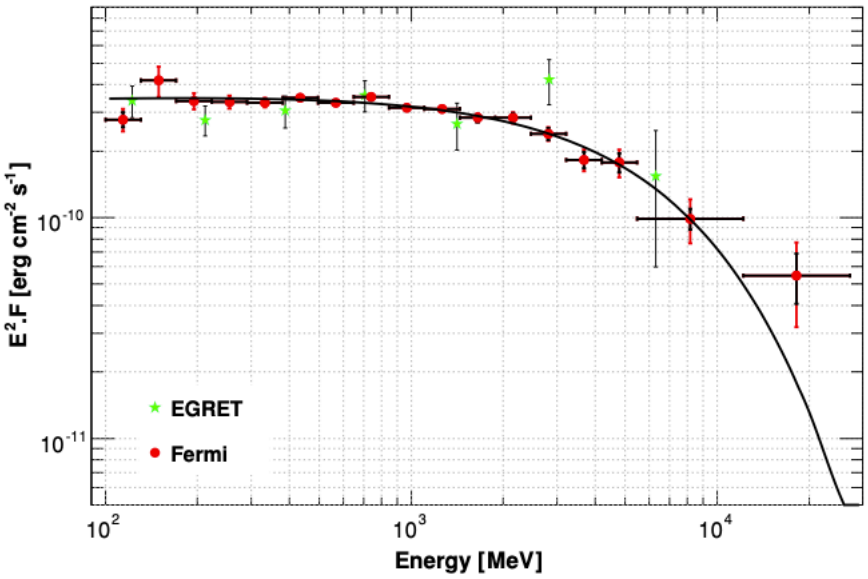

Figure 3.11 Spectral energy distribution of the Crab Pulsar averaged over the whole pulse period. The black curve represents the best-fit model, obtained with a power law with an exponential cut-off. The LAT spectral points are in red; EGRET data points in green. The statistical errors are shown in black, while the red lines take into account both the statistical and systematic errors. Results of both experiments agree in the 100 MeV-8 GeV energy range. Plot from Abdo et al. (2010a)

3.3.5 Observations with the MAGIC Telescopes

These observations and analysis of the Crab Pulsar are used to validate the performance of the Sum-Trigger-II system in order to apply it to the other Galactic sources that I studied with the MAGIC telescopes.

Data Sample and Analysis Procedure

The Crab Pulsar and its surrounding have been studied by MAGIC for decades and are objects of continuous interest. The source is observable from the location of the MAGIC telescopes from November to May. The data used for the analysis presented here were collected over several years in stereoscopic mode (from 2015 to 2019) with the Sum-Trigger-II system. Moon and twilight data were discarded due to the higher energy threshold and lower sensitivity inherent to these observations. The MC data sample used was created especially for this analysis, suitable to analyze Sum-Trigger-

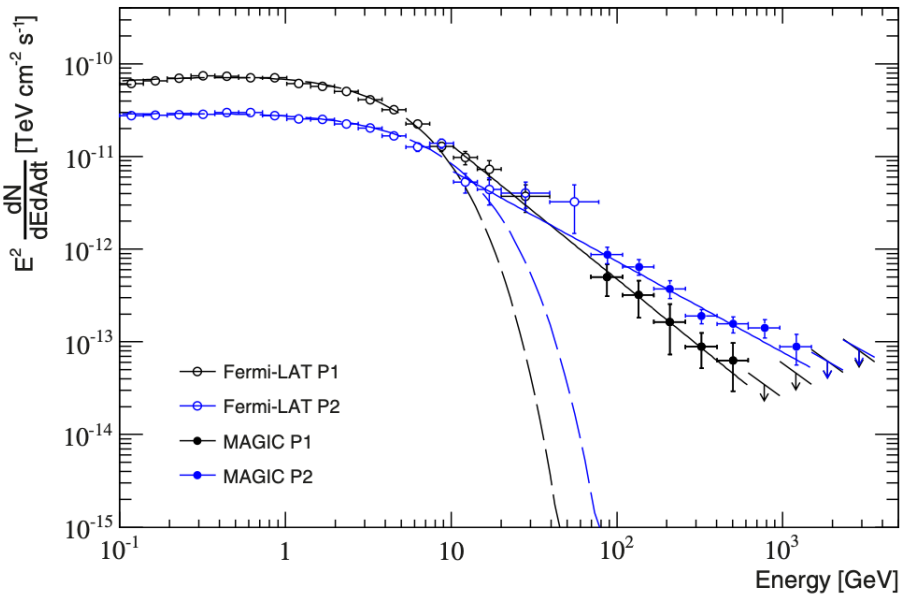

Figure 3.12 SED of the Crab P1 (black circles) and P2 (blue circles) at HE and VHE (open and filled circles). The results of the power law with exponential cutoff fits to the *Fermi*-LAT points are shown by dashed lines (Aleksić et al., 2014), whereas the joint *Fermi*-LAT/MAGIC fits to power-law functions above 10 GeV are shown by solid lines. Plot from Ansoldi et al. (2016).

II data. As the nebula surrounding the pulsar is strong and can be detected in few minutes, the reconstructed Nebula signal was used as a data quality check of my analysis. I selected only runs with a L3 rate higher than 500 Hz; I set a strict requirement of excellent atmospheric conditions, a minimum of 0.85 atmospheric transmission at an altitude of 9km. In total, 110 hours of good data quality were selected.

As already explained, the observations of VHE gamma rays cannot be done without accumulating a lot of background coming from events triggered by CRs. To improve the signal-to-noise ratio, I applied cuts in order to reject events that are not photon-like. In order to compute these cuts, I used a background sample, taken from the anti-source position in the camera and a gamma-ray MC sample to avoid overtraining. The cuts are energy dependent and those applied to the pulsar analysis to search for pulsed emission rely on hadronness and θ^2 distributions. The sample used for the computation are divided in 30 logarithmic energy bins; the cuts used for this analysis are reported in table 3.1.

Spectral Energy Distribution

Figure 3.13 shows the SED of P1 and P2 of the Crab Pulsar obtained with `flute`. For the calculation of the SED of the pulsed emission, I set an efficiency of 75% in the θ^2 cuts and 90% in the hadronness cuts. The background considered in

Table 3.1 Energy-dependent cuts computed for the Crab MAGIC analysis. Here, for convenience, I reported only the cuts in the energy range $\sim$ 20-300 GeV.

E_{min} [GeV]	E_{max} [GeV]	θ^2 [deg^2]	Hadronness
16	22	0.15	0.95
22	30	0.16	0.91
30	41	0.15	0.71
41	55	0.11	0.51
55	75	0.08	0.44
75	102	0.05	0.45
102	139	0.04	0.47
139	189	0.03	0.45
189	257	0.03	0.42
257	350	0.02	0.37

order to compute the number of excess events from P1, P2 and the Bridge is taken from the OFF region between P2 and P1. The effective time was computed taking into account the dead time of the readout system after each event recorded of 26×10^{-6} s. Each data set was split into 30 logarithmic spaced bins between 5 GeV and 50 TeV. The effective area used for the flux estimation was computed using the reconstructed energy of the MC events, averaged over the zenith range covered (5-30 degrees). The SED for P1, P2 and the Bridge are well described by a power-law function defined as:

$$\frac{dN}{dE} = f \times \left(\frac{E}{150\text{GeV}} \right)^{-\alpha} \tag{3.13}$$

where f is the normalization factor ($f_{P1} = 1.1 \times 10^{-11}$ TeV^{-1} cm^{-2} s^{-1} and $f_{P2} = 2.0 \times 10^{-11}$ TeV^{-1} cm^{-2} s^{-1}); 150 GeV is the normalization energy and α the spectral index ($\alpha_{P1} = 3.2$ and $\alpha_{P2} = 2.9$). The ULs of the differential flux were obtained by following the Rolke & López (2001) method under the assumption of a Gaussian systematic uncertainty in the detection efficiency, with a standard deviation of 30% systematic uncertainty in the flux level. Hereafter, the ULs are given at 95% C.L..

The spectral points and ULs are listed in Table 3.2. In Figure 3.13, I also computed the Crab Nebula spectrum, as a sanity check, using the whole sample of data, with the same cuts and energy binning as for the pulsar analysis. The nebula spectrum is usually described by a log-parabola function:

$$\frac{dN}{dE} = f_0 \left(\frac{E}{E_0} \right)^{-\alpha + \beta \log(E/E_0)} \tag{3.14}$$

where f_0 is the flux normalization, α the index, β the curvature index and E_0 the normalization energy. For the fit in Figure 3.13 (green curve) I used the parameters reported in Aleksić et al. (2015): f_0= 3.23 × 10^{-11} TeV^{-1} cm^{-2} s^{-1}, α = 2.47, β= -0.24 and E_0=1 TeV. The spectral points and ULs of the nebula are listed in Table 3.3.

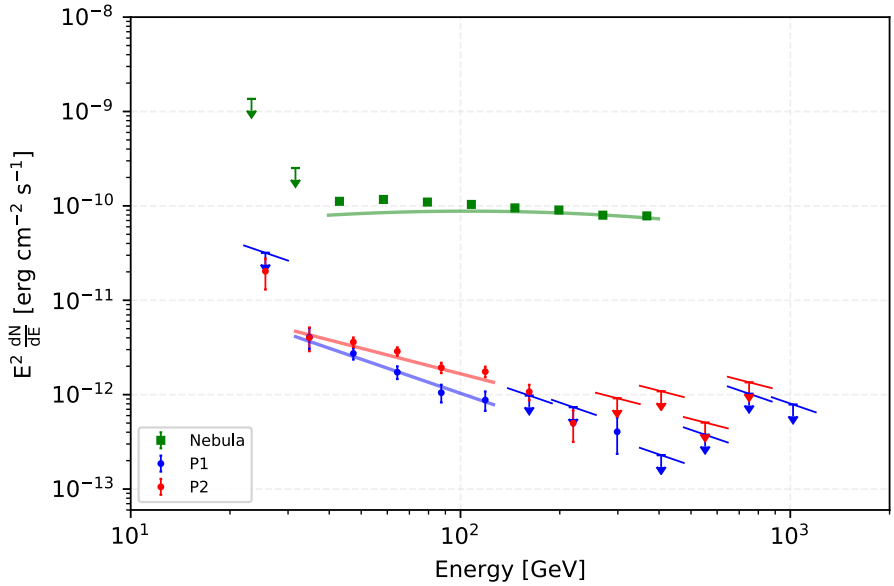

Figure 3.13 SED of the Crab P1 (blue circles) and P2 (red circles) measured by MAGIC between 5 GeV and 50 TeV. The Crab Nebula spectrum is also shown for comparison (green square).

Light Curve and Detection of the Pulsation

As explained in Section 2.2.8.2, the detection of pulsed emission relies on the ToA of the photons coming from the observed pulsar. Each event detected by telescopes is recorded together with its ToA using a high precision GPS clock coupled with a rubidium clock and, during this step, the corrections of the Earth's motion with respect to the pulsar are applied. The phase of the events and the timing correction are computed and applied using the already mentioned software: `tempo2`. After this step the events are characterized by their phases according to the pulsar rotation period. The ephemeris were calculated specifically for this analysis.

In order to characterize the emission from the different components of the source, the phaseogram (i.e. the number of events as a function of the pulsar phase) was computed for two different energy ranges: 20-100 GeV and 20-100; the lowest energy corresponds to the energy threshold calculated from the MC data sample. The phaseograms are binned

Energy [GeV]	Bin Center [GeV]	P_1 $E^2\,dN/dEdAdt$ [TeV cm^{-2} s^{-1}] $\times 10^{-13}$	P_2 $E^2\,dN/dEdAdt$ [TeV cm^{-2} s^{-1}] $\times 10^{-13}$
22-30	25	<198.7	127.8 ± 45.6
30-41	35	25.4 ± 6.3	25.1 ± 7.0
41-55	47	17.1 ± 2.3	22.5 ± 2.6
55-75	64	10.8 ± 1.7	18.0 ± 1.8
75-102	87	6.5 ± 1.4	12.1 ± 1.5
102-139	119	5.5 ± 1.3	11.0 ± 1.4
139-189	162	<6.1	6.7 ± 1.2
189-257	220	<4.6	3.1 ± 1.1
257-350	299	2.5 ± 1.1	<5.7
350-475	406	<1.4	<6.8
475-646	552	<2.3	<3.1
646-878	750	<6.4	<8.4
879-1194	1020	<4.9	-

Table 3.2 Crab Pulsar spectral points of the MAGIC measurements shown in Figure 3.13.

in 40 regularly-spaced bins between phases φ=0 and φ=1. In the search for the pulsation of the Crab Pulsar, the phase boundaries for P1 and P2 pulses and for the background region are defined a priori. The main peak P1 $\in$ [0,0.026 $\cup$ 0.980,1] and the interpulse P2 $\in$ [0.377,0.422] (Ansoldi et al., 2016); the interval [0.520,0.870] is considered as the OFF region (Fierro et al., 1998), which is the background considered to be subtracted from the histogram. The significance of the signal was computed using several statistical tests: the χ^2, the Z_{10}-test and the H-test[‖] (de Jager et al., 1989). But only the Li&Ma significance (Li & Ma, 1983), based on the likelihood ratio test (see Section 2.2.6.3), uses the information a priori of the expected position of the peak (signal region) in the light curve. Figure 3.14 shows the folded pulse profile that I obtained between 20 and 100 GeV and between 20 and 300 GeV with 110 hours of observations. It is possible to see that both pulses, for both energy ranges, are detected with high statistical significance; for the range 20-100 GeV: 9.6σ and 13σ for P1 and P2, respectively, with the total being 15.2σ. For the range 20-300 GeV: 10.5σ and 15.1σ for P1 and P2, respectively, with the total being 17.1σ. Table 3.4 summarizes the number of excess N_{ex} events with their corresponding significance for different integral energy ranges.

Since the detection significance $\mathcal{S}$ is limited by the large background, its square is expected to scale linearly with the observation time: $\mathcal{S} = s\sqrt{t}$. The resulting *quality factor* s for the pulsed component of the Crab emission with MAGIC is $s = 1.44\sigma/\sqrt{h}$ for 20-100 GeV and, $s = 1.69\sigma/\sqrt{h}$ for 20-300 GeV.

[‖]The χ^2 test depends on the phaseogram binning; the Z_{10}-test depends on a priori fixed harmonics number, usually 10; the H-test is the maximum of many Z-test of different harmonics number.

Energy [GeV]	Bin Center [GeV]	Nebula $E^2\, dN/dEdAdt$ [TeV cm^{-2} s^{-1}] $\times 10^{-11}$
20-27	23	<85.1
27-37	32	<15.7
37-50	43	6.9 ± 0.2
50-68	58	7.3 ± 0.1
68-92	79	6.9 ± 0.1
92-126	108	6.5 ± 0.1
126-171	146	5.9 ± 0.1
171-232	199	5.6 ± 0.1
232-316	270	5.0 ± 0.1
315-4298	367	4.9 ± 0.1

Table 3.3 Crab Nebula spectral points of the MAGIC measurements shown in Figure 3.13.

Energy Range	P1		P2		P1+P2	
[GeV]	N_{ex}	Significance	N_{ex}	Significance	N_{ex}	Significance
20 -100	2844 ± 299	9.60σ	3967 ± 308	13.02σ	6812 ± 452	$15.20\,\sigma$
20 -300	3194 ± 308	10.40σ	4379 ± 318	$15.03\,\sigma$	7934 ± 4673	17.10σ

Table 3.4 Number of excess events and corresponding significance of P1 and P2 for different energy ranges in about 110 hours of data.

Variability

It is interesting to check if the pulsed flux measured by MAGIC is stable or not. The possibility of a temporal variability of the pulsed flux was also subject of investigation during the years: the *Fermi*-LAT satellite, since 2008, continues to monitor the Crab Pulsar and these observations show no sign for variability at energies below 10 GeV. This is different to what we can see in the radio band, where Giant Radio Pulses (GRP)** are frequently observed (Howard et al., 1968; Enoto et al., 2021). Above 10 GeV the *Fermi*-LAT statistics is too low to estimate possible variability on time scales shorter than a month and thus, further search for temporal variability at higher energies is still an open topic. I show here the study of the long-term light curve of the Crab pulsar with the goal of search for variability in the energy range above 30 GeV on time scales of a month. A month period is the time interval between two full moons and during the

**The giant radio pulse is a form of sporadic pulsar emission with radio fluences at least an order of magnitude higher than those of regular pulses. The origin is unknown. In particular, these pulses are bright, sometimes exceeding a megajansky (MJy, 1 Jy = 10^{-26} W m^{-2} Hz^{-1}) for a few nano- to microseconds.

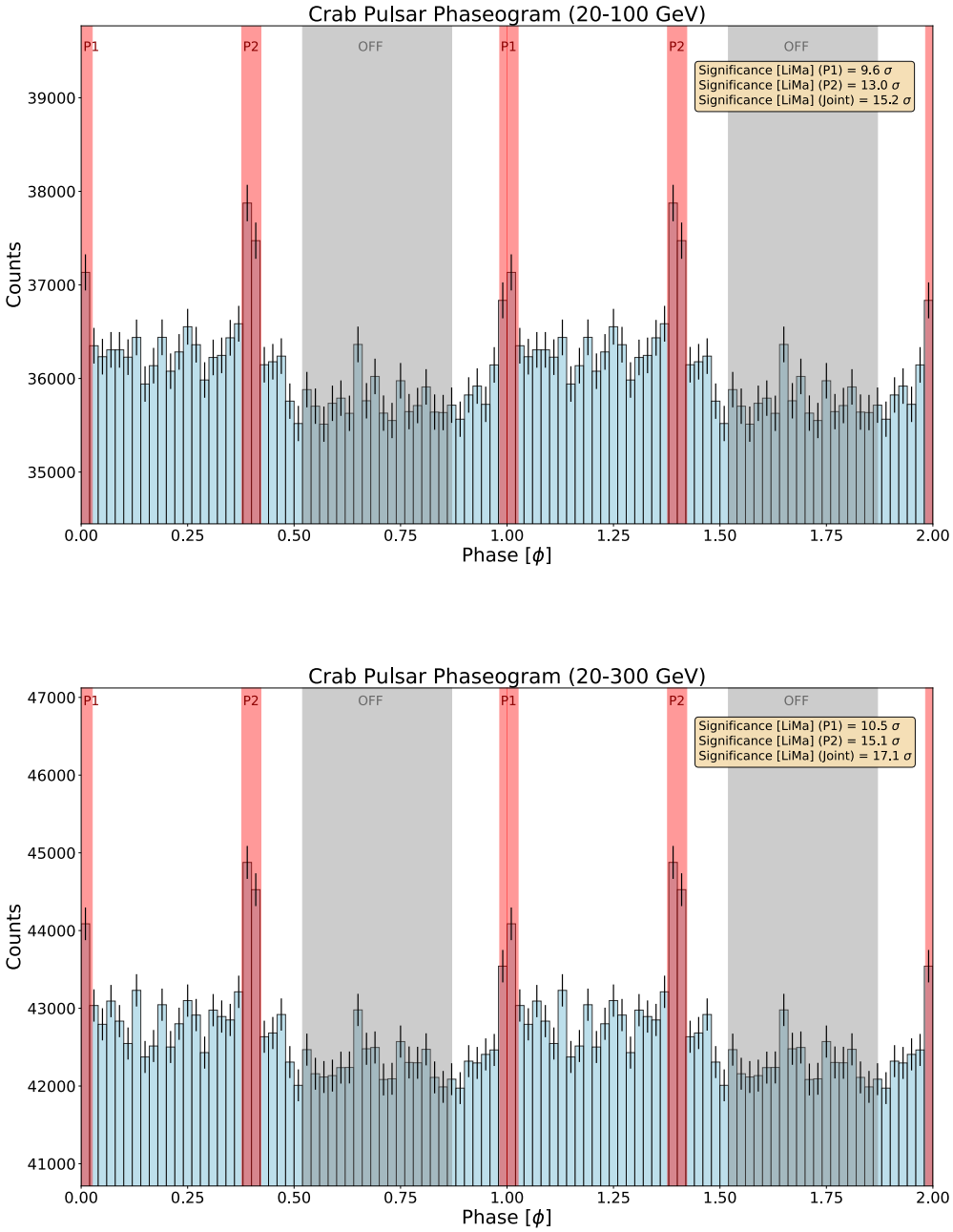

Figure 3.14 Phaseogram of Crab Pulsar in the energy range 20-100 GeV (*top panel*); 20-300 GeV (*bottom panel*). The red area are the signal region for P1 and P2; the grey region is the region used to estimate the background. The Bridge region is the area between P1 and P2. Two full rotations are displayed for an easier interpretation.

moon period pulsar observations are impossible and they are necessarily interrupted during full moon period.

No variability was detected during the time span of the observations. Figure 3.15 presents the light curve of the pulsed emission of the sum of P1 and P2 for a monthly binning and the flux was calculated above 30 GeV. The data sets was tested for variability with a simple X^2 test (goodness-of-fit with respect to the average flux). As we said, the light curve does not significantly supports a time variation of the flux and the σ^2 over the number of degrees of freedom (NDF) for the total pulsed emission is σ^2/NDF=18.8/14.

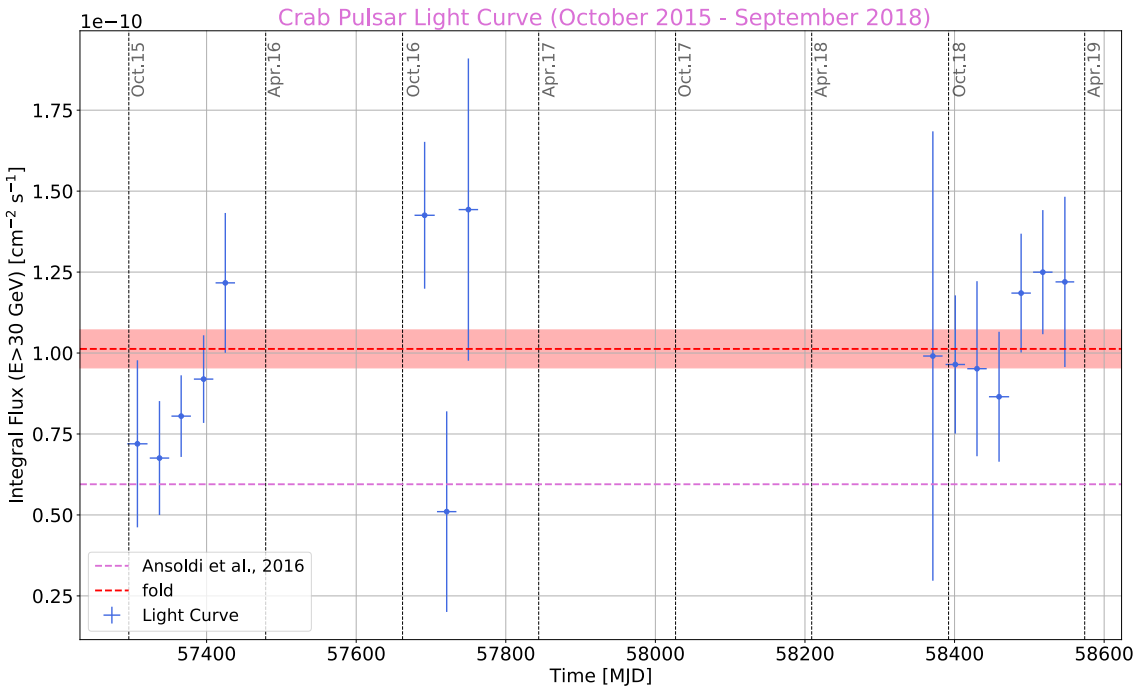

Figure 3.15 Monthly flux of Crab Pulsar above 30 GeV, plotted against time in MJD. No significant deviation from a constant can be seen (σ^2 test). The red horizontal dotted line is the integral flux obtained from the folding method (which delivers an estimate of the optimal parameters for the fitted model): 1.01×10^{-10} cm^{-2} s^{-1}; the shaded red region is the corresponding error. The integral flux, above 30 GeV, from Ansoldi et al. (2016) is also reported for comparison. The difference between the two fluxes can be related to the systematics error.

3.4 Millisecond Pulsars

Another important discovery was the first MSP PSR B1937+21, detected by Backer et al. (1982) using the Arecibo telescope. This pulsar has a spin period of 1.56 ms, making it the fastest-spinning pulsar known at the time and showed a lower spin period derivative compared to the other pulsars.

In general, MSPs are categorized as pulsars with spin-periods P<20–30 ms and a spin period derivative $\dot{P} \leq 10^{-17}$s/s (Lorimer, 2009). These pulsars have significantly low magnetic fields (B$\simeq 10^{7}$-10^{10} G). The fastest-spinning MSP rotates 716 times per second with a period of 1.39 ms (Hessels et al., 2006). MSPs can be classified according to their observed multi-wavelength emission and the location within the Galaxy. Roughly 140 of them are located in Globular Clusters and about 240 in the Galactic Disk (Konar & Chahal, 2019).

3.4.1 Pulsar Recycling Mechanism

The old pulsars that have evolved into the pulsar *graveyard* in the P-$\dot{P}$ diagram can "acquire" a new life. In this section I describe the basic idea behind this process, in which a slowly spinning pulsar is *recycled* to spin at a few millisecond period.

The formation of a MSP begins in a binary system and an illustration of this process is shown in Fig. 3.16. It begins with a massive supergiant star ($M \geq 8\ M_{\odot}$) and a Sun-like star (Figure 3.16, first panel). In a few million years the more massive of the two stars exhausts its nuclear fuel, its core implodes forming a rapidly spinning and energetic NS, and the SN explosion blows away material from the external shells (Figure 3.16, second panel). The system remains gravitationally bound. The pulsar's rotating magnetic field (approximated by a dipole) releases electromagnetic radiation which spins down the pulsar over a few million years; this increases the pulsar's spin period. As the $\dot{P}$ decreases and P increases over the time, the pulsed emission from the pulsar decreases and can become non-detectable. It has now entered the pulsar *graveyard*. After the discovery of the first millisecond pulsar, PSR B1937+21, Radhakrishnan & Srinivasan (1982) and Alpar et al. (1982) proposed that it must have been spun-up by the accretion of angular momentum from a previous companion. This idea was motivated by the low spin period derivative and hence low inferred magnetic field and further, there was no associated SN remnant despite the rapid spin-period. Radhakrishnan & Srinivasan (1982) had coined the term "recycling" for this accretion-driven spun up. After billions of years the low-mass companion evolves and expands in a red giant. It overflows its Roche Lobe (Figure 3.16, third panel) accreting mass

and angular momentum onto the NS. In this phase, bright X-ray emission is produced from the accretion disk and the binary is referred as a LMXB in outburst. Once the accretion stops, a radio pulsar with reduced magnetic field and millisecond duration spin period emerges. Strong winds from the pulsar slowly erode the companion star (Figure 3.16, fourth panel).

There are two types of binaries containing MSPs whose classification depends on the mass of the companion star and on the stellar type:

- **Black Widows (BWs)** are MSP binaries containing a low mass ($\leq$ 0.1 $M_{\odot}$) and a semi-degenerate companion, often in a very compact orbit (1.5-3.5 hours). In these systems the companion is slowly ablated by the pulsar wind that is impinging on it. The first BW discovered provided further proof that pulsar recycling mechanism can form an isolated MSP, like PSR B1937+21 (Fruchter et al., 1988). This suggests that there may be similar systems in which the companion is being more strongly irradiated, and may eventually be ablated completely if it is already of lower mass and more tenuous.

- **Redbacks (RBs)** have non-degenerate, more massive than black widows' mass companion (0.1-0.4 $M_{\odot}$) and a main sequence-like companion (Roberts, 2013). Their orbital period (4-15 hours) is longer than that of black widows and typically they show more extensive radio eclipses. The companion in the RBs survives the pulsar wind erosion.

Following the spider analogy, these systems have been nicknamed *redbecks* and *black widows* because, as in Australian spider species, females feed on their less massive male companions after mating. Both systems are characterised by very short orbital periods (P<1 day). These systems are crucial to understand the MSP recycling scenario and the formation of isolated MSPs. They are also a way to study the acceleration, composition and shock dynamics of the MSP winds, and infer accurate MSP mass measurements through pulse timing. Recently, the RB class has drawn considerable attention due to three systems that have been observed to transition from an accretion-powered disk state to a rotationally-powered pulsar state on short timescales ($\leq$ month), proving the suspected evolutionary link between LLMXBs and MSPs and showing that the MSP recycling process in RBs may be ongoing. I will introduce this particular class, the transitional MSPs, in next Section 3.5.

3.5 Transitional MSPs

Observations over the past decade have demonstrated that the evolution from an LMXB to a MSP during the pulsar recycling process is not a unidirectional process. The so-called tMSPs are a class of NS binary systems that switch back

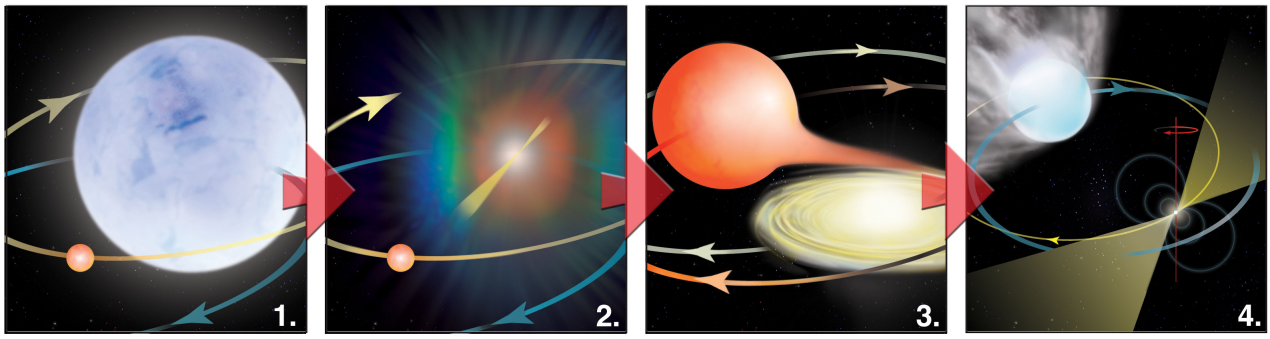

Figure 3.16 A four panel figure illustrating the hypothesized formation and evolution of a MSP through the *pulsar recycling mechanism*. Illustration credit: Bill Saxton, NRAO.

and forth, on multi-year timescales, between an observable MSP and a LMXB-like state, where an accretion disk is observed and an active low-level accretion into the NS magnetosphere takes place.

Since the discovery of the first tMSP, PSR J1023+0038 (Archibald, 2015), other two similar systems have been found in the Milky Way: IGR J18245−2452 in the globular cluster M28 (Papitto et al., 2013a) and XSS J12270−4859 (de Martino et al., 2010a; Bassa et al., 2014). All these three confirmed tMSPs are RBs when they are in the MSP state.

tMSPs are the key to track the long evolutionary link between accreting NSs in LMXBs and MSPs in binary systems. Furthermore, they provide a more detailed understanding of the physical processes that spin-up NS to millisecond periods. A clarification: for these sources the term "LMXB state" is atypical of LMXB systems in general; some papers in the literature have referred to this state as the "sub-luminous accretion disk state", which is more suitable. IGR J1824−2452 is the only tMSP system observed to enter a high X-ray luminosity ($> 10^{36}$ erg s^{-1}) state that resembles a canonical LMXB in outburst.

In Chapter 6 I will give an overview of the well-established tMSP systems.

4

PSR J2229+6114

4.1 PSR J2229+6114

Discovery and Morphology

PSR J2229+6114 (hereafter J2229) is a young and energetic pulsar and it is located at low Galactic latitude (ℓ, b) = (106°.6, 2°.9). This pulsar is thought to provide the energy powering the arc-shaped PWN G106.65+2.96, dubbed "Boomerang", which is part of the cometary shaped SNR G106.3+2.7 discovered and described by Joncas & Higgs (1990) and Pineault & Joncas (2000). J2229 was discovered at radio frequencies in the error region of the unidentified EGRET source 3EG J2227+612 after the end of the *Compton Gamma-Ray Observatory (CGRO)* mission (Halpern et al., 2001a). The pulsed signal was also detected in the X-ray band with a spin period P of 51.6 ms and a rotational

energy loss rate, also defined as the spin-down luminosity, of $\dot{E}$= 2.2× 10^{37} erg s^{-1}; J2229 is one of the gamma-ray pulsar with the highest spin-down power (the first is PSR J0537-6910 in the Large Magellanic Cloud and the second one is the Crab Pulsar). The pulsar is located at the North edge of the bright radio head and the radio emission (see Figure 4.1, green contours) comes from a shock which is driven into the surrounding medium either by the motion of the pulsar or by the PWN expansion.

The characteristic age of the pulsar, assuming a pure magnetic dipole field and a significantly faster spin period at birth, is τ = 10,460 yr. The magnetic field at the surface of the NS can be as high as 2.0 × 10^{12} G (Halpern et al., 2001a) instead, in the PWN, the magnetic field is of about 2.6 mG. Through analyses of atomic hydrogen H1 and molecular cloud distribution a distance of 0.8 kpc was determined (Kothes et al., 2001) for the system (pulsar and synchrotron nebula), in contrast with the larger distance of 3 kpc estimated from the X-ray absorption by Halpern et al. (2001a). The distance of J2229 was also estimated with the Dispersion Measure (DM) method*. The conversion of DM to distance depends on the electron density model used. Over the years, different Galactic electron density models have been derived from independent distance measurements to pulsars; the most famous models are NE2001 (Cordes & Lazio, 2002) and the YMW16 (Yao et al., 2017). It is possible to compare these two models using the new Python package called `PYGEDM` (Price et al., 2021). For J2229, considering a DM of 205 cm^{-3} pc (from the Third Pulsar Catalogue, Limyansky, 2019), it is possible to find a distance of about 5 kpc if we assume the NE2001 model and, for YMW16, of about 7.5 kpc. Hence, from these estimates, the distance of 3 kpc, derived from the X-ray absorption, is the closest to the value obtained using the model of YMW16.

For the following values of the luminosities, a distance of 3 kpc was considered: the X-ray luminosity, calculated between 2 and 10 keV, is 1.3× 10^{32} erg s^{-1}; while the gamma-ray luminosity, above 100 MeV, is 3.7×10^{35} erg s^{-1} (Halpern et al., 2001b).

*The electrons in the interstellar medium disperse the pulse signal received by radio telescopes from a radio pulsar. This manifests itself as a broadening of an otherwise sharp pulse when the pulsar is observed over a given bandwidth. The amount of dispersion is proportional to the integrated column density of free electrons between an observer and the pulsar. For the density of electrons we have to consider a specific Galactic electron density model which depends on the distance to the pulsar. Thus, a measurement of the DM allows an estimation of the distance to the pulsar. The DM, expressed in cm^{-3} pc, is defined as

$$DM = \int_0^d n_e(l)dl. \tag{4.1}$$

where n_e is the free electron number density and d the distance to the pulsar.

In Figure 4.1 it is possible to see SNR G106.3+2.7 and its cometary structure: a compact *head* of high surface brightness located in the northeastern part of the system and an elongated *tail* of low surface brightness extending toward the southwest (Pineault & Joncas, 2000). The *head* region, extends about 3′, is associated with the PWN powered by the energetic pulsar; a small H I shell envelops the PWN and this implies that the PWN is either pushing the H I gas outward or ionizing the atomic hydrogen gas in its vicinity (Kothes et al., 2001). A dense shell-like structure of H I is present also in the southeastern region of the head region and probably it is caused by the encounter of the SNR shock with the dense medium. The SNR has strong X-ray and gamma-ray emission (Halpern et al., 2001b). The *tail* region is expanding in a low density H bubble that is thought to be excavated by the stellar winds of the progenitor massive star.

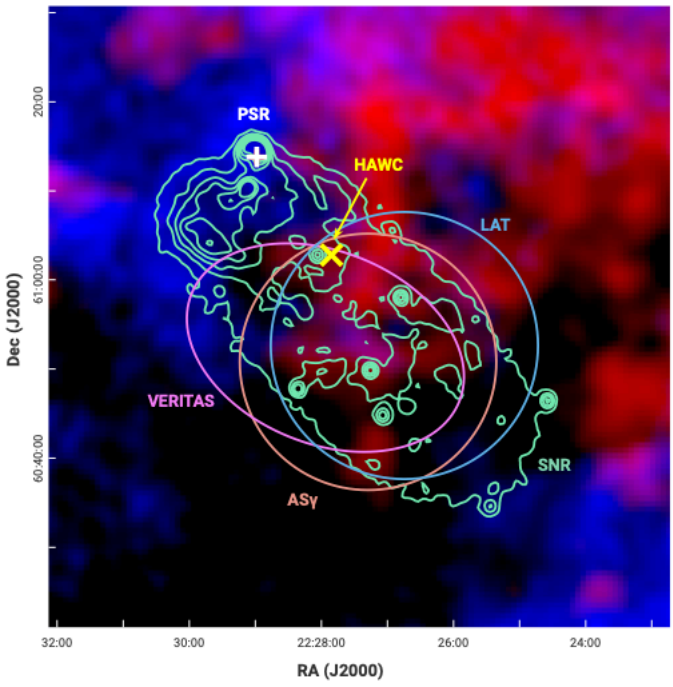

Figure 4.1 Distribution of the gas around the SNR G106.3+2.7. Blue color represents the distribution of H I gas and red color shows the CO emission of a dense molecular cloud. The green contours are the 1.4 GHz radio continuum of the SNR. The white cross is the pulsar. The magenta ellipse, cyan and orange circles represent the gamma-ray emission detected by VERITAS, *Fermi*-LAT and Tibet ASγ, respectively. The yellow cross shows the best-fit position of the HAWC source (HAWC J2227+610). Image from Ge et al. (2021).

In recent years, the gamma-ray community has shown a great interest in this complex region. In particular, MILAGRO (*Multiple Institution Los Alamos Gamma Ray Observatory*) detected the first extended VHE emission, up to 35 TeV, coming from the entire system (Abdo et al., 2007). VERITAS reported the detection of VHE gamma-ray emission (between 0.9 and 16 TeV) from the elongated radio extension of the SNR, see Figure 4.2, at about 0.4° away from the position of the pulsar and they named it VER J2227+608 (Acciari et al., 2009a). *Fermi*-LAT reported GeV gamma-ray emission, between 3 and 500 GeV, from the *tail* region of the SNR, near VER J2227+608, based on a study of ten years of data (Xin et al., 2019). Moreover, also the data collected by the *Astro-rivelatore Gamma ad Immagini LEggero (AGILE)* satellite reported gamma-ray pulsations above 100 MeV (Pellizzoni et al., 2009). Recently, the HAWC, LHAASO and *Tibet ASγ (Air Shower Gamma Ray)* experiments detected emission up to 100 TeV from the SNR (see Figure 4.1). The discovery and the study of many new gamma-ray pulsars will provide strong constraints on the location of the gamma-ray emitting regions.

As discussed before, the Boomerang Nebula is surrounded diffuse X-ray emission which is described by a hard non-thermal spectrum with a photon index 1.5 (Halpern et al., 2001b). In particular, this extended X-ray emission in the *head* region can be produced by electrons escaping the PWN which are probably accelerated *in situ*, as it is possible to understand by the fast X-ray cooling. For more details, see Ge et al. (2021). This X-ray emission can be considered as an indicator of an efficient particle acceleration, especially, in young SNRs (a few thousand years old). Actually, SNR G106.3+2.7 is the first middle-aged[†] SNR detected with X-ray synchrotron emission and this favors the particles acceleration. Furthermore, in the *tail* region, where the SNR is located and the magnetic field is not so weak, it is possible that the acceleration of PeV protons (1 PeV = 10^{15} eV) takes place. In particular, the presence of a dense molecular cloud can be the target for the interactions of CR protons escaping the SNR at PeV energies. So, this can be a source of PeV Galactic CRs and this is theoretically sustained by the fact that SNRs that expands in stellar winds cavities are promising PeV accelerators (Ge et al., 2021). Only future high performance instruments, such as CTA and the current LHAASO (*Large High Altitude Air Shower Observatory*) will be able to detect PeV protons.

[†]In Vink (2020) a "young" SNR is defined as a SNR with an age lower than 1000-2000 yr, an X-ray emission from ejecta and shock velocities higher than 1000 km s^{-1}. When the SNR is in the adiabatic phase, it is slightly older and it is labeled as "mature". Once the shock velocity drops below 200 km s^{-1}, the SNR become bright in optical-radiative shocks; this signs the transition to the so called "middle-age" phase.

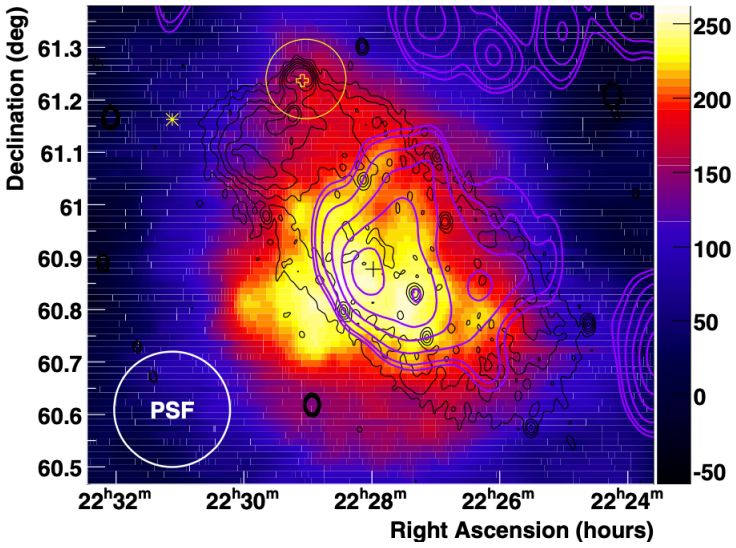

Figure 4.2 Sky map of TeV gamma-ray emission from G106.3+2.7 detected by VERITAS. The color scale indicates the number of excess gamma-ray events from the region. The centroid of the TeV emission is indicated with a thin black cross; the open yellow cross shows the position of PSR J2229+6114. Image from Acciari et al. (2009a).

From the observations by ROSAT (*ROentgen SATellite*) and ASCA (*Advanced Satellite for Cosmology and Astrophysics*) satellites, the total flux of the extended diffuse X-ray source, between 2-10 keV, is about 1.56×10^{-12} erg cm^{-2} s^{-1}, with a power-law photon index of 1.51 ± 0.14 (Halpern et al., 2001a). Later, Li et al. (2008), using *Chandra* satellite observations, confirmed that the X-ray flux is dominated by the extended source. PSR J2229+6114 is one of the most energetic pulsars known, with a spin-down power of 2.2×10^{37} erg s^{-1}; following the ATNF Pulsar Catalogue[‡] (Manchester et al., 2005) the pulsar with the highest spin-down power is PSR J0537-6910 in the Large Magellanic Cloud (4.9×10^{38} erg s^{-1}) and the second one is the Crab Pulsar (4.5×10^{38} erg s^{-1}). J2229 is significantly more luminous than the very close (d$\sim$0.28 kpc) and brightest persistent source of gamma rays in the sky: the Vela Pulsar (PSR B0833-45). Morphologically, J2229 is very similar to the Vela PWN because both of them have a possible jet and an incomplete elliptical arc (interpreted as a equatorial shock in the pulsar's wind).

The vast majority of the almost 300 gamma-ray pulsars detected by *Fermi*-LAT[§] are well described by a power-law model with an exponential cut-off around a few GeV. Abdo et al. (2009) reported the detection of *Fermi*-LAT gamma-ray pulsations (above 0.1 GeV); the spectrum is fitted with a power law with an exponential cut-off leading to an integral

[‡] https://www.atnf.csiro.au/research/pulsar/psrcat/

[§] https://confluence.slac.stanford.edu/display/GLAMCOG/Public+List+of+LAT-Detected+Gamma-Ray+Pulsars

photon flux of $(3.77 \pm 0.22) \times 10^{-7}$ cm^{-2} s^{-1}. In Figure 4.3 the *Fermi*-LAT spectrum of J2229 is reported. The source was modeled by a power law with a simple exponential cut-off between phases 0.15 and 0.65; the solid line shows the phase-averaged spectral energy distribution from a likelihood fit, with $N_0 = (5.2 \pm 0.4) \times 10^{-8}$ cm^{-2} s^{-1}, a spectral index $\Gamma = (1.85 \pm 0.06)$ and a cut-off energy $E_C = (3.6 \pm 0.6)$ GeV. The observed spectral cut-off could be determined by the production of magnetic pairs or by the photon-photon absorption as this would prevent that VHE photons escape from the system. The observed integrated energy flux calculated by Abdo et al. (2009) is $(23.7 \pm 0.7) \times 10^{-11}$ erg cm^{-2} s^{-1}.

In Section 4.2.2 the most recent updated gamma-ray results from the Second *Fermi*-LAT Catalog of gamma-ray pulsars (2PC) will be considered.

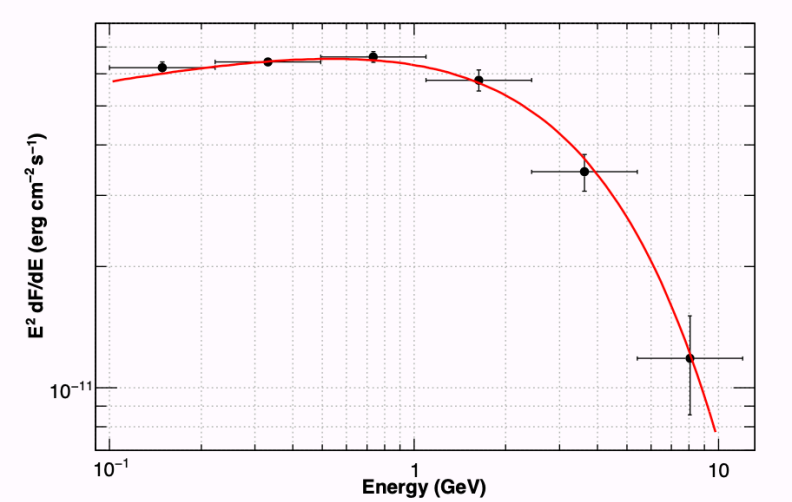

Figure 4.3 Phase-averaged spectral energy distribution for J2229 assuming a power-law fit with an exponential cut-off (solid line). The spectral points were obtained for 6 logarithmically-spaced energy bins and performing spectral analysis in each interval, assuming a power law shape for the source. From Abdo et al. (2009).

Light Curve in different Energy Ranges

Figure 4.4 shows the light curve of J2229 in different energy bands. The source presents a radio pulse profile (bottom panel) with a single sharp peak, while in the X-ray band (second panel from bottom) two peaks, separated by $\Delta\varphi$=0.5, are visible. The gamma-ray light curve of the J2229 covers a wide range in phase (more or less the 50% of the total emission) and this suggests that the gamma-ray beam covers a broad solid angle. This behaviour favors the outer

magnetospheric emission models, in particular the OG and the SG models (see Section 3.2.5) (Abdo et al., 2009). Detecting new pulsars in the VHE range is essential in order to understand the physics of particle acceleration and the pulsar evolution.

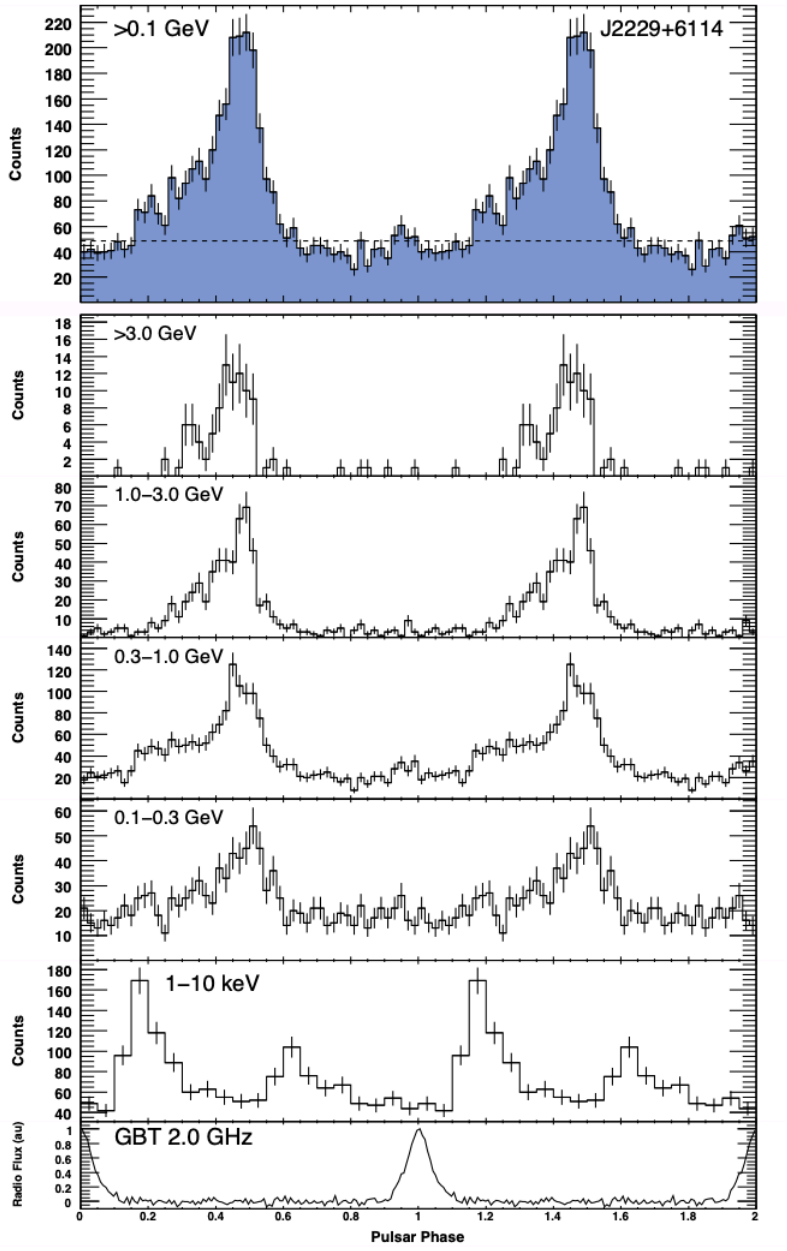

Figure 4.4 **Top panel**: light curve of PSR J2229+6114 above 0.1 GeV showing two pulse periods with 50 bins per period. The dashed line shows the background level, estimated from an annulus surrounding the pulsar position during the off-pulse phase. **Four subsequent panels:** energy dependent phase histograms for PSR J2229+6114 in the four indicated energy ranges, each displayed with 50 bins per pulse period. **Second panel from the bottom:** light curve in the 1–10 keV band from the *XMM* satellite. The highest peak of the X-ray profile lags the radio pulse by $\varphi = 0.17 \pm 0.02$. **Bottom panel:** radio pulse profile from Green Bank Telescope (GBT) at a center frequency of 2 GHz with 128 phase bins. Plot from Abdo et al. (2009).

Timing Irregularities

The rotation of J2229, as all the young pulsars, suffers from glitches and timing noise. In particular, timing noise refers to unexpected and unmodelled features in the timing residuals relative to a simple slowdown model. On the other hand, glitches are moderate changes in the pulsar rotation rate, often followed by a relaxation and are interpreted to be the result of a rapid transfer of angular momentum between the inner superfluid and the outer crust of the NS (Espinoza et al., 2011). Through the study of glitches it is possible to investigate the interior of a NS (including moments of inertia of the superfluid regions) and the properties of matter at supernuclear density. The glitch is characterized by a sharp cusp-like shape (see Figure 4.5) and it is thought to be originated by angular exchange through collective vortex unpinning events induced when the angular velocity lag between the superfluid and the crustal normal matter exceeds a critical threshold.

Gügercinoğlu et al. (2020) analyzed the time solution of J2229 using data between September 2008 and January 2020 and in this period the source glitched seven times. From this analysis they determined a breaking index n=2.63.

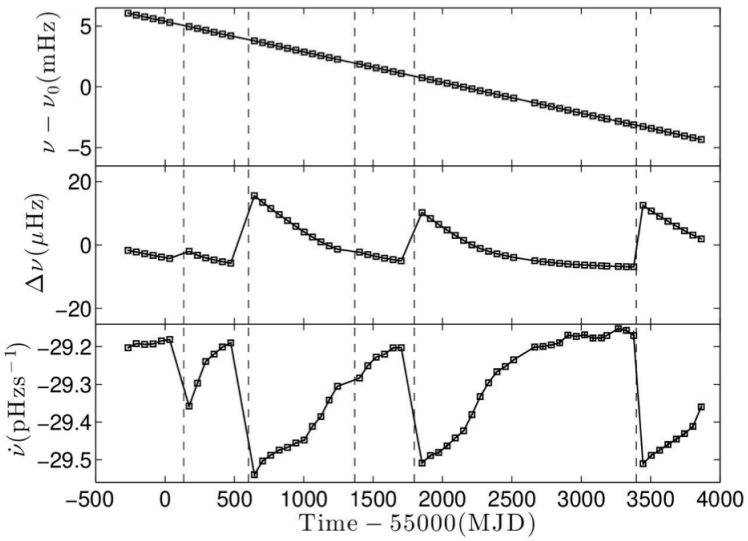

Figure 4.5 The spin evolution of PSR J2229+6114 in the range MJD 54732-58865 (September 2008-January 2020). The **top panel** shows the frequency evolution with respect to fidicual value ν_0=19.36 Hz obtained in the analysis of Gügercinoğlu et al. (2020). The **middle panel** shows the pulse-frequency residuals $\Delta\nu$, obtained by subtraction of the pre-glitch timing solution. The **bottom panel** shows the variation of the spin-down rate. The glitch epoches are indicated by vertical dashed lines. Figure from Gügercinoğlu et al. (2020).

4.2 Observations with MAGIC

Let us introduce the MAGIC data set of the J2229 and the non-standard analysis performed due to the trigger system used for data taking.

4.2.1 Data Sample and Analysis Procedure

For the MAGIC telescopes, PSR J2229+6114 is observable from July up to November at zenith angles below 40°. The observation campaign of the pulsar covers the period between 18 October 2019 to 28 November 2019 (Cycle 15) for about 28 hours. All the data were taken using the low-energy threshold Sum-Trigger-II system (Dazzi et al., 2021), described in Section 2.2.1.7, and in a zenith angle range between 5° and 40°. In order to exclude data affected by adverse weather conditions or technical problems, I used information and measurements of the LIDAR system and the Cloudiness parameter (see Section 2.2.1.8). For a more detailed check I looked also into the pertinent runs and logbooks of each observation night provided after each night of data taking; for this reason I selected only data that reported LIDAR transmission values higher than 0.8 measured from 9 km above the telescopes. These selection criteria resulted in about 19 hours of good quality data that I used for the later analysis. The whole data set belongs to the same analysis period, namely `ST_03_07_SUMT`[¶], and all the data were taken in *wobble-mode* (Fomin et al., 1994) pointing at four different positions situated 0.4° away from the source in order to evaluate the background simultaneously with the pulsar's observations (see Section 2.2.3.2).

The data were processed using the standard MAGIC analysis package MARS (Zanin et al., 2013) and a detailed description of the MAGIC analysis chain can be found in Section 2.2.4.1. The resulting images were cleaned using the Sum-Trigger-II system cleaning algorithm (the *MaTaJu* cleaning, see Section 2.2.8.3). The cleaned shower images were then parametrized using an extended version of the Hillas parameters (Hillas, 1984) and, in order to separate hadronic from gamma-induced air showers, the RF technique is applied and a *Hadronness* parameter is assigned to each event. As described in section 2.2.6, the stereo data rely on LUTs for the energy reconstruction, which are obtained from the MC simulations corresponding to the dedicated analysis period. To estimate the arrival direction of the events the DISP RF method is used: the DISP parameters are obtained separately for each telescope by a RF and then combined in

[¶] For the naming convention see Section 2.2.5.1

the stereoscopic image to compute the reconstructed source position. The angular distance between the reconstructed arrival direction and the assumed source position is defined as θ.

The last step of the pulsar data analysis is the assignment of a pulse phase to each event and to do this I used the `Tempo2` package (see Section 2.2.8.2). The ephemeris used was provided by the *Fermi*-LAT collaboration for contemporaneous data and tested on the satellite's data. As the VHE signal form the pulsar is expected to be weak and standard cuts are not optimized for detecting weak sources, the cut values are determined by fixing their efficiency to 75% for the θ^2 and 90% for the *Hadronness* parameter; the size cuts in both telescopes was settled at 20 phe. Figure 4.6 shows the distribution of the gamma-ray events surviving the analysis cuts applied for J2229 (reported in Table 4.3) and this yields an energy threshold of 38 GeV. The spectral index applied to the pulsar was Γ=4 and it was derived from a preliminary *Fermi*-LAT analysis using 10 years of data.

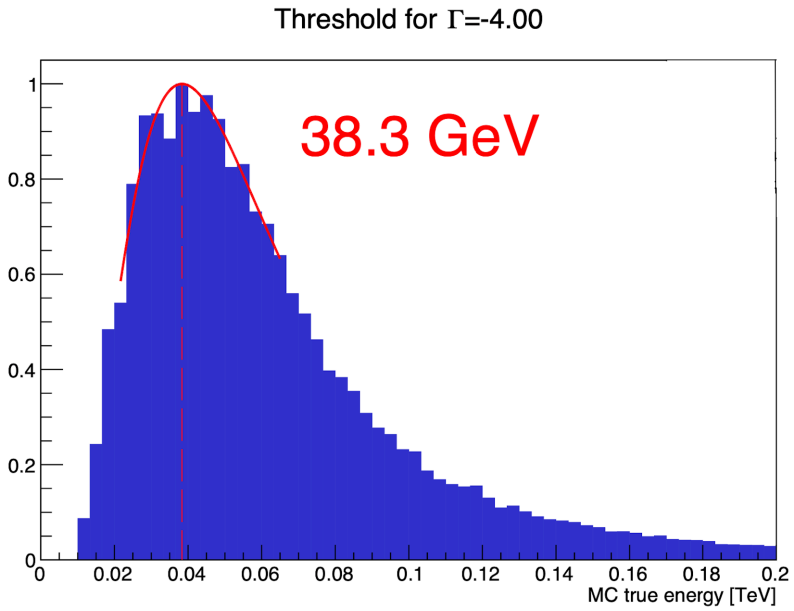

Figure 4.6 The gaussian fit to the true energy distribution, in logarithmic space, yields an energy threshold of about 38 GeV (red dashed line). This energy is obtained after having applied, in the Zd range between 5° and 40°, a cut of 20 phe and hadronness and θ^2 cuts given by efficiencies from MC.

4.2.2 Energy Spectrum

Figure 4.7 shows the SED of J2229, including MAGIC data. The *Fermi*-LAT data are taken from 2PC (Abdo et al., 2013). The numerical values are reported in Table 4.1 and Table 4.2. The MAGIC differential ULs of the source are well fitted by a power-law function $d\Phi/dE = f_0(E/150\ \mathrm{GeV})^{-\Gamma}$ with $f_0 = 1.1\times10^{-11}$ cm^{-2} s^{-1} and Γ=4. The

2PC spectrum follows a power-law with an exponential cut-off model: $dN/dE = \mathrm{K}\,(\mathrm{E}/\mathrm{E}_0)^{-\Gamma}\,\exp(-\mathrm{E}/\mathrm{E}_{cut})^{b}$, with the prefactor K=1.66$\times 10^{-10}$ ph cm^{-2} s^{-1} MeV^{-1}, the energy scale E_0 = 0.54 GeV, Γ=(1.8$\pm$0.1), the cut-off energy E_{cut} =(4.3$\pm$0.3) GeV and the exponential index b=1 (Abdo et al., 2013).

Table 4.3 summarizes the resulting cuts efficiencies. These optimized cuts are used to extract the events for the pulsar light curves presented in the next Section.

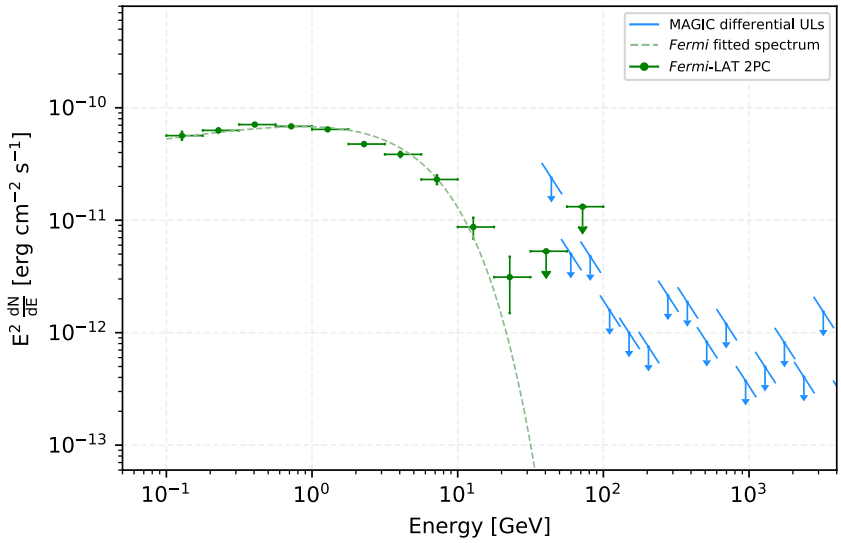

Figure 4.7 J2229 spectral energy distribution in the range between 38 GeV and 50 TeV. Blue arrows are the VHE ULs reported in this work. Green arrows and points are the data from the *Fermi*-LAT 2PC Abdo et al. (2013). The green dashed line represents the power-law with exponential cut-off model of 2PC.

4.2.3 Pulsar Light Curve

Figure 4.8 shows the pulsar light curves in three different energy ranges: from 38 GeV to 100 GeV, between 100 and 500 GeV and above 500 GeV, after having applied the signal extraction cuts reported in Table 4.3. The value of the minimum energy is the energy threshold calculated as explained before. Equation 17 in Li & Ma (1983) (see Section 2.2.6.3) was used to evaluate the significance of the signal; the on-pulse and off-pulse intervals were chosen *a priori* following the preliminary analysis of *Fermi*-LAT. The on-pulse phase corresponds to the interval [0.4-0.55]; the off-pulse phase to the interval [0.0-0.4]$\cup$[0.55-1.0]. No significant pulsed signal was found (see Table 4.4). Moreover, region-independent signal tests (H-test and Z^2 (de Jager et al., 1989), see Section 3.3 for details) was calculated, also with null

Energy Range [GeV]	Bin Center [GeV]	MAGIC Flux $E^2\, dN/dEdAdt$ [TeV cm^{-2} s^{-1}] $\times 10^{-13}$
38.00-51.66	43.96	<148.63
51.66-70.22	59.76	<313.21
70.22-95.45	81.23	<29.76
95.45-129.75	110.43	< 9.88
129.75-176.38	150.11	<6.23
176.38-239.76	204.05	<4.67
239.76-325.92	277.38	<13.35
325.92-443.05	377.0	<11.67
443.05-602.26	512.56	<5.15
602.26-818.69	696.76	<7.46
818.69-1112.88	947.14	<2.33
1112.88-1512.81	1287.50	<3.10
1512.81-2056.4	1750.18	<5.08
2056.44-2795.4	2379.12	<2.52
2795.44-3800	3234.07	<9.58
3800-5165.5	4396.26	<1.73
7021.83-9545.17	8123.62	<2.87
9545.17-12975.29	11042.90	<3.51
12975.29-17638.04	15011.24	<5.68

Table 4.1 Boomerang Pulsar ULs of the MAGIC measurements shown in Figure 4.7.

result (see Table 4.4).

Energy Range [GeV]	Bin Center [GeV]	2PC Flux $E^2\, dN/dEdAdt$ [erg cm^{-2} s^{-1}] $\times 10^{-12}$
0.10-0.18	0.13	(56.53±4.76)
0.19-0.32	0.23	(62.94±2.56)
0.32-0.56	0.41	(70.90±1.99)
0.56-1.00	0.72	(68.37±1.87)
1.00-1.78	1.28	(64.23±1.93)
1.78-3.16	2.28	(47.57±1.95)
3.16-5.62	4.05	(38.52±2.15)
5.62-10.00	7.20	(23.04±2.16)
10.00-17.78	12.80	(87.01±1.84)
17.78-31.62	22.76	(31.17±1.63)
31.62-56.23	40.48	<52.96
56.23-100.00	71.99	<13.19

Table 4.2 Boomerang Pulsar flux points and ULs of the *Fermi*-LAT 2PC data shown in Figure 4.7.

E_{min} [GeV]	E_{max} [GeV]	θ^2 [deg^2]	Hadronness
38.00	51.66	0.13	0.66
51.66	70.22	0.10	0.52
70.22	95.45	0.08	0.48
95.45	129.75	0.06	0.50
129.75	176.38	0.05	0.52
176.38	239.76	0.04	0.52
239.76	325.92	0.03	0.51
325.92	443.05	0.02	0.48
443.05	602.26	0.02	0.46
602.26	818.69	0.02	0.42
818.69	1112.88	0.02	0.39
1112.88	1512.81	0.02	0.34
1512.81	2056.44	0.01	0.30
2056.44	2795.44	0.01	0.27
2795.44	3800.00	0.01	0.24
3800.00	5165.55	0.01	0.23
5165.55	7021.83	0.01	0.23
7021.83	9545.17	0.01	0.24
9545.17	12975.29	0.01	0.27
12975.29	17638.04	0.01	0.31
17638.04	23976.38	0.01	0.41
23976.38	32592.44	0.01	0.45
32592.44	44304.75	0.02	0.37

Table 4.3 Energy-dependent θ^2 and hadronness cuts computed with `flute` for the Boomerang pulsar MAGIC analysis.

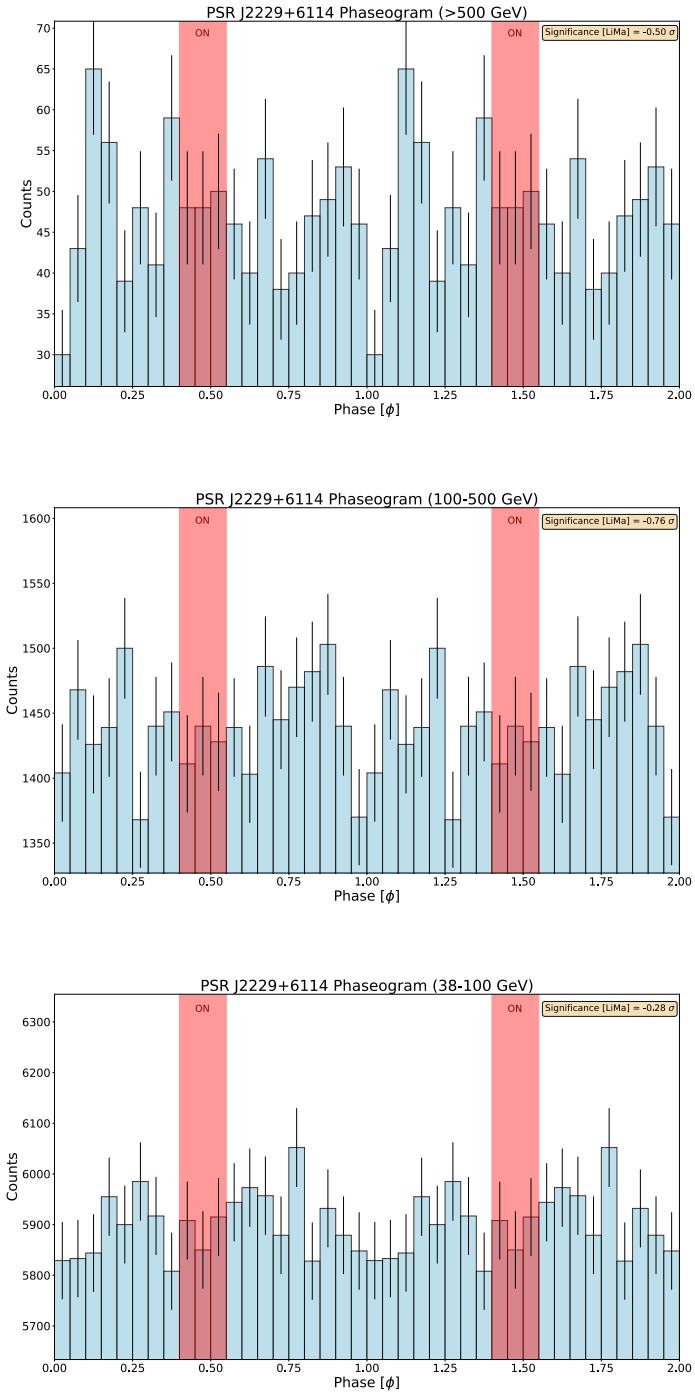

Figure 4.8 Phaseograms of the Boomerang pulsar for three different energy ranges: above 500 GeV (top panel), 100-500 GeV (middle panel), 38-100 GeV (bottom panel). The phaseograms contains about 19 hours of MAGIC data. Two cycles are shown for clarity. The grey area denotes the ON signal phase region. No significant pulsation is detected (see Table 4.4).

Energy Range	Test
[GeV]	Li&Ma
38 - 100	-0.28σ
100 - 500	-0.81σ
>500	-0.50σ

Table 4.4 MAGIC Pulsed emission Signal Tests' Result for J2229.

4.3 Conclusions

The analysis of MAGIC data from the pulsar J2229 shows, unfortunately, no significant signal detection. Although this source is detected up to 20 GeV in the *Fermi*-LAT energy range (2PC), the non detection by MAGIC could be due to various reasons. Since the source was not detected, we computed upper limit, as reported in Table 4.1. Assuming a spectrum similar to the one preliminary one calculated with *Fermi*-LAT data, an observed photon index of 4 was adopted for the upper limit calculations.

A non-detection could be explained in different way: a low target photon field or, for example, the instrument sensitivity limit. The scenario of a low target photon medium can decrease the IC interaction opportunities. Another explanation can be that pulsars with small viewing angles or small magnetic inclination angles are often not expected to produce detectable gamma-ray emission, either because of their emission beams not crossing the line of sight to the Earth or as a result of weak modulation in the emission and this makes them difficult to detect (Guillemot & Tauris, 2014). For the particular case of the OG model, the gamma-ray detectability is determined by the combination of the magnetic inclination angle and the viewing angle. Guillemot & Tauris (2014) found that MSPs that are non-detected in gamma-rays tend to have smaller viewing angles in general. The presence of the observed spectral cut-off can be explained by the magnetic pair-production or the photon-photon absorption that could prevent VHE photons to escape from the system. In conclusion, finding new pulsars in the VHE is extremely crucial to help us progress in the understanding of the physics at the place of the particles acceleration and the evolution of pulsars.

5

The Millisecond Pulsar PSR J0218+4232

PSR J0218+4232 is a MSP and it is one of the best candidates for very high-energy gamma-ray emission thanks to the high magnetic field strength at the light-cylinder radius ($B_{LC} \sim 3.2 \times 10^5$ G). It was one of the first MSPs detected by *Fermi*-LAT at high energy. For the study presented in this chapter, 11.5 years of *Fermi*-LAT data and about 90 hours of MAGIC stereoscopic observations, collected from November 2018 and November 2019, were analyzed in order to search for pulsed or unpulsed emission from the MSP. This work led to the scientific publication *"Search for Very High-Energy Emission from the millisecond pulsar PSR J0218+4232"*, in The Astrophysical Journal Acciari et al. (2021), where I played a central role in the data analysis, group organization and writing of the article.

5.1 The Source

PSR J0218+4232 (hereafter J0218) is a MSP with a period of 2.3 ms in a two-day orbit around a helium low mass (∼0.2 $M_{\odot}$) white dwarf companion (Bassa et al., 2003). It was discovered by Navarro et al. (1995) as a steep spectrum, highly polarized and a compact radio source during a low-frequency radio study of the unrelated radio SN 1986J. Its broad radio peak has a large unpulsed component ($\sim$ 50%) and this makes it unusual, suggesting that the MSP may be an *aligned rotator*, a pulsar in which the magnetic field is aligned with the axis of rotation. This was later supported by polarimetric radio studies (Stairs et al., 1999).

J0218 is one of the youngest and most energetic MSPs known with a characteristic age of τ <0.5 Gyr and a spindown power of 2.4×10^{35} erg s^{-1}. The magnetic field at the light cylinder is extremely intense ($B_{LC} \sim 3.2 \times 10^5$ G) and only slightly weaker than young Crab-like pulsars (Saito et al., 1997). The determination of its distance has been under debate, Du et al. (2014) estimated a distance of 6.3 kpc and these results were significant because they made J0218 by far the most luminous gamma-ray pulsar. Subsequent measures of the parallax with the Very Long Baseline Interferometry (VLBI) determined a distance of 3.15 kpc, which is comparable to values obtained for the rest of the MSP population (Verbiest & Lorimer, 2014). Table 5.1 provides a summary of the main properties of J0218.

J0218 was detected as a steady source of soft X-rays (0.1-2.4 keV) and gamma-rays (above 100 MeV) with the High Resolution Imager (HRI) of *ROSAT* and *EGRET*, respectively (Verbunt et al., 1996). In particular, the MSP showed a pulsed X-ray emission (with a significance of about 5σ) with a Crab-like double-pulse profile (Kuiper et al., 1998). The profile is characterized by a sharp main pulse with an indication of a second peak at a phase separation of $\Delta\varphi \sim$ 0.47. Thereafter, Mineo et al. (2000) reported for the first time temporal and spectral emission properties of J0218 in the broad band 1–10 keV obtained with the satellite *BeppoSAX*. Follow-up investigations have also been conducted with *Chandra*, in the energy range between 0.08–10 keV (Kuiper et al., 2002), and *XMM-Newton* between 0.2–10.0 keV (Webb et al., 2004), which confirmed that the two sharp pulses are described by a hard non-thermal spectrum. From these observations they confirmed the previously detected pulsations of J0218 and showed that the folded light curve depends on energy. Figure 5.1 shows the comparison of the J0218 X-ray profile in absolute phase with the radio and gamma-ray profiles. Within the uncertainties of each of the measurements, the X-ray pulses are aligned with two of the three radio pulses at 610 MHz and with the gamma-ray pulses. Kuiper et al. (2003) and Deneva et al. (2019) reported high-resolution spatial and timing observations of J0218 performed with the Rossi X-ray Timing Explorer

Table 5.1 Timing ephemeris for PSR J0218+4232, obtained with the Nançay radio telescope. We used the DE436 Solar System ephemeris, with time units in barycentric dynamic time (TDB). We use the ELL1 binary model for low eccentricity orbits, where EPS1 and EPS2 represent the first and second Laplace-Lagrange parameters (Lange et al., 2001). For the detailed definition of all parameters included in the timing model, please read the `Tempo2` manual (Hobbs et al., 2006b).

Timing and binary parameters	
R.A., α (J2000.0)	$02^{h}\,18^{m}\,06.35863(1)^{s}$
Decl., δ (J2000.0)	$+42^{\circ}32'17.3722(2)''$
Frequency, $F0$ (Hz)	430.461059981036121O6(6)
1st frequency derivative, $F1$, (Hz s^{-1})	$-1.434128(1) \times 10^{-14}$
PMRA ($\dot{\alpha}/cos\delta$, mas yr^{-1})	5.32(3)
PMDEC ($\dot{\delta}$, mas yr^{-1})	-3.68(6)
PEPOCH (MJD)	56000
POSEPOCH (MJD)	56000
DMEPOCH (MJD)	56000
DM (cm^3 pc)	61.2374(7)
DM1 (cm^3 pc s^{-1})	-0.0004(2)
BINARY MODEL	ELL1
PB (d)	2.0288460845(6)
A1 (lt-s)	1.9844348(2)
TASC (MJD)	49148.5799767(2)
EPS1	$5.0(2)\times10^{-6}$
EPS2	$4.9(2)\times10^{-6}$
START (MJD)	53579.2
FINISH (MJD)	58960.5
UNITS	TDB (Barycentric Dynamical Time)
EPHEM	DE436
Derived parameters	
Period, P (ms)	2.32309053
1st period derivative, $\dot{P}$ ($s\,s^{-1}$)	7.739×10^{-20}
Characteristic age, τ_c (yr)	4.8×10^{8}
Spin-down power, $\dot{E}$ (erg s^{-1})	2.4×10^{35}
Surface B-field strength, B_S (G)	4.3×10^{8}
Light-cylinder B-field, B_{LC} (G)	3.1×10^{5}
Distance, d (kpc)	$3.15^{+0.85}_{-0.60}$
ON pulse region	(0.34–0.98)
OFF pulse region	[0,0.34)$\cup$(0.98,1]

(RXTE) (at energies above 10 keV) and *NICER* (at energies between 0.2 keV and 12 keV), respectively. J0218 was also observed with the *Nuclear, Spectroscopic Telescope Array* (*NuSTAR*) satellite, in the hard X-ray range 3–79 keV (Gotthelf & Bogdanov, 2017). They detected a hard X-ray pulse profile with a resolution down to 15 μs and for the first time a pulsed emission up to 25 keV. Rowan et al. (2020) performed X-ray observations with *NICER* (in the energy range: 0.2-12 keV) and they found that the separation between pulse components of J0218 decreases with the increasing of the energy. The pulse profile is reported in Figure 5.2.

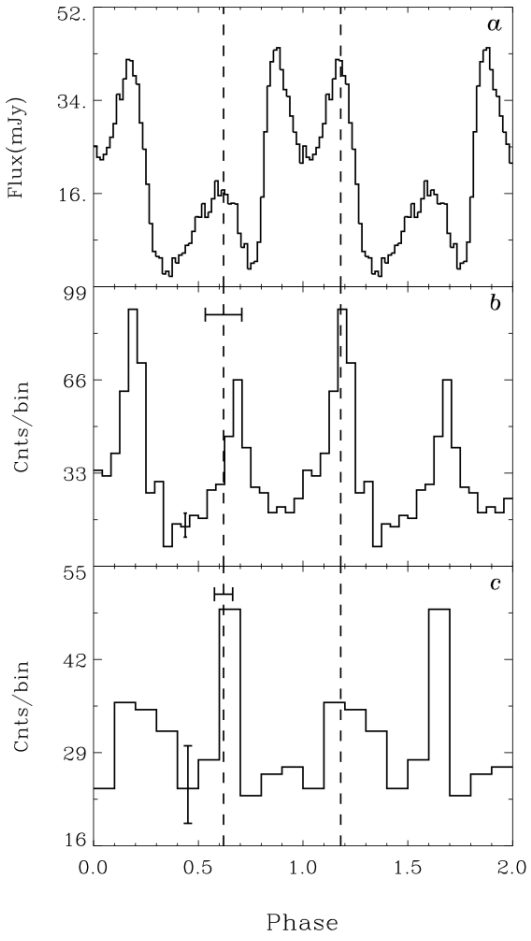

Figure 5.1 Multiwavelength pulse profiles of J0218 in absolute phase. (*a*) Radio pulse profile at 610 MHz. (*b*) *Chandra* X-ray pulse profile (0.08–10 keV). (*c*) EGRET gamma-ray pulse profile (0.1–1 GeV). The absolute timing accuracies of the X-ray and gamma-ray profiles are shown as horizontal bars centered on phase 0.62. The dotted lines indicate the positions of the two pulses in the 610 MHz radio profile that coincide with the high-energy pulses. Figure from Kuiper et al. (2002).

The source J0218 is very close to one of the most famous TeV blazars, 3C 66A (0.97° separation, see Figure 5.3), and for this its gamma-ray emission has been often confused with it. 3C 66A is classified as an intermediate-frequency-peaked BL Lac object and its low-energy component extends from radio to soft X-rays with a peak in the optical band.

The blazar 3C 66A was associated with the source 2EG J0220+4228 of the Second EGRET Catalog (Thompson et al., 1995, 2EG) and in the third EGRET Catalog (Hartman et al., 1999, 3EG) 3EG J0222+4253 was identified with the blazar on its emission above 1 GeV. Looking to Figure 5.4 it is possible to see that 3C 66A is the evident counterpart for the 1-10 GeV window, whereas J0218 is the most likely counterpart for the 100-300 MeV energy range. Between 300 and 1000 MeV both sources contribute to the excess. Furthermore, Kuiper et al. (2000) reported marginal evidence

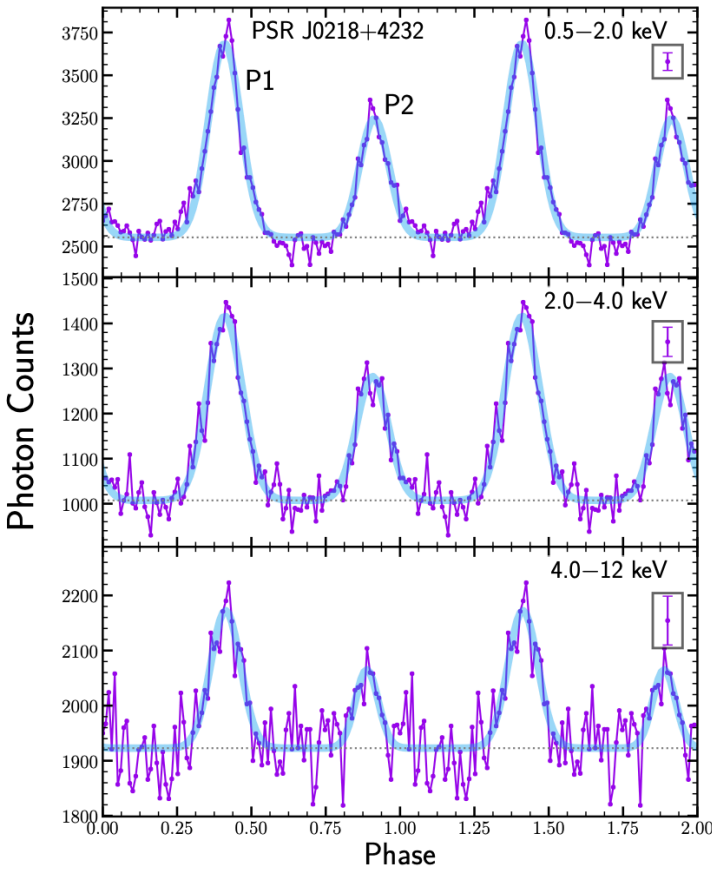

Figure 5.2 Phase folded pulse profile for J0218 with 100 phase bins obtained with *NICER*. The boxed point shows the characteristic error bar for each profile. Plot from Rowan et al. (2020).

(about 3.5σ) for the detection of pulsed gamma-ray emission from J0218, making it potentially the first MSP detected at these energies.

Only with the launch of the Large Area Telescope (LAT) (Atwood et al., 2009), the primary instrument on the *Fermi* satellite, it was possible to identify that next to the blazar 3C 66A there was a strong source (with a significance higher than 19σ) reported in the First *Fermi*-LAT Catalog: 1FGL J0218.1+4232 (Abdo et al., 2010b). The certain detection of GeV gamma-ray pulsations confirmed the identification of the source with the MSP J0218 (Abdo et al., 2010c). The LAT pulse profile showed a broad single-peaked gamma-ray light curve, like the EGRET one reported by Kuiper et al. (2000) or the double-peaked X-ray pulse profile showed in Kuiper et al. (2002) and Webb et al. (2004).

J0218 was identified with hints of pulsed emission above 10 GeV (Ackermann et al., 2013), and the Third Catalog of Hard *Fermi*-LAT Sources (Ajello et al., 2017, 3FHL) contained a source associated with J0218 (3FHL J0218.3+4230)

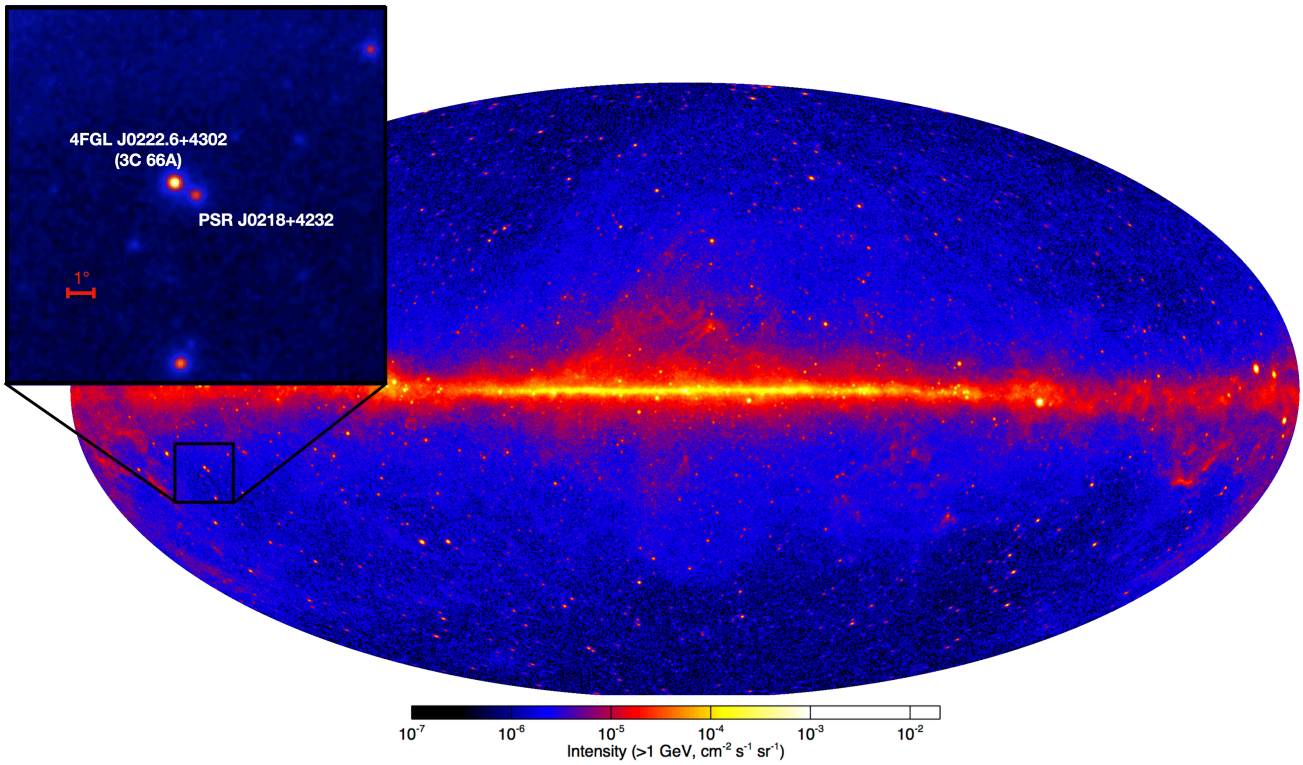

Figure 5.3 *Fermi*-LAT all-sky map showing location of J0218. The background map shows the 12-year (August 4, 2008 - August 4, 2020) all-sky intensity map, generated using gamma-ray data above 1 GeV, in Galactic coordinates. The square inset region shows the $15^\circ \times 15^\circ$ counts map centered on J0218, generated with the 11.5 years of data analyzed in this work (from 2008 August 4 to 2020 February 10), using all events above 1 GeV. Note the bright gamma-ray blazar 3C 66A (4FGL J0222.6+4302) located less than one degree away from J0218.

which exhibited pulsations above 10 GeV, and even above 25 GeV (Saz Parkinson et al., 2017), despite the limited statistics due to the small effective area of the LAT at these energies, compared to ground-based gamma-ray telescopes. In particular, the sensitivity of these telescopes, like MAGIC, depends on their large effective area and on their ability to reject the cosmic-ray background. Given the challenges of performing background rejection with MAGIC in the 10-100 GeV range, it is not surprising that MAGIC is less sensitive than *Fermi*-LAT at these energies, despite its much larger effective area. All these *Fermi* preliminary results provided strong motivations for observing the source at higher energies using ground-based gamma-ray telescopes.

The MSP J0218 was observed in October 2004 during the commissioning phase (mono observations with MAGIC-1) of MAGIC telescopes for a total of 13 hours. J0218 was in the same field of view of the BL Lac 3C 66A (Oña-Wilhemi

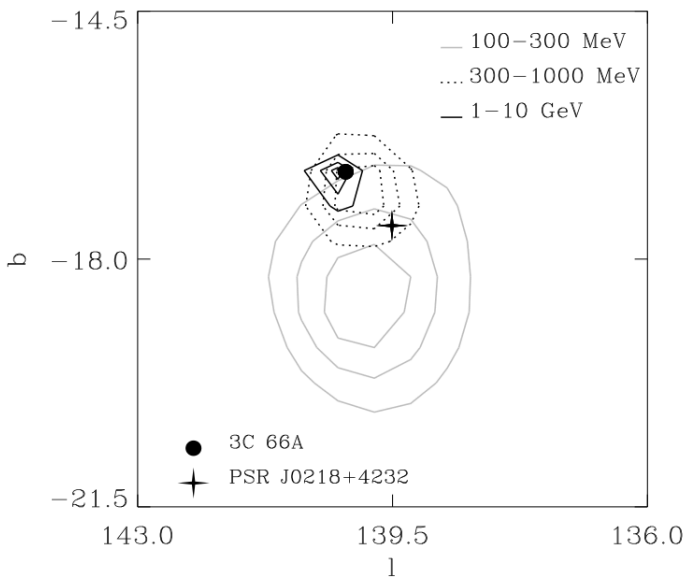

Figure 5.4 1,2 and 3σ location confidence contours of gamma-ray source 2EG J0220+4228 in three different broad energy intervals. Between 100-300 MeV 3C 66A is located outside the 3σ contour, whereas between 1-10 GeV this is the case for J0218. Plot from Kuiper et al. (2000).

et al., 2005). Later, J0218 was observed again for 20 hours, between October 2006 and January 2007, but no emission was detected, and a 3σ flux upper limit of $< 9.4 \times 10^{-12}$ cm^{-2} s^{-1} was obtained above an energy threshold of 140 GeV (Anderhub et al., 2010). This non-detection of J0218 was consistent with some of the theoretical gamma-ray model predictions (Harding et al., 2005) and the possible pulsed TeV predicted emission seemed to be below the MAGIC sensitivity in the explored energy range. Since then, the MAGIC telescopes performance has significantly improved (Aleksić et al., 2016a).

5.2 Observations with *Fermi*-LAT

5.2.1 Data Sample and Analysis Procedure

For the *Fermi*-LAT analysis 11.5 years of Pass 8 data are used (Atwood et al., 2013; Bruel et al., 2018) from 2008 August 4 to 2020 February 10 (MJD 54682.7 - 58890). In order to select the events in an energy range from 100 MeV to 870 GeV and in a square region of $15^\circ \times 15^\circ$, centered on the position of 4FGL J0218.1+4232 (RA=34.53440, DEC=42.54590), the python package `Fermipy` was used (Wood et al., 2017). Events with zenith angles larger than 900 have been excluded from the analysis, in order to avoid contaminations from the Earth albedo gamma-rays. We further

ensured the selection only included events at times where the LAT was in normal science configuration and taking good data.

We report in Figure 5.3 the *Fermi*-LAT all-sky gamma-ray intensity map for energies >1 GeV, highlighting the region around J0218; it is also shown the blazar 3C 66A, located at 97° from J0218 and its gamma-ray counterpart (4FGL J0222.6+4302) which has a flux, above 1 GeV, of 1.6×10^{-8} cm^{-2} s^{-1} ($> 160\sigma$) in 4FGL, compared to 5.2×10^{-9} cm^{-2} s^{-1} (73.5σ) for J0218. For the analysis of J0218 the *flaring* periods of 3C 66A were excluded, due to the fact that blazars are variable sources; this strategy was not useful because during the entire period of 11.5 years of the observations the blazar was quite active, as it is possible to see from the *Fermi*-LAT light curves of J0218 and 3C 66A in Figure 5.5. In Figure 5.6 it is possible to see the zoom of the 1 year period covered by the MAGIC observations, showing that, at GeV energies, 3C 66A is brighter than J0218.

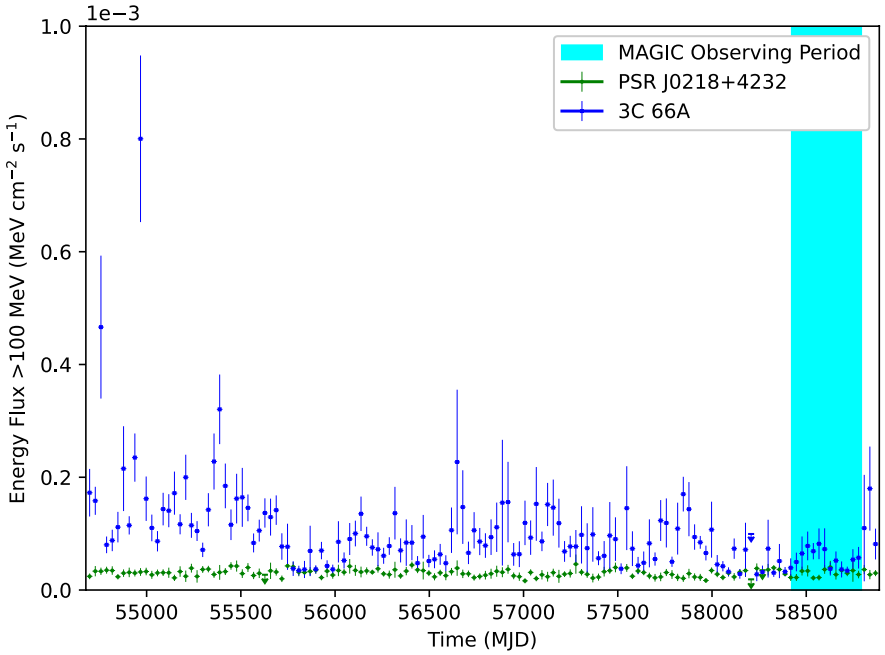

Figure 5.5 Light curve showing J0218 (green circles) and 3C 66A (blue squares). The LAT data ranges from 2008 August 4 to 2020 February 10 (MJD 54682.7 - 58890), and covers the 100 MeV - 870 GeV energy bands. The time period of MAGIC observations (MJD 58424 - 58791) is shown in cyan. Note the larger variability and gamma-ray flux of 3C 66A. To generate this plot, background sources were fixed to the value in the region model, and the normalizations of 3C 66A and J0218 were allowed to vary.

The data were analyzed with a binned likelihood analysis using spatial bins of 0.1°× 0.1° and eight logarithmically

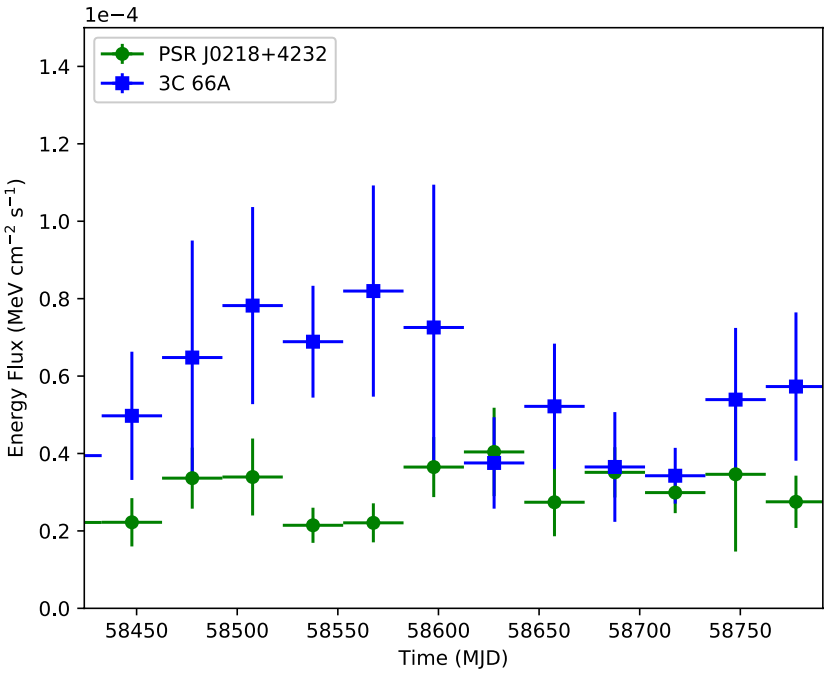

Figure 5.6 *Fermi*-LAT light curve showing J0218 (green circles) and 3C 66A (blue squares) zoomed in on the time period of MAGIC observations (MJD 58424 - 58791). Note that 3C 66A has a significantly larger flux than J0218 most of the time.

spaced bins per decade of energy. The initial region model was selected from the 8-year of the *Fermi*-LAT Fourth Source Catalog (Abdollahi et al., 2020, 4FGL) by including sources located in a square area of $40^\circ \times 40^\circ$ centered on 4FGL J0218.1+4232. *Fermi*-LAT does not measure the energy of the photons with infinite precision. For Pass 8, the energy resolution is $<10\%$ between 1 GeV and 100 GeV, about $\sim$20% at 100 MeV, and $\sim$28% at 30 MeV and for this the LAT measures only the energy of photons with finite resolution[*]. As a consequence, as recommended by the *Fermi* Science Support Center (FSSC), a correction for this energy dispersion must be applied to all sources (except the isotropic diffuse emission). This dispersion correction is applied during the fitting of the model and two energy bins are added above and below the analysis energy range, and filled with a number of photons that is extrapolated from the existing model. The number of photons in each energy bin is then scaled by a factor relating to the instrument response functions, in order to account for the possibility photons with sufficiently large energy uncertainty may have a true energy that lies in a neighboring energy bin. The fitting of the source spectra in the region model is carried out in a iterative process and the sources with a TS below 10 are removed from the model. The TS in this case is defined as

[*] https://www.slac.stanford.edu/exp/glast/groups/canda/lat_Performance.htm

TS=$-2\ln(\mathcal{L}_0/\mathcal{L}_1)$ where $\mathcal{L}_1$ is the probability that a model which includes the source of interest matches the data and $\mathcal{L}_0$ is the probability that the same model without the source of interest matches the data[†]. The tool `Minuit` was used to perform the final iteration of the fit and through it the minimum value of a multi-parameter function is found and it used to analyze the shape of the function around the minimum (James, 1994). In addition to the spectral parameters of J0218, the normalization and index of the Galactic diffuse emission (modeled with a power-law spectrum), the normalization of the isotropic diffuse emission, and the normalizations of background sources with a TS of at least 100 were allowed to vary.

The MSP J0218 was modeled with a power-law with an exponential cut-off: $\frac{dN}{dE} = N_0(\frac{E}{E_0})^{\gamma}\exp(-aE^b)$, where the exponential index b was fixed to a "sub-exponential" value of 2/3 because this source is too faint for it to be left free and 2/3 approximates the values of other brighter pulsars (Abdollahi et al., 2020). In Table 5.2 we report the gamma-ray spectral parameters for J0218.

Table 5.2 Gamma-ray spectral parameters for the total emission from PSR J0218+4232. Photon and energy flux cover the entire 100 MeV - 870 GeV energy range.

Parameter	Value
N_0 (ph cm^{-2} s^{-1} MeV^{-1}).....	$(2.07 \pm 0.03) \times 10^{-11}$
γ	-1.76 ± 0.01
E_0 (MeV)	821.6 (fixed)
a	$(6.19751 \pm 0.00007) \times 10^{-3}$
b	0.6667 (fixed)
Photon flux (photons cm^{-2} s^{-1})	$(7.67 \pm 0.15) \times 10^{-8}$
Energy flux (MeV cm^{-2} s^{-1}) ...	$(3.05 \pm 0.04) \times 10^{-5}$

The events in a region of 5°, centered in J0218, were considered in order to understand if they are originated from the MSP or the blazar 3C 66A; the tool `gtsrcprob` was used to assign to these events a probability (*weight*) and discriminate to which source of the model they belong. Then, the pulsar timing software package `TEMPO2` was used to assign the pulsar rotational phases φ_i to the events (Hobbs et al., 2006a) using the pulsar ephemeris obtained with the Nançay radio telescope, given in Table 5.1.

The region model mentioned before was used to calculate the source spectrum and the flux points for the theoretical modeling described in Section 5.4. Three energy bins between 12.38 - 28.99 GeV were combined in order to produce a flux point instead of an upper limit, and, in order to extract the overall spectrum of J0218, the normalization of the

[†] https://fermi.gsfc.nasa.gov/ssc/data/analysis/documentation/Cicerone/Ciceroe_Likelihood/Likelihood_overview.html

isotropic and Galactic diffuse emission components were allowed to vary while `Minuit` fit the spectral parameters (summarized in Table 5.2). To generate flux points, the index of the Galactic diffuse emission was also allowed to vary, along with the normalizations of background sources with a TS of at least 500 or which lie within 5° of 4FGL J0218.1+4232. The spectrum of J0218 is replaced by a power-law with an index of -2, and `Minuit` is used to fit the normalization of this modified spectrum within each energy bin. The result is interpreted as either a flux point or an upper limit, depending on the significance with which the power-law source was detected.

5.2.2 Spectral Energy Distribution

In Figure 5.7 the *Fermi*-LAT spectrum of this analysis is reported and Table 5.2 reports the best-fit spectral parameter and Table 5.3 shows the spectral values and upper limits. It is possible to note that the spectrum falls steeply at energies above 10 GeV and that above 20 GeV there are only upper limits. These results are consistent with previous LAT results reported in 4FGL (Abdollahi et al., 2020) and 3FHL (Ajello et al., 2017) and in particular the latter reported an index of $\Gamma = -4.5$ when fitting the >10 GeV data with a simple power-law.

5.2.3 Light Curve

An analysis similar to that done in the First *Fermi*-LAT Catalog of >10 GeV sources (Ackermann et al., 2013, 1FHL) and in Saz Parkinson et al. (2017) was performed in order to test for a possible emission above 10 GeV. A *low-energy* Probability Density Function (PDF) was defined, PDF_{LE}, and it is based on the best estimate fit of the 1-10 GeV events (see Figure 5.8, top panel). For the *high-energy* PDF, PDF_{HE}, the family of distributions given by $\mathrm{PDF}_{HE}(\varphi) = (1-x) + x{\cdot}\mathrm{PDF}_{LE}(\varphi)$, with $0 \leq x \leq 1$, was considered. The maximum of the unbinned likelihood function derived from this PDF, with respect to x, was calculated; in this way the $\mathcal{L}(\hat{x})$ was obtained and it was compared to the null hypothesis, for x=0, that means that there is no pulsation, i.e. $\mathrm{PDF}_{HE}(\varphi)$=1. By construction, $\mathcal{L}(0) = 1$, so the test statistic (TS=$-2\ln(\mathcal{L}(0)/\mathcal{L}(\hat{x}))$ can be simplified to TS = $2\ln\mathcal{L}(\hat{x})$. Following the Wilks' theorem, the measured TS value was converted into a tail probability (or p-value) assuming that for the null hypothesis the TS follows a χ^2 distribution with 1 degree of freedom (Wilks, 1938).

The events between 1 and 10 GeV were selected (with a probability greater than 50% of coming from the pulsar, as

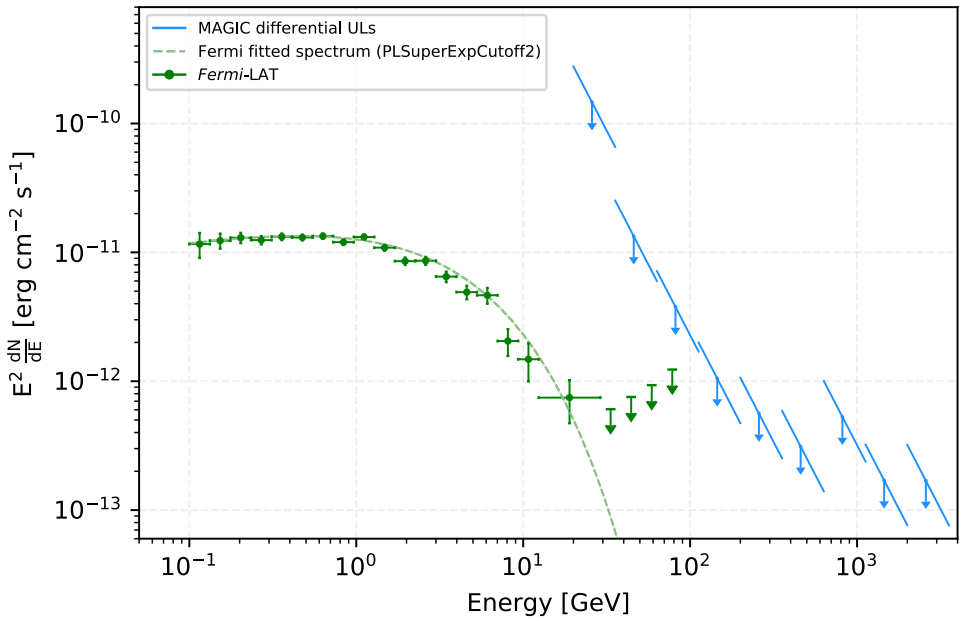

Figure 5.7 Spectrum of the millisecond pulsar J0218 measured by *Fermi*-LAT (green points and upper limits) and the MAGIC telescopes (light blue upper limits). The green dashes represent the fit of the *Fermi*-LAT data with an exponentially cutoff power-law model. Note that the width of the error region is narrower than the dashes showing the best-fit model. Although included, it is difficult to distinguish in this plot. For the MAGIC analysis we assumed a spectral index $\Gamma = -4.5$ obtained from the spectral index of the power-law fit to the high-energy (>10 GeV) part of the *Fermi*-LAT spectrum.

obtained with the Fermi Science Tool[‡] `gtsrcporb`) and the histogram created was used to generate a *low-energy template*. In order to obtain a *smooth* kernel density estimator of this histogram (defined as *low-energy template*), the non-parametric `SOPIE` (Sequential Off-Pulse Interval Estimation) package was used (Schutte & Swanepoel, 2016). The estimation of the off-pulse interval of the light curve was defined with the median value of the results obtained from four different goodness-of-fit tests: Kolmogorov–Smirnov, Cramér–von Mises, Anderson–Darling, and Rayleigh test statistics[§]. Figure 5.8 (top panel) shows the 1-10 GeV histogram together with the resulting *low-energy template* and the estimated off-pulse interval calculated using `SOPIE`. About the emission at higher energies, above 10 GeV, only the events in the in the 95% containment radius of the point-spread function (0.5/0.8 degrees for front/back converting events) are considered; then, a likelihood test to determine if these events are coming from a similar distribution function, as represented by the lower energy template. In order to claim evidence for emission at a specific energy a threshold

[‡] https://fermi.gsfc.nasa.gov/ssc/data/analysis/software/

[§] For details: https://cran.r-project.org/web/packages/SOPIE/SOPIE.pdf

Table 5.3 *Fermi*-LAT spectral points and Upper Limits. Centers of energy bins are reported. *Fermi*-LAT data utilizes 32 logarithmically spaced bins between 100 MeV and 870 GeV. Three bins, spanning 12.38 - 28.99 GeV, were combined in order to produce a flux point instead of an upper limit. As such, a total of 30 bins are reported for the *Fermi*-LAT.

	Fermi-LAT
E	**E^2dN/(dEdAdt)**
[GeV]	[TeV cm^{-2} s^{-1}]
0.12	$(7.24 \pm 1.58) \times 10^{-12}$
0.15	$(7.69 \pm 1.02) \times 10^{-12}$
0.20	$(8.11 \pm 0.73) \times 10^{-12}$
0.27	$(7.77 \pm 0.57) \times 10^{-12}$
0.36	$(8.25 \pm 0.48) \times 10^{-12}$
0.48	$(8.15 \pm 0.42) \times 10^{-12}$
0.63	$(8.34 \pm 0.38) \times 10^{-12}$
0.84	$(7.50 \pm 0.36) \times 10^{-12}$
1.11	$(8.22 \pm 0.37) \times 10^{-12}$
1.48	$(6.79 \pm 0.36) \times 10^{-12}$
1.96	$(5.34 \pm 0.35) \times 10^{-12}$
2.61	$(5.37 \pm 0.38) \times 10^{-12}$
3.46	$(4.05 \pm 0.38) \times 10^{-12}$
4.59	$(3.07 \pm 0.37) \times 10^{-12}$
6.10	$(2.90 \pm 0.40) \times 10^{-12}$
8.10	$(1.28 \pm 0.30) \times 10^{-12}$
10.75	$(9.24 \pm 3.01) \times 10^{-13}$
18.95	$(4.66 \pm 1.71) \times 10^{-13}$
33.40	$< 3.79 \times 10^{-13}$
44.35	$< 4.71 \times 10^{-13}$
58.88	$< 5.82 \times 10^{-13}$
78.18	$< 7.69 \times 10^{-13}$
103.80	$< 1.33 \times 10^{-12}$
137.80	$< 1.38 \times 10^{-12}$
183.00	$< 1.80 \times 10^{-12}$
243.00	$< 2.40 \times 10^{-12}$
322.60	$< 3.19 \times 10^{-12}$
428.30	$< 4.29 \times 10^{-12}$
568.70	$< 5.83 \times 10^{-12}$
755.00	$< 8.10 \times 10^{-12}$

p-value of 0.05 was set. The same test was done for events with energies above 25 GeV. The bottom panel of Figure 5.8 shows the distribution of 58 (17) events above 10 (25) GeV, leading to a p-value of 0.01, thus showing evidence for emission above 10 GeV and, marginally, above 25 GeV. A test for emission above 30 GeV was done but this leads to a p-value that was not significant ($p > 0.05$).

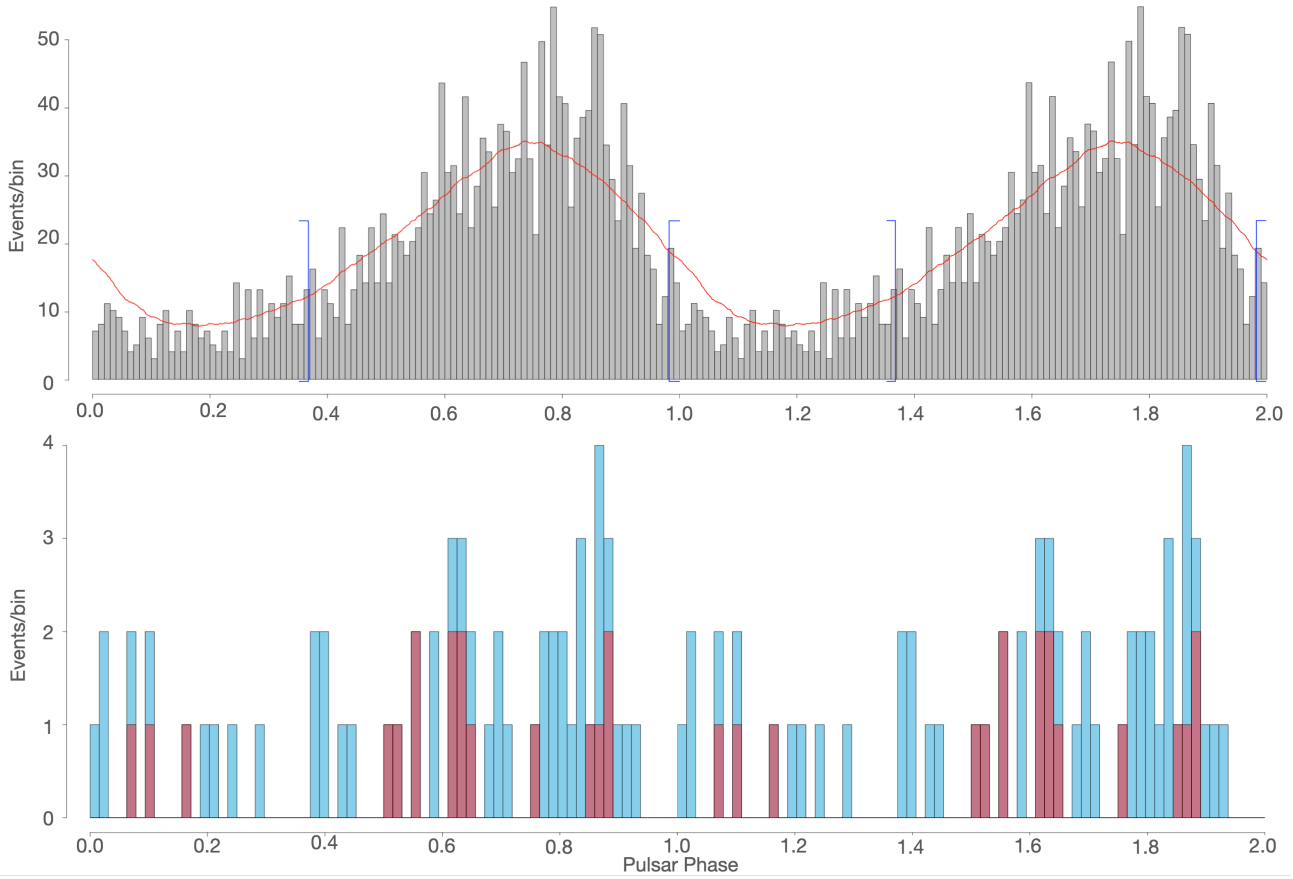

Figure 5.8 **Top panel** – Histogram of the 1–10 GeV events for PSR J0218+4232, along with the smooth circular kernel density estimator (red line) fitted to the data, which we define as the *low-energy* template in our subsequent searches for pulsed emission above 10 GeV. Two rotation cycles are shown, with 100 bins per cycle. The blue brackets indicate the estimated off-pulse interval, $[0–0.34)\cup(0.98,1]$, obtained using `SOPIE` (Schutte & Swanepoel, 2016). **Bottom panel** – Search for high-energy pulsations using LAT standard events above 10 GeV. The blue histogram are the 58 events above 10 GeV in energy, while the pink histogram are the 17 events above 25 GeV. Two rotation cycles are shown, with 65 bins per cycle.

5.3 Observations with MAGIC

5.3.1 Data Sample and Analysis Procedure

MAGIC telescopes have been used in order to search for the VHE emission component of J0218. The data were collected in the stereoscopic mode with the Sum-Trigger-II system (see Section 2.2.1.7), a system designed to improve the performance of the telescope in the sub-100 GeV energy range (Dazzi et al., 2021). J0218 was observed from 2018 November 2 to 2019 November 4 (MJD 58424 - 58791) in the zenith angle range between 13 and 30 degrees, for a max-

imum sensitivity at low-energies. The wobble mode was used for robust flux and background estimation by pointing the telescopes 0.4° away from the source (Fomin et al., 1994). The weather conditions were monitored continuously by measuring the atmospheric transmission with the LIDAR system that operates together with the MAGIC telescopes Fruck et al. (2014). The sub-100 GeV particle showers produce faint Cherenkov radiation and consequently they are more affected by the lower atmospheric transmissions. For this reason, a strict requirement of excellent atmospheric conditions was set with a minimum of 0.85 atmospheric transmission at an altitude of 9km. After discarding around 20% of the total data, 87 hours of good quality data remained. All the MAGIC data were analyzed with the MARS (Zanin et al., 2013) and the dedicated algorithm for calibration and image cleaning of Sum-Trigger-II data was applied. This enabled us to improve the performance and achieve an energy threshold of 20 GeV. The higher-level analysis follows the standard pipeline (Aleksić et al., 2016b).

5.3.2 Spectral Energy Distribution

MAGIC data were analyzed to search for possible pulse and un-pulsed emission above 20 GeV. In Figure 5.9 the skymap of the region around J0218 is shown and no emission is observed from the MSP. The bright spot observed in the image is the blazar 3C 66A, which is significantly detected as a by-product of the observations centered on J2018. The rotational phases are assigned to each event with the Tempo2 package (Hobbs et al., 2006a) which used the same ephemeris used in the LAT analysis described in Section 5.2.1. Given the broad pulse shape in the high-energy band, the use of the off-pulse region to estimate the background would lead to large uncertainties due to its lower ratio compared to the on-pulse. For this reason three source-free reflected-region backgrounds located at the same distance from the FoV center were chosen and is expected to have the same acceptance as the region containing the source (Berge et al., 2007). The upper limits (ULs) to the differential flux were obtained by following the method of Rolke & López (2001) assuming a Gaussian systematic uncertainty in the detection efficiency, with a standard deviation of 30% systematic uncertainty in the flux level. The ULs will be given at 95% C.L.. It was assumed a spectral index of Γ= - 4.5 obtained from the power-law fit to the high-energy (>10 GeV) *Fermi*-LAT data, as reported in the Third Hard Source Catalog (Ajello et al., 2017, 3FHL).

In Figure 5.7 the MAGIC ULs are reported (indicated with blue arrows) together with the green points and ULs from the *Fermi*-LAT analysis. The numerical values are reported in Table 5.4.

Table 5.4 MAGIC spectral points and Upper Limits. Centers of energy bins are reported. MAGIC utilizes 14 logarithmically spaced bins between 20 GeV and 63 TeV. No upper limits are obtained for the last five MAGIC bins (i.e. E > 3.56 TeV) because they have zero counts.

	MAGIC
E	**E^2dN/(dEdAdt)**
[GeV]	[TeV cm^{-2} s^{-1}]
25.83	$< 9.12 \times 10^{-11}$
45.93	$< 8.32 \times 10^{-12}$
81.68	$< 2.36 \times 10^{-12}$
145.25	$< 6.57 \times 10^{-13}$
258.30	$< 3.50 \times 10^{-13}$
459.34	$< 1.94 \times 10^{-13}$
816.84	$< 3.30 \times 10^{-13}$
1452.58	$< 1.06 \times 10^{-13}$
2583.09	$< 1.05 \times 10^{-13}$

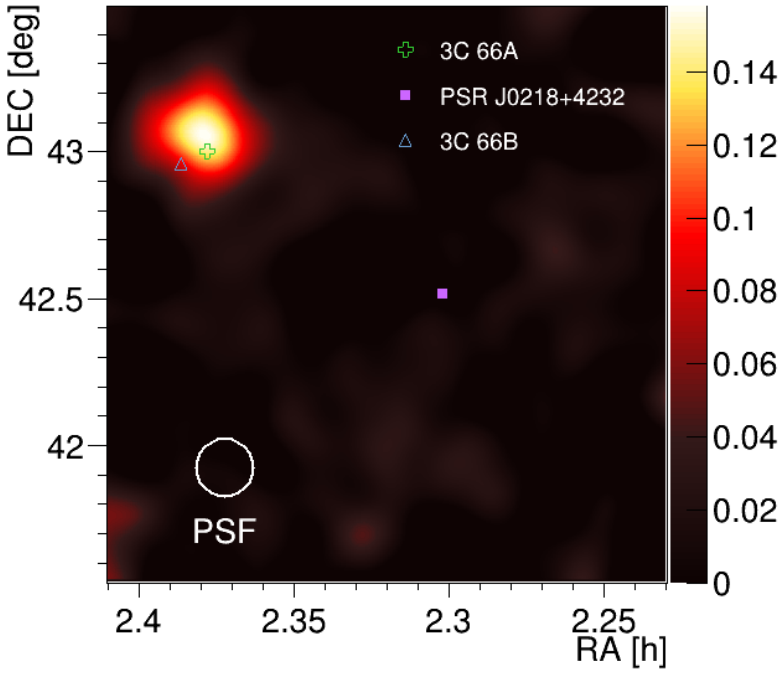

Figure 5.9 MAGIC skymap of the region around PSR J0218+4232 (indicated by a purple square) above 20 GeV. The relative flux (in arbitrary units) is calculated by the number of smeared excess events divided by the residual background flux within 0.1 degrees (Zanin et al., 2013). Although no VHE emission is detected from J0218, the blazar 3C 66A (green cross), a well-known VHE source (Acciari et al., 2009b; Aliu et al., 2009b), is seen with high significance.

5.3.3 Light Curve

The search for pulsed signal in the lowest energy decade started at the energy threshold of the MAGIC observations. The phase-folded light curve is reported in Figure 5.10 and it is computed in the energy range form 20 GeV to 200 GeV. In order to determine if the events come from the distribution functions represented by the lower energy template, the same unbinned likelihood test described in Section 5.2.3 is done. No evidence for pulsation (p-value $\gg 0.05$) is found. The standard pulsation search, looking at *ON* and *OFF* events, is performed and the on-pulse region was selected as the phase interval between 0.34-0.98 and shown as the gold area in Figure 5.10, as defined by our *Fermi*-LAT analysis (see the top panel of Figure 5.8 and Table 5.1). The source-free reflected-region backgrounds, defined with a grey horizontal band in Figure 5.10, were used for calculating the significance of the excess events using Eq.17 of Li & Ma (1983), and no significant pulsation was found (0.057σ). A region-independent signal tests (χ^2 and H-test) were also calculated (de Jager et al., 1989), and both with null results (5.54σ, for 11 degrees of freedom, and 0.05σ, respectively).

5.4 Theoretical Modelling

The spectrum of J0218 was modeled from UV to VHE gamma-rays with 14 orders of magnitude in energy and using a numerical force-free magnetosphere model for the global magnetic field, computing the individual trajectories of particles injected at the NS surface. For the model two populations of particles are considered: primary electrons/positrons along field lines that connect to the current sheet and are accelerated by an assumed parallel electric field distribution, and secondary electrons/positrons from polar cap pair cascades along field lines where there is no accelerating electric field. The dynamics and radiation of the particles are followed from the NS surface to a distance of two light cylinder radii ($2R_{lc}$) and radiated photons are stored in energy-dependent sky maps of observer angle versus rotation phase (Harding & Kalapotharakos, 2015; Harding et al., 2018). The particles radiate Synchrotron-Curvature (SC) and IC emission. The pitch angles for SC are maintained through cyclotron resonant absorption of radio photons emitted above the PC (Harding et al., 2008) and the radius of curvature of the particle trajectory is assumed to be in the inertial observers' frame. The IC requires that trajectories be followed twice, once to store the SC radiation emissivity and another to compute the local photon densities from the stored emissivity and radiate IC (Harding & Kalapotharakos, 2015; Harding et al., 2018).

The main assumptions of the model are the parallel electric field ($E_{||}$) distribution, the source of pairs, pair multiplicity

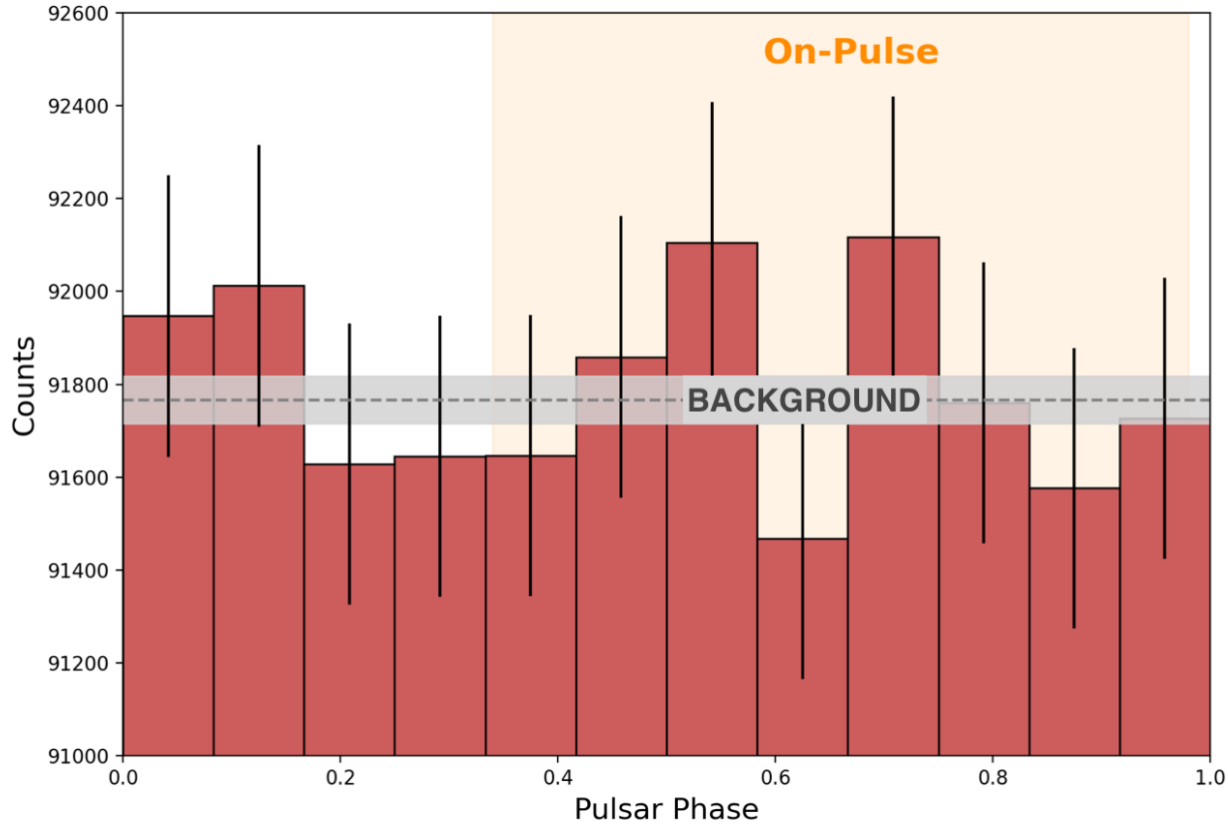

Figure 5.10 Search for VHE pulsations using MAGIC events between 20 - 200 GeV, shown with the red histogram. We used the same on-pulse interval as LAT analysis, [0.34-0.98], presented with the golden area. The grey horizontal dashed line within the one sigma uncertainty band indicates the average number of OFF events collected from three reflected-region backgrounds in the FoV. No significant pulsation is detected.

and their injection distribution on the PC, and the mechanism for generating the pitch angle. Furthermore, the model requires the observed parameters of the pulsar (P and $\dot{P}$). The assumptions on the distribution of the magnetic and electric field distribution are based on results of Particle-In-Cell (PIC) simulations showing that pulsars producing high pair multiplicity have near-force-free magnetospheres and that the highest parallel electric fields are in the current sheet. If the pair multiplicity increases, also the pair SC (mostly Synchrotron Radiation (SR)) and the pair IC (mostly SSC) increases. Increasing the parallel electric field increases the SC of primaries, increases the high-energy cutoff (GeV), and increases the IC (at 10 TeV).

For J0218, a magnetic inclination angle $\alpha = 45°$, a viewing angle $\zeta = 65°$, and a pair multiplicity of $M_+ = 10^5$ are assumed. In Figure 5.11 we show the model predictions, including the various individual emission components.

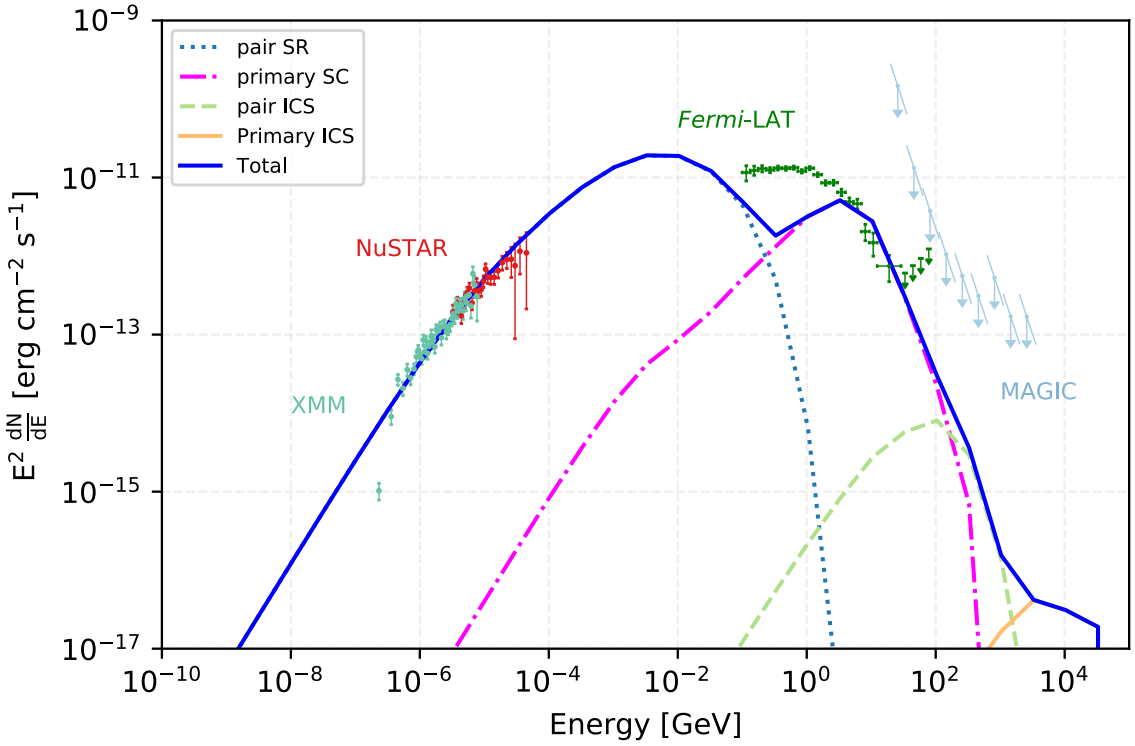

Figure 5.11 Model predictions for the spectrum of phase-averaged emission from accelerated particles and pairs in PSR J0218+4232, for an assumed magnetic inclination angle $\alpha = 45°$ and viewing angle $\zeta = 65°$. The solid orange line represents the predicted Inverse Compton Scattering (ICS) component due to accelerated SC-emitting primaries scattering the pair SR component (blue dotted line). The thick blue line identifies the overall emission model. Data points show the soft (XMM) and hard (NuSTAR) X-ray emission (Gotthelf & Bogdanov, 2017), as well as the LAT spectral points and MAGIC upper limits obtained in this work. Note that the LAT and MAGIC spectral points and upper limits represent the total (pulsed plus unpulsed) emission, however, given the broad peak and large pulsed fraction (see Figure 5.8), the differences between this and the *pulsed* spectrum would be slight, and would not significantly affect the model fit parameters. Note that the gamma-ray data are identical to those in Figure 5.7.

A SC model was also considered where all unknowns are reduced to just a few parameters that represent the observed spectrum (Torres, 2018; Torres et al., 2019). This model follows the particle trajectories in a generic region of a pulsar magnetosphere threaded by an accelerating parallel electric field; this region is located around the light cylinder, and particles are assumed to enter it at x_{in} with a (sizeable) pitch angle α. The model parameterizes the magnetic field by a power law $B(x) = B_s(R_s/x)^b$ (see the discussion in Viganò et al., 2015a), where x is the distance along the field line, b is referred to the magnetic gradient, B_s is the surface magnetic field, and R_s is the pulsar radius. If $E_{||}$ and b are free

parameters, and the period and its derivative $(P, \dot{P})$ are known, the model solves the equations of motion that balance acceleration and losses by SC radiation (see Cheng & Zhang, 1996; Viganò et al., 2015b), computing the total emission. The distribution of particles are assumed to emit towards us and can be parameterized as $dN_e/dx \propto e^{-(x-x_{\rm in})/x_0}$, where the inverse of x_0/R_{lc} is referred to as the *contrast*.

Figure 5.12 shows the results of the model with best fit parameters, $log(E_{||}/\mathrm{V\,m^{-1}})$=10.92, $\log(x_0/R_{lc})$=−4.20 and b=3.70. The agreement between the model description and the broad-band data is acceptable (the fractional residual errors are of the order ∼10%), despite the significant increase in the precision of each spectral measurement and the number of data points.

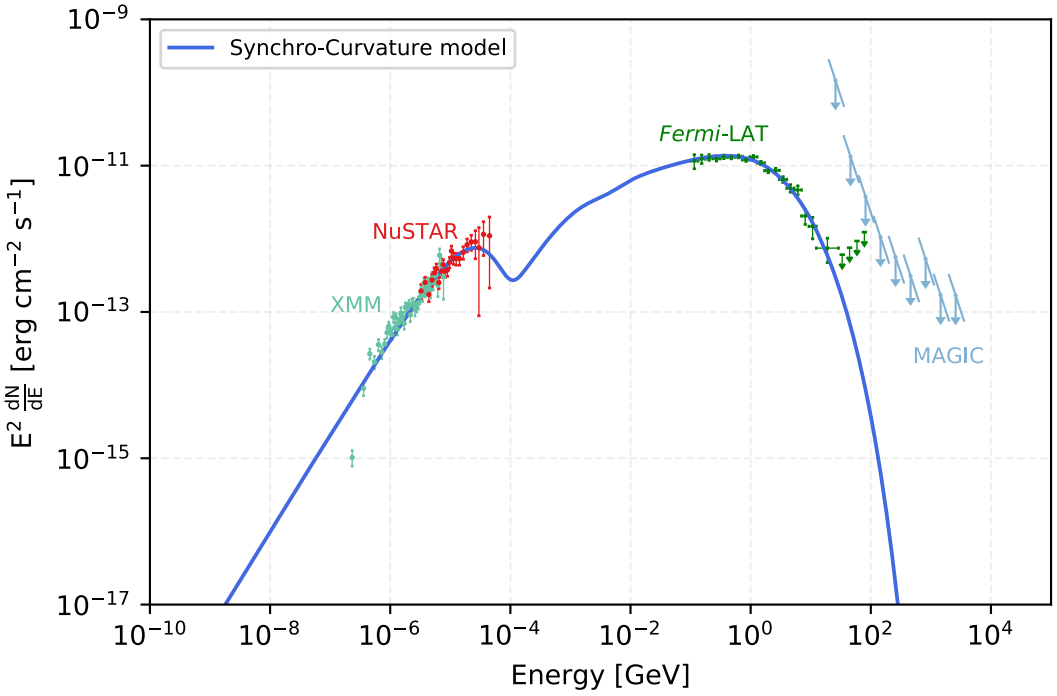

Figure 5.12 Broad-band spectrum of J0218, from the X-ray (XMM and NuSTAR) to the gamma-ray (*Fermi*-LAT and MAGIC) range, along with the best fit to the synchro-curvature model (Torres, 2018). The model is described by these parameters: $log(E_{||}/\mathrm{V\,m^{-1}})$=10.92, $\log(x_0/R_{lc})$=−4.20, and b=3.70. Note that the X-ray and gamma-ray data are identical to those in Figure 5.11.

5.4.1 Discussion and Conclusions

Pulsar experts started to develop new self-consistent models able to explain the emission from pulsars in the VHE regime from when their pulsed emission was detected by ground-based Cherenkov telescopes. In particular, the Crab Pulsar was detected by the MAGIC-I telescope at energies above 25 GeV between 2007 and 2009 (Aleksić et al., 2011) and later VERITAS (VERITAS Collaboration et al., 2011) and both MAGIC telescopes (Aleksić et al., 2012b) detected it at energies above $\sim$ 100 GeV. The MAGIC Collaboration has reported the detection of pulsed photons with energies up to 1.5 TeV (Ansoldi et al., 2016). Also gamma-ray pulsations from Vela Pulsar were been detected by the H.E.S.S. telescope (in monoscopic mode) in the energy range 20-100 GeV (H. E. S. S. Collaboration et al., 2018a), and later up to TeV energies (Harding et al., 2018). Another big milestone for the MAGIC telescopes was the development of the Sum-Trigger-II system that significantly improved the sensitivity of these telescopes at energies below 100 GeV (see section 2.2.1.7). It is thanks to this system that Geminga Pulsar was detected between 15 GeV and 75 GeV and making it third gamma-ray pulsar (and the first *middle-aged* one) to be detected with ground-based Cherenkov telescopes. More details can be found in MAGIC Collaboration et al. (2020). Furthermore, the H.E.S.S. Collaboration reported in the conference paper of Spir-Jacob et al. (2019b) the detection of a hint for gamma-ray pulsations from the pulsar PSR B1706-44, and this, if confirmed, will be the fourth detection of a pulsar from the ground, after the Crab, Vela and Geminga pulsars.

The MSP of this work, J0218, belongs to a small but varied population of MSPs with a well-characterized broad-band non-thermal energy distribution. J0218 has a different spectrum with respect to that of some MSPs studied in X-ray by Coti Zelati et al. (2020) where the SED E^2dF/dE decreases with the energy (see Figure 5.13).
An other characteristic is that the fitted magnetic gradient b (which measures how fast the magnetic field declines along the particle trajectory) for J0218 and other MSPs within the synchro-curvature model is larger than for normal pulsars (Torres, 2018). This is perhaps the result of the larger B_{lc} of MSPs compared to typical pulsars, due to the smaller size of R_{lc}. These assumptions need to be taken into account when making predictions for their observability at lower energies based only on the gamma-ray data. Fits to the gamma-ray data alone are mostly insensitive to the value of the magnetic gradient, and assuming a lower b could lead to incorrect predictions that an MSP is undetectable in the X-ray band. Furthermore, the relevant scales for the production of the pulsar's spectrum (given by x_0) is small in comparison with the light cylinder radius. And this is valid in general for MSPs, where the light cylinder is already orders of magnitude

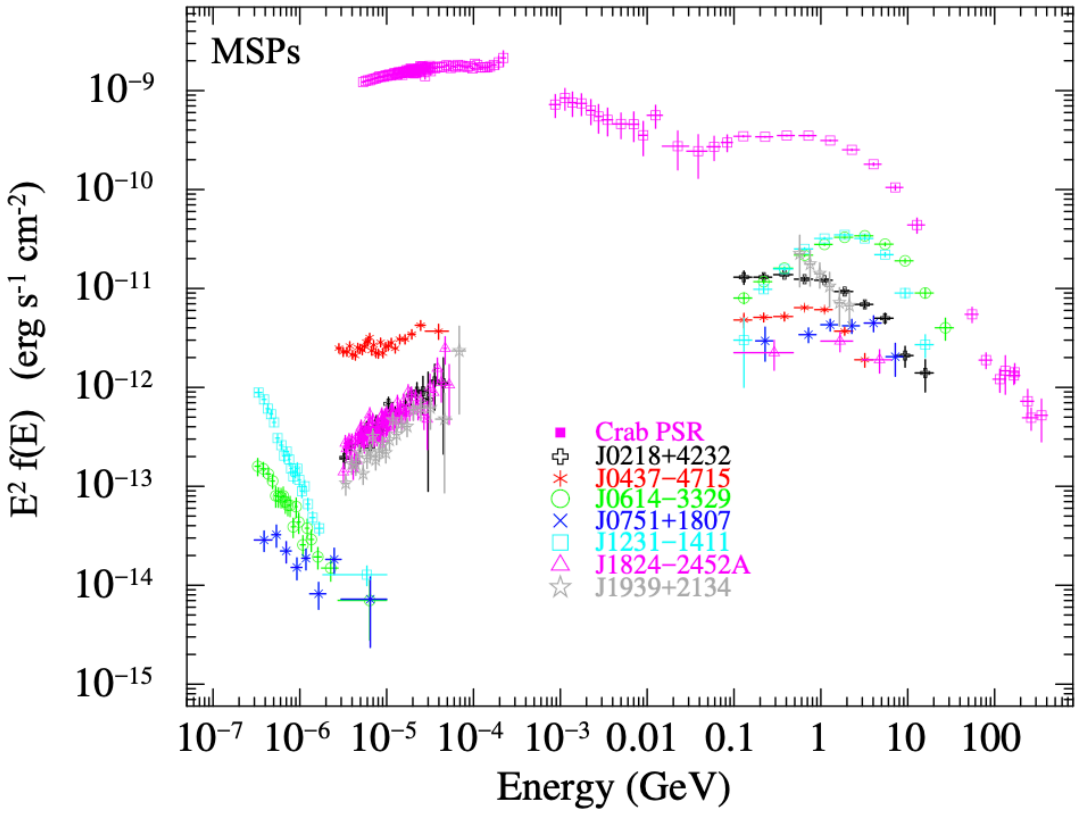

Figure 5.13 Phase-averaged non-thermal X-ray and gamma-ray SEDs of MSPs analyzed by Coti Zelati et al. (2020).

smaller than in normal pulsars: the values of x_0/R_{lc} imply a relevant region of emission $\ll 1$ km.

For the MAGIC analysis, due to the large on-pulse interval in the LAT phaseogram, a reflected-region background subtraction approach was applied in order to subtract the background events from the off-pulse region. After this, no evidence of emission (either pulsed or unpulsed) is found in MAGIC data and the measured MAGIC upper limits are well above our two theoretical model predictions for VHE emission. The component of the curvature radiation (CR) from particles accelerated mostly in the current sheet is expected to fall to flux levels too low at VHE energies for detection by MAGIC and the ICS components from both pairs (mostly SSC) and accelerated primaries are predicted to be at even lower flux levels.

Most models for gamma-ray emission from pulsars do not predict high levels of ICS and SSC emission for MSPs. For example, in the model used for this work and described in Harding & Kalapotharakos (2015) and Harding et al.

(2018), the pairs that come from the PC cascade and MSP surface magnetic fields are so low that the photons need to have much higher energies to produce pairs by one-photon magnetic pair production than do normal pulsars. For this reason the MSP pair spectra are shifted to much higher energies, with a particle Lorentz factor $\gamma \sim 10^4 - 10^7$ (Harding & Muslimov, 2011), and this will produce higher energy SR near the light cylinder. In particular, due to the fact that the VHE emission is most likely ICS or SSC, and both particles and photons have higher energies, the VHE emission will be Klein-Nishina limited (see Section 1.2.1.5) and therefore it is suppressed. The OG models cannot be sustained by MSPs because pairs are produced near the PC as described by the models of Harding & Muslimov (2011).

In MSPs the SR spectra seem to extend to higher energy (at least the energetic ones that have non-thermal emission) and for this, SR photons and the particles that produce them must be at higher energy. The CTA is expected to have significantly better sensitivity than MAGIC in the 10-100 GeV range, and this and other pulsars will thus be prime targets for observation (Burtovoi et al., 2017). On the other hand, pulsars like J0218 are also good sources for MeV telescopes, such as AMEGO (McEnery et al., 2019), that can detect the predicted SR peaks around 1 - 10 MeV.

6

Transitional Millisecond Pulsars

6.1 Introduction to tMSPs

As introduced in Section 3.5, tMSPs are a class of neutron star binaries containing a recycled MSP, spun up by accretion from a low-mass companion to spin periods of the order of milliseconds (Alpar et al., 1982). tMSPs switch between an accretion-powered LMXB state and a rotation-powered Radio Millisecond Pulsar (RMSP) state. During the RMSP phase, they are associated with the *redback* class of pulsars (see Section 3.4.1 for details). In Figure 6.1 we report a sketch of the LMXB phase (left panel) and the RMSP state (right panel). The transitions between the two states occur on a time scale of a few days to weeks, and are accompanied by drastic changes across the electromagnetic spectrum. The origin of these transitions is still debated and, for this, intense multi-wavelength campaigns have been carried out to investigate the phenomenology in both the states.

During the RMSP state the optical emission is indistinguishable from that of non-tMSP redback systems, while in the accretion-powered state the emission exhibits bimodal flickering and flaring (Kennedy et al., 2018; Shahbaz et al., 2018), which are also visible in the X-ray, and this indicates that an accretion disk is present (Patruno et al., 2014; Linares, 2014). The presence of the disk is further confirmed by the strong double-peaked Hα emission line in the optical spectrum seen during the accretion-powered state (Halpern et al., 2013), which fully disappears in the radio state. During the accretion state the tMSPs exhibit a flat radio spectrum that suggests a self-absorbed synchrotron emission, possibly originating in an outflow in the form of a compact, partially self-absorbed jet, as suggested by Deller et al. (2015a,b). In the radio state the emission in the radio band is pulsed and the spectrum is a steep power-law, typical of optically thick synchrotron emission (Patruno et al., 2014; Archibald et al., 2009), as it is also observed in rotation-powered MSPs.
In the next Sections we give a more detailed description of these states.

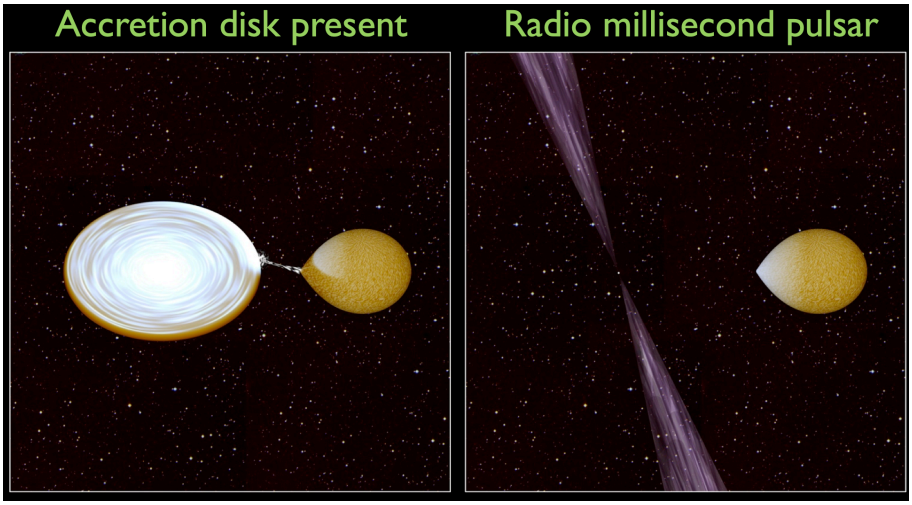

Figure 6.1 An illustrative sketch of the LMXB phase (left) and the RMSP state (right) of tMSPs. During the LMXB the pulsar is being spu-up as the companion overflows its Roche Lobe and transfers mass and angular momentum onto the NS via an accretion disk; in the RMSP phase the pulsar shows pulsations in the radio band with a period of the order of milliseconds. The pulsar wind can ablate the material from the companion star.

These sources are a unique opportunity to study the evolution and the accretion mechanism of pulsar binary systems. LMXBs are the predecessors of *spiders* (black widows and redbacks) and many other types of MSP binaries, but the mechanism by which the accretion is deactivated is not yet known (Chen et al., 2013), nor is the mechanism by which the magnetic field decays when recycled (Konar & Bhattacharya, 1997; Cumming et al., 2001). As it was mentioned in Section 3.5 (Archibald et al., 2009; Papitto et al., 2013b) tMSPs can be the missing link between these two populations:

the accreting X-ray pulsars and isolated MSPs.

Since the discovery of the first tMSP, PSR J1023+0038 (Archibald et al., 2009, hereafter J1023), two other systems of this type, IGR J18245−2452 in the globular cluster M28 (Papitto et al., 2013a), and XSS J12270−4859 (de Martino et al., 2010b, hereafter J1227), have been found. In addition to these three confirmed tMSPs, there are also several promising candidates that display observational properties similar to tMSPs: such as 3FGL J1544−1128 (Bogdanov, 2016), 3FGL J0427.9−6704 (Strader et al., 2016) and Terzan 5 CX1 (Bahramian et al., 2018).

In the radio pulsar state, tMSPs display typical redback pulsar properties: radio pulsations (Archibald et al., 2009; Papitto et al., 2013b) and a faint X-ray luminosity, $L_X \lesssim 10^{32}$erg s^{-1}, (Linares, 2014). Instead, during the accretion state, the radio pulsations become undetectable and are replaced with bright, flat-spectrum radio continuum emission (Deller et al., 2015a), the X-ray luminosity increases, $L_X \sim 10^{33}$erg s^{-1} (Bogdanov et al., 2015), and the gamma-ray flux shows an increment of at least a factor of five relative to the pulsar state (Torres et al., 2017). In Figure 6.2 we report the *Fermi*-LAT light curves of J1023 and J1227.

J1023 and J1227, described in more details in Section 6.2 and 6.3, are potentially interesting for the VHE band because, during the LMXB state, in the *Fermi*-LAT energy range (0.1-10 GeV), they have a flux of about 10^{34}erg s^{-1}, which is up to ten times higher than that observed during the RMSP state (Papitto & Torres, 2015). This fact makes them particularly interesting for a possible detection with the future CTA. In section 6.6 I describe the CTA simulations carried out for the two tMSPs J1023 and J1227.

6.2 PSR J1023+0038

J1023 (ℓ, b = 243°.49, +45°.78) was first detected in May 2002 as a variable 1.4 GHz radio source (Bond et al., 2002) which showed, in the optical spectrum, clear characteristics (double peaked emission lines of the Balmer series, He I and He II) of an accretion disk around a compact object. Later, Thorstensen & Armstrong (2005) identified J1023 as a NS-LMXB system and the observations revealed the existence of strong irradiation. In 2007 the *Robert C. Byrd Green Bank Telescope* detected radio pulsations and showed that J1023 hosts a 1.69 millisecond radio pulsar in a 4.75 hr orbit around a 0.2 $M_\odot$ companion star (Archibald et al., 2009). Finally, at the end of 2013 the source returned to a LMXB state (where it has remained until now), the double-peaked optical emission lines re-emerged and the radio pulsar signal

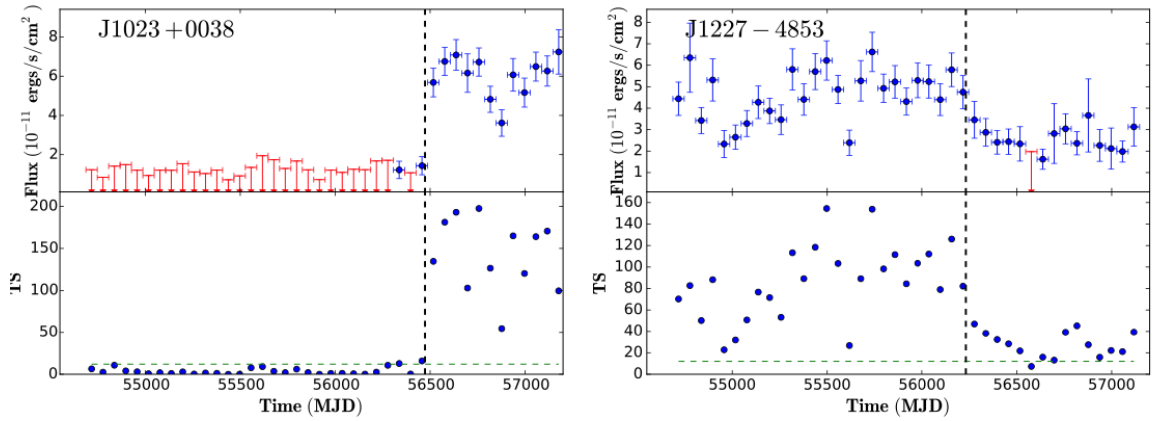

Figure 6.2 Long-term light curves of the transitional millisecond pulsars J1023 and J1227; from Torres et al. (2017). The known (Bassa et al., 2014; Stappers et al., 2014) state transitions are indicated by vertical dashed lines. The red lines show the flux upper limits.

switched off (Stappers et al., 2014). The average X-ray luminosity in the disk state never exceeded the value of $L_X \sim 10^{33}$ erg s^{-1} and this indicates that the accretion episodes are characteristic of a *sub-luminous* disk. The parallax distance of J1023 is 1.37 kpc (Deller et al., 2012).

As we mentioned before, in the sub-luminous disk state J1023 has a gamma-ray flux (E>100 MeV) brighter by a factor of 5 than in the radio state (Stappers et al., 2013; Torres et al., 2017), as shown in the light curve of Figure 6.2. The average *Fermi*-LAT spectrum is described by a power-law with an index $\Gamma = 2.0$ and a cut-off at an energy of 3.7 GeV (Torres et al., 2017, see Figure 6.4). Above 100 GeV, no significant steady and pulsed gamma-ray emission was found using the ground-based gamma-ray telescope VERITAS (Aliu et al., 2016). Only an UL was reported (Figure 6.6), and this permitted to constrain the magnetic field strength in the shock region of the source. Aliu et al. (2016) found a magnetic field in the shock region higher than $\sim$ 2 G during the radio state and higher than $\sim$ 10 G in the LMXB state.

J1023 is the first optical MSP ever detected as it shows pulsed optical emission discovered by Ambrosino et al. (2017) and later confirmed by our group with the fast photon counter Aqueye+ in Asiago (Zampieri et al., 2019). Figure 6.3 shows the background-substracted pulse shape of J1023, obtained with Aqueye+. Optical and X-ray pulsations have similar shapes and this indicates that they may be produced in a similar way.

From the values of ν and $\dot{\nu}$ in Burtovoi et al. (2020), we can derive a spin-down luminosity of $\sim 5.4 \times 10^{34}$ erg s^{-1}, in agreement with the ATNF Pulsar Catalogue (Manchester et al., 2005).

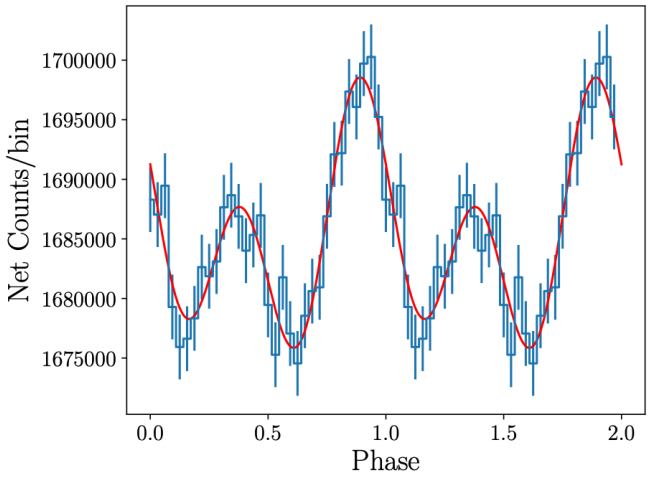

Figure 6.3 Background-substracted pulse shape of J1023 obtained folding all the Aqueye+ optical observations of January 2018 with the timing solution reported in Zampieri et al. (2019) and with 32 bins per period. Two rotational phases are shown. The solid line shows the fit with two sinusoidal components plus a constant. From Zampieri et al. (2019).

6.3 PSR J1227−4853

J1227 (ℓ, b = 298°.96, +13°.78) is very similar to J1023 under many aspects. It was initially detected as a hard X-ray source and tentatively identified as a cataclysmic variable, similarly to J1023, based on the double-horned emission lines (typical of an accretion disk) in its optical spectrum (Masetti et al., 2006). Later, its unusually low X-ray low luminosity was considered to be typical of the sub-luminous state of tMSPs (de Martino et al., 2010a). Therefore, it was suggested that J1227 was a NS in a LMXB. J1227 transitioned from a disk to a radio pulsar state between 2012 November 14 and December 21. This transition was characterized by the disappearance of the emission lines in the optical spectrum and a softening of the emission proprieties observed in the radio, optical, X-ray and gamma-ray bands (Bassa et al., 2014; Torres et al., 2017). From the end of 2012, J1227 behaves as a rotation-powered redback pulsar and radio observations with the *Giant Metrewave Radio Telescope* discovered a pulsar with a 1.69 ms spin period, in a binary system with an orbital period of 6.9 hr (Roy et al., 2015). J1227 has a similar distance as J1023, 1.37 kpc (Jennings et al., 2018).
In both states, J1227 shows gamma-ray emission in the *Fermi*-LAT band. Before the transition to the radio state, the gamma-ray emission was a factor of 2 higher (Torres et al., 2017, see Figure 6.4). In the sub-luminous disk state the source spectrum is described by a power-law with a spectral index of 2.3 and a spectral cut-off at E_{cut}=10.8 GeV; in the radio pulsar state the spectrum is reproduced with a power-law with a cut-off at E_{cut}=5.3 GeV and a spectral index of

2.0 (Torres et al., 2017). The spin-down luminosity during the accretion state is $\sim 9.1 \times 10^{34}$ erg s^{-1}, which is about 10^3 times the X-ray luminosity during the MSP state (Roy et al., 2015).

6.4 The states of tMPSs

Here I give a more in depth description of the two characteristic states of the tMSPs.

The rotation-powered state During the radio state, tMSPs are very faint objects at all wavelengths and behave as redback system. They show irregular radio eclipses when the secondary is at the inferior conjunction of the orbit; these eclipses originate from the thin and dense layers of ionised material that the pulsar wind drives off from the surface of the donor close to the inner Lagrangian point, and partly surrounds the system (Archibald et al., 2013).

The X-ray spectra are described by a power-law that extends up to ~70 keV (Papitto & de Martino, 2020). A soft thermal component (0.1–10 keV) is also detected and is probably produced by hot spots on the NS surface. The orbital variability of the X-ray emission has a large amplitude (de Martino et al., 2015, >25%), with a maximum occurring when the companion is at the superior conjunction, in phase with the radio eclipses. This large orbital variability can be explained assuming that the observed flux is produced by synchrotron emission from the intrabinary shock originating by the interaction of the pulsar wind with the material of the companion star near the inner Lagrangian point L_1, or directly at the donor surface (Arons & Tavani, 1993; Bogdanov et al., 2011). The minimum of the X-ray emission is determined by the occultation of the shock by the secondary star when it is at the inferior conjunction of the orbit.

tMSPs are energetic enough to convert part of their spin-down power into HE emission; during the radio state they have a luminosity of a few $\times 10^{33}$erg s^{-1} (0.1–100 GeV) and a Power-Law (PL) spectrum with a photon index $\Gamma \sim$ 2.3–2.4 (Tam et al., 2010; Takata et al., 2014). A marginally significant high energy cut-off at $\sim$ 5.3 GeV was detected only in J1227 (Torres et al., 2017); the *Fermi*-LAT spectra of J1227 and J1023 during the radio pulsar state and the sub-luminous disk state are shown in Figure 6.4.

Gamma-ray pulsations were reported at a significance of 3.7σ from J1023 (Archibald et al., 2013) and 5σ from J1227 (Johnson et al., 2015). The gamma-ray pulse profile (E>100 MeV) of J1227 is characterized by one broad peak which is almost aligned with the main peak of the radio pulse profile at 1.4 GHz (Johnson et al., 2015).

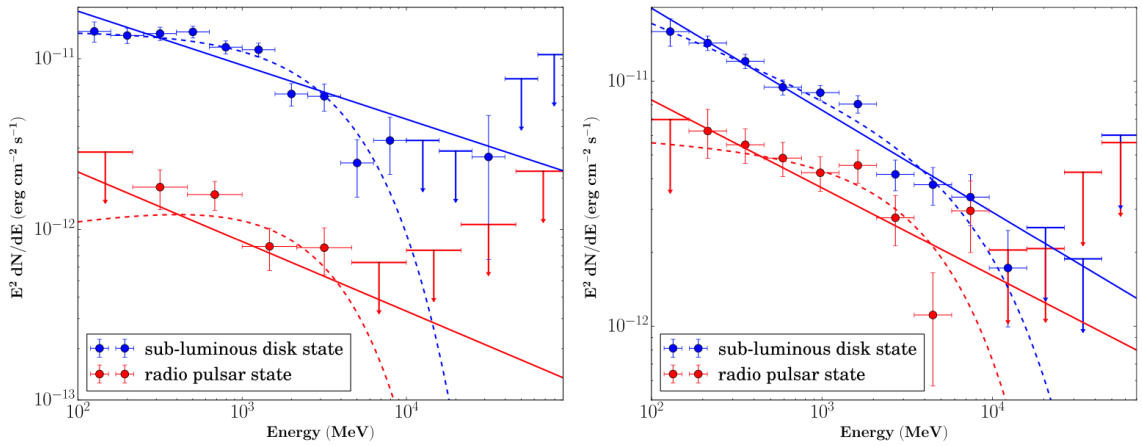

Figure 6.4 *Fermi*-LAT spectra of J1023 (left) and J1227 (right) in the radio pulsar state (red) and the sub-luminous disk state (blue). The corresponding fitted models are shown with solid lines (for a PL) and dotted lines (for a Power-Law with Exponential Cut-off (PLEC). From Torres et al. (2017).

The sub-luminous disk state During the accretion disk state tMSPs are characterised by an X-ray luminosity of about 10^{33}-10^{34} erg s^{-1}. J1023 is in the sub-luminous disk state since 8 years (June 2013); J1227 behaved as such between 2003 and 2012, with the beginning of the disk state possibly occurring at earlier times. Figure 6.2 shows transitions from a radio pulsar state (low gamma-ray state) to a sub-luminous disk state (high gamma-ray state) for J1023, and the opposite transitions for J1227.

In the X-ray band these systems are characterized by *high/low* intensity modes and by sporadic flares. The X-ray light curve of J1023 is shown in the top-left panel of Figure 6.5. For about 80% of the time J1023 lies in the high mode, emitting a roughly constant X-ray luminosity ($\sim \times 10^{33}$erg s^{-1}); sharp transitions to the low mode occur on a timescale of 10 s. The X-ray luminosity observed in the low mode is also roughly constant and about one order of magnitude fainter than in the high mode, but still a few times brighter than the rotation-powered state. The duration of these modes ranges from a few tens of seconds to hours, although there does not seem to be a characteristic length or recurrence time. As proposed by Miraval Zanon et al. (2020), there are two different physical scenarios that can explain the rapid variability between high and low modes. In the first scenario the transitions between the high and low modes are accounted for by propeller to radio-ejection pulsar states (accompanied by X-ray pulsations powered by accretion), during which the pulsar wind prevents matter from falling onto the neutron star surface (Papitto & Torres, 2015). In the second scenario, these transitions can be explain by an approaching or receding inner disk just outside the light cylinder (accompanied by X-ray pulsations powered by rotation): during the high mode the radio pulsar is always active

and the intrabinary shock is located just outside the light cylinder, while it expands during the low mode. The flaring mechanism is independent of the high-to-low mode transitions (Miraval Zanon et al., 2020). Low and high modes are more evident in the ultraviolet band (Papitto & de Martino, 2020).

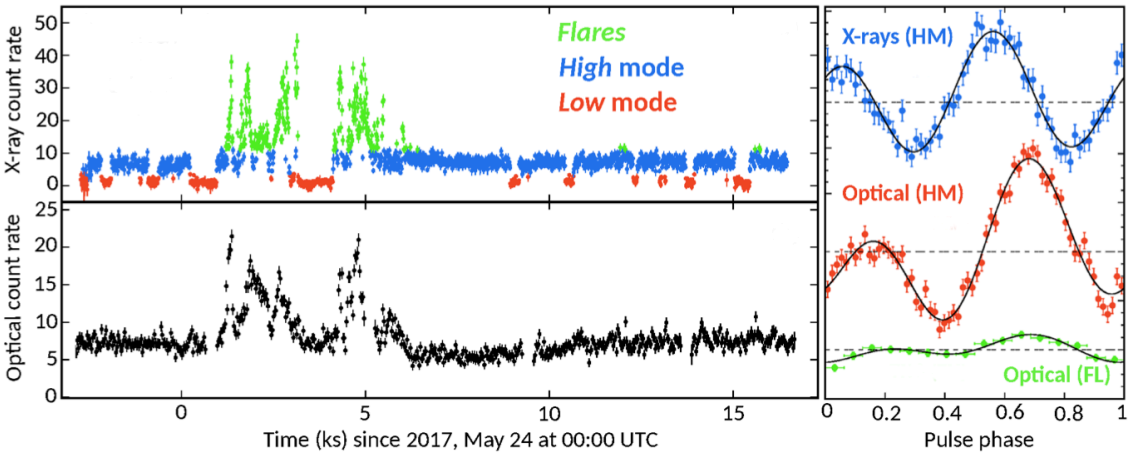

Figure 6.5 X-ray (top-left panel) and optical (bottom-left panel) light curves of J1023 in the sub-luminous disk state observed simultaneously with XMM-Newton and SiFAP at TNG. High mode, low mode and flares phases are plotted in blue, red and green, respectively. The right panel shows the X-ray pulse profile during the high mode (blue points) and the optical pulse profiles in the high (red points) and flare (green points). From Papitto et al. (2019)

The gamma-ray brightening when the system switches from the rotation-powered to the sub-luminous disk state is one of the most unexpected features of tMSPs. In the sub-luminous state tMSPs become a few times brighter than in the rotation-powered state and slightly more luminous than in the X-ray band. The gamma-ray spectra of both **tMSPs** in this state are well described by a power-law with index $\Gamma_\gamma \approx 2.0$ with a marginal evidence of a cut-off between 4 and 10 GeV (Torres et al., 2017). A high-energy component (E> 5 GeV) was recently claimed to emerge in the spectrum of J1023 at orbital phases corresponding to the pulsar descending node (Xing et al., 2018), but this result is still to be confirmed. So far, in the TeV regime, only upper limits have been obtained (Aliu et al., 2016); the VERITAS UL is reported in Figure 6.6.

A radio continuum emission is seen from both J1023 and J1227 and is interpreted as self-absorbed synchrotron emission from material out-flowing from the system (Fender, 2016). Simultaneous radio and X-ray observations of J1023 unveiled that when the source switched from the high to the low X-ray mode, the radio flux suddenly increased and its spectrum became steeper (Papitto & de Martino, 2020). In J1023 and J1227, flares were observed to occur almost

simultaneously in the X-ray, UV, optical, and near-infrared and this suggests a common underlying process (de Martino et al., 2010b, 2014). The X-ray flares emit most of the energy and they last from a few minute to a few hours. Multi-band simultaneous observations of the bright flares suggest that they are produced in a hotter and optically thin medium , like an accretion disk corona and/or hot fireball ejecta (Shahbaz et al., 2015). J1023 and J1227 show X-ray and optical pulsations at the NS spin period only during the high mode (Archibald, 2015; Papitto et al., 2019) which disappear during the low modes. During the flaring mode only very weak optical pulsations are observed (Papitto et al., 2019), see Figure 6.5.

Due to the presence of the newly-formed accretion disk, the optical flux of tMSPs in the sub-luminous state is $\sim 1-2$ magnitudes brighter than in the rotation-powered state (Bassa et al., 2014; Pallanca et al., 2013). The optical spectra is dominated by a blue continuum and strong, double-peaked emission lines of H and He produced in an optically thick accretion disk (de Martino et al., 2014; Coti Zelati et al., 2014). The inner disk radius is larger than the Alfvén radius*. The optical emission originates in the outer disk regions (Papitto & de Martino, 2020).

6.5 High Energy Emission Models

The rotation-powered state As already mentioned above, during the RMSP state there are strong and evident eclipses that last about 0.1–0.4 in orbital phase (Archibald et al., 2009). These eclipses, at superior conjunction, must be caused by material driven off the surface of the companion by the impinging pulsar wind (Archibald et al., 2009).

Bogdanov et al. (2011) hypothesized that X-ray emission can originate closer to the secondary star, near the inner Lagrangian point (L1), than to the pulsar. The X-ray luminosity is consistent with being produced at the shock front between a magnetically dominated pulsar wind and the stellar material. In the case of a magnetically dominated wind, the shock should occur in a relatively strong magnetic field ($B \sim 40$G) due to the small separation between the pulsar and the companion (Bogdanov et al., 2011). During this phase a strong modulation in optical and in X-rays with the orbital period of the system is observed; the X-ray modulation is produced by the variation of the viewing angle of the *intrabinary shock* (Bogdanov et al., 2011), while the optical modulation by the variation with orbital phase of the

*The Alfvén radius is the radius where the ram pressure of the infalling gas is equal to the magnetic pressure of the dipole magnetic field of the NS.

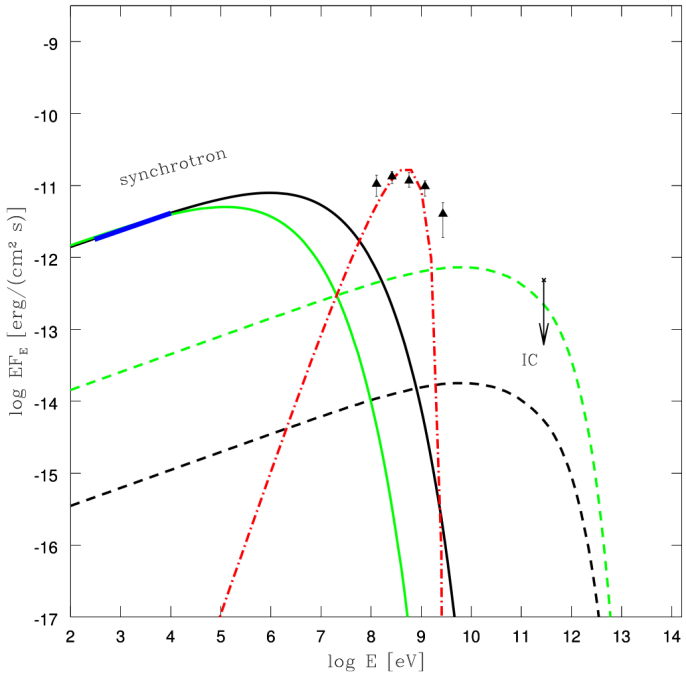

Figure 6.6 Broadband spectrum of J1023 during the accretion disk state. The thick blue line shows the X-ray emission detected with *Swift* in 2013 November (Takata et al., 2014) and the black triangles represent the *Fermi*-LAT HE gamma-ray detection in 2013. The arrow shows the VERITAS UL (Aliu et al., 2016). Solid and dashed lines correspond to the synchrotron and IC emission possibly coming from a shock for different values of the magnetic field. From Aliu et al. (2016).

irradiated portion of the companion.

The X-ray spectrum shows two components (Archibald et al., 2010): a strong dominant non-thermal component and a fainter thermal one that probably originates from the hot polar caps of the pulsar and optically thin thermal plasma responsible for the radio eclipses. The non-thermal component originates at the intrabinary shock and to this component can contribute also the pulsar magnetosphere emission (Archibald et al., 2010). This makes the pulsar very similar to the majority of the "recycled" MSPs detected in X-rays.

The X-ray data can be described by synchrotron emission from relativistic electrons exhibiting a PLEC spectral shape (Aliu et al., 2016). In the case that the GeV emission is produced in the pulsar magnetosphere, the typical spectral shape is a PLEC and this can be a result of curvature acceleration in a gap region in the magnetosphere (Harding et al., 2005). In particular, synchrotron photons can inverse-Compton scatter on relativistic electrons and become VHE photons.

In these singular systems there is the opportunity to study the properties of the termination shock due to the fact that the relativistic wind of the MSP is very close to the companion star (Papitto & de Martino, 2020). Tavani (1991) al-

ready predicted that HE photons generated by the particles accelerated at the termination shock would have been able to evaporate the late-type companion star. The first models were applied to the first black window pulsar discovered, PSR B1957+20, and Arons & Tavani (1993) found that synchrotron emission is the main cooling mechanism of the relativistic particles accelerated in the shock, yielding an X-ray output which exceeds the magnetospheric pulsar emission. Furthermore, the luminosity of the shock synchrotron emission depends on the strength of the magnetic field beyond the shock.

The electron population has a power-law energy spectrum and this favours the scenario of a shock-driven magnetic reconnection in a striped pulsar wind (Sironi et al., 2015).

Another model suggests that an additional source of heating could arise from a fraction of the wind particles that threads the companion field lines and is channeled to its surface (Romani & Sanchez, 2016); this implies a very active magnetic star with star-spots or flares but, in no tMSPs an indication of a magnetically active star was found (de Martino et al., 2015).

The accretion-disk state As noted above, the transition to the sub-luminous disk phase is accompanied by a significant increase in gamma-ray flux (Takata et al., 2014; Johnson et al., 2015). There are currently various theoretical models that can explain the VHE gamma emission in this phase:

- The gamma-ray emission can be produced by the interaction between the accretion disk and the pulsar wind. Takata et al. (2014) and Deller et al. (2015a) proposed that IC scattering of the cold relativistic pulsar wind off the soft UV photons from the disk produces the observable gamma-rays. Furthermore, some fraction of the pulsar wind interacts with material close to the intrabinary shock, resulting in an increase of the X-ray flux. Figure 6.7 shows a schematic view of the various model components for J1023 during this state.

- Coti Zelati et al. (2014) proposed that the radio pulsar is ensurounded in the intrabinary matter and that the pulsar wind truncates the disk far from the pulsar ($d \approx 10^9 - 10^{10}$ cm). The electrons accelerated at the intrabinary shock up-scatter the disk UV photons to yield the observed gamma-rays. These electrons also interact with the magnetic field in the shock to emit synchrotron X-ray photons. This model was proposed before the discovery of the optical and X-ray pulsations. Coti Zelati et al. (2014) show that this model can explain the X-ray/gamma-ray emission of other MSPs but failed to do so for tMSPs in the disk state.

- Papitto & Torres (2015) hypothesized that during the disk state the *propeller* mechanism is active: not all the

material falls on the NS surface but part of it is expelled along the magnetic field lines, because the centrifugal force at the co-rotation radius r_{co}[†] exceeds the gravitational force. They showed that the gamma-ray emission can be produced by SSC at the turbulent boundary between a propelling magnetosphere and the disk in-flow, where electrons can be accelerated to relativistic energies. X-rays are also produced by synchrotron emission in the same region. Furthermore, the transitions between the high and low modes could be due to a switching between an accretion/propeller and a rotation-powered state (Linares et al., 2014; Campana et al., 2016). In the low mode, the pulsar wind would terminate in a shock beyond the light cylinder, which would hide the radio pulses and produce the power-law X-ray spectrum. In the high mode, instead, the disk would get close to r_{co} and most of the emission would be produced at the boundary between the disk and the propelling magnetosphere (Campana et al., 2016). The penetration of the disk within the light cylinder would force some magnetic field lines to open, explaining the enhanced spin-down observed in the disk state compared to the radio pulsar state (Jaodand et al., 2016; Burtovoi et al., 2020).

◇ In the LMXB state, J1023 shows optical and X-ray pulsations and sudden X-ray luminosity jumps between a *low* and a *high* flux mode (see Section 6.4). During the low modes, the continuum radio spectrum suggests the existence of an outflow (Bogdanov et al., 2015). The source stays in this mode for 20% of the time with an average X-ray luminosity $L_X \sim 10^{32}$ erg s^{-1}, whereas it stays in the high mode for about the 70-80% of the time with $L_X \sim 10^{33}$ erg s^{-1}. There are also sporadic flares reaching luminosities of about $L_X \sim 10^{34}$ erg s^{-1} (Jaodand et al., 2016). The switches between these modes occur on a timescale of tens of seconds.

Jaodand et al. (2021) found that the UV luminosity varies during the low and high modes in phase with the X-ray luminosity and that the UV luminosity is a factor of $\sim 25\%$ higher. J1023 is the first UV MSP with strong evidence of that UV pulsations in the high-mode, with a similar waveform as the X-ray pulsations (Jaodand et al., 2021). Furthermore, the optical modes are opposite with respect UV/X-ray modes. Two broad-band emission components have been proposed: one from radio to near-infrared/optical and one from optical to hard X-rays. The first one is brighter when the second component is dimmer (and vice-versa). Jaodand et al. (2021) suggested that these components are linked to the accreting and ejected material (high modes occur when accreting matter reaches the light cylinder and possibly the neutron star surface (inflow), and low modes occur when matter is ejected in a collimated outflow) and that the optical/UV/X-ray pulsations can arise from a shocked accretion

[†]Radius at which the angular velocity of the star $\Omega_\star$ matches the Keplerian angular velocity of the disk: $r_{co} = [GM_\star/\Omega_\star^2]^{1/3}$

flow channeled by the magnetic field of the NS.

◇ Papitto et al. (2019) suggested that these systems could be the prototype of a few hundred km-sized pulsar wind nebula, where the relativistic and highly magnetized wind interacts with the in-flowing disk matter just beyond the light cylinder. A shock is created and the wind periodically deposits energy by accelerating electrons at the shock. Optical and X-ray pulses are produced via synchrotron emission and in Figure 6.8 it is represented a schematic view of the pulsar wind scenario. Two pulses of optical/X-ray synchrotron radiation will be then observed every spin cycle of the pulsar, whose relative amplitude depends on the magnetic inclination angle, as well as on the viewing angle.

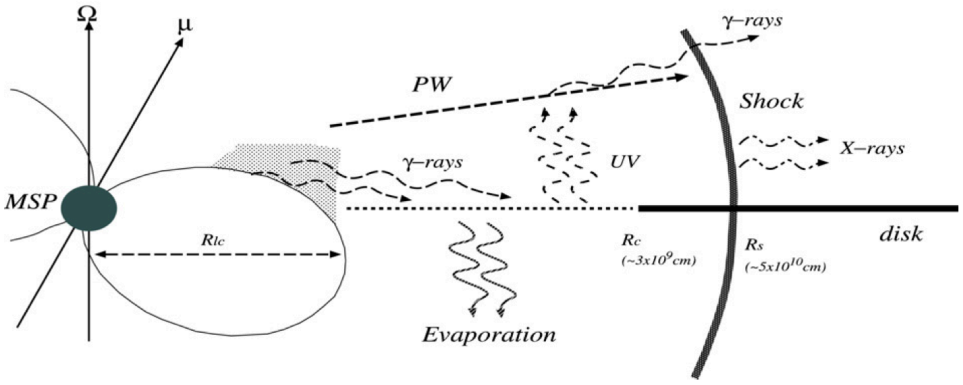

Figure 6.7 Schematic view of the multi-wavelength emissions components of J1023 system during the LMXB state (Takata et al., 2014). The accretion disk extends beyond the light cylinder radius (R_{lc}). R_s is the distance of the intrabinary shock from the pulsar. Takata et al. (2014) hypothesized that UV and optical photons are mainly produced by the disk at $\sim 10^{9-10}$ cm. The interaction between the pulsar wind and the stellar wind creates a shock and produces the nonthermal X-ray photons. Inverse Compton of the cold relativistic pulsar wind off UV/optical photons from the disk produces the gamma-rays. From Takata et al. (2014).

6.6 CTA Simulations

As mentioned in Section 6.1, the observed average gamma-ray flux of some tMSPs shows a five-fold increase as the radio pulsar transits to the LMXB state (Stappers et al., 2014). Despite that, none of the tMSPs have been detected within the TeV domain by the current generation of IACTs. In this work I explore the feasibility of detecting tMSPs with CTA and the prospects that these observations may offer for constraining the energetics of the particles accelerated in

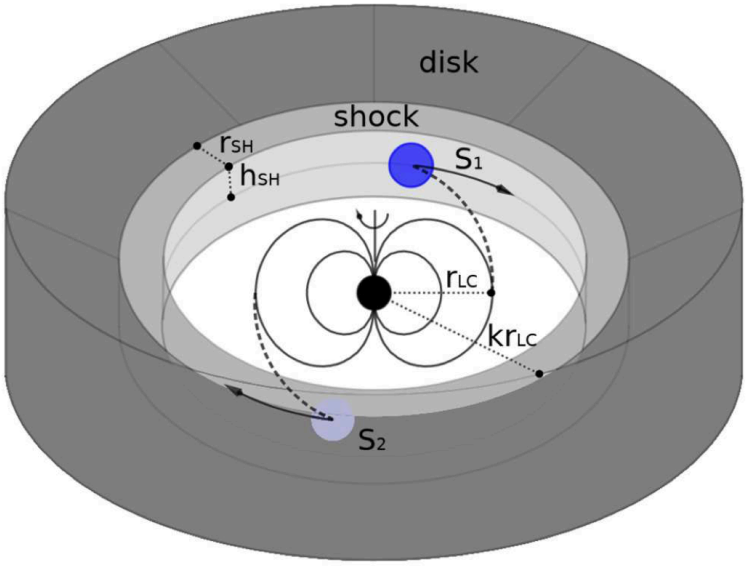

Figure 6.8 Schematic diagram of the pulsar wind scenario that Papitto et al. (2019) propose to explain the optical and X-ray pulses observed from J1023. Dashed lines represent the current sheet which expands from the light cylinder surface at r_{LC} as an Archimedean spiral. Its arms crosses the termination shock (shaded in light gray) at S_1 and S_2 where particles are accelerated to relativistic energies. As long as the particle energy is quickly radiated away and the size of the shock is smaller than a few light cylinder radii, two bright synchrotron-emitting spots (drawn in blue) rotate at the shock surface. An observer will see pulses of radiation because the intensity received from S_1 (farther from the observer) is modulated by the angle under which the spot is seen, and the emission coming from S_2 is absorbed by the optically thick disk in-flow (shaded in dark gray). From Papitto et al. (2019).

the intrabinary shock.

To test the capabilities of CTA to detect emission from these sources I first studied the HE gamma-ray emission from *Fermi*-LAT when they are in the LMXB state in order to obtain the spectral parameters of the source. The two spectral models that have been considered for the CTA simulations are, for both the systems, the Log Parabola (LP) and the Broken Power-Law (BPL). A PLEC with a cut-off at a few GeV was not considered because it would not make it possible a detection at VHE. On the other hand, a simple PL model would clearly produce more favorable predictions, but we discarded it because we consider it too optimistic.

PSR J1023+0038 The source is in the LMXB state since 2013. I assumed, as input spectra for the simulations, the LP and the BPL with the same parameters obtained from the preliminary analysis of the *Fermi*-LAT data ($\sim$ 8 years of data). The parameters are reported in Table 6.1.

Table 6.1
Spectral input parameters of J1023 inferred from an analysis of the *Fermi*-LAT data in the accretion phase (June 2013-February 2021).

Spectral Models	Spectral Parameters
Broken Power-law (BPL)	$N_0 = (0.06 \pm 0.01) \times 10^{-10}$ γ_1=-2.12±0.03 γ_2=-2.91±0.06 E_b=1.15±0.09
Log-Parabola (LP)	$N_0 = (0.34 \pm 0.007) \times 10^{-10}$ α=2.23 ±0.02 β=0.16±0.02 E_b=0.524

Note: N_0 is the prefactor in unit of photons cm^{-2} s^{-1} MeV^{-1}; the break energy E_b is in GeV; the errors are the statistical uncertainties.

For the simulations I used both South and North site IRFs[‡] of the baseline array made available by CTA Consortium (Observatory & Consortium, 2016). I simulated three observations with different observing times centered at the position of the source: 50 hours of observation, 100 hours of observation and 200 hours of observation. I simulated observations lasting up to 200 hours in order to test the results achievable with CTA under the best assumptions regarding the observing time. This procedure is repeated for 100 times to account for the statistical fluctuations that can arise from different simulations[§]. I binned the simulated data into 20 logarithmic energy bins in the energy range 0.03-100 TeV and I fitted them with the same models given in input.

In Table 6.2 I show the results of the unbinned analysis for the BPL model. From 200 hours of observation with CTA South, I obtain an overall detection significance of 10.7σ (TS $\simeq$ 114.8). I report also the spectral parameters measured in the simulations. The simulations with the LP model failed to produce upper limits because the model could not converge. This was probably due to the fact that the statistics for the CTA simulations was too low. The resulting spectrum of J1023 is shown in Figure 6.9 for 200 hours (CTA South).

[‡]For this work I used the version prod3b-v2 of the IRFs. They are referred to as the baseline configuration with 118 telescopes divided in total on both sites. Currently, the new IRFs are the prod5-v0.1 version (Observatory & Consortium, 2021) and are referred to the first construction phase with an array configuration of 4 LSTs and 9 MSTs in the Northern site and 14 MSTs and 37 SSTs in the southern site.

[§]Different simulations are based on a different random seed for the Monte Carlo generator that samples the input source models to produce observed photon energies and arrival directions. This is achieved through the random number generator provided in the GammaLib library (Knödlseder et al., 2016).

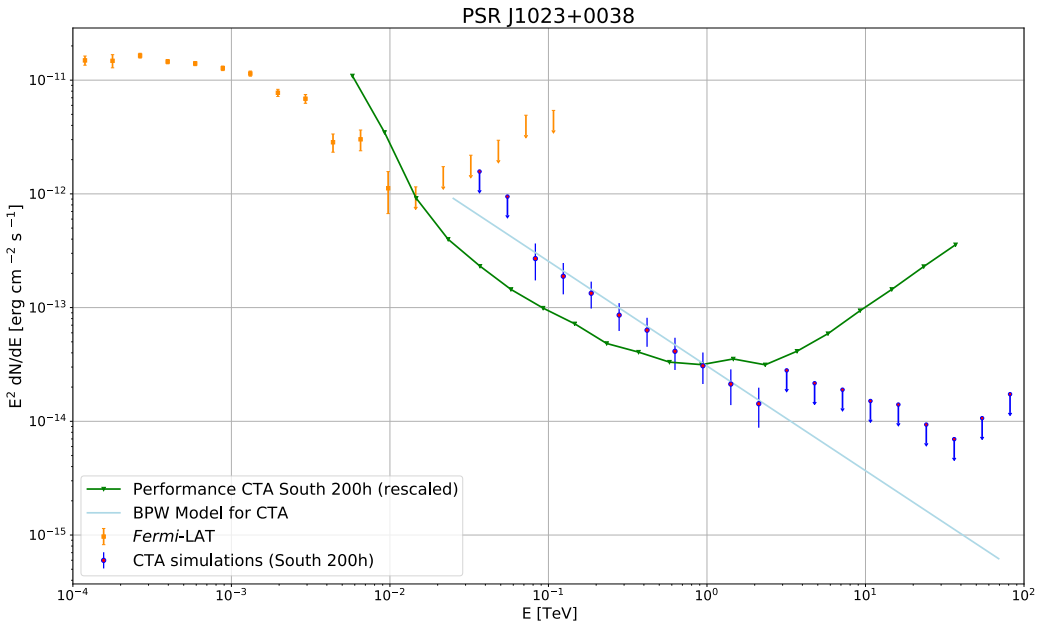

Figure 6.9 CTA South simulations for the tMSP J1023 considering the BPL model. In this plot I report only the results for 200 hours of observations. The CTA performance (green curve), rescaled for 200 hours, is also shown [prod3b-v2]. *Fermi*-LAT data during the accretion phase are reported in orange.

Table 6.2 Results for the unbinned maximum likelihood on the simulated observations for the BPL model (North and South) considering 50, 100 and 200 hours of observation for J1023. In the bottom table the spectral parameters measured in the 200 hours (South) simulations are reported.

	Hours	TS	Significance [σ]
North	50	18.50	4.30
	100	39.86	6.31
	200	77.15	8.78
South	50	29.36	5.42
	100	55.47	7.45
	200	114.77	10.71

PSR J1227−4853 J1227 was in the LMXB state between the 2008 and the 2012 and the *Fermi*-LAT analysis that I performed is consistent with the values reported by Xing & Wang (2015) and Torres et al. (2017). As for J1023, the two spectral models considered for the CTA simulations are the LP and the BPL.

As input models for the CTA simulations we considered the output from the *Fermi*-LAT analysis (see Table 6.3). We performed batches of 100 simulations using only the South IRFs and 50, 100 and 200 hours of observations. The simulated data were binned into 20 logarithmic energy bins in the energy range 0.03-100 TeV.

Spectral Model	Spectral Parameters
BPL	$N_0 = 7.31 \times 10^{-12}$ γ_1=-2.12 γ_2=-2.92 E_b=1.15

Note: N_0 is the prefactor in unit of photons cm^{-2} s^{-1} MeV^{-1}; the break energy E_b is in GeV.

Table 6.3
Spectral input parameters of J1227 inferred from an analysis of the *Fermi*-LAT data in the accretion phase between August 2008 and November 2012.

Models	Spectral Parameters
Broken Power-law (BPL)	$N_0 = (2.71 \pm 0.71) \times 10^{-12}$ γ_1=-2.23±0.04 γ_2=-2.77±0.10 E_b=1.32±1.44
Log-Parabola (PL)	$N_0 = (3.26 \pm 0.91) \times 10^{-11}$ α=2.28 ±0.05 β=0.09±0.02 E_b=4.45±5.42

Note: N_0 is the prefactor in units photons cm^{-2} s^{-1} MeV^{-1}; the break energy E_b is in GeV; the errors are the statistical uncertainties.

In Table 6.4 I show the results of the unbinned analysis for the BPL model. From 200 hours of observation with CTA South I obtain an overall detection significance of 15.9σ (TS $\simeq$ 253.9). I report also the spectral parameters measured in the simulations. As for J1023, simulations considering the LP model failed to produce upper limits. The resulting spectrum of J1227 is shown in Figure 6.10 and, as for J1023, I reported only the results for 200 hours of observation.

Table 6.4 Results for the unbinned maximum likelihood on the simulated observations for the BPL model (North and South) considering 50, 100 and 200 hours of observation for J1227. In the bottom table the spectral parameters measured in the 200 hours (South) simulations are reported.

	Hours	TS	Significance [σ]
South	50	66.26	8.14
	100	128.04	11.31
	200	253.99	15.94

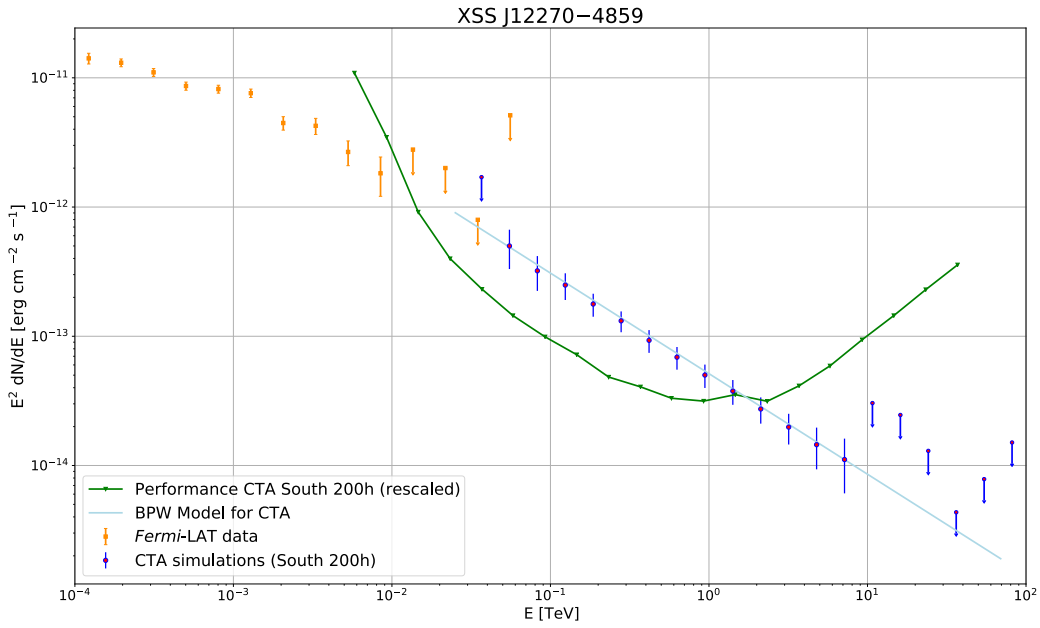

Figure 6.10 CTA South simulations for the tMSP J1227 considering the BPL model. In this plot I show only the results for 200 hours of observation. The CTA performance (green curve) is also shown, rescaled for 200 hours [prod3b-v2]. *Fermi*-LAT data during the accretion phase are reported in orange.

6.6.1 Discussion

These simulations show that CTA will have the sensitivity to detect the VHE emission from tMSPs, during their accretion disk state, in case their spectrum does not exponentially decay but has a PL tail extended beyond the *Fermi*-LAT energy range and consistent with the shape inferred at a few GeV. Measuring the spectral shape and putting strict limits to it will be extremely important to understand the physical processes that produce the gamma-ray emission in these sources. Also, these measurements are important to better constrain the physical models of these systems and the particle injection spectrum.

Spectral Model	Spectral Parameters
BPL	$N_0 = 3.15 \times 10^{-12}$
	γ_1=-2.23
	γ_2=-2.78
	E_b=1.33

Note: N_0 is the prefactor in unit of photons cm^{-2} s^{-1} MeV^{-1}; the break energy E_b is in GeV.

I modelled the combined GeV-TeV spectral energy distribution of the systems as synchrotron emission from a leptonic particle population. I used `naima`[¶], an open source Python package that computes the photon spectrum of a homogeneous distribution of relativistic electrons and protons (Zabalza, 2015). `naima` provides a set of functions that allow to fit theoretical and observed photon spectra through a Markov Chain Monte Carlo (MCMC) procedure, obtaining probability distribution functions for the particle distribution parameters. The Synchrotron radiation is produced by all charged particles in the presence of magnetic fields, and is ubiquitous in the emitted spectrum of leptonic sources. With `naima` it is possible to test if a simple electron distribution can explain the combined spectra of *Fermi*-LAT and CTA.

For these sources, whose physical mechanism and dynamics are still poor understood, I considered two scenarios: the IC and the Synchrotron emission. For the IC model, using the densities of the photon fields of the donor and the disk at the intrabinary shock radius, I did not find solutions with an acceptable energetic for the population of electrons. For this reason I discarded the IC model from the following analysis.

SYNCHROTRON Following Papitto et al. (2019), in the case of synchrotron emission, I considered a magnetic field B of 4.5×10^5 G. They hypothesized that the emission is coming within a few LC radii away (<100 km) from the pulsar, where the medium is permeated by such a large magnetic field and the synchrotron emission is the dominant mechanism for electrons accelerated in the disk/wind intrabinary shock; in this scenario the shock is very close to the LC of the pulsar and to the inner edge of the disk.

In Figures 6.11 and 6.12 I report the fitted synchrotron `naima` SED to the data of J1023 and J1227, respectively. The parameters of the distribution of the electrons (that follows a BPL) are reported in Table 6.5 (J1023) and Table 6.6 (J1227). For the BPL fit of J1227 I assumed the same E_b and γ_1 of J1023 because leaving them free to vary leads to overestimating the flux of the source (which comes out to be even larger than that of the Crab pulsar).

The agreement is better for J1023 because we adopted the value of the magnetic field inferred for this source. J1023 is also the best studied tMSP, for while the largest amount of data is available. As we can see in Figure 6.13, where real data for the source J1023 are reported (from optical to gamma rays), our synchrotron emission model is in agreement with the observed emission. As argued by Papitto et al. (2019) J1023 can be considered a prototype of a few hundred

[¶] `https://naima.readthedocs.io/en/latest/index.html`

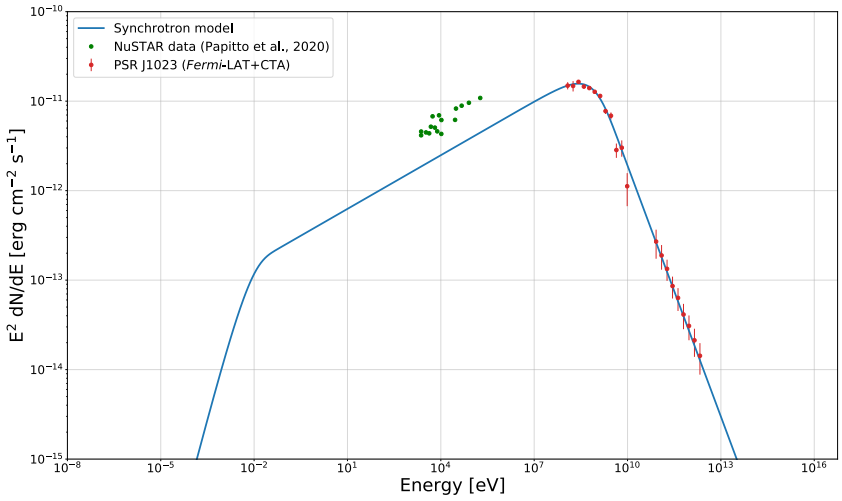

Figure 6.11 Results of the fitted synchrotron `naima` spectral model to the *Fermi*-LAT data and CTA simulations of J1023, assuming a magnetic field of 4.5×10^5 G. For clarity, the *NuSTAR* data (green points) from Papitto & de Martino (2020) are also reported.

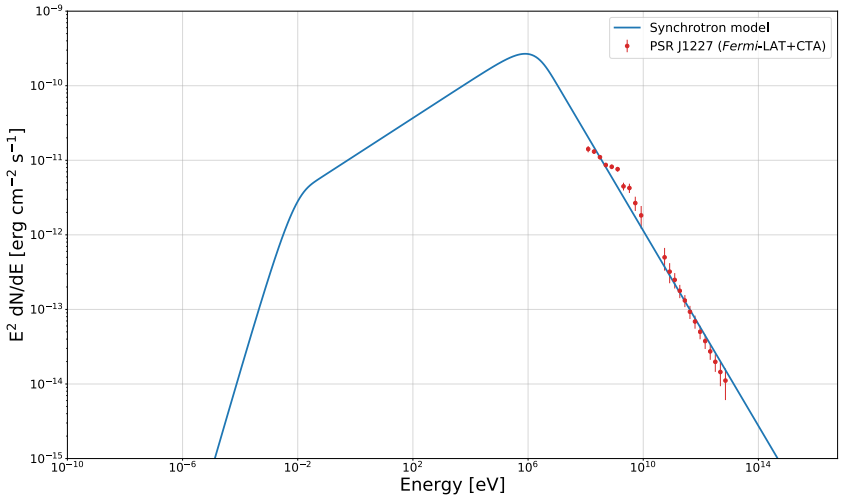

Figure 6.12 Results of the fitted synchrotron `naima` SED to the *Fermi*-LAT data and CTA simulations of J1227, assuming a magnetic field of 4.5×10^5 G.

km-sized PWN, and provide an unique opportunity to study the intrabinary region and the pulsar wind properties in the high magnetisation regime rather than where they are particle-dominated.

The synchrotron emission model with an high magnetic field from a region in the vicinity of the LC, appears to be consistent with the evidences coming from the optical and the X-ray bands (Papitto et al., 2019). In this scenario, the electrons lose all their energy and are not able to feed the IC emission.

Table 6.5 Derived parameters of the BPL model for J1023. γ_1 and γ_2 are the first and second power law index, E_b is the break energy of the electron population.

Parameter	*Fermi*-LAT and CTA
BPL	$N_0 = 7.01 \times 10^{44}$ eV^{-1} γ_1=-2.58 γ_2=-3.94 E_b=7.59 GeV

Table 6.6 Derived parameters of the BPL model for J227. γ_1 and γ_2 are the first and second power law index, E_b is the break energy of the electron population.

Parameter	*Fermi*-LAT and CTA
BPL	$N_0 = 6.89 \times 10^{43}$ eV^{-1} γ_1=-2.58 γ_2=-3.77 E_b=7.59 GeV

I calculated the total energy that electrons should achieve to be accelerated and produce a very bright synchrotron emission for the assumed magnetic field. In the case of J1023 I obtained an energy of about 4×10^{29} erg and for J1227 it is about 10^{31} erg.

6.7 Spin-down rate of the transitional millisecond pulsar PSR J1023+0038 in the optical band with Aqueye+

In order to understand the mechanism powering this source during the low-luminous disk state, a crucial piece of information is the average spin-down rate of J1023. During my PhD I also worked on these type of measurements using the high time resolution photon counter Aqueye+[‖] mounted at the 1.82 m Copernicus telescope in Asiago. This fast photon counter has a field of view of few arcsec and the capability of time tagging the detected photons with sub-ns time accuracy (Barbieri et al., 2009; Zampieri et al., 2015). In the work of Burtovoi et al. (2020) we report the first measurements of the timing solution and the frequency derivative of J1023 based entirely on optical data. We analyzed five observing runs of Aqueye+ taken in three years (2018-2020). The data have been reduced with the dedicated QUEST software (Zampieri et al., 2015, v. 1.1.5); the arrival time of each photon was referred to the barycenter of the solar

[‖] https://web.oapd.inaf.it/zampieri/aqueye-iqueye/index.html

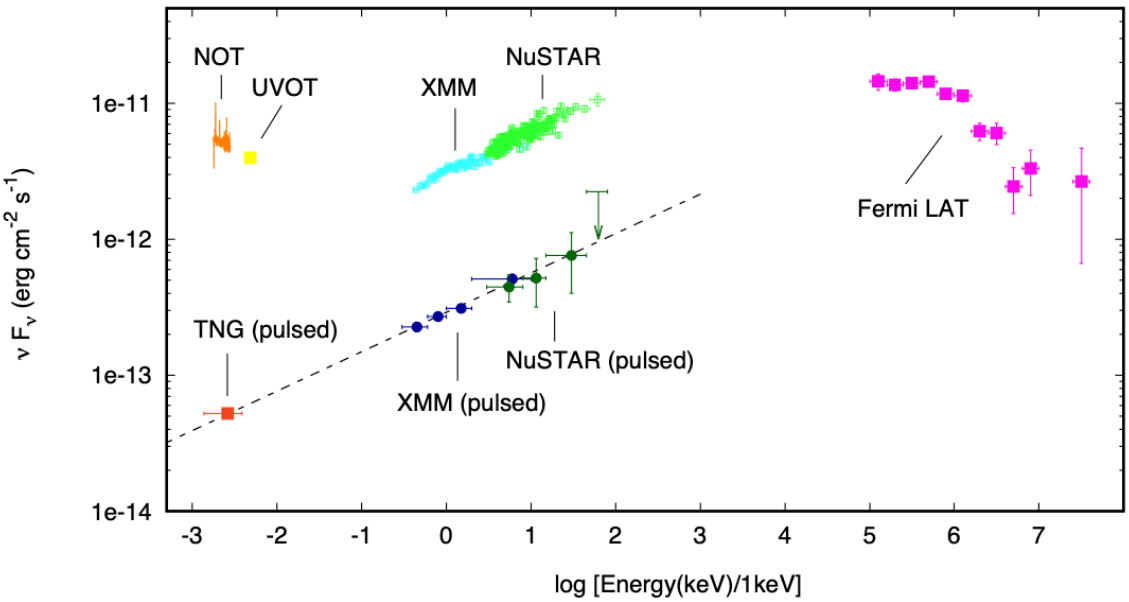

Figure 6.13 Total and pulsed spectral energy distribution of J1023 in the *high* mode, corrected for interstellar extinction. The NOT optical spectrum is plotted with an orange line. The average pulsed *TNG/SiFAP* optical flux observed in May 2017 is plotted with a red square. The flux observed by *Swift* is plotted with a yellow square. The total and pulsed X-ray flux observed by *XMM-Newton* are plotted with light and dark blue points, respectively. The total and pulsed X-ray flux observed by *NuSTAR* are plotted with light and dark green points, respectively. Magenta squares show the average *Fermi*-LAT spectrum measured by Torres et al. (2017).

system using the `TEMPO2` package (Hobbs et al., 2006a) and the JPL ephemerides DE405[**].

We found that in 2018-2020 the spin-down rate of J1023 is $\dot{\nu} = (-2.53 \pm 0.04) \times 10^{-15}$ Hz^2, which is about 20% slower than that measured from the X-ray observations taken in 2013-2016 by Jaodand et al. (2016) with *XMM-Newton* ($\dot{\nu}_x = -3.04 \times 10^{-15}$ Hz^2) and about 5% faster than that measured in the radio band during the rotation-powered state ($\dot{\nu}_r = -2.40 \times 10^{-15}$ Hz^2; Jaodand et al. (2016)).

On the other hand, the value of the spin down rate inferred from previous X-ray measurements (Jaodand et al., 2016) implies that the pulsar is spinning down at a rate approximately 27% faster than the rate measured during the radio phase. Haskell & Patruno (2017) suggested that this increase in spin-down rate is compatible with GW emission and, in particular, it is caused by the creation of a 'mountain' (i.e. asymmetries in the mass distribution, supported either by crustal or magnetic strains) during the accretion phase. The fact that the value found in this work is about 5% faster than the radio value, suggests in fact that the losses due to the GW emission are lower than proposed in Haskell & Patruno

[**] `https://ssd.jpl.nasa.gov/?planet_eph_export`

(2017). Our results are more in line with the scenario reported by Papitto et al. (2019): optical and X-ray pulses, that originate from a common underlying physical mechanism, are produced by synchrotron emission at the intrabinary shock that forms where a striped pulsar wind meets the accretion disk, within a few light cylinder radii away (∼100 km) from the pulsar. In this case the average pulsar spin down should be dominated by the magnetic dipole and pulsar wind emission, and hence be comparable to that measured during the radio pulsar phase.

In the next future, it will be extremely challenging and important to perform these optical observations in synergy with the observations at the highest energies (with MAGIC, LST and the future CTA observatory). Multiwavelength observations are essential to understand the geometry and the size of these systems, the mechanisms that are feeding them, the energetic of the particles that are created and accelerated in these still poorly known sources.

7

Conclusion and Future Prospects

In this thesis I focused on the study and the characterization of the VHE emission component from Galactic sources, such as pulsars, millisecond pulsars and transitional millisecond pulsars.

This study was done, mainly, analyzing data from the MAGIC telescopes. All the MAGIC analyses were performed with the novel stereoscopic trigger, the Sum-Trigger-II system, that enhances the sensitivity of the telescopes below 100 GeV. Observations in the energy range between 10 GeV and 100 GeV are crucial to distinguish between different emission models of pulsars in the HE and VHE ranges as it is not yet clear what are the processes that allow some peculiar pulsars to exceed the cut-off of the radiation curvature. The Sum-Trigger-II allows to reduce the MAGIC energy threshold by a factor of two, improving the sensitivity at these energies (Dazzi et al., 2021). To take full advantage of

the lowered energy threshold, the observation required a specialized data analysis procedure that I learned during my first year of PhD at the two Sum-Trigger-II analysis schools.

My efforts were concentrated on three objects: the Crab pulsar, PSR J0218+4232 and PSR J2229+6114. The Crab pulsar is a well known gamma-ray emitter with a pulsed emission detected up to TeV energies (Ansoldi et al., 2016); PSR J0218+4232 is one of the youngest and most energetic MSPs known to date and *Fermi*-LAT studies have suggested that it may be one of the best candidates to search for VHE gamma-ray emission. PSR J2229+6114 is another young and energetic pulsar whose pulsed GeV emission was detected with the *Fermi*-LAT satellite (Abdo et al., 2009). For the study of the Crab pulsar with MAGIC, presented in Chapter 3, a data sample gathering 110 hours of good data was collected. These observations aimed at searching for a possible variability of the flux at the very high energies but, as reported in Section 3.3.5, no significant flux variability was found in the MAGIC Sum-Trigger Crab observations. The spectra of the Crab pulsar and nebula were measured down to 20 GeV and they are well characterized by a power-law function and a log-parabola, respectively. The study of the light curve above 20 GeV allowed a significant detection of the signal from P1, P2 and the interpeak region (the bridge), located between P1 and P2, up to 300 GeV. This results demonstrates that MAGIC is a powerful instrument to probe the gamma-ray sky in the 20 GeV to 100 GeV energy range, where satellite missions suffer from low photon statistics.

In Chapter 4 the MAGIC analysis of the pulsar PSR J2229+6114 is presented. I analyzed about 28 hours taken with the Sum-Trigger-II system. The MAGIC spectral energy distribution, in the range between 38 GeV and 50 TeV, shows only ULs and, from the phasoegram, no significant signal detection was found. Although this source is detected up to 20 GeV in the *Fermi*-LAT energy range, the non detection with MAGIC could be due to various reasons: a low target photon field, or the instrument sensitivity limit, or the fact that the pulsar has a small viewing angle and so the gamma-ray emission is not detectable (Guillemot & Tauris, 2014).

In Chapter 5 I present the major work and result of my doctoral project: the MAGIC analysis of the millisecond pulsar PSR J0218+4232. The results are reported in the paper "Search for Very High-Energy Emission from the millisecond pulsar PSR J0218+4232" (Acciari et al., 2021). The observation and data analysis of about 90 hours of good data from the MAGIC telescopes resulted in no significant detection, so upper limits above 20 GeV were calculated. The data were fitted with a power-law function. In addition to the MAGIC data, 11.5 years of *Fermi*-LAT data were

also analyzed and we find evidence for pulsed emission above 25 GeV. The *Fermi*-LAT data, between 100 MeV and 870 GeV, are well described by a power-law with an exponential cut-off, defined as $\frac{dN}{dE} = N_0(\frac{E}{E_0})^{\gamma} exp(-aE_b)$, where $N_0 = 2.07 \times 10^{-11}$ ph cm^{-2} s^{-1} MeV^{-1}, E_0=821.6 MeV, $\gamma = -1.76$, a= 6.2 $\times 10^{-3}$ and b=2/3.
The measured MAGIC upper limits are well above the two theoretical model predictions considered for VHE gamma-ray emission and the curvature radiation component, from particles accelerated mostly in the current sheet, is expected to fall to VHE flux levels that are too low to be detected with MAGIC. The IC components from both pairs (mostly SSC) and accelerated primaries are predicted to be at even lower flux levels. After the experimental observations and theoretical modeling, we conclude that it is extremely challenging to detect VHE emission from PSR J0218+4232 with the current generation of IACTs, and maybe even with future ones, such as the CTA.

The last work presented in this Thesis was carried out within the framework of the CTA project. The subject of this study are the tMSPs. These sources show transitions from a rotation-powered regime, in which they behave like radio pulsars, to a regime in which they accrete and emit intense high-energy radiation like X-ray binary systems, and vice versa. I simulated observations of the two tMSPs PSR J1023+0038 and XSS J12270-485 with CTA North and South during their disk accretion phase, state in which they show an enhanced gamma-ray emission. The simulations show that CTA will have the sensitivity to detect the VHE emission from tMSPs, during their accretion disk state, in case their spectrum does not exponentially decay but has a PL tail extending beyond the *Fermi*-LAT energy range and consistent with the shape inferred at a few GeV. Furthermore, the combined GeV-TeV spectral energy distribution of the systems was modelled as synchrotron emission from a leptonic particle population in order to shed light on its origin.

For improving our understanding of the physics of gamma-ray pulsars, MSPs, and tMSPs, it will be extremely important to detect more of them, and to build a larger sample of this mysterious family. The MAGIC telescopes equipped with the Sum-Trigger-II system, as well as the up-coming LST telescopes of the CTA Observatory, can and should perform a systematic search for other similar objects. Furthermore, also the simulations and prospects presented in the CTA paper on Galactic transients sources (López-Oramas et al., 2021), could improve our understanding of the physics of these systems.

Glossary

a.s.l. above sea level. 31

ACM Active Mirror Control. 42

ADC Analog-to-Digital Converter. 45, 59

AGN Active Galactic Nuclei. 48, 90

AMC Active Mirror Control. 40, 41, 82

APNS Accretion-Powered Neutron Star. 100

Az Azimuth. 39, 42, 47, 77

BH Black Hole. 17, 19, 96, 97, 100

BPL Broken Power-Law. 180–185, 187

BW Black Widow. 125

C Carbon. 96, 98

C.L. Confidence Level. 80, 118, 157

C.U. Crab Units. 72

CC Central Control. 38, 54

CCD Charge-Coupled Device. 40, 42

CCO Compact Central Object. 100, 103, 104

CH Counting House. 43, 44, 50–53

CMB Cosmic Microwave Background. 7

CoG Center of Gravity. 66, 68

CORSIKA COsmic Ray SImulations for KAscade. 60

CR Cosmic Ray. 3–9, 31, 130

CTA Cherenkov Telescope Array. iii, x, 27, 37, 38, 88, 89, 91, 92, 130, 165, 169, 179–185, 189, 193

DAQ Data AcQuisition. 44–46, 55, 59

DC Direct Current. 56

DM Dispersion Measure. 128

DRS Domino Ring Sampler. 58, 59

DRS4 Domino Ring Sampler version 4. 44–46

DT Discriminator Threshold. 46

EAS EAS. 4, 21, 27, 28, 31, 34, 46, 48, 49

EBL Extragalactic Background Light. 15

EM Electromagnetic. 31–34, 50, 58

Fe Iron. 96

FoV Field of View. 40, 42, 47, 50, 63, 76, 82, 87, 90, 160

FWHM Full Width Half Maximum. 43, 49, 50

GCN GRB Coordinate Network. 54

GPS Global Positioning System. 53, 119

GRB Gamma-Ray Burst. 19, 20, 22, 38, 48, 54, 90

GW Gravitational Wave. 38, 188

GZK Greisen-Zatsepin-Kuzmin. 6, 7

H Hydrogen. 96, 98, 175

HE High Energy. 6, 15, 21, 22, 55, 95, 103, 109, 112–115, 117, 172, 176, 177, 180, 191

He Helium. 96, 98, 175

HMXB High Mass X-ray Binary. 17, 101

HV High Voltage. 56

IACT Imaging Atmospheric Cherenkov Telescope. iii, 21, 24, 27, 34, 35, 72, 81, 82, 88, 111, 179, 193

IC Inverse Compton. 13–15, 17, 109, 110, 112, 114, 115, 142, 159, 160, 176, 177, 185, 186, 193

ICS Inverse Compton Scattering. 161, 164, 165

IMXB Intermediate Mass X-ray Binary. 101

INAF Istituto Nazionale di AstroFisica. 41

INFN Istituto Nazionale di Fisica Nucelare. 41, 45

INS Isolated Neutron Star. 100, 103, 104

IPRC Individual Pixel Rate Control. 56

IR Infrared. 30, 53, 109, 110, 115

IRF Instrument Response Function. 72, 73, 76, 181, 182

ISM Interstellar Medium. 17, 84

LAT Large Area Telescope. 147

LC Light Cylinder. 105, 110, 115, 185, 186

LE Low Energy. 55

LED Light-Emitting Diode. 40, 43

LIDAR LIght Detection And Ranging. 42, 52, 53, 65, 82, 136, 157

LMXB Low Mass X-ray Binary. 17, 18, 100, 125, 126, 167–171, 179, 180, 182

LoNS Light of the Night Sky. 48–51

LP Log Parabola. 180–183

LST Large Size Telescope. 37, 90, 92, 181, 189, 193

LUT Look-Up Table. 42, 67, 136

MAGIC Major Atmospheric Gamma-ray Imaging Cherenkov. iii, ix–xi, xiii, 16, 19, 24, 25, 27, 30, 35, 37, 38, 40, 41, 43–48, 50–62, 64–66, 69–77, 79–83, 86, 88, 95, 113, 115, 116, 118, 120, 121, 136, 137, 140–143, 148–151, 154, 156–165, 189, 191–193

MARS MAGIC Analysis and Reconstruction Software. 59, 60, 62, 66, 67, 69, 87, 136, 157

MC Monte Carlo. 49, 57, 60–62, 68, 72, 73, 75, 76, 78, 79, 82, 83, 87, 116–119, 136

MCMC Markov Chain Monte Carlo. 185

Mg Magnesium. 96

MOLA MAGIC OnLine Analysis. 55

MPI Max Planck Institute. 41

MSP Millisecond Pulsar. iii, xi, 101, 103, 104, 124–126, 142–144, 147, 148, 152, 157, 163–165, 167–170, 172, 176–178, 192, 193

MST Medium Size Telescope. 90, 92, 181

Ne Neon. 96

Ni Nichel. 96

NN Next Neighbour. 46, 47, 63

NS Neutron Star. 16, 17, 19, 96–109, 124–126, 128, 135, 159, 169, 171, 175, 178, 179

NSB Night Sky Background. 34, 42, 46, 59, 62, 63, 82

O Oxygen. 96

OG Outer Gap. 109, 110, 133, 142, 165

ORM Observatorio del Roque de los Muchachos. 35, 37, 38

OSA On-Site Analysis. 54, 60

PC Polar Cap. 109, 110, 159, 160, 165

PDF Probability Density Function. 153

PL Power-Law. 172, 173, 180, 183, 184, 193

PLEC Power-Law with Exponential Cut-off. 173, 176, 180

PMT Photomultiplier Tubes. 23, 40, 42–44, 46–50, 54, 56, 62, 82, 86, 90

PSF Point Spread Function. 21, 42, 77

PULSAR PULSer And Recorder. 45

PWN Pulsar Wind Nebula. 17, 91, 127–131, 186

QE Quantum Efficiency. 42

RB Redback. 125, 126

RF Random Forest. 67, 68, 87, 136

RMS Root Mean Square. 68

RMSP Radio Millisecond Pulsar. 167–169, 175

RPP Rotation-Powered Pulsar. 99

RRAT Rotating Radio Transient. 103, 104

SA SuperArehucas. 54

SBIG Santa Barbara Instrument Group. 41, 42

SC Synchrotron-Curvature. 159–162

SED Spectral Energy Distribution. 81, 115, 117–119, 137, 163, 185, 186

SG Slot Gap. 109, 110, 133

SiPM Silicon PhotoMultiplier. 91

SMBH Supermassive Black Hole. 18–20

SN Supernova. 11, 15, 19, 96, 111, 124

SNR Supernova Remnant. 6, 15, 17, 91, 100, 127, 129, 130

SR Synchrotron Radiation. 160, 165

SSB Solar System Barycenter. 84

SSC Synchrotron Self Compton. 14, 115, 160, 164, 165, 178, 193

SST Small Size Telescope. 91, 92, 181

SumT Sum-Trigger-II. 44

tMSP Transitional Millisecond Pulsar. iii, 18, 101, 125, 126, 167–169, 171–174, 177, 179, 182, 184, 185, 193

ToA Time of Arrival. 83–85, 119

TPU Trigger Processing Unit. 47

TS Test Statistics. 77, 151–153

UHE Ultra High Energy. 7, 10, 21, 23

UHECR Ultra High Energy Cosmic Ray. 6, 7

UL Upper Limit. 80, 118, 119, 170, 174, 176, 192

UV Ultraviolet. 28–30, 100, 110, 159, 177, 178

VHE Very-High-Energy. iii, 4, 10, 13, 15–23, 27, 35, 71, 91, 95, 102, 110–112, 114, 115, 117, 130, 132, 133, 137, 138, 142, 156, 158–160, 163–165, 169, 176, 177, 180, 184, 191–193

VLZA Very Large Zenith Angle. 42

WD White Dwarf. 96–98

Zd Zenith distance. 39, 42, 47, 57, 61, 62, 77

References

Abdo, A. A., Allen, B., Berley, D., et al. 2007, ApJL, 664, L91, doi: 10.1086/520717

Abdo, A. A., Ackermann, M., Ajello, M., et al. 2009, ApJ, 706, 1331, doi: 10.1088/0004-637X/706/2/1331

—. 2010a, ApJ, 708, 1254, doi: 10.1088/0004-637X/708/2/1254

—. 2010b, apjs, 188, 405, doi: 10.1088/0067-0049/188/2/405

—. 2010c, apjs, 187, 460, doi: 10.1088/0067-0049/187/2/460

Abdo, A. A., Ajello, M., Allafort, A., et al. 2013, apjs, 208, 17, doi: 10.1088/0067-0049/208/2/17

Abdollahi, S., Acero, F., Ackermann, M., et al. 2020, VizieR Online Data Catalog, J/ApJS/247/33

Abramowski, A., Acero, F., Aharonian, F., et al. 2012, ApJ, 757, 158, doi: 10.1088/0004-637X/757/2/158

Acciari, V. A., Beilicke, M., Blaylock, G., et al. 2008, ApJ, 679, 1427, doi: 10.1086/587736

Acciari, V. A., Aliu, E., Arlen, T., et al. 2009a, ApJL, 703, L6, doi: 10.1088/0004-637X/703/1/L6

—. 2009b, ApJL, 693, L104, doi: 10.1088/0004-637X/693/2/L104

Acciari, V. A., Ansoldi, S., Antonelli, L. A., et al. 2021, arXiv e-prints, arXiv:2108.11373. https://arxiv.org/abs/2108.11373

Acharya, B. S., Actis, M., Aghajani, T., et al. 2013, Astroparticle Physics, 43, 3, doi: 10.1016/j.astropartphys.2013.01.007

Ackermann, M., Ajello, M., Allafort, A., et al. 2013, apjs, 209, 34, doi: 10.1088/0067-0049/209/2/34

Aharonian, F., Bogovalov, S., & Khangulyan, D. 2012, Nature, 482, 507, doi: 10.1038/nature10793

Aharonian, F., Akhperjanian, A., Barrio, J., et al. 2001, A&A, 370, 112, doi: 10.1051/0004-6361:20010243

Aharonian, F., Akhperjanian, A. G., Aye, K. M., et al. 2004, A&A, 425, L13, doi: 10.1051/0004-6361:200400055

—. 2005, A&A, 442, 1, doi: 10.1051/0004-6361:20052983

Aharonian, F., Akhperjanian, A. G., Bazer-Bachi, A. R., et al. 2006, A&A, 460, 743, doi: 10.1051/0004-6361:20065940

Aharonian, F., An, Q., Axikegu, et al. 2020, arXiv e-prints, arXiv:2010.06205. https://arxiv.org/abs/2010.06205

Aharonian, F. A. 2004, Very high energy cosmic gamma radiation : a crucial window on the extreme Universe (World Scientific Publishing Co Pte Ltd), doi: 10.1142/4657

Aharonian, F. A., Akhperjanian, A. G., Bazer-Bachi, A. R., et al. 2007, A&A, 469, L1, doi: 10.1051/0004-6361:20077299

Ajello, M., Atwood, W. B., Baldini, L., et al. 2017, apjs, 232, 18, doi: 10.3847/1538-4365/aa8221

Albats, P., Frye, G. M., & Zych, A. D. 1972, Nature, 240, 221, doi: 10.1038/240221a0

Albert, J., Aliu, E., Anderhub, H., et al. 2007, Nuclear Instruments and Methods in Physics Research A, 583, 494, doi: 10.1016/j.nima.2007.09.048

—. 2008, Nuclear Instruments and Methods in Physics Research A, 588, 424, doi: 10.1016/j.nima.2007.11.068

Aleksić, J., Alvarez, E. A., Antonelli, L. A., et al. 2011, ApJ, 742, 43, doi: 10.1088/0004-637X/742/1/43

—. 2012a, Astroparticle Physics, 35, 435, doi: 10.1016/j.astropartphys.2011.11.007

—. 2012b, A&A, 540, A69, doi: 10.1051/0004-6361/201118166

Aleksić, J., Ansoldi, S., Antonelli, L. A., et al. 2014, A&A, 565, L12, doi: 10.1051/0004-6361/201423664

—. 2016a, Astroparticle Physics, 72, 61, doi: 10.1016/j.astropartphys.2015.04.004

—. 2016b, Astroparticle Physics, 72, 76, doi: 10.1016/j.astropartphys.2015.02.005

Aleksić, J., Ansoldi, S., Antonelli, L., et al. 2015, Journal of High Energy Astrophysics, 5-6, 30–38, doi: 10.1016/j.jheap.2015.01.002

Aliu, E., Anderhub, H., Antonelli, L. A., et al. 2008, Science, 322, 1221, doi: 10.1126/science.1164718

—. 2009a, Astroparticle Physics, 30, 293, doi: 10.1016/j.astropartphys.2008.10.003

—. 2009b, ApJL, 692, L29, doi: 10.1088/0004-637X/692/1/L29

Aliu, E., Archambault, S., Archer, A., et al. 2016, ApJ, 831, 193, doi: 10.3847/0004-637X/831/2/193

Alpar, M. A., Cheng, A. F., Ruderman, M. A., & Shaham, J. 1982, Nature, 300, 728, doi: 10.1038/300728a0

Ambrosino, F., Papitto, A., Stella, L., et al. 2017, Nature Astronomy, 1, 854, doi: 10.1038/s41550-017-0266-2

Anderhub, H., Antonelli, L. A., Antoranz, P., et al. 2010, ApJ, 710, 828, doi: 10.1088/0004-637X/710/1/828

Ansoldi, S., Antonelli, L. A., Antoranz, P., et al. 2016, A&A, 585, A133, doi: 10.1051/0004-6361/201526853

Archibald, A. 2015, in APS Meeting Abstracts, Vol. 2015, APS April Meeting Abstracts, B9.001

Archibald, A. M., Kaspi, V. M., Bogdanov, S., et al. 2010, ApJ, 722, 88, doi: 10.1088/0004-637X/722/1/88

Archibald, A. M., Kaspi, V. M., Hessels, J. W. T., et al. 2013, arXiv e-prints, arXiv:1311.5161. https://arxiv.org/abs/1311.5161

Archibald, A. M., Stairs, I. H., Ransom, S. M., et al. 2009, Science, 324, 1411, doi: 10.1126/science.1172740

Arka, I., & Dubus, G. 2013, A&A, 550, A101, doi: 10.1051/0004-6361/201220110

Arons, J. 1983, ApJ, 266, 215, doi: 10.1086/160771

Arons, J., & Scharlemann, E. T. 1979, ApJ, 231, 854, doi: 10.1086/157250

Arons, J., & Tavani, M. 1993, ApJ, 403, 249, doi: 10.1086/172198

Atoyan, A., & Dermer, C. D. 2012, ApJL, 749, L26, doi: 10.1088/2041-8205/749/2/L26

Atwood, W., Albert, A., Baldini, L., et al. 2013, arXiv e-prints, arXiv:1303.3514. https://arxiv.org/abs/1303.3514

Atwood, W. B., Abdo, A. A., Ackermann, M., et al. 2009, The Astrophysical Journal, 697, 1071–1102, doi: 10.1088/0004-637x/697/2/1071

Atwood, W. B., Abdo, A. A., Ackermann, M., et al. 2009, ApJ, 697, 1071, doi: 10.1088/0004-637X/697/2/1071

Auger, P., Ehrenfest, P., Maze, R., Daudin, J., & Fréon, R. A. 1939, Reviews of Modern Physics, 11, 288, doi: 10.1103/RevModPhys.11.288

Baade, W., & Zwicky, F. 1934, Proceedings of the National Academy of Science, 20, 254, doi: 10.1073/pnas.20.5.254

Backer, D. C., Kulkarni, S. R., Heiles, C., Davis, M. M., & Goss, W. M. 1982, Nature, 300, 615, doi: 10.1038/300615a0

Bahramian, A., Strader, J., Chomiuk, L., et al. 2018, ApJ, 864, 28, doi: 10.3847/1538-4357/aad68b

Barbieri, C., Naletto, G., Occhipinti, T., et al. 2009, Journal of Modern Optics, 56, 261, doi: 10.1080/09500340802450565

Bassa, C. G., van Kerkwijk, M. H., & Kulkarni, S. R. 2003, A&A, 403, 1067, doi: 10.1051/0004-6361:20030384

Bassa, C. G., Patruno, A., Hessels, J. W. T., et al. 2014, MNRAS, 441, 1825, doi: 10.1093/mnras/stu708

Becker, W., Kramer, M., & Sesana, A. 2018, Space Science Reviews, 214, doi: 10.1007/s11214-017-0459-0

Bednarek, W. 2012, MNRAS, 424, 2079, doi: 10.1111/j.1365-2966.2012.21354.x

Bell, A. R. 1992, MNRAS, 257, 493, doi: 10.1093/mnras/257.3.493

Bennett, K., Bignami, G. F., Boella, G., et al. 1977, A&A, 61, 279

Berge, D., Funk, S., & Hinton, J. 2007, A&A, 466, 1219, doi: 10.1051/0004-6361:20066674

Bigongiari, C. 2005, in International Europhysics Conference on High Energy Physics, HEP2005, 20. https://arxiv.org/abs/astro-ph/0512184

Biland, A., Garczarczyk, M., Anderhub, H., et al. 2008, in International Cosmic Ray Conference, Vol. 3, International Cosmic Ray Conference, 1353–1356. https://arxiv.org/abs/0709.1574

Bogdanov, S. 2016, ApJ, 826, 28, doi: 10.3847/0004-637X/826/1/28

Bogdanov, S., Archibald, A. M., Hessels, J. W. T., et al. 2011, ApJ, 742, 97, doi: 10.1088/0004-637X/742/2/97

Bogdanov, S., Archibald, A. M., Bassa, C., et al. 2015, ApJ, 806, 148, doi: 10.1088/0004-637X/806/2/148

Bond, H. E., White, R. L., Becker, R. H., & O'Brien, M. S. 2002, PASP, 114, 1359, doi: 10.1086/344381

Borla Tridon, D., Goebel, F., Fink, D., et al. 2009, arXiv e-prints, arXiv:0906.5448. https://arxiv.org/abs/0906.5448

Bretz, T., Dorner, D., Wagner, R. M., & Sawallisch, P. 2009, Astroparticle Physics, 31, 92, doi: 10.1016/j.astropartphys.2008.12.001

Bruel, P., Burnett, T. H., Digel, S. W., et al. 2018, arXiv e-prints, arXiv:1810.11394. https://arxiv.org/abs/1810.11394

Brun, P. 2012, in American Institute of Physics Conference Series, Vol. 1446, Frontiers of Fundamental Physics: The Eleventh International Symposium, ed. J. Kouneiher, C. Barbachoux, T. Masson, & D. Vey, 268–280, doi: 10.1063/1.4732717

Burke, B. F., & Graham-Smith, F. 2014, An Introduction to Radio Astronomy (Cambridge University Press)

Burtovoi, A., Saito, T. Y., Zampieri, L., & Hassan, T. 2017, MNRAS, 471, 431, doi: 10.1093/mnras/stx1582

Burtovoi, A., Zampieri, L., Fiori, M., et al. 2020, MNRAS, 498, L98, doi: 10.1093/mnrasl/slaa133

Campana, S., Coti Zelati, F., Papitto, A., et al. 2016, A&A, 594, A31, doi: 10.1051/0004-6361/201629035

Carrasco-Casado, A., Vilera, M., Vergaz, R., & Cabrero, J. F. 2013, AO, 52, 2353, doi: 10.1364/AO.52.002353

Chen, H.-L., Chen, X., Tauris, T. M., & Han, Z. 2013, ApJ, 775, 27, doi: 10.1088/0004-637X/775/1/27

Cheng, A. F. 1986, Johns Hopkins APL Technical Digest, 7, 348

Cheng, K. S., & Zhang, J. L. 1996, ApJ, 463, 271, doi: 10.1086/177239

Cherenkov, P. A. 1934, Dokl. Akad. Nauk SSSR, 2, 451, doi: 10.3367/UFNr.0093.196710n.0385

Chernyakova, M., Malyshev, D., Paizis, A., et al. 2019, A&A, 631, A177, doi: 10.1051/0004-6361/201936501

Cocke, W. J., Disney, M. J., & Taylor, D. J. 1969, Nature, 221, 525, doi: 10.1038/221525a0

Cordes, J. M., & Lazio, T. J. W. 2002, arXiv e-prints, astro. https://arxiv.org/abs/astro-ph/0207156

Coti Zelati, F., Torres, D. F., Li, J., & Viganò, D. 2020, MNRAS, 492, 1025, doi: 10.1093/mnras/stz3485

Coti Zelati, F., Baglio, M. C., Campana, S., et al. 2014, MNRAS, 444, 1783, doi: 10.1093/mnras/stu1552

CTA Consortium. 2019, in European Physical Journal Web of Conferences, Vol. 209, European Physical Journal Web of Conferences, 01038, doi: 10.1051/epjconf/201920901038

Cumming, A., Zweibel, E., & Bildsten, L. 2001, ApJ, 557, 958, doi: 10.1086/321658

Davies, J. M., & Cotton, E. S. 1957, Solar Energy, 1, 16, doi: 10.1016/0038-092X(57)90116-0

Dazzi, F. 2012, PhD thesis, Udine (Italy)

Dazzi, F., Schweizer, T., Ceribella, G., et al. 2021, IEEE Transactions on Nuclear Science, 1, doi: 10.1109/TNS.2021.3079262

De Angelis, A., & Pimenta, M. 2018, Introduction to Particle and Astroparticle Physics (pringer Nature), doi: 10.1007/978-3-319-78181-5

de Jager, O. C., Raubenheimer, B. C., & Swanepoel, J. W. H. 1989, A&A, 221, 180

de Martino, D., Falanga, M., Bonnet-Bidaud, J. M., et al. 2010a, A&A, 515, A25, doi: 10.1051/0004-6361/200913802

—. 2010b, A&A, 515, A25, doi: 10.1051/0004-6361/200913802

de Martino, D., Casares, J., Mason, E., et al. 2014, MNRAS, 444, 3004, doi: 10.1093/mnras/stu1640

de Martino, D., Papitto, A., Belloni, T., et al. 2015, MNRAS, 454, 2190, doi: 10.1093/mnras/stv2109

de Naurois, M. 2019, The Astronomer's Telegram, 13052, 1

de Naurois, M., & Mazin, D. 2015, Comptes Rendus Physique, 16, 610, doi: 10.1016/j.crhy.2015.08.011

de Naurois, M., & Mazin, D. 2015, Comptes Rendus Physique, 16, 610–627, doi: 10.1016/j.crhy.2015.08.011

Deller, A. T., Archibald, A. M., Brisken, W. F., et al. 2012, ApJL, 756, L25, doi: 10.1088/2041-8205/756/2/L25

Deller, A. T., Moldon, J., Miller-Jones, J. C. A., et al. 2015a, ApJ, 809, 13, doi: 10.1088/0004-637X/809/1/13

—. 2015b, ApJ, 809, 13, doi: 10.1088/0004-637X/809/1/13

Deneva, J. S., Ray, P. S., Lommen, A., et al. 2019, ApJ, 874, 160, doi: 10.3847/1538-4357/ab0966

Doro, M., Bastieri, D., Biland, A., et al. 2008, Nuclear Instruments and Methods in Physics Research A, 595, 200, doi: 10.1016/j.nima.2008.07.073

Du, Y., Yang, J., Campbell, R. M., et al. 2014, ApJL, 782, L38, doi: 10.1088/2041-8205/782/2/L38

Dubus, G. 2013, A&A Rev., 21, 64, doi: 10.1007/s00159-013-0064-5

Duyvendak, J. J. L. 1942, PASP, 54, 91, doi: 10.1086/125409

Enoto, T., Terasawa, T., Kisaka, S., et al. 2021, Science, 372, 187, doi: 10.1126/science.abd4659

Espinoza, C. M., Lyne, A. G., Stappers, B. W., & Kramer, M. 2011, MNRAS, 414, 1679, doi: 10.1111/j.1365-2966.2011.18503.x

Evoli, C. 2018, The Cosmic-Ray Energy Spectrum, Zenodo, doi: 10.5281/zenodo.4309926

Fawley, W. M., Arons, J., & Scharlemann, E. T. 1977, ApJ, 217, 227, doi: 10.1086/155573

Fender, R. 2016, Astronomische Nachrichten, 337, 381, doi: 10.1002/asna.201612317

Fermi, E. 1949, Phys. Rev., 75, 1169, doi: 10.1103/PhysRev.75.1169

Fierro, J. M., Michelson, P. F., Nolan, P. L., & Thompson, D. J. 1998, ApJ, 494, 734, doi: 10.1086/305219

Fomin, V. P., Stepanian, A. A., Lamb, R. C., et al. 1994, Astroparticle Physics, 2, 137, doi: 10.1016/0927-6505(94)90036-1

Fraija, N., Dichiara, S., Pedreira, A. C. C. d. E. S., et al. 2019, ApJ, 885, 29, doi: 10.3847/1538-4357/ab3e4b

Freire, P. C. C., & Tauris, T. M. 2014, MNRAS, 438, L86, doi: 10.1093/mnrasl/slt164

Fritz, G., Henry, R. C., Meekins, J. F., Chubb, T. A., & Friedman, H. 1969, PASP, 81, 539

Fruchter, A. S., Stinebring, D. R., & Taylor, J. H. 1988, Nature, 333, 237, doi: 10.1038/333237a0

Fruck, C., Gaug, M., Zanin, R., et al. 2014, arXiv e-prints, arXiv:1403.3591. https://arxiv.org/abs/1403.3591

Funk, S., Hermann, G., Hinton, J., et al. 2004, Astroparticle Physics, 22, 285, doi: 10.1016/j.astropartphys.2004.08.001

Gaug, M. 2006, PhD thesis, Autonomous University of Barcelona

Ge, C., Liu, R.-Y., Niu, S., Chen, Y., & Wang, X.-Y. 2021, The Innovation, 2, 100118, doi: 10.1016/j.xinn.2021.100118

Gold, T. 1968, Nature, 218, 731, doi: 10.1038/218731a0

Goldreich, P., & Julian, W. H. 1969, ApJ, 157, 869, doi: 10.1086/150119

Gotthelf, E. V., & Bogdanov, S. 2017, ApJ, 845, 159, doi: 10.3847/1538-4357/aa813c

Greisen, K. 1966, Phys. Rev. Lett., 16, 748, doi: 10.1103/PhysRevLett.16.748

Gügercinoğlu, E., Ge, M. Y., Yuan, J. P., & Zhou, S. Q. 2020, arXiv e-prints, arXiv:2011.14788. https://arxiv.org/abs/2011.14788

Guillemot, L., & Tauris, T. M. 2014, MNRAS, 439, 2033, doi: 10.1093/mnras/stu082

H. E. S. S. Collaboration, Abdalla, H., Aharonian, F., et al. 2018a, A&A, 620, A66, doi: 10.1051/0004-6361/201732153

—. 2018b, A&A, 620, A66, doi: 10.1051/0004-6361/201732153

Haefner, D., Schweizer, T., Shayduk, M., Mirzoyan, R., & Teshima, M. 2012, IEEE Transactions on Nuclear Science, 59, 289, doi: 10.1109/TNS.2011.2182619

Halpern, J. P., Camilo, F., Gotthelf, E. V., et al. 2001a, ApJL, 552, L125, doi: 10.1086/320347

Halpern, J. P., Gaidos, E., Sheffield, A., Price-Whelan, A. M., & Bogdanov, S. 2013, The Astronomer's Telegram, 5514, 1

Halpern, J. P., Gotthelf, E. V., Leighly, K. M., & Helfand, D. J. 2001b, ApJ, 547, 323, doi: 10.1086/318361

Harding, A., & Muslimov, A. 2005, Ap&SS, 297, 63, doi: 10.1007/s10509-005-7576-z

Harding, A. K. 2013, Frontiers of Physics, 8, 679, doi: 10.1007/s11467-013-0285-0

Harding, A. K., & Kalapotharakos, C. 2015, ApJ, 811, 63, doi: 10.1088/0004-637X/811/1/63

Harding, A. K., Kalapotharakos, C., Barnard, M., & Venter, C. 2018, ApJL, 869, L18, doi: 10.3847/2041-8213/aaf3b2

Harding, A. K., & Muslimov, A. G. 2011, ApJ, 743, 181, doi: 10.1088/0004-637X/743/2/181

Harding, A. K., Stern, J. V., Dyks, J., & Frackowiak, M. 2008, ApJ, 680, 1378, doi: 10.1086/588037

Harding, A. K., Usov, V. V., & Muslimov, A. G. 2005, ApJ, 622, 531, doi: 10.1086/427840

Hartman, R. C., Bertsch, D. L., Bloom, S. D., et al. 1999, apjs, 123, 79, doi: 10.1086/313231

Haskell, B., & Patruno, A. 2017, Phys. Rev. Lett., 119, 161103, doi: 10.1103/PhysRevLett.119.161103

Heck, D., Knapp, J., Capdevielle, J. N., Schatz, G., & Thouw, T. 1998, CORSIKA: a Monte Carlo code to simulate extensive air showers. (Forschungszentrum Karlsruhe Report)

Hess, V. F. 1912, Phys. Z., 13, 1084

Hessels, J. W. T., Ransom, S. M., Stairs, I. H., et al. 2006, in American Astronomical Society Meeting Abstracts, Vol. 207, American Astronomical Society Meeting Abstracts #207, 209.07

Hillas, A. M. 1984, ARA&A, 22, 425, doi: 10.1146/annurev.aa.22.090184.002233

Hirotani, K. 2008, ApJL, 688, L25, doi: 10.1086/595000

—. 2011, ApJL, 733, L49, doi: 10.1088/2041-8205/733/2/L49

—. 2013, ApJ, 766, 98, doi: 10.1088/0004-637X/766/2/98

Hobbs, G., Edwards, R., & Manchester, R. 2006a, Chinese Journal of Astronomy and Astrophysics Supplement, 6, 189

Hobbs, G. B., Edwards, R. T., & Manchester, R. N. 2006b, MNRAS, 369, 655, doi: 10.1111/j.1365-2966.2006.10302.x

Holder, J., Acciari, V. A., Aliu, E., et al. 2008, in American Institute of Physics Conference Series, Vol. 1085, American Institute of Physics Conference Series, ed. F. A. Aharonian, W. Hofmann, & F. Rieger, 657–660, doi: 10.1063/1.3076760

Howard, W. E., Staelin, D. H., & Reifenstein, E. C. 1968, iaucirc, 2110, 2

James, F. 1994, CERN Program Library Office

Jaodand, A., Archibald, A. M., Hessels, J. W. T., et al. 2016, ApJ, 830, 122, doi: 10.3847/0004-637X/830/2/122

Jaodand, A. D., Hernández Santisteban, J. V., Archibald, A. M., et al. 2021, arXiv e-prints, arXiv:2102.13145. https://arxiv.org/abs/2102.13145

Jennings, R. J., Kaplan, D. L., Chatterjee, S., Cordes, J. M., & Deller, A. T. 2018, ApJ, 864, 26, doi: 10.3847/1538-4357/aad084

Johnson, T. J., Ray, P. S., Roy, J., et al. 2015, ApJ, 806, 91, doi: 10.1088/0004-637X/806/1/91

Joncas, G., & Higgs, L. A. 1990, AAPS, 82, 113

Kang, M.-M., Qiao, B.-Q., Yao, Y.-H., et al. 2020, ApJ, 900, 67, doi: 10.3847/1538-4357/aba529

Katagiri, H., Enomoto, R., Ksenofontov, L. T., et al. 2005, ApJL, 619, L163, doi: 10.1086/427980

Kennedy, M. R., Clark, C. J., Voisin, G., & Breton, R. P. 2018, MNRAS, 477, 1120, doi: 10.1093/mnras/sty731

Kirk, J. G., Lyubarsky, Y., & Petri, J. 2009, The Theory of Pulsar Winds and Nebulae, Vol. 357 (Becker, Werner), 421, doi: 10.1007/978-3-540-76965-1_16

Kirsch, M. G. F., Kendziorra, E., & Staubert, R. 2004, in Young Neutron Stars and Their Environments, ed. F. Camilo & B. M. Gaensler, Vol. 218, 331

Knödlseder, J., Mayer, M., Deil, C., et al. 2016, A&A, 593, A1, doi: 10.1051/0004-6361/201628822

Konar, S., & Bhattacharya, D. 1997, MNRAS, 284, 311, doi: 10.1093/mnras/284.2.311

Konar, S., & Chahal, M. 2019, Research Notes of the American Astronomical Society, 3, 88, doi: 10.3847/2515-5172/ab2c06

Kothes, R., Uyaniker, B., & Pineault, S. 2001, ApJ, 560, 236, doi: 10.1086/322511

Kuiper, L., Hermsen, W., Cusumano, G., et al. 2001, A&A, 378, 918, doi: 10.1051/0004-6361:20011256

Kuiper, L., Hermsen, W., & Stappers, B. 2003, in Pulsars, AXPs and SGRs Observed with BeppoSAX and Other Observatories, ed. G. Cusumano, E. Massaro, & T. Mineo, 31–36

Kuiper, L., Hermsen, W., Verbunt, F., & Belloni, T. 1998, A&A, 336, 545

Kuiper, L., Hermsen, W., Verbunt, F., et al. 2002, ApJ, 577, 917, doi: 10.1086/342220

—. 2000, A&A, 359, 615. https://arxiv.org/abs/astro-ph/0005338

Lange, C., Camilo, F., Wex, N., et al. 2001, MNRAS, 326, 274, doi: 10.1046/j.1365-8711.2001.04606.x

Lattimer, J. M. 2004, Science, 304, 536–542, doi: 10.1126/science.1090720

Lattimer, J. M., & Prakash, M. 2001, ApJ, 550, 426, doi: 10.1086/319702

Li, T. P., & Ma, Y. Q. 1983, ApJ, 272, 317, doi: 10.1086/161295

Li, X., Lu, F., & Li, Z. 2008, The Astrophysical Journal, 682, 1166–1176, doi: 10.1086/589495

Li, Y., Zhang, B., & Lü, H.-J. 2016, apjs, 227, 7, doi: 10.3847/0067-0049/227/1/7

Limyansky, B. 2019, in AAS/High Energy Astrophysics Division, Vol. 17, AAS/High Energy Astrophysics Division, 109.32

Linares, M. 2014, ApJ, 795, 72, doi: 10.1088/0004-637X/795/1/72

Linares, M., Bahramian, A., Heinke, C., et al. 2014, MNRAS, 438, 251, doi: 10.1093/mnras/stt2167

Longair, M. S. 2002, Frascati Phys. Ser., 24, 3

Longair, M. S. 2011, High Energy Astrophysics (Cambridge University Press)

Lopez-Coto, R. 2015, PhD thesis, Universitat Autonoma de Barcelona

López-Coto, R., Mazin, D., Paoletti, R., Blanch Bigas, O., & Cortina, J. 2016, Journal of Instrumentation, 11, P04005, doi: 10.1088/1748-0221/11/04/P04005

López-Oramas, A., Bulgarelli, A., Chaty, S., et al. 2021, arXiv e-prints, arXiv:2108.03911. https://arxiv.org/abs/2108.03911

Lorimer, D. R. 2009, Radio Pulsar Statistics, Vol. 357 (Springer), 1, doi: 10.1007/978-3-540-76965-1_1

Lorimer, D. R., & Kramer, M. 2004, Handbook of Pulsar Astronomy, Vol. 4 (Cambridge University Press)

Lundmark, K. 1921, PASP, 33, 225, doi: 10.1086/123101

Lyne, A., & Graham-Smith, F. 2012, Pulsar Astronomy (Cambridge University Press)

Lyne, A. G., & Graham-Smith, F. 1990, Pulsar astronomy (Cambridge University Press)

MAGIC Collaboration, Acciari, V. A., Ansoldi, S., et al. 2019, Nature, 575, 455, doi: 10.1038/s41586-019-1750-x

—. 2020, A&A, 643, L14, doi: 10.1051/0004-6361/202039131

Manchester, R. N., Hobbs, G. B., Teoh, A., & Hobbs, M. 2005, aj, 129, 1993, doi: 10.1086/428488

Marandon, V., Jardin-Blicq, A., & Schoorlemmer, H. 2019, in International Cosmic Ray Conference, Vol. 36, 36th International Cosmic Ray Conference (ICRC2019), 736. https://arxiv.org/abs/1908.07634

Masetti, N., Morelli, L., Palazzi, E., et al. 2006, A&A, 459, 21, doi: 10.1051/0004-6361:20066055

Mazin, D., Cortina, J., & Teshima, M. 2017, in American Institute of Physics Conference Series, Vol. 1792, 6th International Symposium on High Energy Gamma-Ray Astronomy, 080001, doi: 10.1063/1.4969022

Mazin, D., Tescaro, D., Garczarczyk, M., Giavitto, G., & Sitarek, J. 2014, arXiv e-prints, arXiv:1410.5073. https://arxiv.org/abs/1410.5073

McCann, A. 2011, in International Cosmic Ray Conference, Vol. 7, International Cosmic Ray Conference, 208, doi: 10.7529/ICRC2011/V07/1090

McEnery, J., van der Horst, A., Dominguez, A., et al. 2019, in Bulletin of the American Astronomical Society, Vol. 51, 245. https://arxiv.org/abs/1907.07558

Millikan, R. A., & Cameron, G. H. 1926, Physical Review, 28, 851, doi: 10.1103/PhysRev.28.851

Mineo, T., Cusumano, G., Kuiper, L., et al. 2000, A&A, 355, 1053

Mirabel, I. F. 2006, Science, 312, 1759, doi: 10.1126/science.1129815

Miraval Zanon, A., Campana, S., Ridolfi, A., D'Avanzo, P., & Ambrosino, F. 2020, A&A, 635, A30, doi: 10.1051/0004-6361/201936356

Mirzoyan, R. 1997, in International Cosmic Ray Conference, Vol. 7, International Cosmic Ray Conference, 265

Muraishi, H., Tanimori, T., Yanagita, S., et al. 2000, A&A, 354, L57. https://arxiv.org/abs/astro-ph/0001047

Naumann-Godó, M., Beilicke, M., Hauser, D., Lemoine-Goumard, M., & de Naurois, M. 2008, in American Institute of Physics Conference Series, Vol. 1085, American Institute of Physics Conference Series, ed. F. A. Aharonian, W. Hofmann, & F. Rieger, 304–307, doi: 10.1063/1.3076666

Navarro, J., de Bruyn, A. G., Frail, D. A., Kulkarni, S. R., & Lyne, A. G. 1995, ApJL, 455, L55, doi: 10.1086/309816

Nolan, P. L., Arzoumanian, Z., Bertsch, D. L., et al. 1993, ApJ, 409, 697, doi: 10.1086/172699

Oña-Wilhemi, E., de los Reyes, R., Contreras, J. L., et al. 2005, in International Cosmic Ray Conference, Vol. 4, 29th International Cosmic Ray Conference (ICRC29), Volume 4, 247

Observatory, C. T. A., & Consortium, C. T. A. 2016, CTAO Instrument Response Functions - version prod3b-v2, prod3b-v2/v1.0.0, Zenodo, doi: 10.5281/zenodo.5163273

—. 2021, CTAO Instrument Response Functions - prod5 version v0.1, v0.1, Zenodo, doi: 10.5281/zenodo.5499840

Pacini, D. 1912, Il Nuovo Cimento, 3, 93, doi: 10.1007/BF02957440

Pacini, F. 1968, Nature, 219, 145, doi: 10.1038/219145a0

Pallanca, C., Dalessandro, E., Ferraro, F. R., Lanzoni, B., & Beccari, G. 2013, ApJ, 773, 122, doi: 10.1088/0004-637X/773/2/122

Papitto, A., & de Martino, D. 2020, arXiv e-prints, arXiv:2010.09060. https://arxiv.org/abs/2010.09060

Papitto, A., & Torres, D. F. 2015, ApJ, 807, 33, doi: 10.1088/0004-637X/807/1/33

Papitto, A., Hessels, J. W. T., Burgay, M., et al. 2013a, The Astronomer's Telegram, 5069, 1

Papitto, A., Ferrigno, C., Bozzo, E., et al. 2013b, Nature, 501, 517, doi: 10.1038/nature12470

Papitto, A., Ambrosino, F., Stella, L., et al. 2019, ApJ, 882, 104, doi: 10.3847/1538-4357/ab2fdf

Patruno, A., Archibald, A. M., Hessels, J. W. T., et al. 2014, ApJL, 781, L3, doi: 10.1088/2041-8205/781/1/L3

Pellizzoni, A., Pilia, M., Possenti, A., et al. 2009, ApJL, 695, L115, doi: 10.1088/0004-637X/695/1/L115

Pétri, J. 2012, MNRAS, 424, 2023, doi: 10.1111/j.1365-2966.2012.21350.x

Pineault, S., & Joncas, G. 2000, aj, 120, 3218, doi: 10.1086/316863

Pons, J. A., Viganò, D., & Rea, N. 2013, Nature Physics, 9, 431, doi: 10.1038/nphys2640

Potekhin, A. Y., Pons, J. A., & Page, D. 2015, Space Sci. Rev., 191, 239, doi: 10.1007/s11214-015-0180-9

Price, D. C., Flynn, C., & Deller, A. 2021, PASA, 38, e038, doi: 10.1017/pasa.2021.33

Ptuskin, V. S., Rogovaya, S. I., Zirakashvili, V. N., et al. 1993, A&A, 268, 726

Radhakrishnan, V., & Srinivasan, G. 1982, Current Science, 51, 1096

Roberts, M. S. E. 2013, in Neutron Stars and Pulsars: Challenges and Opportunities after 80 years, ed. J. van Leeuwen, Vol. 291, 127–132, doi: 10.1017/S174392131202337X

Rolke, W. A., & López, A. M. 2001, Nuclear Instruments and Methods in Physics Research A, 458, 745, doi: 10.1016/S0168-9002(00)00935-9

Rolke, W. A., López, A. M., & Conrad, J. 2005, Nuclear Instruments and Methods in Physics Research A, 551, 493, doi: 10.1016/j.nima.2005.05.068

Romani, R. W. 1996, ApJ, 470, 469, doi: 10.1086/177878

Romani, R. W., & Sanchez, N. 2016, ApJ, 828, 7, doi: 10.3847/0004-637X/828/1/7

Rowan, D. M., Ghazi, Z., Lugo, L., et al. 2020, ApJ, 892, 150, doi: 10.3847/1538-4357/ab718f

Roy, J., Ray, P. S., Bhattacharyya, B., et al. 2015, ApJL, 800, L12, doi: 10.1088/2041-8205/800/1/L12

Saito, Y., Kawai, N., Kamae, T., et al. 1997, ApJL, 477, L37, doi: 10.1086/310512

Saz Parkinson, P., Belfiore, A., Fidalgo, D., et al. 2017, in Proceedings of the 7th International Fermi Symposium, 8. https://arxiv.org/abs/1712.06808

Schutte, W. D., & Swanepoel, J. W. H. 2016, MNRAS, 461, 627, doi: 10.1093/mnras/stw1335

Shahbaz, T., Dallilar, Y., Garner, A., et al. 2018, MNRAS, 477, 566, doi: 10.1093/mnras/sty562

Shahbaz, T., Linares, M., Nevado, S. P., et al. 2015, MNRAS, 453, 3461, doi: 10.1093/mnras/stv1686

Sironi, L., Keshet, U., & Lemoine, M. 2015, Space Sci. Rev., 191, 519, doi: 10.1007/s11214-015-0181-8

Sitarek, J., Gaug, M., Mazin, D., Paoletti, R., & Tescaro, D. 2013, Nuclear Instruments and Methods in Physics Research A, 723, 109, doi: 10.1016/j.nima.2013.05.014

Spir-Jacob, M., Djannati-Ataï, A., Mohrmann, L., et al. 2019a, arXiv e-prints, arXiv:1908.06464. https://arxiv.org/abs/1908.06464

—. 2019b, arXiv e-prints, arXiv:1908.06464. https://arxiv.org/abs/1908.06464

Staelin, D. H., & Reifenstein, Edward C., I. 1968, Science, 162, 1481, doi: 10.1126/science.162.3861.1481

Stairs, I. H., Thorsett, S. E., & Camilo, F. 1999, apjs, 123, 627, doi: 10.1086/313245

Stappers, B. W., Archibald, A., Bassa, C., et al. 2013, The Astronomer's Telegram, 5513, 1

Stappers, B. W., Archibald, A. M., Hessels, J. W. T., et al. 2014, ApJ, 790, 39, doi: 10.1088/0004-637X/790/1/39

Strader, J., Li, K.-L., Chomiuk, L., et al. 2016, ApJ, 831, 89, doi: 10.3847/0004-637X/831/1/89

Sturrock, P. A. 1971, ApJ, 164, 529, doi: 10.1086/150865

Takata, J., Li, K. L., Leung, G. C. K., et al. 2014, ApJ, 785, 131, doi: 10.1088/0004-637X/785/2/131

Tam, P. H. T., Hui, C. Y., Huang, R. H. H., et al. 2010, ApJL, 724, L207, doi: 10.1088/2041-8205/724/2/L207

Tavani, M. 1991, ApJL, 379, L69, doi: 10.1086/186156

Tavani, M., Barbiellini, G., Argan, A., et al. 2009, Astronomy & Astrophysics, 502, 995–1013, doi: 10.1051/0004-6361/200810527

Thompson, D. J., Bertsch, D. L., Dingus, B. L., et al. 1995, apjs, 101, 259, doi: 10.1086/192240

Thorstensen, J. R., & Armstrong, E. 2005, aj, 130, 759, doi: 10.1086/431326

Tomozawa, Y. 2013, Journal of Modern Physics, 4, 385, doi: 10.4236/jmp.2013.43054

Torres, D. F. 2018, Nature Astronomy, 2, 247, doi: 10.1038/s41550-018-0384-5

Torres, D. F., Ji, L., Li, J., et al. 2017, ApJ, 836, 68, doi: 10.3847/1538-4357/836/1/68

Torres, D. F., Viganò, D., Coti Zelati, F., & Li, J. 2019, MNRAS, 489, 5494, doi: 10.1093/mnras/stz2403

Trimble, V. 1973, PASP, 85, 579, doi: 10.1086/129507

Verbiest, J. P. W., & Lorimer, D. R. 2014, MNRAS, 444, 1859, doi: 10.1093/mnras/stu1560

Verbunt, F., Kuiper, L., Belloni, T., et al. 1996, A&A, 311, L9

VERITAS Collaboration, Acciari, V. A., Aliu, E., et al. 2009, Nature, 462, 770, doi: 10.1038/nature08557

VERITAS Collaboration, Aliu, E., Arlen, T., et al. 2011, Science, 334, 69, doi: 10.1126/science.1208192

Vidaña, I. 2018, European Physical Journal Plus, 133, 445, doi: 10.1140/epjp/i2018-12329-x

Viganò, D., Torres, D. F., Hirotani, K., & Pessah, M. E. 2015a, MNRAS, 447, 2649, doi: 10.1093/mnras/stu2565

—. 2015b, MNRAS, 447, 1164, doi: 10.1093/mnras/stu2456

Vink, J. 2020, Physics and Evolution of Supernova Remnants, doi: 10.1007/978-3-030-55231-2

Wagner, R. M. 2006, PhD thesis, Max-Planck-Institut für Physik, Föhringer Ring 6, 80805 München, Germany

Webb, N. A., Olive, J. F., & Barret, D. 2004, A&A, 417, 181, doi: 10.1051/0004-6361:20040032

Weekes, T. C. 2003, Very high energy gamma-ray astronomy (CRC Press)

Weekes, T. C., Cawley, M. F., Fegan, D. J., et al. 1989, ApJ, 342, 379, doi: 10.1086/167599

Wilks, S. S. 1938, Ann. Math. Statist., 9, 60, doi: 10.1214/aoms/1177732360

Will, M. 2017, in European Physical Journal Web of Conferences, Vol. 144, European Physical Journal Web of Conferences, 01002, doi: 10.1051/epjconf/201714401002

Wood, M., Caputo, R., Charles, E., et al. 2017, in International Cosmic Ray Conference, Vol. 301, 35th International Cosmic Ray Conference (ICRC2017), 824. https://arxiv.org/abs/1707.09551

Xin, Y., Zeng, H., Liu, S., Fan, Y., & Wei, D. 2019, ApJ, 885, 162, doi: 10.3847/1538-4357/ab48ee

Xing, Y., & Wang, Z. 2015, The Astrophysical Journal, 808, 17, doi: 10.1088/0004-637x/808/1/17

Xing, Y., Wang, Z.-X., & Takata, J. 2018, Research in Astronomy and Astrophysics, 18, 127, doi: 10.1088/1674-4527/18/10/127

Yao, J. M., Manchester, R. N., & Wang, N. 2017, ApJ, 835, 29, doi: 10.3847/1538-4357/835/1/29

Zabalza, V. 2015, in International Cosmic Ray Conference, Vol. 34, 34th International Cosmic Ray Conference (ICRC2015), 922. https://arxiv.org/abs/1509.03319

Zampieri, L., Burtovoi, A., Fiori, M., et al. 2019, MNRAS, 485, L109, doi: 10.1093/mnrasl/slz043

Zampieri, L., Naletto, G., Barbieri, C., et al. 2015, in Society of Photo-Optical Instrumentation Engineers (SPIE) Conference Series, Vol. 9504, Photon Counting Applications 2015, ed. I. Prochazka, R. Sobolewski, & R. B. James, 95040C, doi: 10.1117/12.2179547

Zanin, R., Carmona, E., Sitarek, J., et al. 2013, in International Cosmic Ray Conference, Vol. 33, International Cosmic Ray Conference, 2937

Zatsepin, G. T., & Kuz'min, V. A. 1966, Soviet Journal of Experimental and Theoretical Physics Letters, 4, 78